BENEFICIATION OF SELECTED PESTICIDES AND AN ANTIHYPERLIPIDEMIC AGENT *VIA* CYCLODEXTRIN COMPLEXATION AND CO-CRYSTALLISATION

Vaughan Jean Maurel

Thesis presented for the degree of

DOCTOR OF PHILOSOPHY

In the Department of Chemistry

University of Cape Town

September 2016

Supervisors:

Professor Mino R. Caira

Professor Susan A. Bourne

"The chymists are a strange class of mortals, impelled by an almost insane impulse to see their pleasures amid smoke and vapour, soot and flame, poisons and poverty. Yet among all these evils I seem to live so sweetly that may I die if I were to change places with the Persian King"

Johann Joachim Becher
Physica Subterranea, 1667

ACKNOWLEDGEMENTS

My thanks go to:

Professor Mino Caira for his excellent supervision, inspiration, guidance and infinite patience.

Professor Susan Bourne for her co-supervision, guidance and support.

Dr Clive Oliver for all his help and advice on crystallography.

Dr Hong Su for the single crystal data collection and help with processing data.

Professor Luigi Nassimbeni for help whenever it was asked for and inspiration in all matters scientific.

Professor Elba Buján and Professor Rita Hoyos de Rossi for their support and guidance during my time at the Universidad Nacional de Córdoba.

Nikki Dare for her help with the initial synthesis of some of the products presented here.

Dr Dyanne Cruickshank for teaching me much of what I now know and her friendship over the years.

Colleagues past and present from the Centre for Supramolecular Chemistry Research.

Savannah Zacharias for countless cups of tea, sunshine and kind words.

Aneesa Omar for coffee, cooking and conversations to keep me grounded and sane, a fresh perspective and challenging my ideas. Thank you for a great friendship.

My partner Cascia Day. I thank you for the endless support, inspiration and guiding me through the maze that is life. Without you as my beacon I would be lost.

And my parents, without whom I would not be the man I am today.

The financial assistance of the National Research Foundation (NRF) towards this research is hereby acknowledged. Opinions expressed and conclusion arrived at, are those of the author and not necessarily to be attributed to the NRF.

Financial assistance from The University of Cape Town.

Parts of this thesis have been presented at the following conferences:

23rd Congress and General Assembly of the International Union of Crystallography, Montreal, Canada, 5-12 August 2014

Poster Presentation: *Non-covalent interactions of Acipimox in Multi-component Crystals*, V. J. Maurel, N. A. Dare, S. A. Bourne, M. R. Caira

The SACI and RSC Western Cape Young Chemists Symposium, October 2014

Poster Presentation: *Non-covalent interactions of Acipimox in Multi-component Crystals*, V. J. Maurel, N. A. Dare, S. A. Bourne, M. R. Caira

The SACI and RSC Western Cape Young Chemists Symposium, 24th November 2011

Poster Presentation: *Cyclodextrin Inclusion of Fenthion: A Physicochemical Study*, V. J. Maurel, M. R. Caira, S. A. Bourne

Parts of this thesis have been published:

D. L. Cruickshank, N. M. Rougier, V. J. Maurel, R. H. de Rossi, E. I. Buján, S. A. Bourne, M. R. Caira; Permethylated β-cyclodextrin/pesticide complexes: X-ray structures and thermogravimetric assessment of kinetic parameters for complex dissociation. *J Incl Phenom Macrocycl Chem*, 2013, **75**, 47-56.

Vaughan Jean Maurel *September 2016*

BENEFICIATION OF SELECTED PESTICIDES AND AN ANTIHYPERLIPIDEMIC AGENT *VIA* CYCLODEXTRIN COMPLEXATION AND CO-CRYSTALLISATION

The applications of many bioactive molecules are limited by their undesirable physicochemical properties, such as poor aqueous solubility and low thermal stability. The agrochemicals methyl-2,5-dichlorobenzoate (fungicide, DCB) and fenthion (insecticide), as well as the medicinal compound acipimox (lipid-lowering agent) were selected for study in this context.

The cyclodextrin (CD) complexes γ-CD/DCB, 2,6-dimethylated-β-CD/DCB, β-CD/fenthion, permethylated α-CD/fenthion and permethylated β-CD/fenthion, were synthesised. ^{1}H-NMR spectroscopy, thermogravimetric analysis (TGA), differential scanning calorimetry (DSC) and hot stage microscopy (HSM) were used to assess their stoichiometries and thermal behaviours. The complexes 2,6-dimethylated-β-CD/DCB, permethylated α-CD/fenthion and permethylated β-CD/fenthion have 1:1 host-guest stoichiometries, while those for γ-CD/DCB and β-CD/fenthion are 3:4 and 2:1 respectively. Single crystal X-ray structures were elucidated to investigate the modes of DCB inclusion and crystal packing. All of the solid complexes displayed higher thermal stabilities than those of the untreated pesticides. Furthermore, the volatility of the insecticide fenthion (a liquid at 25 °C) was significantly reduced by its transformation to a solid on CD-complex formation.

The solution-state behaviour of fenthion was qualitatively evaluated using UV-visible spectrophotometry and induced circular dichroism. Phase solubility profiles at 25 °C were of type B_S for solubilisation of DCB by β-CD and (2-hydroxypropyl)-β-CD, and for solubilisation of fenthion by β-CD, the respective 1:1 association constants being 737 ± 108 M^{-1}, 412 ± 53 M^{-1} and 789 ± 170 M^{-1}. For solubilisation of fenthion by (2-hydroxypropyl)-β-CD and randomly-methylated β-CD, A_N- and A_P-type behaviours were recorded respectively, with association constants 1863 ± 26 M^{-1} and 3582 ± 106 M^{-1} respectively.

Eight multi-component crystalline systems (co-crystals and salts) of acipimox were isolated *via* its reaction with co-formers 4-aminobenzamide, 4-aminopyridine, benzamide, isonicotinamide, tranexamic acid and urea. NMR spectroscopy revealed 1:1 stoichiometries for all products. Their designation as salts or co-crystals was based on unequivocal evidence gleaned from single crystal X-ray structural studies, these assignments being confirmed by infrared spectroscopy. The melting points and decomposition temperatures of the products containing the coformers 4-aminobenzamide, 4-aminopyridine, isonicotinamide and tranexamic acid were significantly higher than those of untreated acipimox. Equilibrium aqueous solubilities of the multi-component systems ranged from 0.31 to 2.77 times those of untreated acipimox.

COMPOUND CODE NAMES

Listed below are the code names assigned to the products in this thesis:

GCDDCB	γ-cyclodextrin/2,5-dichlorobenzoic acid methyl ester
DMBDCB	DIMEB/2,5-dichlorobenzoic acid methyl ester
BCDFEN	β-cyclodextrin/fenthion
TMAFEN	TRIMEA/fenthion
TMBFEN	TRIMEB/fenthion
ACPABEN	Acipimox/4-aminobenzamide
ACPAPYR	Acipimox/4-aminopyridine
ACPAPYR-W	Acipimox/4-aminopyridine dihydrate
ACPBEN	Acipimox/benzamide hemihydrate
ACPISO	Acipimox/isonicotinamide
ACPTRA	Acipimox/tranexamic acid
ACPTRA-W	Acipimox/tranexamic acid hydrate
ACPUREA	Acipimox/urea

TABLE OF CONTENTS

CHAPTER 1 – INTRODUCTION

SUPRAMOLECULAR CHEMISTRY

The first use of the term "supramolecular chemistry" was to describe the "chemistry of molecular assemblies and of the intermolecular bond" by Jean-Marie Lehn in 1978.[1] It has also been expressed as "chemistry beyond the molecule", "the chemistry of the non-covalent bond" and "non-molecular chemistry".[2] Under such definitions, the vast applications of supramolecular chemistry include, but are not limited to, host-guest systems, molecular devices and machines, self-assembly systems and nanochemistry.[2] This project is focused on two of the sub-categories, namely cyclodextrin inclusion complexes and multi-component crystalline systems (salts and co-crystals).

CYCLODEXTRIN INCLUSION COMPLEXES

Cyclodextrins are macrocyclic structures comprising glucopyranose subunits linked through α-1,4-glycosidic bonds.[3–5] The native cyclodextrins are composed of six, seven or eight of these subunits and are known as α-cyclodextrin, β-cyclodextrin and γ-cyclodextrin, respectively (Figure 1.1a. and Figure 1.1b.). The glucopyranose subunits adopt a $^4C_1$ chair conformation. This results in a truncated cone structure (Figure 1.1c.) whereby the interior cavity is lined by C3-H and C5-H atoms and the lone pairs of the O4 atoms (see Figure 1.1d. for labelling), giving rise to a hydrophobic interior cavity. The hydrophilic -OH groups are located on the primary and secondary rims of the cyclodextrin molecules, which results in the exterior of the molecule having hydrophilic nature.[3–5] The importance of this separation of the hydrophobic and hydrophilic areas of the cyclodextrin is that it allows the formation of inclusion complexes with hydrophobic molecules or moieties.[3–8] Another feature arising from the $^4C_1$ conformation of the glucopyranose subunits is the formation of the hydrogen bonding along the secondary rim between the O2-H and O3-H hydroxyl groups on neighbouring residues. These hydroxyl residues act as either acceptors or donors in the hydrogen bond resulting in both O2-H···O3′ and O2···H-O3′ hydrogen bonds. These have been described as 'flip-flop hydrogen bonds'.[4,9,10] The presence of these hydrogen bonds stabilises the cyclodextrin and slightly limits its solubility. In α-cyclodextrin hydrate structures this hydrogen bonding is only partially complete at the secondary rim. The hydrogen bonding of the secondary rim is complete in β-cyclodextrin, causing it to have the lowest solubility of the three. The largest, γ-cyclodextrin, is a more flexible structure and therefore is the most soluble.[3] The properties of the native cyclodextrins are presented in Table 1.1.

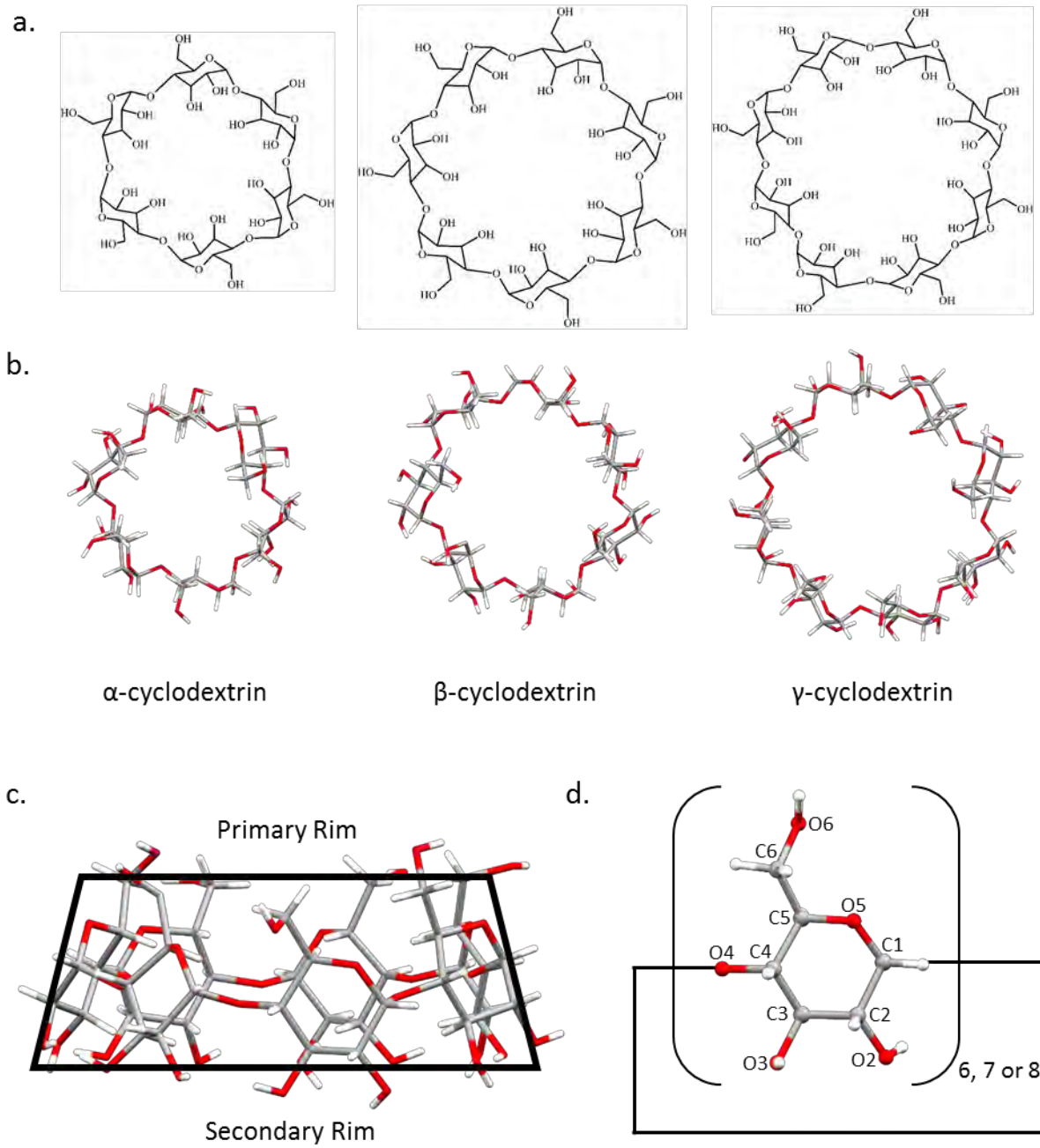

Figure 1.1: a. Chemical structures of the cyclodextrins α-, β- and γ-cyclodextrin, b. the cyclodextrins α-, β- and γ-cyclodextrin showing the macrocyclic structure, c. toroidal shape of a cyclodextrin molecule illustrating the primary and secondary rim and d. labelling scheme of a glucopyranose subunit

Table 1.1: Properties of native cyclodextrins[3,5]

Property	α-cyclodextrin	β-cyclodextrin	γ-cyclodextrin
Number of units	6	7	8
Molar mass (g mol^{-1})	972	1135	1297
Aqueous solubility (mg ml^{-1})‡	127	18.8	256
Cavity diameter (Å)	4.7-5.3	6.0-6.5	7.5-8.3
Torus height (Å)	7.9 ± 0.1	7.9 ± 0.1	7.9 ± 0.1
Cavity volume ($Å^3$)	174	262	427

‡ measured at 25 °C

CHEMICALLY MODIFIED CYCLODEXTRINS

The derivatised cyclodextrins are synthesised by functionalisation of the primary and secondary hydroxyl groups of the native cyclodextrins. The derivatisation with methyl groups can greatly alter the physical properties of the parent cyclodextrin. A noteworthy change in property is the negative temperature coefficient of their aqueous solubility, resulting in higher solubility at lower temperatures. Saenger *et al*.[11,12] have suggested that the formation of a channel type clathrate hydrate enclosing the methylated cyclodextrins is responsible for this phenomenon. The researchers believe that upon heating an aqueous solution of the methylated cyclodextrins the clathrate water molecules regain mobility allowing the cyclodextrins to aggregate.[11,12] The methylation of the hydroxyl groups also deepens the cavity, extending the hydrophobic region. In this study, three crystalline and two amorphous derivatised cyclodextrins were used.

The crystalline cyclodextrins employed in this study are hexakis(2,3,6-tri-*O*-methyl)-α-cyclodextrin (TRIMEA), heptakis(2,3,6-tri-*O*-methyl)-β-cyclodextrin (TRIMEB) and heptakis(2,6-di-*O*-methyl)-β-cyclodextrin (DIMEB). TRIMEA and TRIMEB are permethylated with the O2, O3 and O6 atoms methylated on all of their glucopyranose residues. The lack of hydroxyl groups disrupts the O2-H···O3′ hydrogen bonding present in the parent cyclodextrins. This destabilises the cyclodextrin allowing greater conformational flexibility. In at least one case the loss of the hydrogen bonding network leads to an inversion of a single methyl glucose residue to the $^1C_4$ chair conformation, seen in the TRIMEB monohydrate structure.[13] The selectively methylated cyclodextrin used in this study, DIMEB, is methylated at the O2 and O6 positions. This allows the structure to maintain the O2···H-O3′ hydrogen bonding network, which stabilises the cyclodextrin. Therefore, DIMEB has a similar conformation and geometry to its parent cyclodextrin, albeit with an extended cavity. A schematic representation of these derivatised cyclodextrins is shown in Figure 1.2.

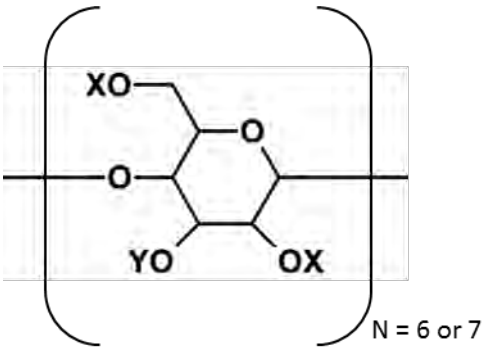

TRIMEA: X, Y = CH_3, N = 6

TRIMEB: X, Y = CH_3, N = 7

DIMEB: X = CH_3, Y = H, N = 7

Figure 1.2: Schematic representation of the methylated cyclodextrins

The two amorphous derivatised cyclodextrins used in this study are randomly methylated-β-cyclodextrin (RAMEB) and 2-hydroxypropyl-β-cyclodextrin (HPBCD). The methylated amorphous cyclodextrin, RAMEB, is often employed as a substitute for DIMEB due to the expense of producing the selectively methylated cyclodextrin. RAMEB is produced on an industrial scale and has been used in the pharmaceutical, cosmetic and agrochemical industries. The use of HPBCD (generally applied as a solubilising agent) has also been evident across these industries. HPBCD is nontoxic and increases bioactive molecule delivery through biological membranes. The extremely high aqueous solubility of HPBCD complexes has been used to create intravenously deliverable drug formulations of poorly soluble drug compounds.[14,15]

CYCLODEXTRIN INCLUSION

Cyclodextrin inclusion complexes form reversibly through non-covalent interactions between a guest and the host molecule (Equation 1.1). Each inclusion complex has a binding constant (also termed: equilibrium constant, association constant, formation constant), K. The binding constant is a measure of the strength of interaction between the host and guest, given by Equation 1.2.

Equation 1.1

$$mG + nH \rightleftharpoons C$$

Equation 1.2

$$K = \frac{[C]}{[G_0 - mC]^m [H_0 - nC]^n}$$

It is understood that several factors drive the host guest complexation reaction. These include hydrophobic interactions, hydrogen bonding, electrostatic interactions, release of high energy water molecules from the interior of the cyclodextrin cavity, released strain energy of the cyclodextrin and van der Waals interactions.[16,17]

BINDING CONSTANTS

To be pharmaceutically relevant the binding constant of the complex must be less than 10 000 M^{-1} so as to not interfere with the pharmacokinetics of the drug upon administration. Fortunately, most cyclodextrin complexes of pharmaceuticals have binding constants between 50 M^{-1} and 2000 M^{-1}, with values greater than 5000 M^{-1} rarely observed.[14] Binding constants are often used as a basic measure for evaluation of a host-guest complexation process and it is therefore imperative to determine this value.

The binding constant can be derived from the results of various experimental methods. UV-Vis spectroscopy can be employed for a guest molecule with a chromophoric moiety. Changes in the molar absorptivity or λ_{max} versus host concentration can be used to calculate the binding constant of the complex. A similar procedure is employed for induced circular dichroism. The formation of an inclusion complex can result in changes in the chemical shifts of the host and/or guest protons in the ^{1}H-NMR spectrum. By measuring these changes and plotting the values against the molar ratio of the host molecules one can evaluate the binding constant and stoichiometry of the complex. Isothermal titration calorimetry allows direct measurement of thermal parameters of complexation from which the binding constants can be calculated.

One of the most readily available methods for binding constant determination is phase solubility analysis, developed by Higuchi and Connors.[18,19] To use this method an excess of the guest compound is added to several cyclodextrin solutions of varying host concentration. This mixture is then agitated until saturation equilibrium is reached. The apparent guest solubility is then determined using an appropriate method (such as UV-Vis spectroscopy or High Performance Liquid Chromatography). The phase solubility profile is then plotted as the apparent concentration of the guest molecule against the increasing concentration of the host. From the profile the complexation behaviour is established and the binding constant can be evaluated. This experimental method will be expanded upon in relevant sections of the research presented.

GEOMETRIC PARAMETERS DESCRIBING CYCLODEXTRINS

Several geometric parameters are employed to describe the conformations of cyclodextrin molecules.[20,21] Once evaluated these are compared with the values obtained for other inclusion complexes and the free host molecules (typically hydrated) to gain a greater understanding of the effect of guest inclusion on the host geometry.

The polygon defined by the O4 atoms is a central feature used to describe the geometric parameters. The distance from the O4 atoms to the centroid generated by the polygon (*l*), the O4···O4′ distance between neighbouring glucose residues (*D*) and the O4···O4′···O4″ angle (ϕ) are

measured using the polygon defined by the O4 atoms and are measures of distortion of the polygon. These geometric parameters can be seen in Figure 1.3. The O4···O4′···O4″···O4‴ torsion angle (*d*) and the deviation from the least-squares plane through the O4 atoms (α), Figure 1.4a., give a measure of planarity of the cyclodextrin polygon. The final parameter defined by the O4 polygon is the tilt angle τ_2 (Figure 1.4b.). This is the angle of intersection of the least-squares plane through the O4 atoms and that through the O4, C4, C1 and O4′ atoms of a glucose ring. The O2···O3′ distance (D_3) gives a measure of the intramolecular hydrogen bonds described above. The final geometric parameter is the torsion angle ω (O5-C5-C6-O6, labels shown in Figure 1.3) whose value indicates the extent to which the C6-O6 bond is directed toward or away from the cyclodextrin cavity.

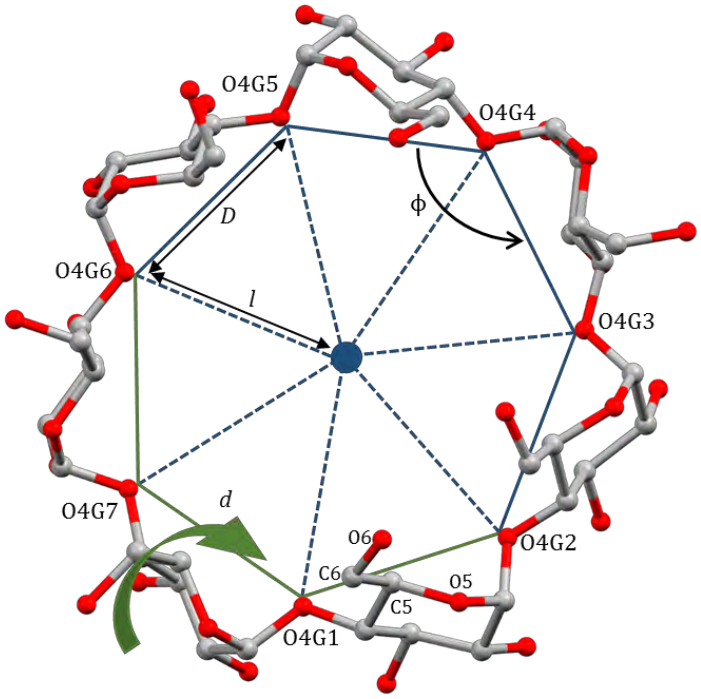

Figure 1.3: Figure of the β-cyclodextrin geometric parameters l, D, ϕ and d as representative of the native cyclodextrins. Hydrogen atoms have been omitted for clarity

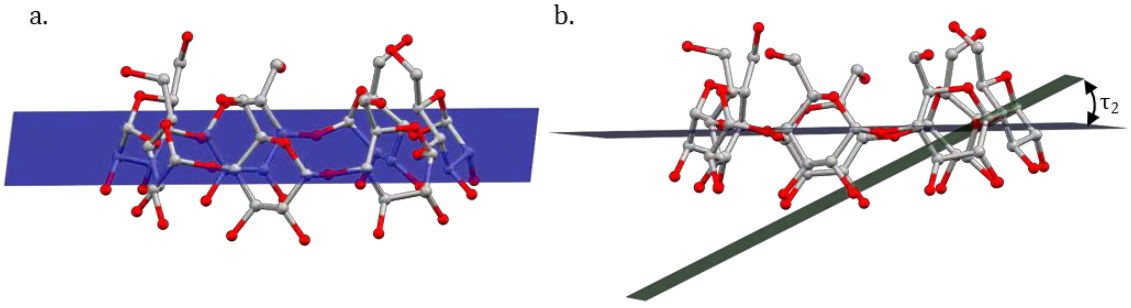

Figure 1.4: a. β-cyclodextrin molecule illustrating a. the O4 least-squares mean plane and b. the tilt angle τ_2 between the O4 least-squares mean plane (blue) and the least-squares plane through O4-C4···C1-O4′ atoms of a glucose residue (green). Hydrogen atoms have been omitted for clarity

In the case of an idealised cyclodextrin molecule the least-squares mean plane would pass through all the O4 atoms. The torsion angles *d* and the deviations of the atoms from the mean O4-plane would be zero and the parameters *l*, *D* and ϕ would be equal for each residue.

A positive value of the torsion angle ω indicates that the group is directed towards the cavity, while a negative value indicates that the group is directed away from the cavity. The tilt angle, τ_2, gives a measure of the inclination of the glucose substituents. The values are generally positive, indicating an inclination of the primary rim of the glucose subunit towards the cavity. The glucose residues of the native cyclodextrins generally all have positive τ_2 values.

PACKING ARRANGEMENTS OF CYCLODEXTRIN COMPLEXES

Cyclodextrin inclusion complexes tend to form monomeric or dimeric structures. These structures pack into two general categories, cage-type and channel-type. In channel-type structures, the cyclodextrin molecules are stacked such that their cavities align to create infinite channels which include the guest molecules. The cyclodextrins within a column are arranged in a head-to-head or head-to-tail manner. The columns are stabilised by hydrogen bonding between the primary and secondary rims of subsequent molecules in head-to-tail arrangements. In head-to-head arrangements, the primary rim hydrogen bonds to the primary rim of the sequential cyclodextrin and similarly at the secondary rim.[5]

The cage-type structures occur when the primary and secondary rims of the cyclodextrin molecules are blocked off by neighbouring cyclodextrin molecules. There are two such motifs, the herringbone- and brickwork-type packing arrangements. Illustrations of these arrangements are shown in Figure 1.5.

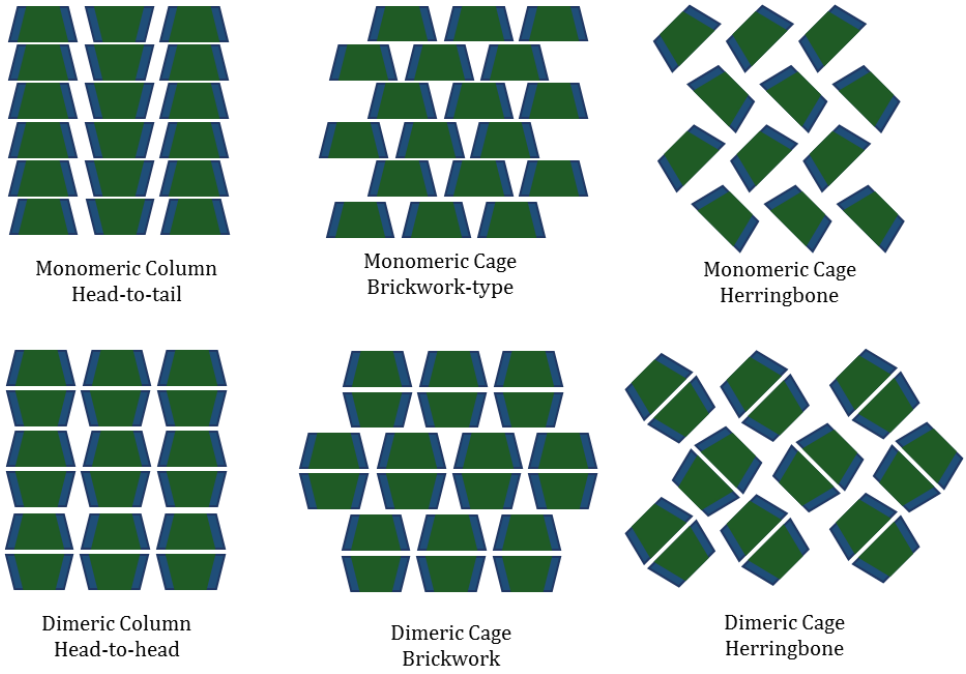

Figure 1.5: Illustrations of cyclodextrin packing arrangements showing common monomeric and dimeric packing motifs

Two cyclodextrin inclusion complexes can be said to be isostructural if the unit cells of the structures have similar dimensions, and the host molecules have similar atomic co-ordinates. The relatively rigid glucose backbone of the host molecules is responsible for the packing arrangement of the inclusion complexes.[22] Isostructural cyclodextrin complexes can have a varying guest molecule and water molecule positions, but very similar host arrangements. Caira[22] and Lubhelwana[23] have characterised several isostructural series of the native and methylated cyclodextrin inclusion complexes. Once a new complex is identified as a member of a particular isostructural series, one can immediately gain a greater understanding of the arrangement of the host molecules within the structure. The dominance of the host molecules on the packing arrangement has the consequence that within an isostructural series, the powder X-ray diffraction (PXRD) patterns of the members have the same principal features, regardless of the guest molecule. One can therefore employ this quick, non-destructive technique to obtain important structural information for an inclusion complex. A further application of the isostructurality of cyclodextrin inclusion complexes is isomorphous replacement (or isostructural replacement). One can use the atomic coordinates of the rigid backbone of the host molecule of a refined crystal structure as a trial model of an unknown complex, if they are members of the same isostructural series. This method is expanded upon in the relevant sections of the thesis.

APPLICATIONS OF CYCLODEXTRINS TO BIOACTIVE MOLECULES

Many reviews on the topic of the applications of cyclodextrins are available.[7,19,24–28] Their uses include, but are not limited to, aqueous solubility enhancement of bioactive compounds, enzyme mimics, food packaging, modified textiles, taste masking, protection against oxidative degradation, cholesterol sequestration, chemical and thermal stability modification and enantioselective chromatographic separations. In this study cyclodextrins will be applied to pesticides, and thus some examples of such systems are presented below.

A study was performed by Szente[29] on five volatile organophosphorus pesticides (malathion, dichlorvos, fenitrothion, chlorpyriphos and sulprofos) with β-cyclodextrin. The β-cyclodextrin inclusion complexes showed slower pesticide vapour release relative to the untreated compounds. The complexes were subjected to evolved gas detection analysis to investigate loss of the pesticide from the formulation. The thermal stability of the products was also investigated. This was done by storing the formulations at 40°C at a relative humidity of 75 % and samples were taken at 1, 2, 3 and 6 weeks and the pesticide content was then evaluated. The β-cyclodextrin/malathion and β-cyclodextrin/chlorpyriphos complexes were shown to greatly reduce the rate of loss of the pesticides when compared to formulation of the pesticides adsorbed on starch. The loss of malathion from the starch formulation was 78 % from 60 °C to 100 °C. Over the same temperature range, only 6 % of this pesticide was lost from the cyclodextrin complex formulation. Similar improvements were seen for chlorpyriphos. The stability test performed on dichlorvos, fenitrothion and malathion β-cyclodextrin complexes showed losses of less than 10 % over the same six-week period. Szente concluded that the use of β-cyclodextrin in these formulations may be considered a starting point to preparing pesticide formulations with extended shelf life.

Cyclodextrins have been employed to improve the solubility and dissolution of pesticides to allow the reduced use of the pesticides while increasing the efficacy. Manolikar and Sawant[30] reported the formation of β-cyclodextrin inclusion complexes with the herbicide isoproturon with improved solubility and dissolution rates over the untreated active compound. Initial phase solubility studies allowed the researchers to determine the 1:1 equilibrium constant of 1890.33 M^{-1}. Dissolution rate studies were then performed on the 1:1 and 1:2 (guest:host) complexes prepared by kneading, co-evaporation and co-precipitation. They found that the co-evaporation product of the 1:1 complex showed the greatest improvement in its dissolution rate over uncomplexed isoproturon. Only 17 % of the untreated herbicide was found to have dissolved after 2 hours, while the kneaded and co-evaporated products showed that the percentage isoproturon dissolved was 50 % and 55 % respectively over the same time. In the 1:2

complexes, the co-precipitation product gave the greatest improvement in dissolution rate, with 76 % of the herbicide dissolved over two hours. They surmised that the improvement in dissolution rates would allow a more rational approach to application of isoproturon with improved efficacy. A similar study was performed by Villaverde *et al.*[31] on an inclusion complex of the herbicide norflurazon with β-cyclodextrin. The phase solubility analysis of this system showed A_L-type behaviour, increasing the apparent solubility of the pesticide 5-fold (at 12 mM β-cyclodextrin) and the $K_{1:1}$ equilibrium constant was calculated to be 360 M^{-1}. The complexes prepared by kneading, spray drying and co-evaporation all showed improved dissolution rates with 100 % of norflurazon dissolving in 5 minutes, compared to only 15 % of untreated norflurazon in 30 minutes. Villarverde *et al.* concluded that the use of β-cyclodextrin/norflurazon inclusion complexes could improve the leaching behaviour of the herbicide in soil, improving its application.

Cyclodextrins occasionally form insoluble complexes with certain guest molecules. This process can be exploited to use these hosts to remove pollutants from water. An example of this is the use of γ-cyclodextrin as a complexation agent to remove the pesticide chlordecone from contaminated water.[32] The pesticide chlordecone was used to control banana weevil populations in the French West Indies for many years. It has since shown to be noxious to humans and it has severely contaminated the soil, rivers and crops of the islands. It has been linked to an increase in central nervous system toxicity in the population surrounding the production sites. Chlordecone is known to have strong persistence and exposure is expected to last several hundred years. Thus far, only one study on the removal of chlordecone from contaminated sites has been performed and it was found that activated charcoal may be used; however, more efficient alternatives would be beneficial. The use of cyclodextrins was therefore investigated. After testing several cyclodextrins, the researchers found that γ-cyclodextrin would be the most suitable agent as chlordecone forms a stable, water-insoluble complex with this host. Simple filtration would provide a bulk method for the removal of the pesticide. The researchers tested the direct extraction of the complex using activated charcoal by preparing a 1 dm^3 sample of contaminated water. A stoichiometric amount of γ-cyclodextrin was added and the complex allowed to precipitate. This mixture was then filtered through activated charcoal. With this method the researchers showed that as little as 15 mg of activated charcoal would suffice to remove 98 % chlordecone from the 1 dm^3 solution once complexation with γ-cyclodextrin was complete. Under similar conditions, without the use of cyclodextrin, activated charcoal removed only 32 % of the pesticide. The researchers also tested the use of a cyclodextrin-modified-activated charcoal substance. The cyclodextrin-modified substance showed a 10-15 % improvement in chlordecone removal over pure activated charcoal. These results show that

cyclodextrins could be used for environmental rehabilitation with the removal of harmful substances from pesticide contaminated water.

While this project will focus on the application of cyclodextrins to pesticides, the most active area of research on cyclodextrin inclusion complexes is their application to pharmaceutically active compounds and as such a few examples will be presented here. Many products containing cyclodextrin formulations of active pharmaceutical ingredients (APIs) are available on the market, for example cisapride/HPBCD (propulsid), nicotine/β-cyclodextrin (Nicorette), chloramphenicol/RAMEB (Clorocil).[24] A study by Gibaud *et al.*[33] was performed in an attempt to improve the solubility and dissolution rate of melarsoprol. This drug is used in the treatment of African trypanosomiasis (sleeping sickness) and recent studies showed that it is very effective in treating several types of refractory leukaemia. However, melarsoprol is a poorly water-soluble drug and is administered intravenously as a propylene glycol solution. In its current formulation the application of this drug can result in complications for the patient, such as pain, burns and necrosis at the site of administration. Therefore, the researchers investigated the use of HPBCD and RAMEB as potential solubilisers of the drug. They found that both HPBCD and RAMEB bind strongly to the guest with remarkably high equilibrium constants of 56077 ± 4205 M^{-1} and 54168 ± 5305 M^{-1} determined from mole-ratio titration plots. The solubility enhancement factors (apparent solubility of the API at 250 mM cyclodextrin/intrinsic solubility of API) were found to be similar, at 7.2×10^3 for both cyclodextrins. This was promising for an aqueous intravenous formulation using HPBCD. The methylated cyclodextrin RAMEB, however, is not suitable for intravenous administration, so its potential as an oral formulation was investigated by testing its dissolution rate relative to the untreated API. The researchers found that the dissolution rate of the RAMEB/melarsoprol complex was vastly higher than that of pure melarsoprol: after 60 minutes the complex was completely dissolved compared to only 60.1 ± 6.1 % of the API. *In vitro* studies performed on the cyclodextrin inclusion complexes showed no loss in cytotoxic effects relative to the untreated melarsoprol.

SALTS AND CO-CRYSTALS

In a special issue of *Crystal Growth & Design* the editors noted in their introduction[34] the revival of the area of co-crystal research. Multi-component crystalline systems offer a huge diversity in structure, composition and properties that are of great interest to solid-state chemists and the pharmaceutical industry.

The exact definition of a co-crystal has been the subject of much recent debate amongst researchers.[35–37] In 2012 a large group of researchers published a response to United Food and Drug Administration (FDA) draft guidelines from December 2011 pertaining to the classification of pharmaceutical co-crystals.[38] The FDA defined co-crystals as: "solids that are crystalline materials composed of two or more molecules in the same crystal lattice." The researchers argue that this definition is restrictive and ambiguous. The definition would limit co-crystals to molecular components, which is not borne out in the literature or patents. The ambiguity of the molecules in the "crystal lattice" arises as all molecular crystals must have two or more molecules in its crystal structure by definition. The authors proposed two alternative definitions of co-crystals. The first, broader definition, is "co-crystals are solids that are crystalline single phase materials composed of two or more different molecular and/or ionic compounds generally in a stoichiometric ratio". The second distinguishes solvates with the definition "co-crystals are solids that are crystalline single phase materials composed of two or more different molecular and/or ionic compounds generally in a stoichiometric ratio which are neither solvates nor simple salts".

In August 2016 the FDA released revised draft guidelines for the appropriate classification of co-crystals, including a listing of data required for submission of a new co-crystal product for assessment and the regulatory implications of the classification.[39] These draft guidelines[40] are intended to clarify the FDA's current thinking on the appropriate classification of pharmaceutical co-crystals. In this draft document they retain the definition of co-crystals as "crystalline materials composed of two or more molecules within the same crystal lattice". However, the FDA makes the further distinction that the co-former interacting with the active pharmaceutical ingredient (API) is neutral and that the interaction is non-ionic. Co-crystals are separate from hydrates and solvates, which are classified under the polymorph umbrella term as "pseudopolymorphs".

Therefore, for the purposes of this study multi-component crystalline systems will be considered as crystalline substances of two or more molecular components. The differentiation between salts and co-crystals will be done on the basis of a proton transfer.[41–43] The distinction between the neutral and ionised components is necessary because the state of ionisation can influence

physicochemical properties, such as stability and solubility.[44] As the recent FDA guidelines indicate, this differentiation between salts and co-crystals has regulatory implications.

Investigations into co-crystallisation of active pharmaceutical ingredients (APIs) are usually performed with compounds ('co-formers' or partner molecules) on the FDA's Generally Recognised As Safe (GRAS) list.[45] The compounds on this list have been shown to be safe under the conditions of intended use by a panel of qualified experts. These substances are often employed in the synthesis of pharmaceutically acceptable co-crystals.

PROPERTIES

The relationship between the structure and physicochemical properties of multi-component crystalline systems is multi-factorial. The presence of two or more components in the crystal can cause unexpected changes to the physicochemical properties of the final product.

Two of the most important properties of salts and co-crystals are their melting point and their aqueous solubility. A survey[44] of 50 multi-component crystalline systems showed that prediction of their properties based on the starting materials is difficult. The survey showed that of the 50 systems analysed, 51 % had a melting point between those of the API and co-former, 39 % had melting points lower than both components, 6 % had melting points higher than both components and 4 % had the same melting point as one of the components. For a given API a correlation is often observed where the melting point of the multi-component crystal system is related to that of the co-former. That is to say, the general trend observed is that with increasing co-former melting point one observes an increase in the melting point of the multi-component crystalline system.[44,46,47]

One of the main reasons for investigating co-crystals and salts is to modify the solubility of an API, either by attempting to raise or decrease the solubility. The mechanism by which co-crystals solubilise the API has been termed "spring-and-parachute" effect.[48–50] The proposed mechanism for this process is based on the initial dissociation of the co-crystal in solution. The more soluble co-former dissolves in solution leaving loosely aggregated API clusters resembling an amorphous phase. These clusters can exhibit similar spikes in concentration as amorphous forms of the drug; this is the "spring" effect. The "parachute effect" is achieved by the time scale required for the API to convert to a stable crystalline form. If several crystalline forms exist, the process will first convert to a more stable polymorph and finally to the apparently most stable crystalline polymorph, following Ostwald's Law of Stages.[49,50] If the drug converts directly to the stable crystalline form, only the "spring" effect is observed.

The relationship between solubility and the melting point of a crystalline substance is complex. A general trend of increasing melting temperatures correlating to decreasing solubility has been observed in many cases. However, this relationship is complicated and has been shown to be non-linear or logarithmic in some cases.[51] Black *et al.*[52] concluded that no correlation existed between melting point and solubility in their study of 25 salts. The difficulty in prediction of the relationship between these properties is attributed to the complicated nature of interactions in multi-component systems compared to crystals containing only a single chemical component.

ADVANTAGES OF SALT/CO-CRYSTAL FORMATION

Salts and co-crystals can impart several advantages over the pure pharmaceutical product. A review published in 2013 by Elder *et al*.[51] gave a detailed outline on the use of salts and co-crystals to improve various aspects of pharmaceutical products. Salts and co-crystals are often used to alter the dissolution rate or solubility of an API. These multi-component crystalline systems can enhance the apparent solubility of the API by several orders of magnitude.[51,53] Another advantage is the existence of a vast library of pharmaceutically acceptable co-formers that can be employed in salt and co-crystal formation. Co-crystals do not require the presence of acid or basic functionalities, enabling the derivatisation of non-ionisable compounds. A further advantage of salts and co-crystals is crystallinity (by definition co-crystals are crystalline). Crystalline products can often lead to increased stability over amorphous products in terms of thermal, hydrolytic and photolytic stability. Polymorphic control is of interest to pharmaceutical scientists and co-crystals exhibit a measure of predictability of polymorphs (although this advantage does not apply for salts).[54,55] In the chemical industry purification by crystallisation of a salt or co-crystal is frequently employed. The advantages presented here highlight the importance of pursuing this line of research.

DISADVANTAGES OF SALT/CO-CRYSTAL FORMATION

While the advantages over an API are numerous for salts and co-crystals, several disadvantages are known. In their review Elder *et al.*[51] outlined several of these. Addressing the dissolution rate and solubility through salt or co-crystal formation has in some cases reduced the apparent solubility of the API, where this was not intended.[53,56,57] As mentioned in the advantages above, predictability of polymorphism is an issue in salt formation. While polymorphs themselves may provide physicochemical improvements to an API their presence adds the developmental issue of characterisation and thermodynamic stability investigations.[58] This issue is less common with co-crystals, but co-crystal polymorphs are known.[54,55] As co-crystals are non-ionic they tend to have lower melting points than salts. In general, APIs with lower melting points can cause

undesirable outcomes in large scale processing, such as plastic deformation which leads to caking and impacts on compressibility during the production of tablets.

APPLICATIONS OF SALTS/CO-CRYSTALS CONTAINING BIOACTIVE MOLECULES

Salts and co-crystals containing pharmaceuticals are generally employed with an aim to improve particular undesirable physicochemical properties. However, co-crystals are also used in preparation and physicochemical property control of other materials such as luminescent organic solid-state materials[59] and explosives.[60] A few examples of the applications of multi-component crystalline systems in pharmacy are presented below.

In 2011 Cheney *et al.*[61] performed a study on the nonsteroidal anti-inflammatory drug meloxicam. Due to the low solubility of the drug under acidic conditions it takes an extended period of time to reach therapeutic levels. If meloxicam were to be implemented for use in acute pain relief, the time to reach therapeutic levels would need to be reduced. Co-crystallisation was investigated as a method to achieve this goal. After screening several co-formers, the co-crystal comprising meloxicam and aspirin was selected and investigated as a potential solution to the slow onset of action problem. During an animal pharmacokinetics study the researchers showed that the co-crystal exhibited an oral bioavailability of 69 % relative to only 16 % for the untreated API. Furthermore, the required therapeutic concentration was achieved in 10 minutes, while the time to reach maximal concentration was unchanged. This study shows the potential for improving the administration of some pharmaceuticals without modifying the mode of action of the drug.

Ribavirin is a broad-spectrum antiviral with high aqueous solubility. It is used in combination therapy for Hepatitis C and requires large regular doses. The high aqueous solubility and large dosages result in large fluctuations in concentration of the active drug in the blood plasma of patients, with undesirable side effects. Chen *et al.*[62] identified co-crystals as a potential method to control the rate of ribavirin release. Three hydrated co-crystals with co-formers 3,5-dihydroxybenzoic acid, gallic acid and barbituric acid were synthesised, characterised and their dissolution investigated. The researchers found that while the untreated ribavirin reached 80 % concentration after 8 minutes, the co-crystals containing 3,5-dihydroxybenzoic acid, gallic acid and barbituric acid attained the same concentration as the API after 64 minutes, 30 minutes and 16 minutes respectively. Chen *et al.* thus showed that the release of an API can be controlled with careful selection of a co-former.

A growing application of co-crystallisation is purification of a product during manufacture. Billot *et al.*[63] employed co-crystallisation as a purification method to large scale synthesis of SAR1 (a SRC kinase inhibitor selected for treatment of myeloid leukaemia). The crude product of the

synthesis was initially a solution in chlorobenzene in which SAR1 represented only 60 % of the dry concentrate. Chromatography and impurity adsorption followed by repeated crystallisations yielded SAR1 of only 90 % purity (below the required standards) with unacceptable residual solvent content. Co-crystallisation was therefore investigated. After screening several co-formers and using phase diagrams it was determined that benzoic acid would be the most suitable co-former. SAR1 and benzoic acid have symmetrical phase diagrams, with similar solubilities in chlorobenzene. The co-crystal was prepared from chlorobenzene to test the feasibility of this process. To cleave the co-crystal, isopropanol was selected as the solvent as the API is insoluble, and benzoic acid is soluble, in isopropanol. In the phase diagram of SAR1 and benzoic acid in isopropanol there is no domain for the co-crystal. After an initial proof of concept study, the method was successfully applied to a small laboratory sample of the crude API showing a purity increase from 60 % to 99 %. The experiment was then scaled up and the additional modification that the benzoic acid be added as a solution in isopropanol to the crude sample was implemented. The effect of the ratio of benzoic acid to SAR1 on sample purity was also tested and found to be negligible at molar ratios between 1 and 2. During the scaling up experiment the kinetics of co-crystal formation necessitated 1.8 equivalents of benzoic acid and a temperature of 40 °C. The extra benzoic acid allows for the potential side reactions with unknown impurities. Cleaving of the co-crystal was achieved through slurrying in isopropanol. The final scaling up to the pilot plant was implemented, returning 10 kg batches of purified SAR1. The final method employed co-crystallisation of the API with benzoic acid. The product was filtered and washed with chlorobenzene. The dried co-crystal was then cleaved by repeated slurrying with isopropanol to ensure completion. This process had an overall yield of 54 % with 99 % purity which was within the International Conference on Harmonization specifications. Billot *et al*. thus managed to implement large scale purification using an efficient co-crystallisation strategy.

INTELLECTUAL PROPERTY

Researchers involved in novel pharmaceutical research rely on patents for protection of their intellectual property. Patents protect the revenue from any products produced from this intellectual property for 20 years from the date of first application. This provides the organisation or researcher awarded the patent market protection and an income stream from which the costs of product development can be recovered. Patents encourage research for the benefit of society by providing an incentive to the inventor before providing the invention to the public.

To be eligible for patent protection an application must fulfil three criteria: novelty, utility and non-obviousness. At the time of applying for a patent, the product must not have been published, or otherwise publicly divulged, this is the requirement for novelty. Utility of a product relies on

the new product being an improvement or having a useful application. The final criterion is non-obviousness; this is the most subjective, as the product must not be obvious or self-evident to a "person having ordinary skill in the art".[64]

Salts and co-crystals fulfil all the requirements for patent applications. Assuming research on the product has, up to the date of patent application, not been published it is considered novel. The vast number of suitable co-formers gives an advantage to the novelty of these products. Utility is generally considered applicable as salts and co-crystals modify the physicochemical properties of the active ingredient, both a useful improvement and new composition of matter. Furthermore, co-crystals and salts have the same therapeutic effects as the untreated API. The requirement that the product be non-obvious is resolved by the lack of predictability in the formation of new crystalline systems and changes in the physicochemical properties resulting from co-crystallisation. Examples are outlined in the preceding sections of the introduction. However, it is worth reiterating that the formation of a salt or co-crystal can improve the dissolution rate and solubility over untreated APIs. This improvement in dissolution rate and solubility is a possible indication of improved bioavailability, clearly fulfilling the utility requirement. Slow release formulations allow fewer dosages with improved effect. Other useful improvements relate to physical stability, among others outlined in the Advantages of Salt/Co-crystal Formation section above. Crystalline structures are often unpredictable; while crystal engineering allows one to possibly predict the individual interactions between two components of a co-crystal or salt, prediction of the overall crystal structure remains elusive. Even if one could predict the crystal structure of a multi-component system, including solvates and polymorphic forms, the prediction of properties is generally impractical. With the current technology and theories, the synthesis of new multi-component crystalline systems is still largely trial-and-error based, and thus non-obvious.

CO-CRYSTAL DESIGN

The successful synthesis of salts and co-crystals still relies on trial-and-error screening experiments. Supramolecular synthons (examples in Figure 1.6), chosen on the basis of crystal engineering, can allow one to narrow the list of all possible co-formers by eliminating unlikely compounds. This however, is no guarantee of success. Many, if not most co-crystals and molecular salts still arise purely from screening experiments.

In silico screening using the Cambridge Structural Database (CSD)[65] by searching for potential hydrogen bonding interactions to investigate in co-crystal formation is often employed. Once suitable supramolecular synthons are identified (examples in Figure 1.6) co-formers with the desired functional groups are selected for experimental screening.

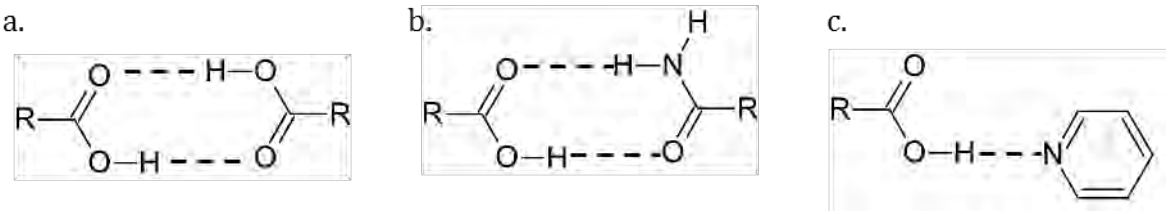

Figure 1.6: Examples of hydrogen bonding synthons often employed in crystal engineering[66]

One parameter used to predict the occurrence of a proton transfer when synthesising multi-component crystalline systems is the difference between the pK_a values (ΔpK_a) of the starting materials. This difference is defined as $\Delta pK_a = pK_a(base) - pK_a(acid)$. It is generally accepted that a proton transfer will occur if the ΔpK_a value is greater than 3. If this difference is less than zero it is likely that a co-crystal will form. Between these limits it is difficult to predict the formation of either a salt or a co-crystal.[42] While the ΔpK_a value is a good indicator for the prediction of a proton transfer the final position of the proton must always be established by X-ray or neutron diffraction or spectroscopic methods. When screening for solid forms of an API it can be useful to remove the constraints of ΔpK_a values.[42] This can lead to an increased hit rate of multi-component crystalline systems with possibly improved physicochemical properties over the untreated API.

BIOACTIVE MOLECULES

Three bioactive molecules are presented for study: two pesticides and one antihyperlipidemic (i.e. lipid-lowering) agent. The two pesticides are 2,5-dichlorobenzoic acid methyl ester (henceforth DCB) and fenthion, and the antihyperlipidemic agent is acipimox. Their chemical structures and selected properties are presented in Table 1.2.

Table 1.2: Chemical structures and physical properties of the bioactive molecules selected for study

Compound	**Chemical Structure**	**Molecular formula and weight (g mol^{-1})**	**Aqueous solubility (mg dm^{-3}) at 20 ℃**	**Melting Point (℃)**
2,5-dichloro-benzoic acid methyl ester	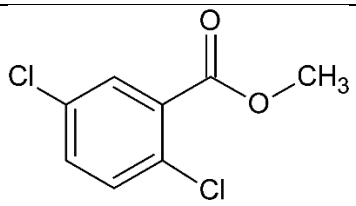	$C_8H_6O_2Cl_2$ 205.04	87.0[67,68]	34.6[68]
Fenthion	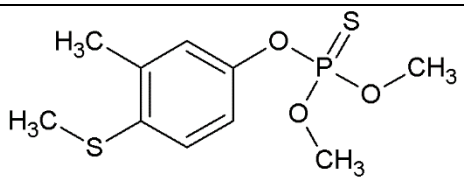	$C_{10}H_{15}O_3PS_2$ 278.33	4.2[67]	7.5[67]
Acipimox	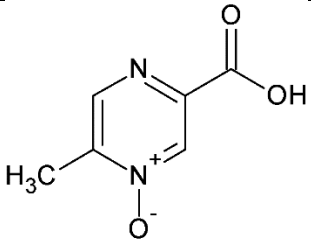	$C_6H_6N_2O_3$ 154.13	15 413‡[69]	177-180[70]

‡ No temperature for determination of the solubility of acipimox was reported

2,5-DICHLOROBENZOIC ACID METHYL ESTER

The compound 2,5-dichlorobenzoic acid methyl ester (DCB) is a plant growth regulator and fungicide. It is generally applied as a waxy formulation for grafting of grapevines to encourage callus formation[68,71,72] and it has recently been reapproved for use in the European Union until 2019. It is sold under the trade name Rebwachs WF, containing 0.35 g/kg DCB and 1g/kg 8-hydroxyquinoline. As this product is generally used indoors, the environmental residual impact has not been investigated in detail. DCB is neurotoxic to rats (acute LD_{50} = 1030 mg kg^{-1}) and has been classified as "harmful" (classification Xn) and "harmful if swallowed" (risk phrase R22) by the European Food Safety Authority.[68] It has also shown potential as a plant growth regulator, but

the efficacy is limited by its poor aqueous solubility.[71] If such an application were to be implemented, the long term environmental impact would require further study; however, early indications are that the environmental damage would be limited. The compound DCB was shown to undergo hydrolysis in water (pH 7) at 50 °C into the products 2,5-dichlorobenzoic acid and methanol. This reaction occurs over the space of approximately 79 hours implying that the pesticide would not be long-lived in the environment.[68]

The hydrolysis of DCB by the bacterium *Burkholderia cepacia* (isolated from soil samples from Bolquère in the south of France) has been investigated.[73] The results showed that this organism is capable of degrading DCB and are promising for the potential application of DCB in an aqueous formulation with minimal environmental impact.

The low solubility and high volatility of DCB are limiting factors in the implementation of this pesticide as a plant growth regulator. A patent for Water Dispersible Granule Composition has recently been awarded by the United States Patent and Trademark Office in which DCB is mentioned as one of the possible agrochemical excipients.[74] This formulation contains several components including insoluble filler, suspension adjuvants and polyvinyl alcohol. Cyclodextrin inclusion may provide an alternative approach to the solubilisation of DCB, as well as the formation of a less volatile solid for transport and handling.

FENTHION

Fenthion (*O,O*-dimethyl *O*-4-methylthio-*m*-tolyl phosphorothioate) is an organothiophosphate insecticide that acts *via* cholinesterase inhibition. It is moderately toxic to mammals (acute LD_{50} = 250 mg kg^{-1}) and is employed as a broad spectrum insecticide used to control various sucking and biting insects. It is highly toxic to birds (acute LD_{50} = 7.2 mg kg^{-1}) and is also marketed as an avicide.[67] Fenthion is used in South Africa for control of the red-billed quelea (*Quelea quelea*), a highly damaging pest.[75] The application of fenthion is however problematic, causing environmental issues with non-target organisms.[75,76] Fenthion adsorbs strongly to soil particles and does not move through the soil.[67,77] Furthermore, due to its very low aqueous solubility it is often combined with severely polluting organic solvents (such as xylene and mineral oil in the formulation AVIGEL) which poses inhalation risks to those working with it.

Fenthion is a highly volatile oil at room temperature, which may lead to exposure of those handling the material. Cyclodextrin inclusion would transform fenthion into a solid material aiding in handling and transport. Formation of a possible inclusion complex could also lower the volatility, reducing exposure through inhalation. Solubilisation of fenthion through cyclodextrin

inclusion may facilitate soil decontamination through the application of cyclodextrins and may also eliminate the need for organic solvents for fenthion application.

ACIPIMOX

Acipimox (a niacin derivative) is a lipid-lowering agent used in the treatment of hypertriglyceridaemia. It has been available since 1984 and over the course of 2013 the Co-ordination Group for Mutual Recognition and Decentralised Procedures – Human (CMDh) prepared a report recommending the restriction of acipimox to its use as an additional or alternative treatment to reduce high triglyceride levels.[78] This report was based on a study (HPS2-THRIVE) which examined long term use of a nicotinic acid and laropiprant combination. Based on this study the European Medicines Agency suspended the use of this combination. Due to the chemical similarities between acipimox and nicotinic acid an investigation into the use of acipimox was subsequently required. These similarities prompted the decision to restrict the use of acipimox to an alternative treatment for reduction of high levels of triglycerides. Acipimox is of particular use for patients who are sensitive to statins or fibrates. The conclusion of the report was that the benefit-risk balance of acipimox-containing products was favourable for the above-mentioned uses.

Acipimox has been identified as a possible aid in improving insulin resistance and glucose tolerance in certain diabetic patients over both the short term and the long term.[79,80] As this is most effective in a fasted state, it requires overnight doses. Supramolecular modification of acipimox may provide the solution in a slow release formulation. While the formation of a sodium salt showed no improvement over the untreated API,[81] co-crystals may provide an alternative methodology to achieve the desired result. This requires screening and characterisation of several acipimox multi-component crystalline systems. Such screening can also give an indication of the structural features of the co-formers that would be most likely to form multi-component crystalline systems with acipimox.

AIMS AND OBJECTIVE

The primary aim of this project is to create new solid-state supramolecular systems with each of the three selected bioactive molecules. Once such systems are identified they will be fully characterised. Cyclodextrin inclusion complexation was identified as the most appropriate method for modifying the physicochemical properties of the pesticides. Cyclodextrins are commercially available on an industrial scale and digested into environmentally innocuous products after application making them ideal for pesticide formulations. Co-crystallisation was selected for the investigations with acipimox as the vast library of GRAS co-formers would enable large variation in the changes to the physicochemical properties of the antihyperlipidemic agent. The specific objectives are as follows:

1. Cyclodextrin Inclusion Complexes
    a. Attempt to form cyclodextrin inclusion complexes with DCB and fenthion with the native cyclodextrins by kneading and co-precipitation. Similarly, investigate methylated cyclodextrins TRIMEA, TRIMEB and DIMEB as potential host molecules.
    b. Upon identifying a new complex, characterise the product through the use of spectroscopic, thermal and crystallographic techniques.
    c. Investigate the phase solubility profile of the guest in the presence of native cyclodextrins (α-cyclodextrin, β-cyclodextrin and γ-cyclodextrin) and commercially available derivatised cyclodextrins (e.g. RAMEB and HPBCD). From these experiments determine the binding constants of the complexes.
2. Co-crystallisation with Acipimox
    a. Screen for potential co-crystals or salts through dry grinding, liquid-assisted grinding and co-precipitation methods.
    b. Upon identification of a new solid phase, investigate methodologies to scale-up the material for comprehensive physicochemical analysis.
    c. Characterise the new form using spectroscopic, thermal and crystallographic methods.
    d. From the single crystal X-ray structure unambiguously identify each product as a salt or co-crystal. Confirm the designation using infrared spectroscopy.
    e. Investigate the differences or similarities in physicochemical properties of the new form relative to those of the untreated API.

REFERENCES

1 J. M. Lehn, *Acc. Chem. Res.*, 1978, **11**, 49–57.

2 J. W. Steed and J. L. Atwood, *Supramolecular Chemistry*, John Wiley & Sons, Inc., Chichester, United Kingdom, 2nd edn, 2009.

3 J. Szejtli, *Chem. Rev.*, 1998, **98**, 1743–1754.

4 H. Dodziuk, *Cyclodextrins and Their Complexes*, Wiley-VCH Verlag GmbH & Co. KGaA, Warsaw, Poland, 2006.

5 W. Saenger, J. Jacob, K. Gessler, T. Steiner, D. Hoffmann, H. Sanbe, K. Koizumi, S. M. Smith and T. Takaha, *Chem. Rev.*, 1998, **98**, 1787–1802.

6 E. M. Martin Del Valle, *Process Biochem.*, 2004, **39**, 1033–1046.

7 J. Szejtli, *Pure Appl. Chem.*, 2004, **76**, 1825–1845.

8 V. T. D'Souza and K. B. Lipkowitz, *Chem. Rev.*, 1998, **98**, 1741–1742.

9 W. Saenger, C. Betzel, B. Hingerty and G. M. Brown, *Nature*, 1982, **296**, 581–583.

10 W. Saenger, C. Betzel, B. Hingerty and G. M. Brown, *Angew. Chem. Int. Ed. (English)*, 1983, **22**, 883–884.

11 A. Kusmin, R. E. Lechner, M. Kammel and W. Saenger, *J. Phys. Chem. B*, 2008, **112**, 12888–12898.

12 T. Aree, H. Hoier, B. Schulz, G. Reck and W. Saenger, *Angew. Chem. Int. Ed. (English)*, 2000, **39**, 897–899.

13 M. R. Caira, V. J. Griffith, L. R. Nassimbeni and B. van Oudtshoorn, *J. Chem. Soc., Perkin Trans. 2*, 1994, 2071–2072.

14 T. Loftsson and M. E. Brewster, *J. Pharm. Pharmacol.*, 2010, **62**, 1607–1621.

15 M. R. de Freitas, L. A. Rolim, M. F. de La Roca Soares, P. J. Rolim-Neto, M. M. de Albuquerque and J. L. Soares-Sobrinho, *Carbohydr. Polym.*, 2012, **89**, 1095–1100.

16 L. Liu and Q. Guo, *J. Incl. Phenom. Macrocycl. Chem.*, 2002, **42**, 1–14.

17 N. A. Todorova and F. P. Schwarz, *J. Chem. Thermodyn.*, 2007, **39**, 1038–1048.

18 T. K. Higuchi and K. A. Connors, *Adv. Chem. Instrum.*, 1965, **4**, 212–217.

19 M. E. Brewster and T. Loftsson, *Adv. Drug Deliv. Rev.*, 2007, **59**, 645–66.

20 K. Harata, *Chem. Rev.*, 1998, **98**, 1803–1828.

21 W. Saenger, in *Inclusion Compounds*, eds. J. L. Atwood, J. E. D. Davies and D. D. MacNicol, Academic Press, London, 1984, Vol. 2, Ch. 8, pp. 231-259

22 M. R. Caira, *Rev. Roum. Chim.*, 2001, **46**, 371–386.

23 S. Lubhelwana, Master's Dissertation, University of Cape Town, 2005.

24 M. E. Davis and M. E. Brewster, *Nat. Rev. Drug Discov.*, 2004, **3**, 1023–35.

25 S. Li and W. C. Purdy, *Chem. Rev.*, 1992, **92**, 1457–1470.

26 A. R. Hedges, *Chem. Rev.*, 1998, **98**, 2035–2044.

27 J. Szejtli, *Starch / Stärke*, 2003, **55**, 191–196.

28 G. Astray, C. Gonzalez-Barreiro, J. C. Mejuto, R. Rial-Otero and J. Simal-Gándara, *Food Hydrocoll.*, 2009, **23**, 1631–1640.

29 L. Szente, *J. Therm. Anal. Calorim.*, 1998, **51**, 957–963.

30 M. Manolikar and M. Sawant, *Chemosphere*, 2003, **51**, 811–816.

31 J. Villaverde, E. Morillo, J. I. Pérez-Martínez, J. M. Ginés and C. Maqueda, *J. Agric. Food Chem.*, 2004, **52**, 864–9.

32 V. K. Rana, R. Kissner, S. Gaspard and J. Levalois-Grützmacher, *Chem. Eng. J.*, 2016, **293**, 82–89.

33 S. Gibaud, S. Ben Zirar, P. Mutzenhardt, I. Fries and A. Astier, *Int. J. Pharm.*, 2005, **306**, 107–121.

34 S. L. Childs and M. J. Zaworotko, *Cryst. Growth Des.*, 2009, **9**, 4208–4211.

35 G. R. Desiraju, *CrystEngComm*, 2003, **5**, 466.

36 J. D. Dunitz, *CrystEngComm*, 2003, **5**, 506.

37 A. D. Bond, *CrystEngComm*, 2007, **9**, 833.

38 S. Aitipamula, R. Banerjee, A. K. Bansal, K. Biradha, M. L. Cheney, A. R. Choudhury, G. R. Desiraju, A. G. Dikundwar, R. Dubey, N. Duggirala, P. P. Ghogale, S. Ghosh, P. K. Goswami, N. R. Goud, R. R. K. R. Jetti, P. Karpinski, P. Kaushik, D. Kumar, V. Kumar, B. Moulton, A. Mukherjee, G. Mukherjee, A. S. Myerson, V. Puri, A. Ramanan, T. Rajamannar, C. M. Reddy, N. Rodríguez-Hornedo, R. D. Rogers, T. N. G. Row, P. Sanphui, N. Shan, G. Shete, A. Singh, C. C. Sun, J. A. Swift, R. Thaimattam, T. S. Thakur, R. K. Thaper, S. P. Thomas, S. Tothadi, V. R. Vangala, N. Variankaval, P. Vishweshwar, D. R. Weyna and M. J. Zaworotko, *Cryst. Growth Des.*, 2012, **12**, 2147–2152.

39 Z. Brennan, *Regululatory Affairs Professionals Society*, http://www.raps.org/Regulatory-Focus/News/2016/08/16/25611/FDA-to-Reclassify-Pharmaceutical-Co-Crystals/ (accessed August 2016), 2016.

40 Regulatory Classification of Pharmaceutical Co-Crystals, *Guidance for Industry*, U.S. Department of Health and Human Services, Food and Drug Administration, 2013.

41 W. M. Haynes, Ed., *CRC Handbook of Chemistry and Physics*, CRC Press/Taylor and Francis, Boca Raton, FL, 96th edn., 2016.

42 S. L. Childs, G. P. Stahly and A. Park, *Mol. Pharm.*, 2007, **4**, 323–338.

43 N. K. Duggirala, M. L. Perry, Ö. Almarsson and M. J. Zaworotko, *Chem. Commun.*, 2016, **52**, 640–655.

44 N. Schultheiss and A. Newman, *Cryst. Growth Des.*, 2009, **9**, 2950–2967.

45 U.S. Food and Drug Admistration, *FDA Generally Recognized as Safe (GRAS)*, http://www.fda.gov/Food/IngredientsPackagingLabeling/GRAS/ (accessed August 2016)

46 M. R. Caira, S. A. Bourne, H. Samsodien, E. Engel, W. Liebenberg, N. Stieger and M. Aucamp, *CrystEngComm*, 2012, **14**, 2541.

47 M. K. Stanton and A. Bak, *Cryst. Growth Des.*, 2008, **8**, 3856–3862.

48 H. R. Guzmán, M. Tawa, Z. Zhang, P. Ratanabanangkoon, P. Shaw, C. R. Gardner, H. Chen, J. Moreau, Ö. Almarsson and J. F. Remenar, *J. Pharm. Sci.*, 2007, **96**, 2686–2702.

49 N. J. Babu and A. Nangia, *Cryst. Growth Des.*, 2011, **11**, 2662–2679.

50 D. D. Bavishi and C. H. Borkhataria, *Prog. Cryst. Growth Charact. Mater.*, 2016, **62**, 1-8.

51 D. P. Elder, R. Holm and H. L. de Diego, *Int. J. Pharm.*, 2013, **453**, 88–100.

52 S. N. Black, E. A. Collier, R. J. Davey and R. J. Roberts, *J. Pharm. Sci.*, 2007, **96**, 1053–1068.

53 D. J. Good and N. Rodríguez-Hornedo, *Cryst. Growth Des.*, 2009, **9**, 2252–2264.

54 C. B. Aakeröy, M. E. Fasulo and J. Desper, *Mol. Pharm.*, 2007, **4**, 317–322.

55 P. Vishweshwar, J. A. McMahon, M. L. Peterson, M. B. Hickey, T. R. Shattock and M. J. Zaworotko, *Chem. Commun.*, 2005, **10**, 4601–4603.

56 L. Sreenivas Reddy, S. J. Bethune, J. W. Kampf and N. Rodríguez-Hornedo, *Cryst. Growth Des.*, 2009, **9**, 378–385.

57 D. Stepanovs, M. Jure, L. N. Kuleshova, D. W. M. Hofmann and A. Mishnev, *Cryst. Growth Des.*, 2015, **15**, 3652–3660.

58 S. R. Chemburkar, J. Bauer, K. Deming, H. Spiwek, K. Patel, J. Morris, R. Henry, S. Spanton, W. Dziki, W. Porter, J. Quick, P. Bauer, J. Donaubauer, B. A. Narayanan, M. Soldani, D. Riley and K. McFarland, *Org. Process Res. Dev.*, 2000, **4**, 413–417.

59 D. Yan, A. Delori, G. O. Lloyd, T. Friščić, G. M. Day, W. Jones, J. Lu, M. Wei, D. G. Evans and X. Duan, *Angew. Chem.*, 2011, **123**, 12691–12694.

60 O. Bolton, L. R. Simke, P. F. Pagoria and A. J. Matzger, *Cryst. Growth Des.*, 2012, **12**, 4311–4314.

61 M. L. Cheney, D. R. Weyna, N. Shan, M. Hanna, L. Wojtas and M. J. Zaworotko, *J. Pharm. Sci.*, 2011, **100**, 2172–2181.

62 J. M. Chen, S. Li and T. B. Lu, *Cryst. Growth Des.*, 2014, **14**, 6399–6408.

63 P. Billot, P. Hosek and M.-A. Perrin, *Org. Process Res. Dev.*, 2013, **17**, 505–511.

64 A. V. Trask, *Mol. Pharm.*, 2007, **4**, 301–309.

65 Cambridge Structural Database and Cambridge Structural Database system, Version 5.37, Cambridge Crystallographic Data Centre, University Chemical Laboratory, Cambridge England, November 2015.

66 G. R. Desiraju, *Angew. Chem. Int. Ed. (English)*, 1995, **34**, 2311–2327.

67 K. A. Lewis, J. Tzilivakis, D. J. Warner and A. Green, *Hum. Ecol. Risk Assess.*, 2016, **22**, 1050-1064.

68 European Chemicals Agency, *CLH Report for methyl 2,5-dichlorobenzoate*, 2011, **1**, 1-59

69 Acipimox | CAS 51037-30-0 | Santa Cruz Biotech, http://www.scbt.com/datasheet-203497-acipimox.html, (accessed August 2016)

70 The Merck Index Online, https://www.rsc.org/Merck-Index/monograph/m1372?q=authorize, (accessed August 2016).

71 T. J. Allen, C. L. Leinweber, D. K. Prince and D. F. Bouchard, *Weed Sci.*, 1975, **23**, 428–432.

72 Conclusion on the peer review of 2,5-dichlorobenzoic acid methyl ester, *EFSA Scientific Report,* 2008, **180**, 1–50

73 G. Philippe, D. Vega and J. Bastide, *FEMS Microbiol. Ecol.*, 2001, **37**, 251–258.

74 R. K. M. Ramdas, US Pat. 20150230471, 2015.

75 R. A. Cheke, A. N. McWilliam, C. Mbereki, E. Van Der Walt, B. Mtobesya, R. N. Magoma, S. Young and J. P. Eberly, *Ecotoxicology*, 2012, **21**, 1761–1770.

76 D. Roux, S. Jooste, E. Truter and P. Kempster, *Ecotoxicol. Environ. Saf.*, 1995, **31**, 164–172.

77 N. V. Kyriakidis, C. Pappas and P. Athanasopoulos, *Food Chem.*, 2005, **91**, 241–245.

78 Acipimox only to be used as additional or alternative treatment to reduce high triglyceride levels, *European Medicines Agency*, EMA/108603/2014, 2013

79 A. T. Santomauro, G. Boden, M. E. Silva, D. M. Rocha, R. F. Santos, M. J. Ursich, P. G. Strassmann and B. L. Wajchenberg, *Diabetes*, 1999, **48**, 1836 – 1841.

80 H. Makimura, T. L. Stanley, C. Suresh, A. L. De Sousa-Coelho, W. R. Frontera, S. Syu, L. R. Braun, S. E. Looby, M. N. Feldpausch, M. Torriani, H. Lee, M. E. Patti and S. K. Grinspoon, *J. Clin. Endocrinol. Metab.*, 2016, **101**, 1123–1133.

81 R. Menon, E. Cefali, I. Wilding, H. Wray and A. Connor, *Biopharm. Drug Dispos.*, 2009, **30**, 508–516.

CHAPTER 2 – EXPERIMENTAL

MATERIALS

CYCLODEXTRINS

The host molecules α-cyclodextrin, β-cyclodextrin, γ-cyclodextrin, TRIMEA [hexakis-(2,3,6-tri-*O*-methyl)-α-cyclodextrin], DIMEB [heptakis-(2,6-di-*O*-methyl)-β-cyclodextrin], TRIMEB [heptakis-(2,3,6-tri-*O*-methyl)-β-cyclodextrin], RAMEB (randomly methylated-β-cyclodextrin) and HPBCD (2-hydroxypropyl-β-cyclodextrin) were all obtained from Cyclolab (Budapest, Hungary). The compounds all had a purity greater than 98%. DIMEB and TRIMEB were also obtained from Sigma-Aldrich (Germany) with a purity greater than 98%.

CO-FORMERS

4-aminobenzamide, 4-aminopyridine, 4-hydroxybenzamide, 4-hydroxybenzoic acid, benzamide, tranexamic acid (*trans*-4-aminocyclohexanecarboxylic acid) and urea were acquired from Sigma-Aldrich (Germany) with a purity greater than 98%.

BIOACTIVE MOLECULES

Acipimox (5-carboxy-2-methyl-1-oxidopyrazin-1-ium) and fenthion (*O,O*-dimethyl *O*-4-methylthio-*m*-tolyl phosphorothioate) were obtained from Sigma-Aldrich (Germany) with >99% purity and used as received. 2,5-dichlorobenzoic acid methyl ester (DCB) was obtained from BOC Sciences, Creative Dynamics Inc. (New York, USA).

SOLVENTS

Anhydrous acetonitrile (99.8 %) and butan-1-ol (99.9 %) were obtained from Sigma-Aldrich (Germany). Methanol (99.5 %), ethanol (99.9 %), propan-2-ol (99.7 %) and dimethyl sulfoxide (99.5 %) were acquired from KIMIX Chemical and Lab Supplies CC (Cape Town, South Africa). 1, 4-dioxane (99 %) and propan-1-ol (99.5 %) were purchased from Merck (Pty) Ltd South Africa (South Africa). All the solvents were used as received.

SUPRAMOLECULAR SYSTEMS PREPARATION

The cyclodextrin inclusion complexes were initially prepared using a 1:1 molar ratio of the pesticides and cyclodextrin host molecule. Similarly, the acipimox multi-component crystalline systems were prepared with an acipimox to co-former 1:1 stoichiometric ratio.

The specific details of preparation of each multi-component system will be discussed before an in-depth analysis of physicochemical properties of the resulting systems.

CYCLODEXTRIN INCLUSION COMPLEXES

Cyclodextrin inclusion complexes were prepared in two distinct ways. These are kneading and co-precipitation.

KNEADING

Equimolar quantities of the guest and host molecules were weighed using a five place analytical balance. The components were combined and ground together with an agate pestle in an agate mortar with dropwise addition of Milli-Q water. This process was continued for 45 minutes during which the paste-like consistency of the sample was maintained. The paste was then analysed for the formation of a new phase from powder X-ray diffraction data. If evidence of a new product was found the paste was recrystallised from water and further analyses were performed.

CO-PRECIPITATION

For the formation of native cyclodextrin inclusion complexes the host was dissolved in Milli-Q water at an elevated temperature (~60-70 °C). The guest was then added to this solution over the course of 10 minutes, approximately 1 mg at a time. The solution was stirred at the elevated temperature for 4 – 6 hours and filtered through a 0.45 μm nylon filter into a clean vial. This solution was then allowed to slowly evaporate on the benchtop or placed in a Dewar flask which was allowed to cool from ~70 °C to room temperature over several days. When preparing inclusion complexes with the methylated cyclodextrin hosts the initial solution containing host and guest was prepared at low temperature (~4 °C) and placed in an oven set at 60 °C to allow crystallisation of the inclusion complex.

MULTI-COMPONENT CRYSTALLINE SYSTEMS

Three methods were used to form co-crystals, salts and solvates. These are dry grinding (DG), liquid-assisted grinding (LAG) and co-precipitation.

DRY GRINDING

Dry grinding was used as the initial screening method. Equimolar quantities of the API and co-former were combined in an agate mortar and ground for approximately 20 minutes using an agate pestle. The resulting powder was then screened for the formation of a new phase by powder X-ray diffraction. The appearance of new peaks and the disappearance of peaks from the components indicated the formation of a new phase. The new phases that arose from the grinding experiments were recrystallised from an appropriate solvent system.

LIQUID-ASSISTED GRINDING

Solvent-assisted or liquid-assisted grinding (LAG) was performed in a similar manner to the DG experiment detailed above, the difference being that the grinding took place with the dropwise addition of a predetermined solvent. The product was analysed as detailed in the Dry Grinding section.

CO-PRECIPITATION

Co-precipitation was performed by combining the API and co-former in a vial. The mixture was then dissolved in an appropriate solvent system. The solution was stirred at elevated temperatures (generally within a few degrees of the solvent boiling point) for several hours. The solution was then filtered through a 0.45 μm nylon filter into a clean vial. The vial was finally sealed with Parafilm M® and left on the benchtop with a few holes in the parafilm to form crystals via slow evaporation.

THERMAL ANALYSIS

Three major analytical techniques were used in the thermal analysis of the products obtained from the above experiments, namely thermogravimetric analysis (TGA), differential scanning calorimetry (DSC) and hot stage microscopy (HSM).

THERMOGRAVIMETRIC ANALYSIS

The technique of TGA is performed to determine the mass loss of a substance as a function of temperature. This experiment is typically performed under a controlled atmosphere, namely dry nitrogen gas, to prevent oxidation during the heating process. The TGA profiles obtained were used to determine the stoichiometry of the supramolecular constructs where the mass loss took

place in one-step for each component. TGA was also used to determine the amount of solvent present in each system and to investigate the thermal stability of the products.

The experiments were performed on a TA Instruments TA-Q500 with Universal Analysis 2000 software and a dry nitrogen flow rate of 60 $cm^3\ min^{-1}$. Crystals were removed from the mother liquor and dried on filter paper to remove any surface solvent. The sample (3-10 mg) was subsequently placed in an alumina crucible and loaded into the furnace, which was heated at a rate of 10 $K\ min^{-1}$ until the desired temperature was achieved.

DIFFERENTIAL SCANNING CALORIMETRY

The DSC experiments measured the difference in heat flow between sample and reference pans. As the energy requirements differ to maintain the same temperature between the pans, endothermic and exothermic events can be monitored. The onset temperatures, temperature ranges and the enthalpy changes of thermal events were determined from the experimental traces. The melting point of the product was compared with those of the starting materials to confirm the formation of a new supramolecular assembly.

The samples were prepared in a similar manner to the TGA samples. The traces were collected on a TA Instruments TA-Q200 Differential Scanning Calorimeter with Universal Analysis 2000 software and a dry nitrogen gas flowrate of 60 $cm^3\ min^{-1}$. Crystals were surface dried on filter paper and a known mass of sample (1-5 mg) was then transferred to the Tzero aluminium sample pan. The pan was then crimped closed with a vented lid. The reference pan was prepared in an identical manner. A heating rate of 10 $K\ min^{-1}$ under dry nitrogen at 60 $cm^3\ min^{-1}$ was used.

HOT STAGE MICROSCOPY

HSM was used to corroborate and confirm the TGA and DSC data obtained. HSM allows one to visually observe physical changes that occur upon heating. The appearance of bubbles indicating solvent loss, changes in opacity or colour, melting and decomposition can all be observed directly *via* HSM. These changes can be difficult to glean directly from the TGA and DSC traces. However, by corroborating data with HSM photographs it was possible to correlate thermal events and hence identify them unambiguously.

The samples were placed in silicone oil on a cover slip and heated at a rate of 10 $K\ min^{-1}$ until decomposition was observed. The heating rate and temperature were controlled using a Linkam TP92 manual temperature control unit connected to a Linkam THMS600 hot stage which was mounted on a Nikon SMZ-10 stereoscopic microscope. Fitted to the microscope was a Sony Digital

Hyper HAD colour video used to capture the micrographs that were viewed with the Soft Imaging System Program, analySIS.[1]

X-RAY DIFFRACTION

Two X-ray diffraction techniques were used to obtain information regarding the newly prepared crystalline materials. The first was single crystal X-ray diffraction used to determine the crystal structure of the systems. Powder X-ray diffraction (PXRD) was used to screen for the formation of a new solid phase as well as to confirm the homogeneity of the bulk sample.

SINGLE CRYSTAL X-RAY DIFFRACTION

For single crystal X-ray diffraction, crystals of sufficient quality for diffraction were selected based upon their size, clarity, regularity and ability to extinguish plane-polarised light in a uniform fashion. Crystals selected were surface dried on filter paper and immediately placed in Paratone N oil[2] to prevent the loss of solvent. The oil also provided a rigid support for the crystal during low temperature data-collections. The crystal was then mounted on a nylon loop and the loop mounted on a goniometer head.

DATA-COLLECTION

The crystal intensity data were collected on two instruments. The first was a Nonius Kappa CCD (Charge Coupled Device) X-ray diffractometer. The radiation source was graphite-monochromated MoK_α radiation ($\lambda = 0.71073$ Å). The radiation was provided by a Nonius FR590 generator running at 50 kV and 30 mA. The second diffractometer used was a Bruker KAPPA APEX II DUO[3] X-ray diffractometer with graphite-monochromated MoK_α ($\lambda = 0.71073$ Å) radiation. The radiation was produced by using a Bruker K780 generator running at 50 kV and 20 mA. During each collection the crystals were maintained at a temperature of either 100(2) K or 173(2) K using a constant nitrogen stream controlled by a Cryostream cooler (Oxford Cryosystems, UK).

The programs DENZO and SCALEPACK[4] were used for unit cell refinement when using the Nonius Kappa diffractometer. Program SAINT[5] was used for unit cell refinement and data reduction when using the Bruker APEX II. All collected intensity data were corrected for Lorentz-polarisation (*Lp*) effects. Multi-scan absorption corrections (program SADABS[6]) were applied when heavy atoms were present in the structure. Once the intensity data were processed the crystal system was determined from the Laue group of the diffraction pattern and the space group was determined from systematic absences. This determination was verified using XPREP,[7] which was also used to prepare the input files for structure determination and refinement.

STRUCTURE SOLUTION AND REFINEMENT

Small multi-component systems were solved by the program SHELXS[8] and the structure refinement was performed using SHELXL.[8]

Isomorphous replacement was the main method used to solve cyclodextrin crystal structures. This was done by using the atomic co-ordinates of the rigid backbone of host molecules from isostructural cyclodextrin systems as trial models.[9] The structure was then refined using SHELXH[8] or SHELXL.[8,10] SHELXL was used after the release of the SHELX-2013[10] software package, which is capable of refining large structures. If isomorphous replacement was not applicable due to the complex not belonging to any known isostructural series, SHELXD[8] was used to solve the structure using direct methods as outlined below.

SHELXS

Smaller structures, such as salts and co-crystals, were solved using SHELXS.[8] SHELXS makes use of direct methods or the Patterson function to achieve a structure solution. Only direct methods were required during the scope of this study.

SHELXD

SHELXD[8] is part of the SHELX suite of programs written to deal with structures too large for the direct methods program SHELXS.[8] The software was based on the program *Shake and Bake* (*SnB*) by Miller *et al.*[11–13] Both SHELXD and *SnB* rely on dual-space iteration algorithms where the phases are calculated in reciprocal space and various strategies applied to attempt to improve the phase refinement; this is referred to as the "shake" part of the algorithm. These improvements are achieved by the use of the minimum function[14,15] in the case of *SnB*, and the tangent formula[16] in the case of SHELXD. The tangent formula is used to derive the phases for the remaining reflections from the most reliable phases. Once the improved phases are obtained, a real space electron density map is calculated incorporating the normalised structure factors derived from the intensities. The highest peaks are assigned as possible atoms and subjected to a random omit map where a given percentage of the top peaks are randomly deleted. The remaining atoms are used to calculate the new phases in reciprocal space and begin the calculation again. A figure of merit is required to determine the validity of the trials, of which successful trials are expanded employing all data using peaklist optimisation. This robust method is well suited to solve large structures, such as cyclodextrin inclusion complexes.

SHELXL/SHELXH

SHELXH[8] is a version of SHELXL[8] used for the refinement of large structures, the difference being that the array dimensions are specified by a parameter in SHELXH. SHELXL and SHELXH otherwise refine structures in the same manner.

The refinement is based on full-matrix least-squares minimisation of the function $\sum w(F_o^2 - F_c^2)^2$. The residual index R_1 (Expression 2.1) shows the agreement between the observed and calculated structure factors, F_o and F_c respectively. The lower the value of R_1 the greater the indication that the structure is acceptable.

Expression 2.1

$$R_1 = \frac{\sum \big| |F_o| - |F_c| \big|}{\sum |F_o|}$$

The residual index wR_2 (Expression 2.2) shows the agreement between the squares of the observed and calculated structure factors, F^2 (i.e. the observed and calculated intensities). However, this refinement enhances the deviation from unity for the goodness-of-fit (S, defined below) and therefore is not directly comparable to refinements against F.

Expression 2.2

$$wR_2 = \sqrt{\frac{\sum w(F_o^2 - F_c^2)^2}{\sum w(F_o^2)^2}}$$

The weighting scheme w in Expression 2.2 is defined in Expressions 2.3 and 2.4 where a and b are chosen such that there is a constant distribution of $[w(F_o^2 - F_c^2)^2]$ with $\sin\theta$ and $\sqrt{F_o/F_{max}}$.

Expression 2.3

$$w = \frac{1}{\sigma^2(F_o^2) + (aP)^2 + bP}$$

Expression 2.4

$$P = \frac{2F_c^2 + max(0, F_o^2)}{3}$$

The goodness-of-fit, S, is given by Expression 2.5 where n and p are the number of reflections and the total number of refinement parameters respectively. S should be close to unity and the ratio n/p should be greater than ten for centrosymmetric space groups.[17] For non-centrosymmetric space groups the ratio should be at least ten if the structure contains heavy atoms and not less than eight if the structure contains only atoms lighter than argon.[17]

Expression 2.5

$$S = \sqrt{\sum \frac{w(F_o^2 - F_c^2)^2}{n - p}}$$

POWDER X-RAY DIFFRACTION

To record PXRD traces two diffractometers were used. Some samples were analysed on a Huber Imaging Plate Guinier Camera 670 with a Ni-filtered CuK_α radiation source (λ = 1.54060 Å). A Philips PW1120/00 X-ray generator running at 40 kV and 20 mA produced the radiation. The diffractometer was fitted with a Huber fine-focus tube PW2273/20 and a Huber Guinier Monochromator Series 611/15. MYLAR® polyester film coated with a thin layer of Paratone N oil[2] suspended in a flat sample holder was used to mount the samples. Samples were scanned over the $4° \leq 2\theta \leq 40°$ range with a 0.005° step size and data were plotted using Microsoft Excel over the desired range.

The other diffractometer used was a Bruker D8 Advance diffractometer fitted with a Lynxeye detector and CuK_α radiation source (λ = 1.54060 Å). The generator was operated at 30 kV and 40 mA. Samples were mounted on a Si low background sample holder and scanned over the $4° \leq 2\theta \leq 40°$ range with a step size of 0.01°. The data were plotted using Microsoft Excel.

Data were analysed in various ways depending on the purpose of the scan. Screening of products from kneading and grinding experiments was performed by comparing the PXRD trace of the product with those of the starting materials. If a new phase is present the traces will differ with the disappearance of various peaks and appearance of new ones. If the product is not a new phase the trace will be a sum of the starting material traces. In the case of experiments involving cyclodextrins, PXRD traces of the products were compared with those for known isostructural series[9] of cyclodextrin inclusion complexes. When a match was obtained, a definitive indication of complex formation resulted. In addition, the space group and approximate unit cell dimensions could be predicted for the new complex. An alternative approach in the determination of new phases is to compare the PXRD trace of the putative complex to the traces of the starting materials. If the diffraction patterns differ resulting from the disappearance of peaks and the appearance of new peaks in the complex trace one can conclude that a new phase has been obtained. This approach was used for cyclodextrins when the complex was not isostructural with a known cyclodextrin inclusion complex series.

To confirm that the single crystal X-ray structure is representative of the bulk product, the powder pattern was calculated from the single crystal structure and compared with the

experimental PXRD pattern. The calculated PXRD pattern was prepared using software packages LAZY PULVERIX[18] or Mercury.[19,20] LAZY PULVERIX comprises two programs that run consecutively; LAZY is the first, where the data are prepared for the calculation of the powder diffraction pattern by PULVERIX. LAZY is used to derive the equivalent atomic positions, Laue-group, systematic absence conditions, atomic scattering factors and coefficients for anomalous dispersion. PULVERIX then calculates the powder diffraction pattern. The positions of the diffraction peaks are calculated from their *d*-spacing and Bragg's law. The intensities (I_{hkl}) of the peaks are calculated using Expression 2.6, where m is the reflection multiplicity factor, L is the Lorentz factor, P the polarisation factor and F_{hkl} is the calculated structure factor. The data are then tabulated and can be plotted as needed.[18]

Expression 2.6

$$I_{hkl} = mLPF_{hkl}^2$$

The program Mercury calculates the Lorentz-polarisation (Lp) corrected powder diffraction pattern. The Lp correction assumes the use of a laboratory X-ray source with fixed slit widths. Absorption, noise and the background are not included in the calculation while hydrogen atoms are assumed to have a U_{iso} value of 0.05 Å^2. The reflections are modelled with pseudo-Voigt peak shapes and a full width at half maximum (FWHM) of 0.1° 2θ. The 000 reflection is generally excluded and the default radiation source is set as CuK_α.[19] The calculated pattern is then plotted using Microsoft Excel.

The spacing of crystallographic planes can vary with temperature, however these changes are unpredictable since crystal shrinkage or expansion is typically anisotropic. Shifts thus occur in the diffraction peak positions resulting from changes in the *d*-spacings. As the PXRD patterns are generally calculated from low temperature structures the values of 2θ are therefore sometimes shifted relative to the experimental pattern collected at room temperature.

FOURIER TRANSFORM INFRARED SPECTROSCOPY

Fourier transform Infrared (FTIR) spectra were collected using a PerkinElmer FT-IR Spectrum spectrometer fitted with a Universal ATR accessory. All samples were scanned over the 4000 to 400 cm^{-1} range at a rate of 4 s (cm^{-1})$^{-1}$.

The data were analysed using the OPUS 7.2 software package. FTIR was used to determine whether a proton was transferred during the formation of the multi-component crystal system resulting in a salt. If no proton transfer occurred the resulting product was confirmed to be a co-crystal.

ULTRAVIOLET-VISIBLE SPECTROSCOPY

Ultraviolet-Visible light (UV-Vis) spectroscopy was used to evaluate the concentration of the API in solution. This was used for phase solubility experiments. Furthermore, interaction of a bioactive molecule with a cyclodextrin can affect absorbance properties of the API. The UV-Vis spectra were recorded on a Shimadzu UV-2101 spectrophotometer and a Cintra 20 UV-Visible spectrophotometer. Data were plotted and analysed using Microsoft Excel.

INDUCED CIRCULAR DICHROISM

Induced Circular Dichroism (ICD) relies on the differing absorbance of left and right circularly polarised light by chiral molecules. Cyclodextrins are not UV active, however the cavity is a chiral environment. The APIs are not chiral, but are UV active. By complexing the API with the cyclodextrin a chiral system that absorbs circularly polarised UV electromagnetic radiation is achieved. This allows one to investigate the nature of the interaction between the host and guest, as well as the orientation of the guest molecule within the cyclodextrin cavity based on the Cotton effect.

The instrument used was a JASCO Model J-810 spectropolarimeter. Samples and blanks were prepared in Milli-Q water filtered through a 0.45 μm filter. The experimental parameters were as follows: N_2 flow rate 15 cm^3 min^{-1}, response 2 s, scanning speed 100 nm min^{-1}, range scanned 200 – 450 nm and accumulation 4. The spectra obtained for the blanks were subtracted from the experimental spectra for all samples.

NUCLEAR MAGNETIC RESONANCE SPECTROSCOPY

Nuclear magnetic resonance (NMR) spectroscopy was used to determine the molar ratio of the components in each of the supramolecular systems. Crystals were dissolved in an appropriate deuterated solvent and the ^1H NMR spectra recorded. The proton signals were integrated and the molar ratio determined by direct comparison of the component signals.

NMR spectroscopy was further used to quantitatively evaluate the concentration of acipimox for equilibrium solubility experiments. This method employed DMSO as an internal standard and the relative integration of the appropriate protons allowed calculation of the final acipimox concentration.

A Bruker 300 MHz spectrometer was used to collect all spectra using the pulse program zq30.[21] The data were evaluated using the Bruker software Topspin[21] and plotted using Microsoft Excel.

REFERENCES

1 Soft Imaging System GmbH, *Digital Solutions for Imaging and Microscopy*, Version 3.1 for Windows (Copyright 1987-2000).

2. Paratone N oil (Exxon Chemical Co., Texas, USA).

3. APEX2, Version 1.0-27, Bruker AXS Inc., Madison, Wisconsin, USA.

4. Z. Otwinowski and W. Minor, *Methods in Enzymology*, eds. C. J. Carter and R. Sweet, Academic Press, 1997, pp. 307–326.

5. Program SAINT, Version 7.60a, Bruker AXS Inc., Madison Wisconsin, USA, **2006**.

6. G. M. Sheldrick, Program SADABS, Version 2.05, University of Göttingen, Germany, **2007**.

7. XPREP, *Data Preperation and Reciprocal Space Exploration*, Version 5.1, © Bruker AXS Inc., **1997.**

8. G. M. Sheldrick, *Acta Cryst.*, 2008, A**64**, 112–122.

9. M. R. Caira, *Rev. Roum. Chim.*, 2001, **46**, 371–386.

10. G. M. Sheldrick, *Acta Cryst.*, 2015, C**71**, 3–8.

11. R. Miller, S. M. Gallo, H. G. Khalak, and C. M. Weeks, *J. Appl. Crystallogr.*, 1994, **27**, 613–621.

12. I. Usón and G. M. Sheldrick, *Curr. Opin. Struct. Biol.*, 1999, **9**, 643–648.

13. G. M. Sheldrick, H. A. Hauptman, C. M. Weeks, R. Miller, and I. Usón, in *International Tables for Crystallography*, eds. E. Arnold and M. Rossmann, Kluwer Academic Publishers, 2001, pp. 333–351.

14. R. Miller, G. T. DeTitta, R. Jones, D. A. Langs, C. M. Weeks, and H. A. Hauptman, *Science*, 1993, **259**, 1430–1433.

15. T. Debaerdemaeker and M. M. Woolfson, *Acta Cryst.*, 1983, A**39**, 193–196.

16. J. Karle and H. Hauptman, *Acta Cryst.*, 1956, **9**, 635–651.

17. IUCr Webmaster, *Data Validation Procedures*, © International Union of Crystallography, http://journals.iucr.org/services/cif/checking/validlist.html, 20/08/2015

18. K. Yvon, W. Jeitschko, and E. Parthé, *J. Appl. Crystallogr.*, 1977, **10**, 73–74.

19. C. F. Macrae, P. R. Edgington, P. McCabe, E. Pidcock, G. P. Shields, R. Taylor, M. Towler, and J. van de Streek, *J. Appl. Crystallogr.*, 2006, **39**, 453–457.

20. C. F. Macrae, I. J. Bruno, J. A. Chisholm, P. R. Edgington, P. McCabe, E. Pidcock, L. Rodriguez-Monge, R. Taylor, J. van de Streek, and P. A. Wood, *J. Appl. Crystallogr.*, 2008, **41**, 466–470.

21. Program TopSpin, Version 3.2, Bruker BioSpin GmbH, 2014.

CHAPTER 3 – 2,5-DICHLOROBENZOIC ACID METHYL ESTER

For convenience 2,5-dichlorobenzoic acid methyl ester will be abbreviated to DCB. This compound is a fungicide of low aqueous solubility (87 mg dm^{-3} at 20 °C).[1] The low solubility makes the application of DCB in a useable form problematic, requiring a wax formulation.[2]

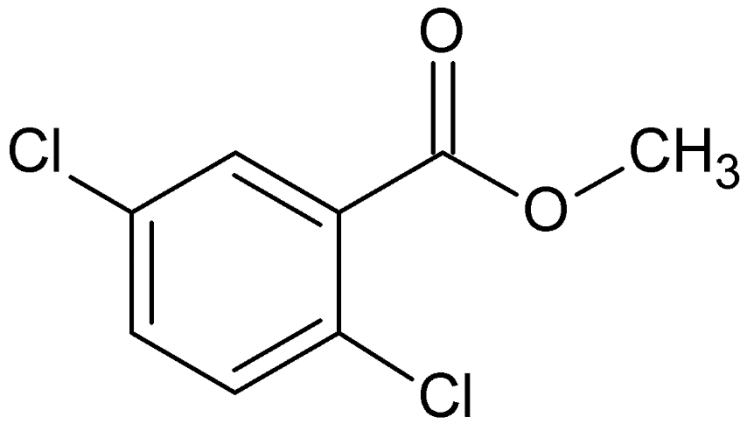

INTRODUCTORY REMARKS

During the experimental investigation into the inclusion of 2,5-dichlorobenzoic acid methyl ester in cyclodextrins various hosts were tried. The inclusion in native cyclodextrins, namely α-cyclodextrin, β-cyclodextrin and γ-cyclodextrin was attempted before the use of methylated cyclodextrins was pursued. Unfortunately only γ-cyclodextrin was successful as a host compound from the native cyclodextrins. Of the methylated derivatives, DIMEB, TRIMEA and TRIMEB were attempted, and only DIMEB gave rise to an inclusion complex.

This chapter will focus on the successful attempts at forming cyclodextrin inclusion complexes with 2,5-dichlorobenzoic acid methyl ester.

γ-CYCLODEXTRIN/(2,5-DICHLOROBENZOIC ACID METHYL ESTER)

The γ-cyclodextrin complex with 2,5-dichlorobenzoic acid methyl ester will be referred to as GCDDCB.

SAMPLE PREPARATION

10 mg (0.049 mmol) of DCB was weighed and combined with 63 mg (0.049 mmol) γ-cyclodextrin in an agate mortar. The mixture was kneaded using an agate pestle with dropwise addition of water for 30 minutes. Attempts to prepare a complex via co-precipitation did not yield single crystals, although powdered samples were obtained. However, this was not considered a serious drawback, since if single crystals had been available, the probability of guest location would have been very low due to predictable disorder of the guest which arises from the four-fold rotational symmetry centred on the cavity. The crystalline samples obtained from this preparation were used for all analyses presented below.

COMPLEX STOICHIOMETRY

A powdered sample obtained from co-precipitation experiments was dissolved in DMSO-d_6 and analysed using ^{1}H-NMR spectroscopy to calculate the stoichiometric ratio of the GCDDCB complex. The labelling scheme of the glucopyranose subunit is shown in Figure 3.1 below. Integration of the C1-H proton signal of γ-CD and the aromatic and methyl DCB proton signals showed a γ-CD:DCB ratio of 3:4 for the complex. The integration values are presented below in Table 3.1 and the spectrum can be seen in Figure 3.2.

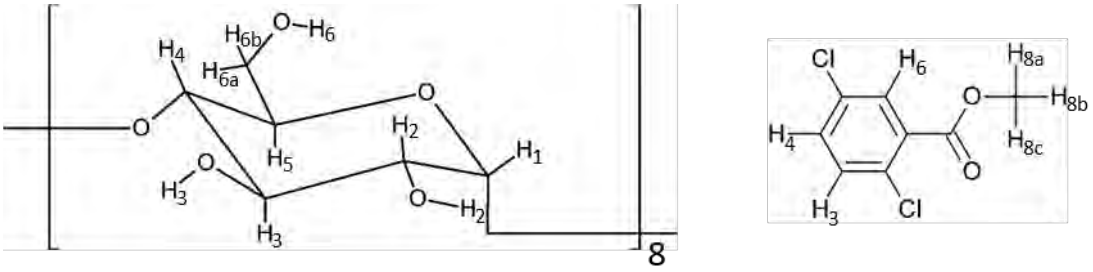

Figure 3.1: Proton labelling of γ-CD glucopyranose subunits (left) and DCB (right)

Table 3.1: Integrals and assignment of host and guest protons used for stoichiometric confirmation

Proton	δ (ppm)	Integration		Experimental/ Theoretical
		Experimental	Theoretical	
γ-cyclodextrin				
C-H_1	4.93	8.00‡	8.00	1
O-H_2 + O-H_3	5.78	16.19	16.00	1.01 ≈ 1
O-H_6	4.54	8.16	8.00	1.02 ≈ 1
2,5-dichlorobenzoic acid methyl ester				
C-H_3 + C-H_4	7.69	2.64	2.67	0.99 ≈ 1
C-H_6	7.90	1.35	1.33	0.98 ≈ 1

‡*Reference Integral*

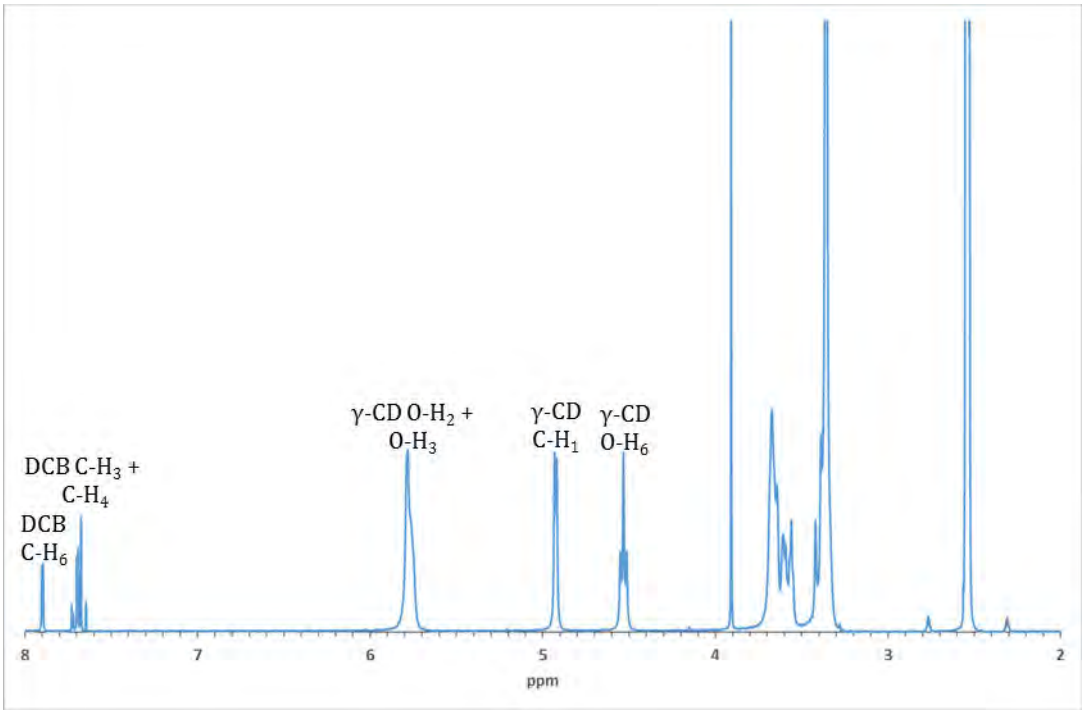

Figure 3.2: NMR spectrum of GCDDCB in DMSO-d_6 to determine the stoichiometric ratio

COMPARATIVE POWDER X-RAY DIFFRACTION

The paste resulting from the kneading preparation was subjected to PXRD to investigate the formation of a new phase. The PXRD traces are shown in Figure 3.3. The experimental trace was compared to the calculated reference pattern of the γ-cyclodextrin inclusion complex of 12-crown-4 (CSD refcode: DOCYID).[3,4] The good correlation between the traces indicates that the materials are isostructural, crystallising in the space group $P42_12$. This indicates that the material prepared by kneading is of a channel type inclusion complex.

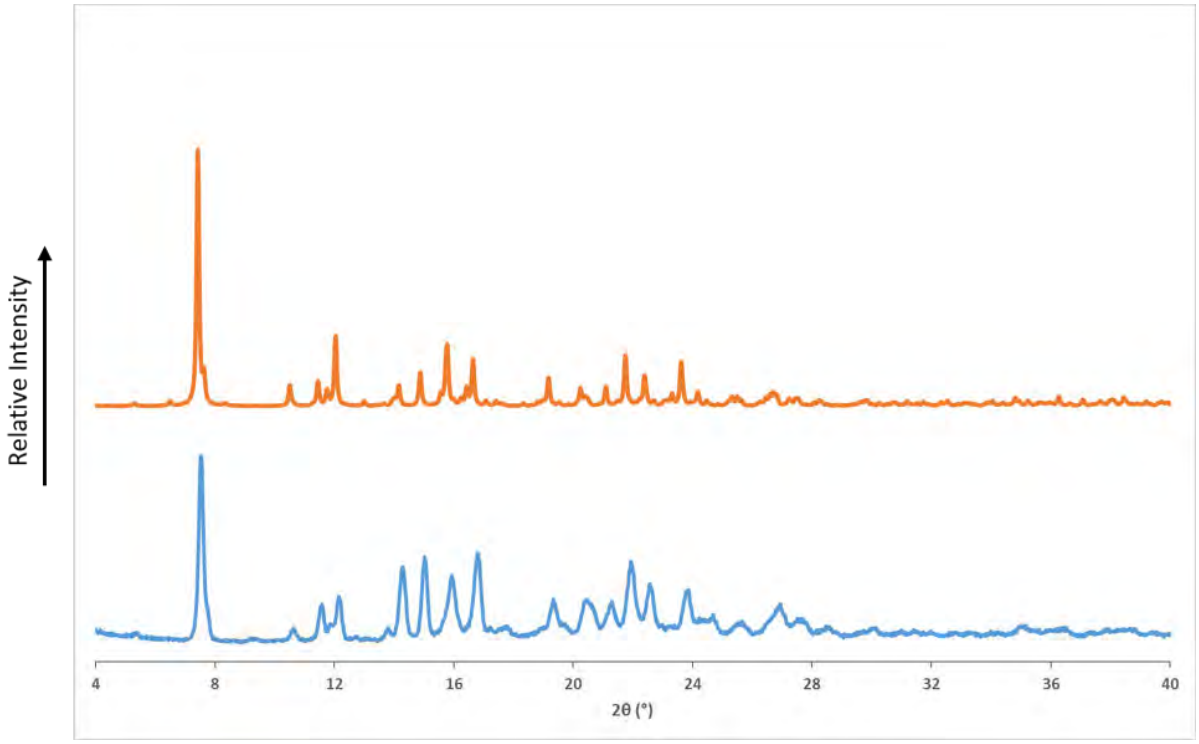

Figure 3.3: Comparative PXRD trace of the putative GCDDCB complex (blue) and the calculated DOCYID reference pattern (orange)

THERMAL ANALYSIS

The TGA and DSC traces of GCDDCB crystals prepared by co-precipitation are presented in Figure 3.4. As can be seen in the TGA trace, there is an immediate mass loss due to dehydration of the inclusion complex. From room temperature to 112 °C a mass loss of 13.0 ± 0.1 % (n = 2) was observed. This mass loss equates to 9.8 ± 0.1 water molecules per cyclodextrin molecule. The DSC trace corroborates the interpretation as the dehydration of the complex by the presence of the broad endotherm over the same temperature range. Furthermore, the HSM image at 100 °C (Figure 3.5) shows the evolution of bubbles indicating solvent loss. A second mass loss occurs starting at 168.0 ± 0.9 °C (n = 2) corresponding to the loss of DCB (calculated mass loss 17.5 %).

This mass loss overlaps with the beginning of the decomposition of the host at 281.9 ± 1.4 °C (n = 2), as shown in Figure 3.4. The stoichiometry of this complex (3:4) had previously been determined by NMR spectroscopy. The degradation of the host is present in the TGA trace as a large mass loss of 66.6 ± 1.0 % (n = 2). The degradation is also evident in the DSC trace over the same temperature range as a large endotherm and is clearly visible in the final two HSM images.

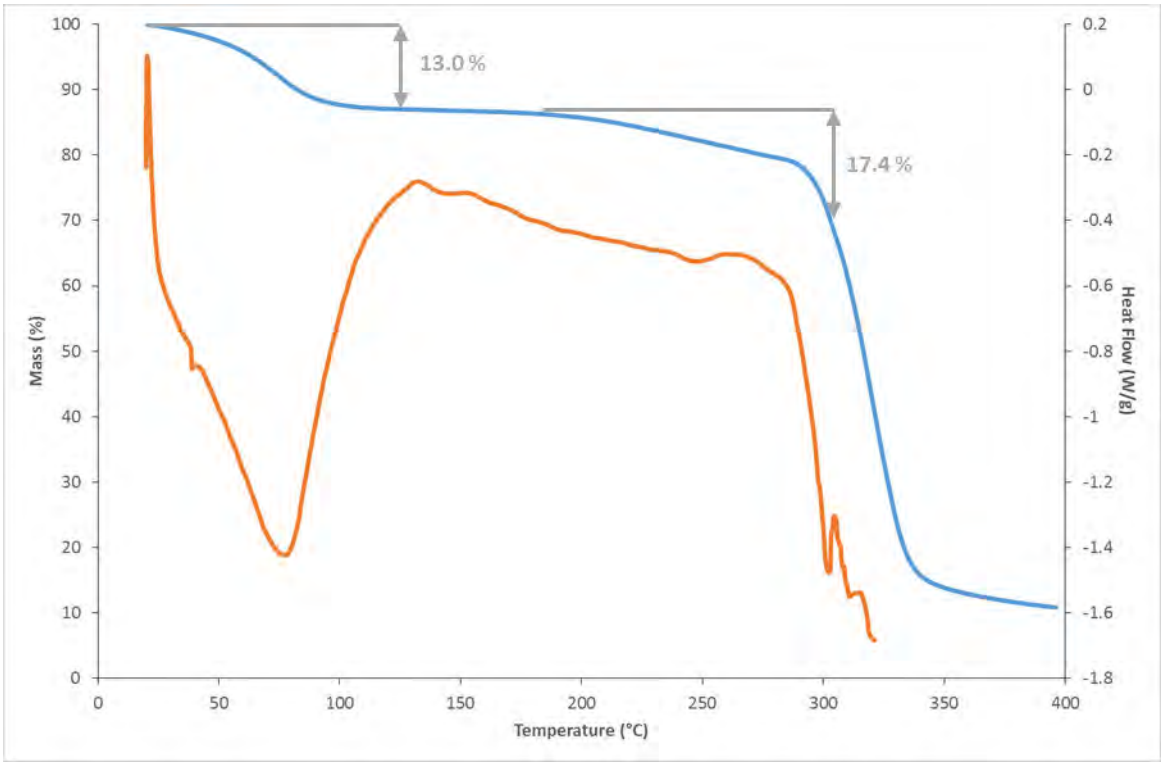

Figure 3.4: Representative TGA (blue) and DSC (orange) traces for GCDDCB

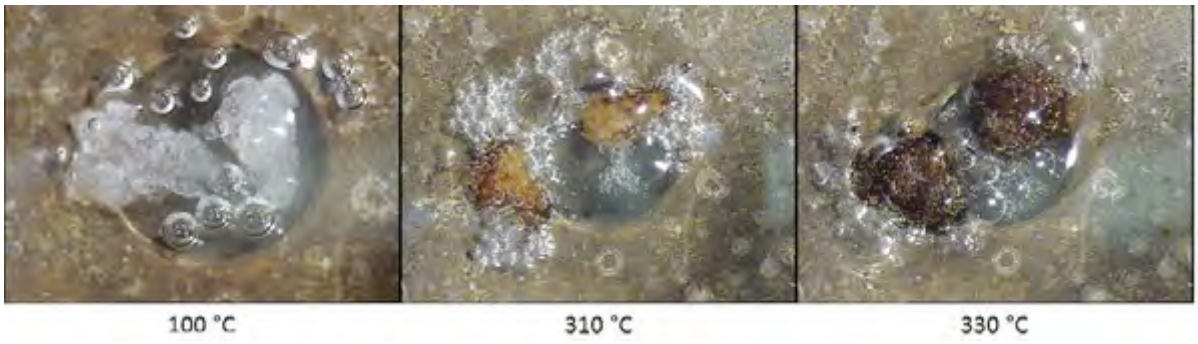

Figure 3.5: Hot stage micrographs showing the GCDDCB complex at various stages of heating

DIMEB/(2,5-DICHLOROBENZOIC ACID METHYL ESTER)

The complex of 2,5-dichlorobenzoic acid methyl ester and DIMEB will be referred to as DMBDCB for convenience.

SAMPLE PREPARATION

This product was synthesised using a co-precipitation method. To create this inclusion complex 64.9 mg (0.049 mmol) of DIMEB was weighed and dissolved in 3 cm^3 Milli-Q water at 4 °C. 10 mg (0.049 mmol) of 2,5-dichlorobenzoic acid methyl ester was slowly added to the cyclodextrin solution and this mixture was then stirred for 3 to 4 hours at 4 °C. This mixture was then heated to 50 °C and cycled back to 4 °C several times to determine the point at which the majority of the complex was in solution. The mixture was then filtered through a 0.45 µm nylon filter into a clean vial. The vial was then placed in a 60 °C oven for several days until large needle-like crystals appeared.

COMPLEX STOICHIOMETRY

The stoichiometry of DMBDCB was determined via thermal analysis. A mass loss of 13.7 ± 0.6 % (n = 2), interpreted as guest release, was observed with an onset temperature of 142.0 ± 1.3 °C. This mass loss corresponds to a complex ratio of 1:1 (calculated mass loss = 13.3 %). Furthermore, no solvent loss is observed for this complex indicating that there are no waters of crystallisation present.

THERMAL ANALYSIS

The thermal analysis of DMBDCB (Figure 3.6) show that there is no solvent loss. A mass loss of 13.7 ± 0.6 % (n = 2), corresponding to the release of one guest molecule per complex unit, occurs with an onset at 142.0 ± 1.3 °C in two steps, with the second continuing smoothly until decomposition of the host at 357.1 ± 1.3 °C. Since the first distinct mass loss of (~8%) corresponds to one half of the total guest mass loss, a possible explanation is that the complex undergoes a rearrangement from a 1:1 to a 2:1 complex. Subsequent guest loss would not necessarily have a similar thermal profile. Figure 3.7 showing the derivative with respect to temperature clearly exposes the presence of the mass loss. Pure DCB melts at a temperature of 39.9 °C and decomposes over a very large range from 49.9 °C to 170.0 °C; as such it is reasonable that the slow two-step mass loss occurring upon heating the complex is the loss of DCB. This is expanded upon in the discussion. The endotherms in the DSC trace corroborate this interpretation with a small endotherm at 149 °C corresponding to the loss of half the guest

molecules and rearrangement of the complex. The second endotherm from 345-392 °C corresponds to decomposition of the host molecule. This analysis is further evidenced by the hot stage microscopy images (Figure 3.8) where there is no apparent solvent loss in the images; the crystals then begin to become opaque in line with the mass loss beginning at 149 °C until decomposition is clearly visible in the final image at 308 °C.

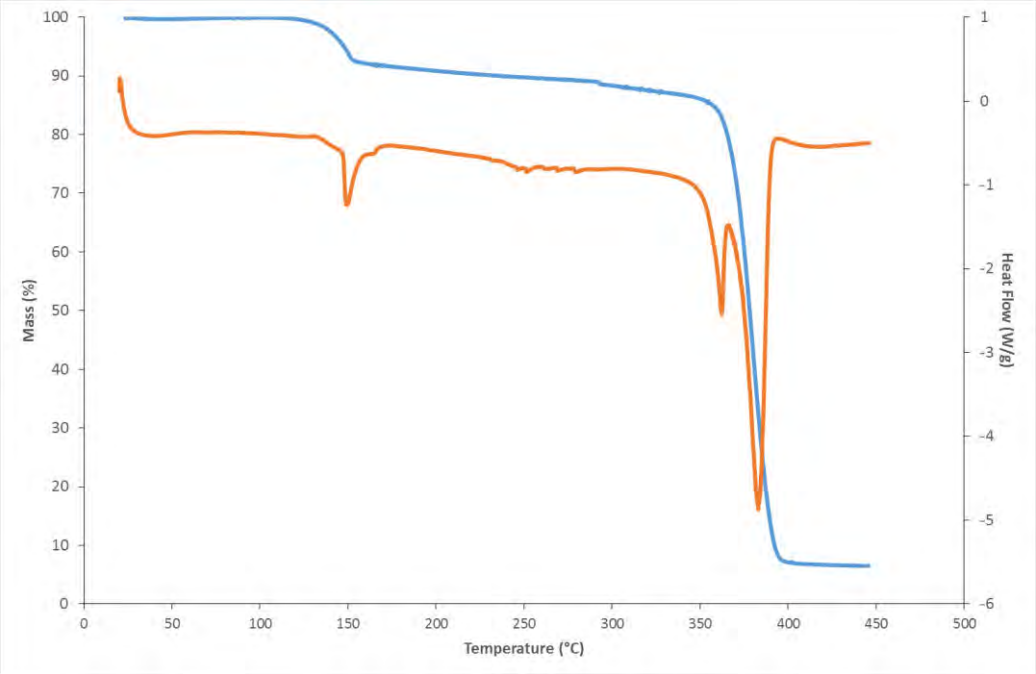

Figure 3.6: Representative TGA (blue) and DSC (orange) traces for DMBDCB

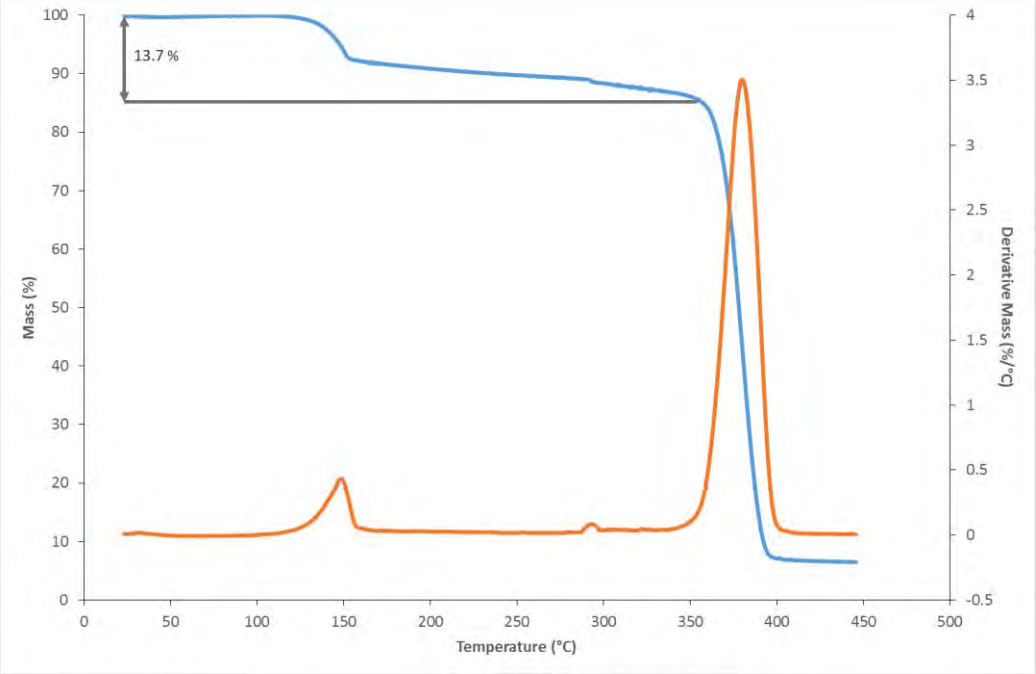

Figure 3.7: TGA trace (blue) showing the derivative with respect to temperature (orange) and mass loss

Figure 3.8: Hot stage micrographs showing the DMBDCB complex at various stages of heating

CRYSTAL STRUCTURE ANALYSIS

The stoichiometry of the complex was determined to be 1:1 from TGA experiments as described above.

DATA COLLECTION AND SPACE GROUP DETERMINATION

Data were collected on a Bruker KAPPA APEX II DUO diffractometer. The X-ray diffraction pattern was determined to have *mmm* Laue symmetry, which in turn indicated that the crystal system was orthorhombic. The space group was determined to be $P2_12_12_1$ by examining the systematic absences. The conditions limiting reflection were *hkl:* none, *h00: h = 2n, 0k0: k = 2n, 00l: l = 2n* confirming the assignment. The data collection was performed at 173 ± 2 K.

STRUCTURE SOLUTION AND REFINEMENT

The program SAINT[5] was used in the unit cell refinement and data reduction. The asymmetric unit comprises one DIMEB molecule and one DCB molecule. The atomic positions of the cyclodextrin host were determined using isomorphous replacement.[6] To perform this structure solution the atomic coordinates of the rigid backbone structure of an isostructural complex were used as a trial model. A CSD search was undertaken to determine if any DIMEB complexes with unit cell data close to those of the DMBDCB complex existed. Eleven isostructural DIMEB complexes were found in the CSD.[4] A good match was found in the inclusion complex of 2,4-dichlorophenoxyacetic acid and DIMEB (refcode: PABNEM).[4,7] The DIMEB backbones of the DMBDCB and DIMEB/(2,4-dichlorophenoxyacetic acid) complexes have very similar atomic co-ordinates. The differences in the unit cell lengths are only 0.3861 Å along the *a*-axis, 0.4916 Å along the *b*-axis and 0.2399 Å along the *c*-axis.

The rigid backbone selected for isomorphous replacement included the non-hydrogen atoms of the glucose rings without the conformationally flexible methoxy substituents. The remaining non-hydrogen atomic co-ordinates were determined through subsequent electron density difference maps. The glucopyranose subunits were labelled G1 through G7 to uniquely identify atoms. All host non-hydrogen atoms were refined anisotropically. The hydrogen atoms of the glucopyranose subunits were revealed in the difference Fourier map; once located they were added using a riding model with a U_{iso} value 1.2 to 1.5 times that of the parent atom.

Table 3.2: Crystallographic data for the single crystal X-ray structure of DMBDCB

Chemical formula	$C_{56}H_{98}O_{35}\cdot C_8H_6Cl_2O_2$
Molar Mass (g mol^{-1})	1536.37
Crystal system	Orthorhombic
Space group	$P2_12_12_1$
Unit cell parameters	
a (Å)	15.2721(8)
b (Å)	18.4884(10)
c (Å)	28.2751(15)
α = β = γ (°)	90.0
Volume (Å^3)	7983.7(7)
Z	4
Density$_{calcd.}$ (g cm^{-3})	1.278
μ [MoKα] (mm^{-1})	0.168
F (000)	3272
Temperature (K)	173(2)
Crystal size (mm)	0.08 x 0.10 x 0.23
Range scanned θ (°)	1.5 - 27.2
Index ranges	h: -19, 19; k: -23, 23; l: -34, 24
ϕ and ω scan angles (°)	0.50
Total number of frames	695
Dx (mm)	39.71
Total number of reflections	50 871
Number of independent reflections	17 658
Number of reflections with I > 2σ(I)	11 630
R_{int}	0.056
R_1 [I > 2σ(I)]	0.0429
wR_2	0.0902
S	0.987
Number of parameters	951
Number of reflections omitted	11
Parameters a, b in w = 1/[σ^2(F_O^2)+(aP)^2+(bP)]	a = 0.0369; b = 0
$(\delta/\sigma)_{mean}$	<0.001
Δρ excursions (e Å^{-3})	-0.22; 0.27

MODELLING OF 2,5-DICHLOROBENZOIC ACID METHYL ESTER

Once the non-hydrogen atoms of the host molecule were modelled the remaining high electron density peaks were assigned to the guest molecule. The molecule was not found to be disordered and furthermore no restraints were required during its refinement. All of the guest non-H atoms were refined anisotropically. The hydrogen atoms were located in the difference Fourier map and then included in idealised positions with a U_{iso} value of 1.2 to 1.5 times that of the parent atom.

GEOMETRIC ANALYSIS OF DMBDCB

The asymmetric unit of DMBDCB comprises a monomeric complex; this is shown in Figure 3.9. The numbering schemes for the guest and host molecules are presented in Figure 3.10.

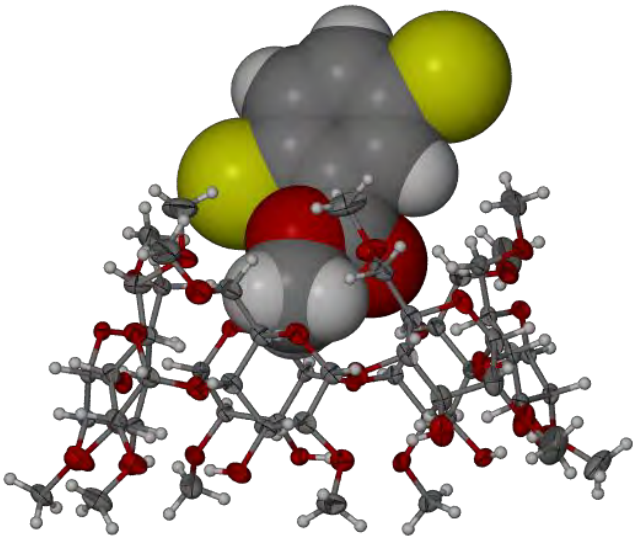

Figure 3.9: The asymmetric unit of the complex DMBDCB. Thermal ellipsoids for the host atoms are drawn at the 50% probability level and the guest atoms are drawn in space-filling mode.

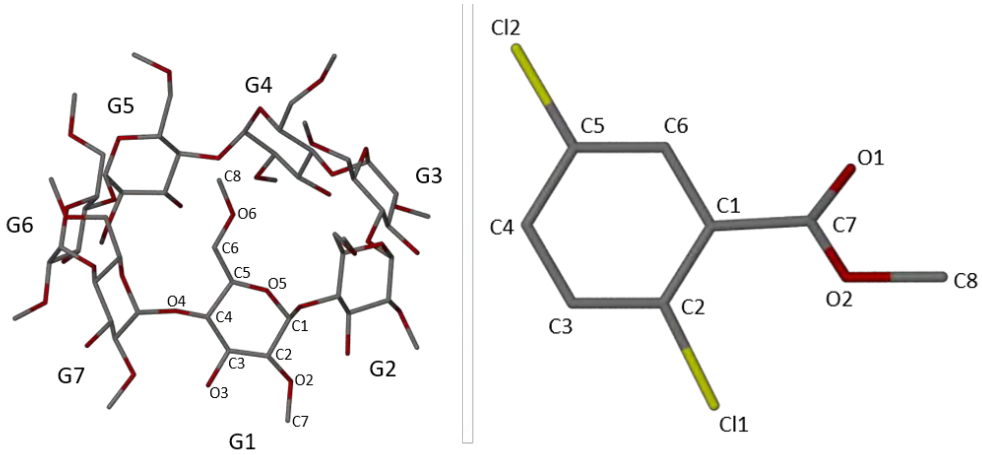

Figure 3.10: Numbering scheme of the glucopyranose rings (left) and guest molecule (right)

HOST CONFORMATION

The torsion angles of the primary methoxy substituents are listed in Table 3.3; this torsion angle, ω, is the O5-C5-C6-O6 dihedral angle. It was found that five of the substituents are directed away from the cyclodextrin cavity, while the G1 and G3 primary methoxy substituents are directed inwards. No intermolecular contacts smaller than the sum of the van der Waals radii were found between the host and guest molecules. The mean close contact distance involving non-hydrogen atoms was found to be 3.700 ± 0.131 Å. These values fall outside the range of intermolecular distances indicating interactions of atoms present in the structure. This shows that there is no steric hindrance for the positioning of the guest molecule at the primary end of the cyclodextrin cavity.

Table 3.3: Torsion angles (ω) for DMBDCB

Glucose Residue	ω (°)‡
G1	81.8
G2	-72.4
G3	84.8
G4	-72.3
G5	-74.7
G6	-64.7
G7	-75.4

‡*Mean e.s.d. 0.3°*

Table 3.4 shows the geometric analysis parameters of the DMBDCB complex. The data show that the DIMEB molecule adopts a circular shape. This can be seen by the very slight variation in the *l*, *D* and ϕ parameters where the mean values are 5.055 ± 0.084 Å, 4.390 ± 0.051 Å and 128.4 ± 1.9° respectively. From the minimal deviations in the values it is clear that the circular shape of the cavity is not distorted. The shape of the macrocyclic structure is maintained by the well-known intramolecular O3(n+1)–H···O2n hydrogen bonds. The deviation of the O4 atoms from the O4 least-squares mean plane are small. The tilt angles τ_2 are all positive indicating that the primary rims of the glucopyranose subunits are all tilting inwards towards the cavity.

There are three known structures of uncomplexed DIMEB hydrates (CSD refcodes: BOYFOK04,[4,8] QIYKEO[4,9] and CEQCUW[4,10]). BOYFOK04 (DIMEB·15H_2O) has been chosen for the principal comparison with the complexed DIMEB molecule as these have the most similar geometric parameters (Tables 3.4 and 3.5). A brief comparison with the other two structures is presented below.

Upon examination of BOYFOK04, relatively small differences between its parameters and those of DIMEB in the DIMEB·DCB complex were observed for the tilt angles, τ_2, and the O4 to O4n centroid distance, *l*. The ranges of τ_2 are similar in both structures (DMBDCB: 3.4° ≤ τ_2 ≤ 24.9° and BOYFOK04: 2.8° ≤ τ_2 ≤ 27.6°). The cavities of the respective DIMEB molecules maintain similarly "round" shapes as evidenced by *l* (DMBDCB: 4.96 Å ≤ *l* ≤ 5.18 Å and BOYFOK04: 4.90 Å ≤ *l* ≤ 5.24 Å). As can be seen from these values, the two DIMEB structures maintain similar shapes whether or not DCB is complexed. Several DIMEB inclusion complexes contain host molecules that are elliptically distorted to accommodate guest molecules, an example of this being the DIMEB inclusion complex of 3-(-6-methoxy-pyridin-3-yl)-5-(4-methylsulfonylphenyl)-pyridin-2-amine.[11] In this case the DIMEB molecule is distorted elliptically to include the 4-(methylsulfonyl)phenyl ring. The guest in DMBDCB is instead included with guest atoms abutting the primary methoxy groups, allowing the circular shape of the cavity to be maintained (see Guest Inclusion section below).

Another feature common to both structures is the 'self-inclusion' of one of the primary methoxy moieties in an adjacent DIMEB molecule; details of this 'self-inclusion' are found in the Crystal Packing section below.

The other two hydrated DIMEB structures show similar ranges in the τ_2 tilt angles and the distance *l*. The τ_2 values range thus: QIYKEO: 4.1° ≤ τ_2 ≤ 29.7° and CEQCUW: 3.6° ≤ τ_2 ≤ 24.3°. The variations in *l* are 4.45 Å ≤ *l* ≤ 5.19 Å and 4.91 Å ≤ *l* ≤ 5.26 Å for QIYKEO and CEQCUW respectively. These values indicate that these DIMEB hydrates similarly maintain their circular shape. Self-inclusion is also present in both these structures, but it is much less pronounced in CEQCUW.

Table 3.4: Geometric analysis parameters for DMBDCB

Residue	*l* (Å)	*D* (Å)	ϕ (°)	*d* (°)	α[a] (Å)	D_3[b] (Å)	τ_2[c] (°)
G1	5.145	4.364	127.2	-6.5	-0.163	2.986	17.7
G2	5.122	4.396	130.3	-3.9	0.181	2.836	3.4
G3	4.962	4.384	129.9	5.9	0.014	2.864	24.9
G4	4.994	4.407	125.4	-0.2	-0.147	2.893	17.0
G5	5.177	4.287	129.9	-0.8	0.046	2.806	6.4
G6	5.019	4.459	130.2	-6.6	0.091	2.966	19.5
G7	4.964	4.434	126.3	11.8	-0.022	2.785	15.0

[a] *mean e.s.d.: 0.002 Å;* [b] *mean e.s.d.: 0.003 Å;* [c] *mean e.s.d.: 0.1°.*

Table 3.5: Geometric analysis parameters for DIMEB·15H$_2$O (ref code: BOYFOK04)[4,8]

Residue	*l* (Å)	*D* (Å)	ϕ (°)	*d* (°)	α (Å)	D_3 (Å)	τ_2 (°)
G1	5.094	4.356	125.9	2.5	-0.112	2.848	11.0
G2	4.896	4.408	127.7	3.4	-0.057	3.043	11.0
G3	5.082	4.471	131.6	0.1	0.187	2.860	27.6
G4	5.237	4.296	128.3	-8.7	-0.067	2.953	18.0
G5	4.901	4.402	123.9	8.0	-0.132	2.809	2.8
G6	4.987	4.442	132.5	1.7	0.119	2.826	18.6
G7	5.196	4.367	129.3	-7.7	0.062	2.952	14.1

GUEST INCLUSION

The guest is partially included in the primary end of the cyclodextrin cavity. The primary methoxy groups extend the volume of the cavity allowing for the inclusion of DCB. Lichtenthaler *et al.* [12,13] have shown that the primary end of methylated cyclodextrins is relatively hydrophilic compared to the secondary end of the cavity. This could account for the inclusion of the relatively polar ester moiety rather than the non-polar aromatic portion of the molecule at the primary side. The aromatic ring and chloro-substituents extend beyond the cyclodextrin cavity. The C1 atom of the aromatic ring is located 2.33(1) Å above the least-square plane through the seven O6 atoms of the cyclodextrin. The portion of the guest outside of the cavity is nestled in interstitial spaces between adjacent DIMEB molecules.

There are very few conformational differences between the DIMEB-included DCB and uncomplexed DCB (refcode: ROFSAH)[4,14] molecules. The O1-C7-C1-C6 and the O2-C7-C1-C2 torsion angles are -37.3(4)° and -40.6(4)° respectively in the uncomplexed structure (numbering in Figure 3.10) while they are -40.0(6)° and -43.1(5)° in the DIMEB inclusion complex. As can be seen from this comparison the conformational differences between these solid state structures of DCB are minimal.

HYDROGEN BONDING INTERACTIONS

There are seven well-known intramolecular hydrogen bonding interactions involved in linking adjacent glucopyranose subunits in the DIMEB molecule. These interactions are the O3(n+1)-H···O2n bonds listed below in Table 3.6

Table 3.6: O3(n+1)–H···O2n Hydrogen bonding parameters

D–H···A	D···A (Å)	Angle (°)
O3G1–H···O2G7	2.785(3)	179
O3G2–H···O2G1	2.986(4)	171
O3G3–H···O2G2	2.836(4)	176
O3G4–H···O2G3	2.864(4)	157
O3G5–H···O2G4	2.893(3)	168
O3G6–H···O2G5	2.806(3)	176
O3G7–H···O2G6	2.966(3)	175

The intramolecular interactions listed above are essential in stabilising the circular nature of the cyclodextrin. There are also several systematic weak C-H···O interactions that are involved with maintaining the same circular structure. The primary rim of the cavity maintains its shape through three C-H···O interactions between C6Gn donors and O5G(n-1) acceptors listed in Table 3.7 below.

Table 3.7: C-H···O interactions stabilising the primary rim of DIMEB

D–H···A	D···A (Å)	Angle (°)
C6G2-H···O5G1	3.213(4)	129
C6G5-H···O5G4	3.285(4)	130
C6G7-H···O5G6	3.204(4)	121

Only one hydrogen bond is formed between the host and guest molecules. The Cl1 atom acts as a hydrogen bond acceptor[15] to the C6G6-H weak hydrogen bond donor. Other than this weak hydrogen bond the inclusion of the guest relies on hydrophobic interactions and van der Waals forces.

CRYSTAL PACKING

The complexes stack in columns arising from a 2_1-axis parallel to the *a*-axis. The O4 least-squares planes of successive DIMEB molecules in each column are inclined at 52.1 °. A combination of these factors gives rise to cage type complex columns. The G2 primary methoxy group of each CD molecule is included in the secondary side of the cavity of the 2_1-related molecule, as can be seen in Figure 3.11. There is no interaction between the 'self-included' primary methoxy group and the DCB guest molecule of the adjacent complex. The 'self-inclusion' of the cyclodextrin closes off the secondary end of the cavity preventing access for guest inclusion from this direction. This arrangement results in a close packed column of host and guest molecules. In this packing arrangement the guest is only partially included via the primary end of the cyclodextrin cavity. This results in the aromatic portion of the molecule being encapsulated in the interstitial spaces as shown in Figure 3.12. The anti-parallel arrangement of columns arising from the twofold screw axes parallel to the *b*- and *c*-axes can be seen in Figure 3.13. The columns interact via weak van der Waals forces.

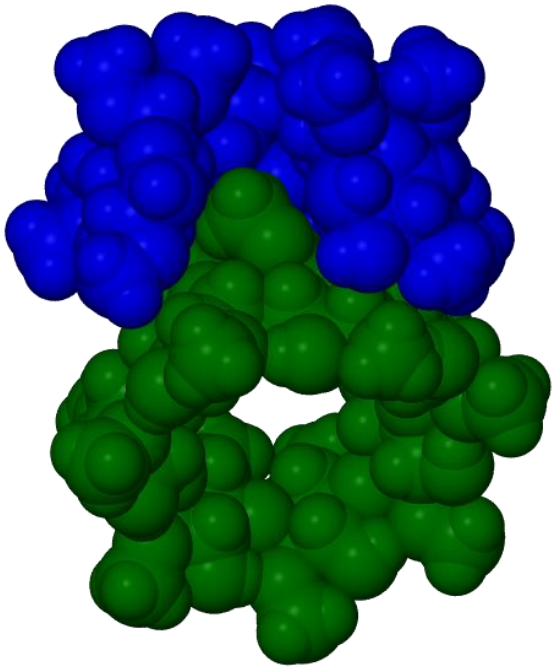

Figure 3.11: Cut-away figure showing the self-inclusion of DIMEB molecules in DMBDCB. The guest molecules have been omitted for clarity.

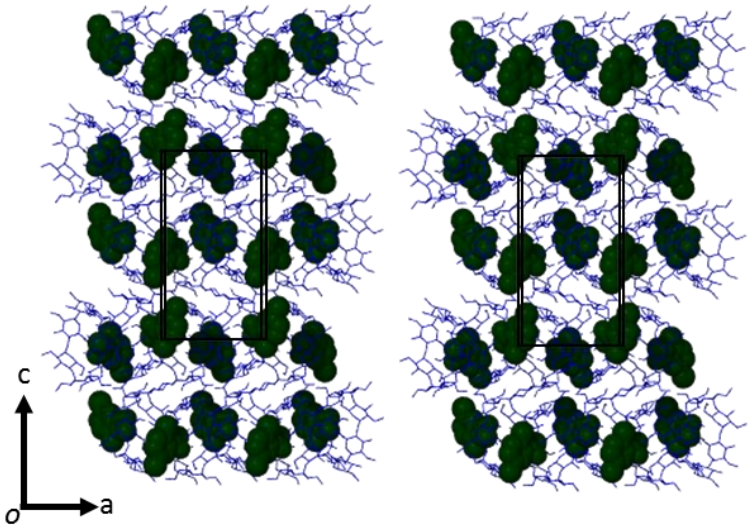

Figure 3.12: Stereo diagram illustrating the arrangement of the aromatic moiety of DCB in the interstitial spaces between DIMEB molecules

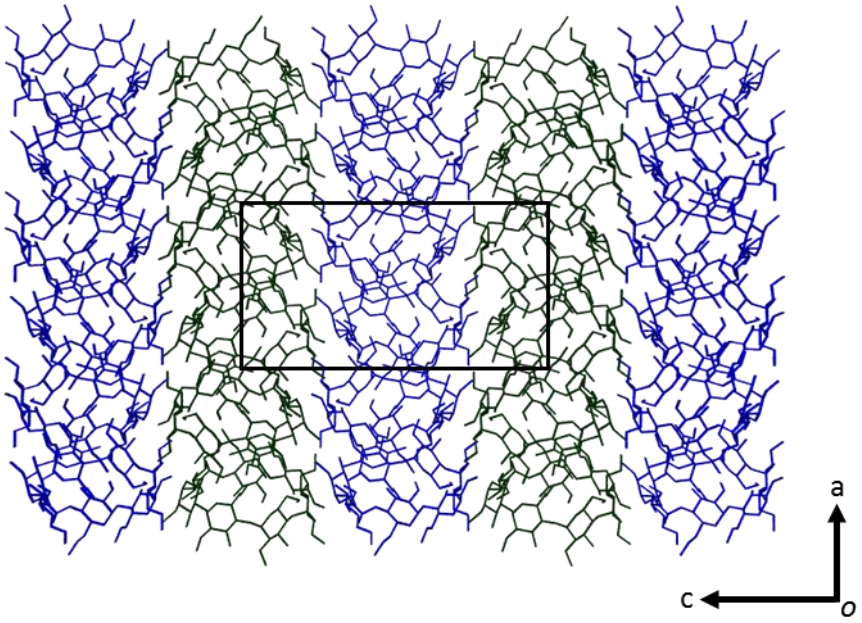

Figure 3.13: Packing of host molecules in DMBDCB viewed along [0 1 0] highlighting the anti-parallel column arrangement. The guest molecules have been omitted for clarity

COMPARATIVE PXRD

The calculated PXRD pattern (based on the refined X-ray crystal structure of the complex) shows good agreement with the experimental pattern of the bulk samples of DMBDCB. The slight differences in the 2θ positions of the peaks result from the low temperature collection of the single crystal intensity data, while the powder diffraction data were collected at room temperature. Upon cooling there is an angular shift in the peak positions most likely due to anisotropic contraction and/or expansion of the unit cell.

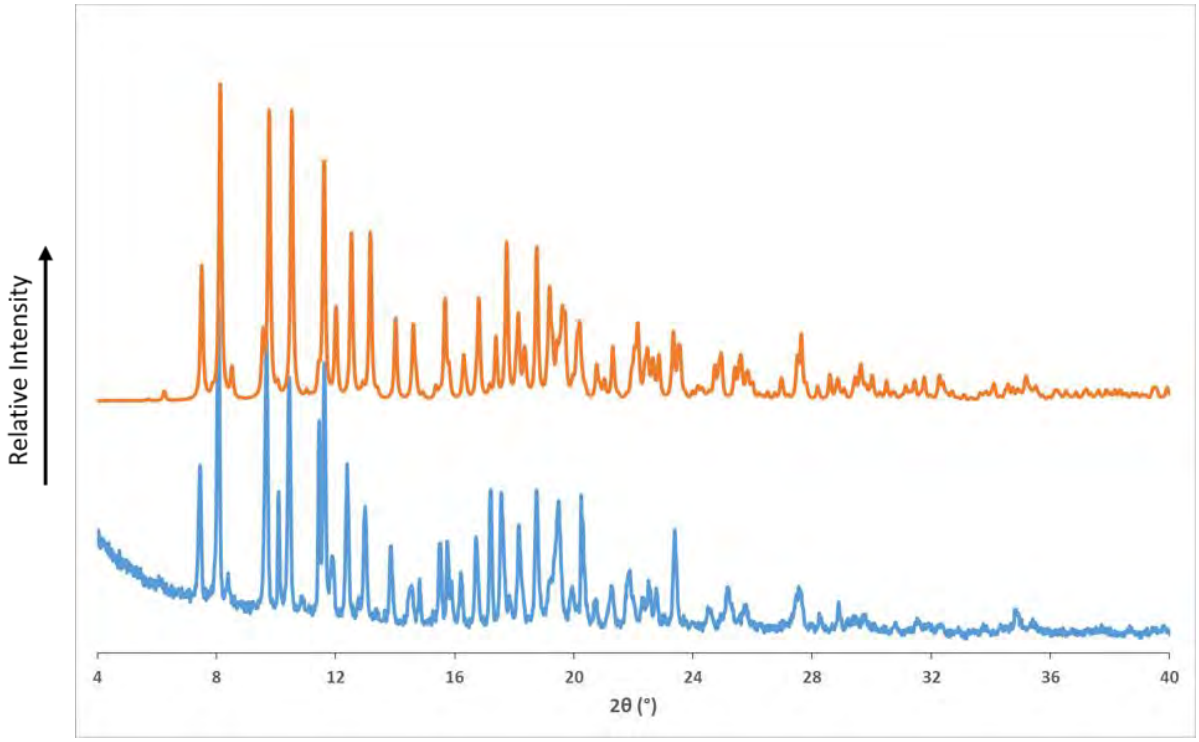

Figure 3.14: The PXRD trace recorded for bulk sample (blue) and the computed PXRD pattern based on the single crystal X-ray structure of DMBDCB (orange)

As described in the section pertaining to structure solution and refinement, the complex chosen for isomorphous replacement was DIMEB·2,4-dichlorophenoxyacetic acid (refcode: PABNEM).[4,7] The differences between the unit cell parameters of this complex and those of the complex DMBDCB are small (Δa = 0.3861 Å, Δb = 0.4916 Å and Δc = 0.2399 Å) as described above. As can be seen in Figure 3.15, the DIMEB backbones of the two complexes have very similar atomic co-ordinates. The packing arrangements of the two complexes are very similar, as shown in Figure 3.16.

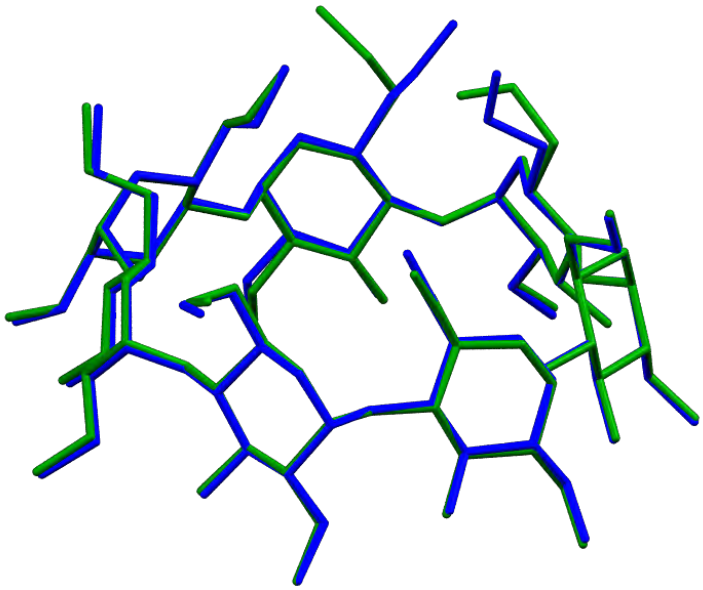

Figure 3.15: Overlay of PABNEM (green) and DMBDCB (blue) host molecules

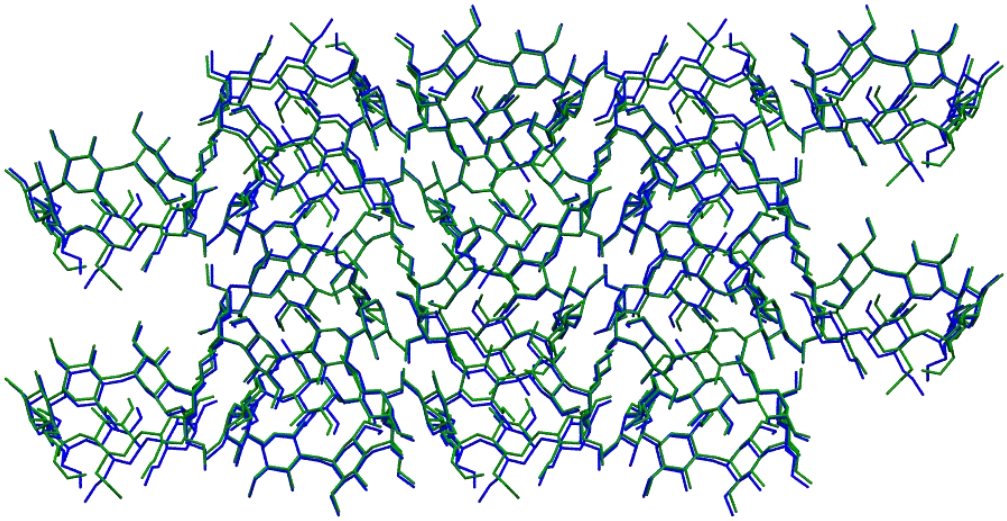

Figure 3.16: Overlay of packed PABNEM (green) host and DMBDCB (blue) host molecules viewed along the [1 0 0] direction

PHASE SOLUBILITY ANALYSIS

Phase solubility analysis is a technique used for determining the effect of a host molecule on the solubility of a guest. The method employed is described below.

SAMPLE PREPARATION

The cyclodextrin phase solubility of DCB was investigated with five cyclodextrins, namely α-CD, β-CD, γ-CD, hydroxypropyl β-cyclodextrin (HPBCD) and randomly methylated β-cyclodextrin (RAMEB).

To perform these experiments aqueous stock solutions of the five cyclodextrins were prepared. These were then diluted to the desired concentrations using Milli-Q water and transferred to polytop vials. All solutions used in the experiments had a volume of 5 cm^3. An excess of DCB was added to each vial and these mixtures were stirred for 72 hours at 750 rpm at a constant temperature of 30 ± 0.5 °C. Once the mixtures were equilibrated they were filtered through a 0.45 μm nylon filter. The intrinsic solubility (S_0) of DCB was determined in a similar manner; a saturated aqueous solution of DCB was prepared, stirred and filtered under the same conditions as the cyclodextrin solutions. The absorbances of the filtered solutions were read using UV-Vis spectroscopy. These solutions were diluted as needed to obtain an absorbance between 0.1 and 1. The concentration of DCB calculated using the molar absorptivity value was obtained from the Beer-Lambert plot.

UV-VISIBLE SPECTROPHOTOMETRY

Figure 3.17 shows the calibration curve used to calculate the molar absorptivity of DCB from the Beer-Lambert law (Expression 3.1).

Expression 3.1

$$A = \varepsilon c l$$

The path length, l, was 1 cm; therefore, the expression shows that if the calibration plot is linear the molar absorptivity, ϵ, is equal to the slope of the plot of A versus the concentration c. From the slope the molar absorptivity was determined to be 1150.1 M^{-1} cm^{-1}.

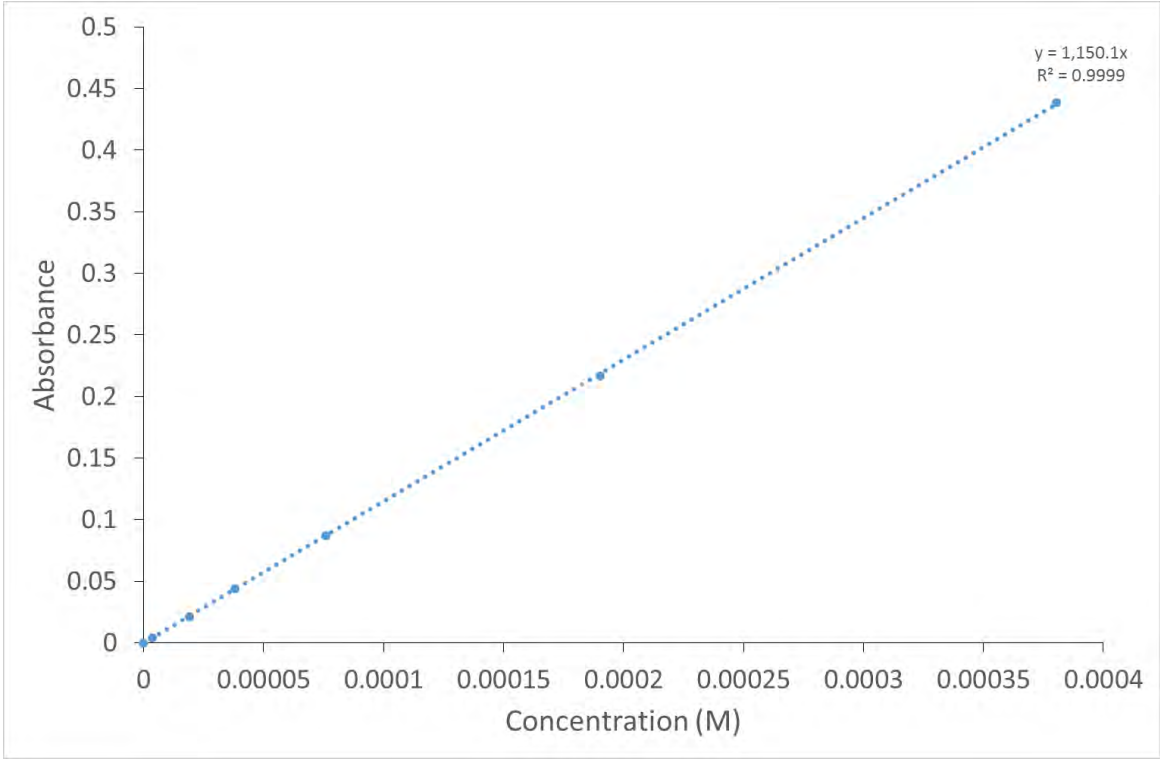

Figure 3.17: Beer-Lambert calibration curve for DCB in water at 30 °C for λ_{max} = 290.56 nm

PHASE SOLUBILITY

The phase solubility results are presented as a function of the apparent solubility of DCB with increasing cyclodextrin concentration. The profiles are classified as either A- or B-type by Higuchi and Connors.[16–18] A-type profiles show linear increases in guest solubility with increasing cyclodextrin concentration. There are three sub-categories of A-type profiles, namely A_L, A_P and A_N. A_L-type curves are characterised by linear increases in apparent guest concentration with increasing host concentration while A_P- and A_N-type show deviations from linearity at higher cyclodextrin concentrations. A_P-type plots show positive deviation while A_N-type plots deviate negatively. Both of these deviations are due to changes in the physical nature of the solution. B-type behaviour is the result of the formation of partially soluble complexes. There are two subtypes, B_S- and B_L-type, where B_S-type behaviour is due to the formation of a moderately soluble complex where the total apparent concentration of the guest increases up to a point where the complex precipitates out of solution. In the case of the B_L-type profiles the complex formed is highly insoluble and immediately precipitates, and therefore these profiles do not give rise to an initial increase in apparent guest concentration as in the B_S-type profile.[16–18]

The results of the phase solubility experiments with α-CD and γ-CD are excluded from the report due to their unreliability. They were erratic due to the precipitation of the complexes within 24 hours. Experiments involving the host compound RAMEB gave equally erratic results which are

therefore not presented here. The results obtained when β-CD and HPBCD were employed are presented below as the absorbance readings were all reliable and above 0.01 units.

β-CYCLODEXTRIN

Shown below in Figure 3.18 is a representative phase solubility plot showing the solubility variation for DCB with increasing concentration of β-CD. It is clear from the profile that the system follows B-type behaviour, namely B_S. This is indicated by the initial linear increase in apparent solubility of DCB, followed by a plateau and a decrease in concentration. This is most likely due to the β-CD/DCB complex having low solubility and precipitating at higher concentrations of β-CD.[17]

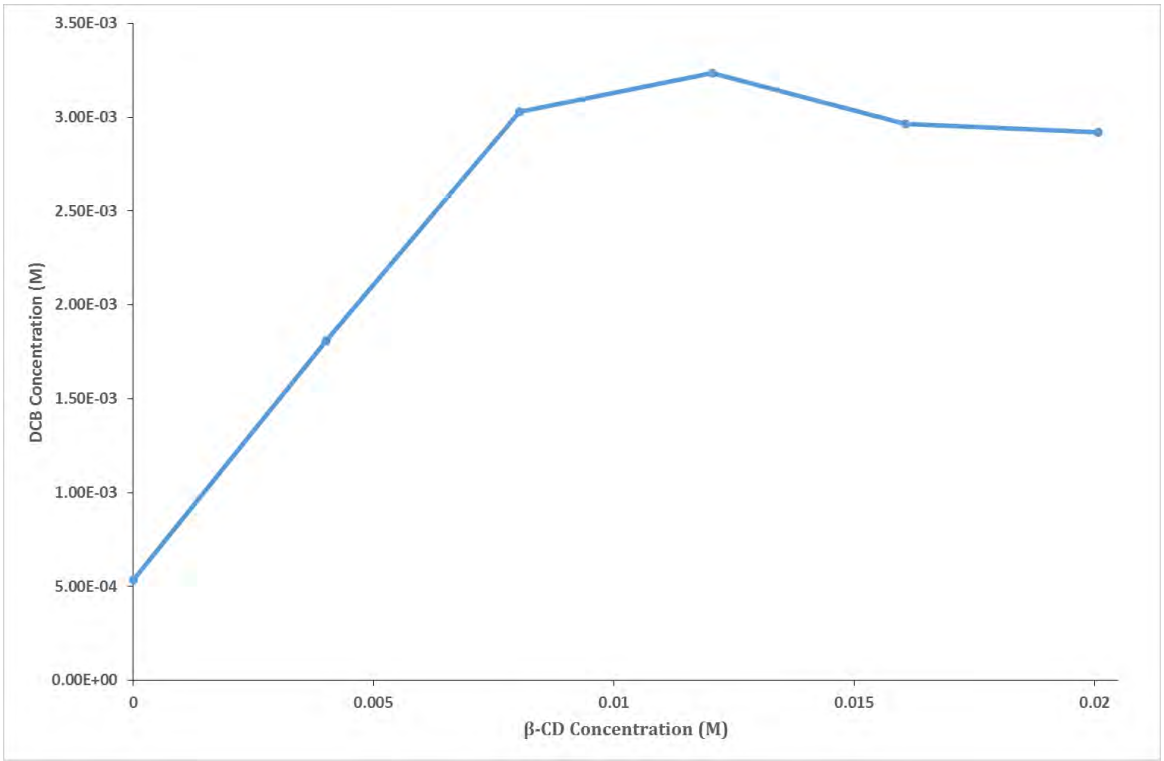

Figure 3.18: Representative phase solubility plot for β-CD with DCB

As the profile is of the type B_S it is possible to calculate the binding constant from Expression 3.2 using the initial slope and intrinsic solubility (S_0) measured experimentally.

Expression 3.2

$$K_{1:1} = \frac{slope}{S_0(1 - slope)}$$

The binding constant was calculated for each repeat of the experiment and the average binding constant was found to be 737 ± 108 M^{-1}. This is a relatively low value indicating that the complex is not very stable in solution. For the guest DCB, the greatest solubility enhancement was found

at a β-CD concentration of 12.0 mM where the apparent solubility of DCB was increased by a factor of 6.4.

HPBCD

The phase solubility profile of DCB with HPBCD (Figure 3.19) indicates that the system follows a B_S profile. This is unexpected for HPBCD as this cyclodextrin usually shows A-type solubility behaviour with guest molecules. As in the case with β-CD, this would imply that an insoluble complex is formed with DCB and precipitates at higher cyclodextrin concentrations.

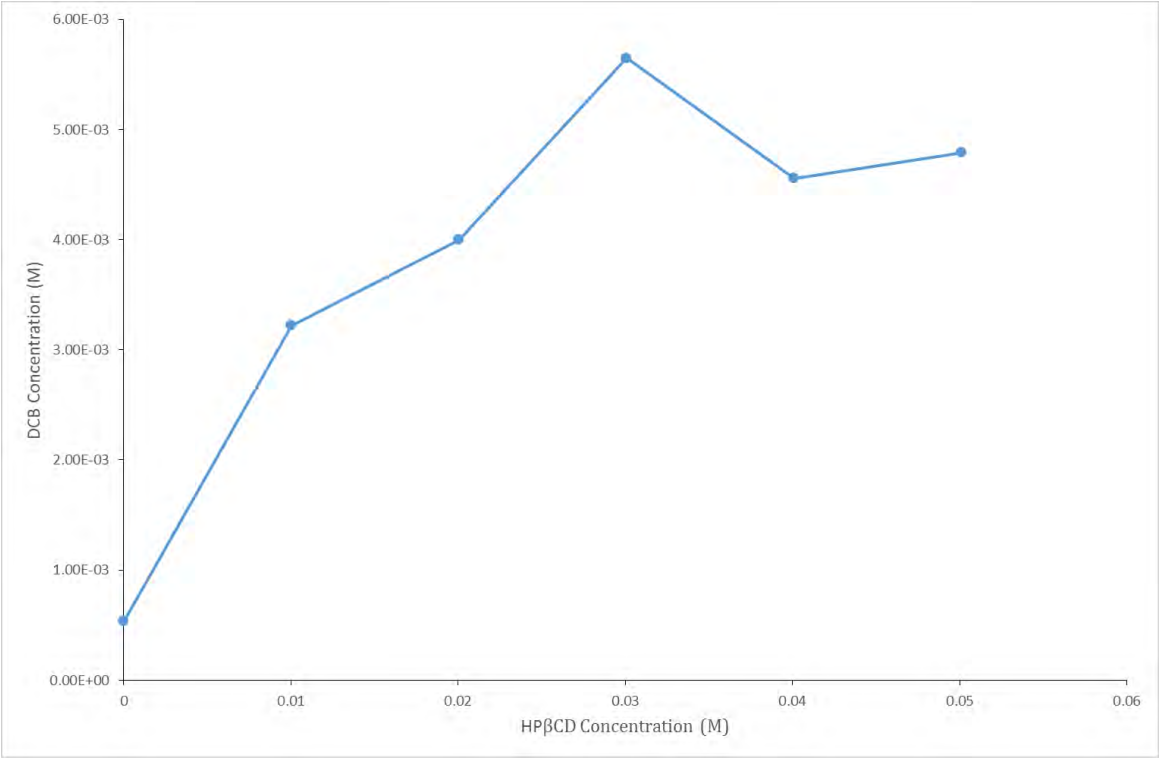

Figure 3.19: Representative phase solubility plot for HPBCD with DCB

The binding constant was calculated in a similar manner to that obtained using β-CD as host as both systems are of type B_S. The average binding constant was found to be very small at 412 ± 53 M^{-1}. HPBCD usually forms complexes with larger binding constants of several thousand M^{-1}. The solubility enhancement was also lower than expected for HPBCD. The increase in apparent solubility was 10.6-fold to 5.65×10^{-3} M using HPBCD at a concentration of 30.1 mM.

DISCUSSION

STOICHIOMETRY AND THERMAL ANALYSIS

The stoichiometry of the GCDDCB and DMBDCB complexes presented in this chapter were determined via ^{1}H-NMR spectroscopy and TGA respectively. The DMBDCB complex was found to have a 1:1 host-guest ratio, while for the GCDDCB complex the ratio is 3:4.

Of the two complexes only GCDDCB contains water in the crystal structure. This is evident from the TGA trace, showing an initial mass loss of 13.0 ± 0.1 % (n = 2) from room temperature to 100 °C; this corresponds to 9.8 ± 0.1 water molecules per cyclodextrin subunit. This is corroborated by the DSC trace showing a broad endotherm indicative of solvent loss. The changing slope of the mass loss indicates that the process is occurring in multiple steps. DMBDCB does not have any waters of crystallisation as evidenced by no mass loss in the TGA trace until 142.0 ± 1.3 °C. The DSC trace and the HSM images are consistent with the data obtained from the TGA experiment.

The enhancement of the thermal stability of DCB due to inclusion is significant. Pure DCB melts at 39.9 °C and begins to decompose at 49.9 °C. The DMBDCB complex only shows a mass loss due to the guest release beginning at 142.0 ± 1.3 °C and the resulting material (DIMEB) only begins to decompose at 357.1 ± 1.3 °C. The GCDDCB complex shows a mass loss attributed to loss of DCB beginning at 168.0 ± 0.9 °C, which continues until decomposition of the residual cyclodextrin beginning at 281.9 ± 1.4 °C. These results show that cyclodextrin complexation of DCB greatly improves its thermal stability.

CONFORMATIONS OF HOST AND GUEST MOLECULES

At the time of writing there are 10 isostructural γ-cyclodextrin inclusion complexes crystallising in the tetragonal space group $P42_12$ in the CSD.[4] The complexes have the unusual Z' value of ¾ owing to the presence of six symmetry-independent glucose residues. In principle, only included guest molecules having internal four-fold rotational symmetry can generally be unambiguously located using X-ray diffraction. The mean unit cell parameters of the 10 isostructural complexes used when confirming the presence of an inclusion complex between γ-CD and DCB are as follows: $a = b = 23.7 \pm 0.1$ Å, $c = 23.1 \pm 0.3$ Å, $\alpha = \beta = \gamma = 90°$. The host molecules in these complexes maintain a round shape stabilised by the well-known O3(n+1)–H···O2n hydrogen bonding network. The weaker C6n-H···O5(n+1) interactions are also systematically present in these structures further stabilising the round shape of the γ-cyclodextrin molecule.[19]

The geometric parameters, specifically *l, D* and ϕ, of the DMBDCB complex indicate that the DIMEB molecule maintains a 'round' shape by virtue of the intramolecular O3(n+1)–H···O2n hydrogen bonds. The variation in the parameters are minimal showing that the molecule maintains its regular heptagonal arrangement. The tilt angles, τ_2, indicate that all of the monomeric subunits tilt inwards at the primary side showing that the truncated toroidal shape is maintained during inclusion of the DCB molecule.

The DCB molecule shows very little conformational difference between the uncomplexed solid form and the complexed form. The torsion angles O1-C7-C1-C6 and O2-C7-C1-C2 are very similar with differences of approximately 3° between the two structures. The chlorine atom, Cl1, is located in such a way as to minimise the steric interactions between the host and guest.

CRYSTAL PACKING

The γ-cyclodextrin inclusion complex with DCB packs in one of the less common space groups, $P42_12$. Of the 800,309 crystal structures in the CSD[4] (at the time of writing) only 58 crystallise in $P42_12$, and of those, 10 are γ-cyclodextrin inclusion complexes. The three independent cyclodextrin molecules are centred on the crystallographic four-fold rotation axis. The γ-cyclodextrins stack in columns parallel to the *c*-axis. Channels arise from the stacked cyclodextrin cavities and the interstitial spaces with diameters of approximately 8 Å and 7 Å respectively. These large spaces allow for the free movement of solvent molecules within the crystal structure. This may be the reason the TGA trace indicates a multi-step solvent loss process. The repeating A-B-C unit is shown in Figure 3.20 and comprises three cyclodextrin molecules. The columns are built from translations of these units. The interactions are head-to-tail, head-to-head and tail-to-tail for the A-C, B-C and A-B units respectively. This arrangement is maintained via a hydrogen bonding network where the secondary hydroxyls of A and B hydrogen bond with each other. The primary hydroxyls of B and C interact while the primary hydroxyls of A hydrogen bond to the secondary hydroxyls of C.[19,20]

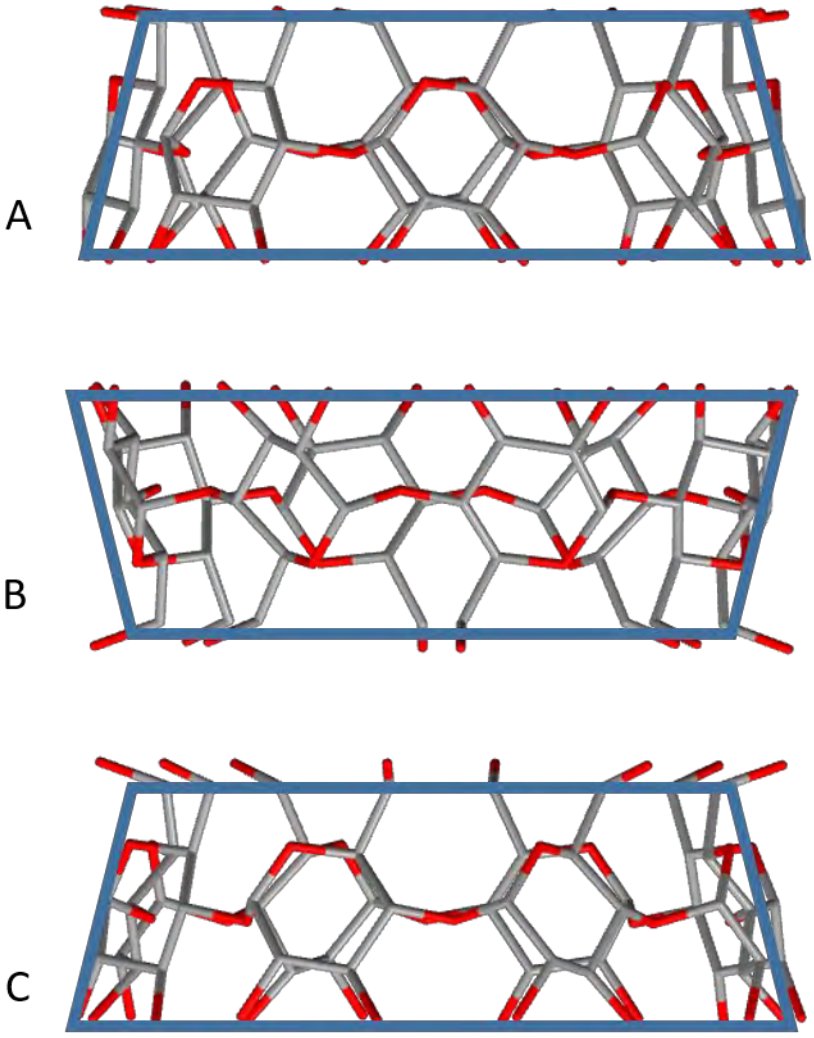

Figure 3.20: Host molecules of the γ-CD/methanol (refcode: NUNRIX)[4,19] inclusion complex repeating unit which form infinite columns. Hydrogen atoms have been omitted for clarity

DMBDCB packs in cage type columns arising from the twofold screw axis parallel with the *a*-axis. The O4 mean planes of sequential DIMEB molecules form an angle of 52.1°. The G2 primary methoxy substituent is included in the adjacent DIMEB molecule causing the cavity to be closed from the secondary side. The columns are crystallographically related by the 2_1-axes parallel to the *b* and *c* cell axes, resulting in close packed columns. The columns interact via van der Waals interactions. Due to the closed off nature of the cavity the DCB molecule is located with the majority of the molecule in the interstitial spaces. The ester moiety is included in the extended primary end of the DIMEB molecule, while the aromatic portion of DCB protrudes into the interstitial spaces.

A total of 22 DIMEB inclusion complexes were found in the CSD crystallising in seven space groups. Of these structures 11 are isostructural with the DMBDCB complex and of these, six of these include the guest molecule *via* the primary end of the host. A further eight complexes crystallise in the same space group ($P2_12_12_1$); however, these are not isostructural with the DMBDCB inclusion complex.

PHASE SOLUBILITY

Phase solubility experiments with DCB were performed with α-CD, β-CD, γ-CD, HPBCD and RAMEB. It was found that the α-CD and γ-CD complexes were very insoluble in water as they precipitated at low cyclodextrin concentrations in a short period of time. RAMEB enhanced the solubility of DCB, but the results were erratic and unreliable. This may be due to aggregation of the complexes in solution, or other complications inherent to the system.

β-CD and HPBCD phase solubility data with DCB exhibited B_S profiles. This profile is characterised by an initial linear increase in apparent guest concentration followed by a plateau and finally a decrease in apparent solubility. This arises due to the formation of a partially soluble complex that increases the apparent concentration of the guest. The maximum concentration of the complex is reached with addition of further cyclodextrin and the complex precipitates. While any uncomplexed guest remains, the system is in equilibrium; however, once the guest is consumed the addition of any further cyclodextrin causes precipitation, decreasing the apparent concentration of the guest.[17]

The B_S-type behaviour exhibited by DCB with β-CD and HPBCD detailed above allowed for the binding constant calculations indicating values of 737 ± 108 M^{-1} and 412 ± 53 M^{-1} respectively. These binding constants are lower than expected signifying that the complexes are not particularly stable in solution. The enhancement in solubility was similarly lower than expected with enhancement factors of 6.4 and 10.6 at 12.0 mM and 30.1 mM for β-CD and HPBCD respectively.

CONCLUSION

The data presented here show that DCB can form an inclusion complex with both native and derivatised cyclodextrins, imparting beneficial physicochemical changes to the compound. In the solid state the thermal stability of DCB was markedly improved by inclusion in γ-cyclodextrin and DIMEB.

In solution the solubility of DCB was increased using both β-cyclodextrin and HPβCD by factors of 6.4 and 10.6 respectively. However, these cyclodextrins both exhibit B_S-type behaviour with DCB indicating that the solubility enhancement is only valid until the solution is saturated with the partially soluble complexes.

The inability to assess the solubility enhancement with γ-CD was due to complex precipitation (as reported above). With DIMEB as the host, on the other hand, paucity of this material due to its high cost precluded phase solubility analysis, which was the reason for choosing RAMEB as an alternative.

Due to the high cost of many chemically modified cyclodextrins this study has been limited to a few selected host compounds. Future exploration of the vast library of such commercially available hosts may yield alternative stable, water soluble solid complexes with DCB.

REFERENCES

1 K. A. Lewis, J. Tzilivakis, D. J. Warner and A. Green, *Hum. Ecol. Risk Assess.*, 2016, **22**, 1050-1064.

2 *Conclusion on the peer review of 2,5-dichlorobenzoic acid methy lester*, 180, EFSA European Food Safety Authority, EFSA Scientific Report, Parma, Italy, 2008.

3 S. Kamitori, K. Hirotsu and T. Higuchi, *J. Chem. Soc., Chem. Commun.*, 1986, 690–691.

4 Cambridge Structural Database and Cambridge Structural Database system, Version 5.37, Cambridge Crystallographic Data Centre, University Chemical Laboratory, Cambridge England, November 2015.

5 Program SAINT, Version 7.60a, Bruker AXS Inc., Madison, WI, USA, **2006**.

6 M. R. Caira, *Rev. Roum. Chim.*, 2001, **46**, 371–386.

7 F. Tsorteki, K. Bethanis and D. Mentzafos, *Carbohydr. Res.*, 2004, **339**, 233–240.

8 T. Aree, H. Hoier, B. Schulz, G. Reck and W. Saenger, *Angew. Chem. Int. Ed. (English)*, 2000, **39**, 897–899.

9 J. J. Stezowski, W. Parker, S. Hilgenkamp and M. Gdaniec, *J. Am. Chem. Soc.*, 2001, **123**, 3919–3926.

10 T. Aree, W. Saenger, P. Leibnitz and H. Hoier, *Carbohydr. Res.*, 1999, **315**, 199–205.

11 L. M. Joseph, Master's Dissertation, University of Cape Town, 2015.

12 F. W. Lichtenthaler and S. Immel, *Starch - Starke*, 1996, **48**, 145–154.

13 S. Immel and F. W. Lichtenthaler, *Starch - Starke*, 1996, **48**, 225–232.

14 T. M. Babar, G. Qadeer, N. H. Rama, A. Ruzicka and Z. Padelkova, *Acta Cryst.*, 2008, E**64**, o1970.

15 L. Brammer, E. A. Bruton and P. Sherwood, *Cryst. Growth Des.*, 2001, **1**, 277–290.

16 T. K. Higuchi and K. A. Connors, *Adv. Chem. Instrum.*, 1965, **4**, 212–217.

17 M. E. Brewster and T. Loftsson, *Adv. Drug Deliv. Rev.*, 2007, **59**, 645–66.

18 T. Loftsson and M. E. Brewster, *J. Pharm. Pharmacol.*, 2010, **62**, 1607–1621.

19 T. Steiner and W. Saenger, *Acta Cryst.*, 1998, B**54**, 450–455.

20 J. Ding, T. Steiner and W. Saenger, *Acta Cryst.*, 1991, B**47**, 731–738.

CHAPTER 4 – FENTHION

Fenthion is an organothiophosphate insecticide, avicide and acaricide. The mode of action is cholinesterase inhibition. Fenthion has a low aqueous solubility of 54-56 mg dm^{-3}.[1] Owing to the low melting point of 7 °C[1] fenthion is an oil at room temperature and no crystal structure has been reported thus far.

This chapter pertains to the inclusion of fenthion in cyclodextrin host molecules. There are two parts to this chapter. Part one focuses on complexation in solution studies performed at the Universidad Nacional de Córdoba as part of a bilateral exchange program. The second part pertains to three solid-state inclusion complexes.

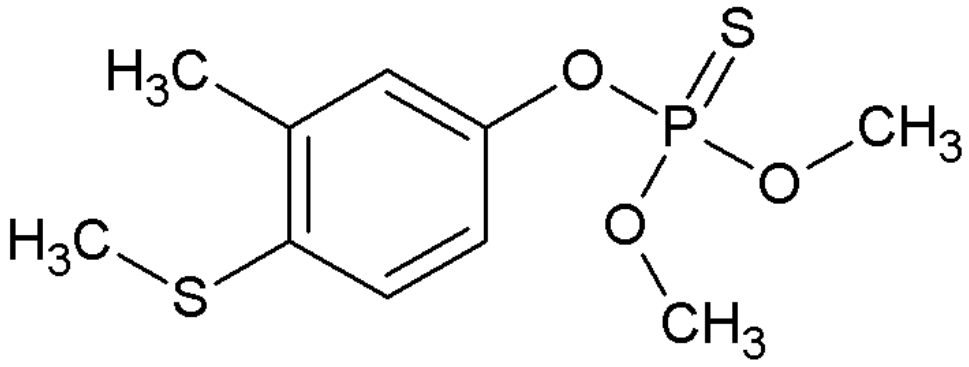

PART 1 – COMPLEXATION IN SOLUTION

The interactions between cyclodextrins and guest molecules can differ in solution and the solid-state. It is therefore highly beneficial to investigate the interactions in both states. The main method of investigation applied to fenthion cyclodextrin inclusion in solution is that of induced circular dichroism. The cyclodextrins investigated in this study are α-cyclodextrin (α-CD), β-cyclodextrin (β-CD), γ-cyclodextrin (γ-CD), hexakis (2,3,6-tri-*O*-methyl)-α-cyclodextrin (TRIMEA), heptakis (2,6-di-*O*-methyl)-β-cyclodextrin (DIMEB) and heptakis (2,3,6-tri-*O*-methyl)-β-cyclodextrin (TRIMEB).

INDUCED CIRCULAR DICHROISM

Induced circular dichroism (ICD) was used to investigate the inclusion of fenthion in solution. The application of this technique relies on the ability of fenthion to absorb ultraviolet (UV) electromagnetic radiation, while cyclodextrin molecules do not absorb in the UV region of the electromagnetic spectrum. Furthermore, fenthion is achiral, so will not rotate plane polarised light. Cyclodextrin molecules, being chiral, will rotate plane polarised light. If a chromophore is included in the cyclodextrin cavity it will induce chirality on the system, rotating plane polarised light in the UV region of the electromagnetic spectrum.

Observations of the change in signal will indicate whether a complex is formed in solution and can provide information pertaining to the relative orientation of the two molecules.

SAMPLE PREPARATION

Owing to the low aqueous solubility of fenthion a co-solvent was required. The solvent 1,4-dioxane was selected for this purpose and 2% solutions with water were found to be sufficient for the requirements of the study.

A stock solution of fenthion was made in 1,4-dioxane. This was mixed with cyclodextrin stock solutions. These mixtures were diluted with Milli-Q water to obtain samples of varying cyclodextrin concentration, but constant fenthion concentration (2.278×10^{-5} mol dm^{-3}) and 2% 1,4-dioxane.

β-CYCLODEXTRIN

The low solubility of fenthion required the use of a 4 cm cuvette to obtain absorbance readings of an appropriate intensity.

From signal changes (Table 4.1) in the ICD spectra (Figure 4.1) it is clear that there is an interaction between the chromophore of fenthion and β-CD. The solid-state information (presented below) would indicate that the chromophoric moiety is embedded within the β-CD cavity as the whole molecule is encapsulated by two β-CD molecules. If the same mode of inclusion occurs in solution it would be reasonable to infer that the effect observed in the ICD spectra is a negative Cotton effect. This would indicate that the transition dipole of fenthion aligned perpendicularly to the axis of symmetry of the cyclodextrin cavity.

There is a strong correlation between the maxima in the UV-Vis spectra and the ICD signal. There are some further correlations in the region around 280 nm where we see a signal above the background noise in the ICD spectra and a shoulder in the UV-Vis spectra. The correlation between the two plots suggests that the chromophoric moiety of fenthion is in a chiral environment giving rise to the ICD signal. Previous work has shown that the use of cyclodextrins as host molecules can cause a slight displacement in the maxima of ICD spectra.[2]

Table 4.1: Induced circular dichroism signals for β-CD with fenthion in solution

[βCD] (mM)	λ_{ICD}	Signal
0	243	Positive
	258	Negative
0.5	244	Positive
	262	Negative
1	242	Positive
	260	Negative
1.5	245	Positive
	259	Negative
2	247	Positive
	260	Negative
3	246	Positive
	262	Negative
4	247	Positive
	259	Negative
5	246	Positive
	261	Negative
5.5	246	Positive
	262	Negative
6	246	Positive
	259	Negative

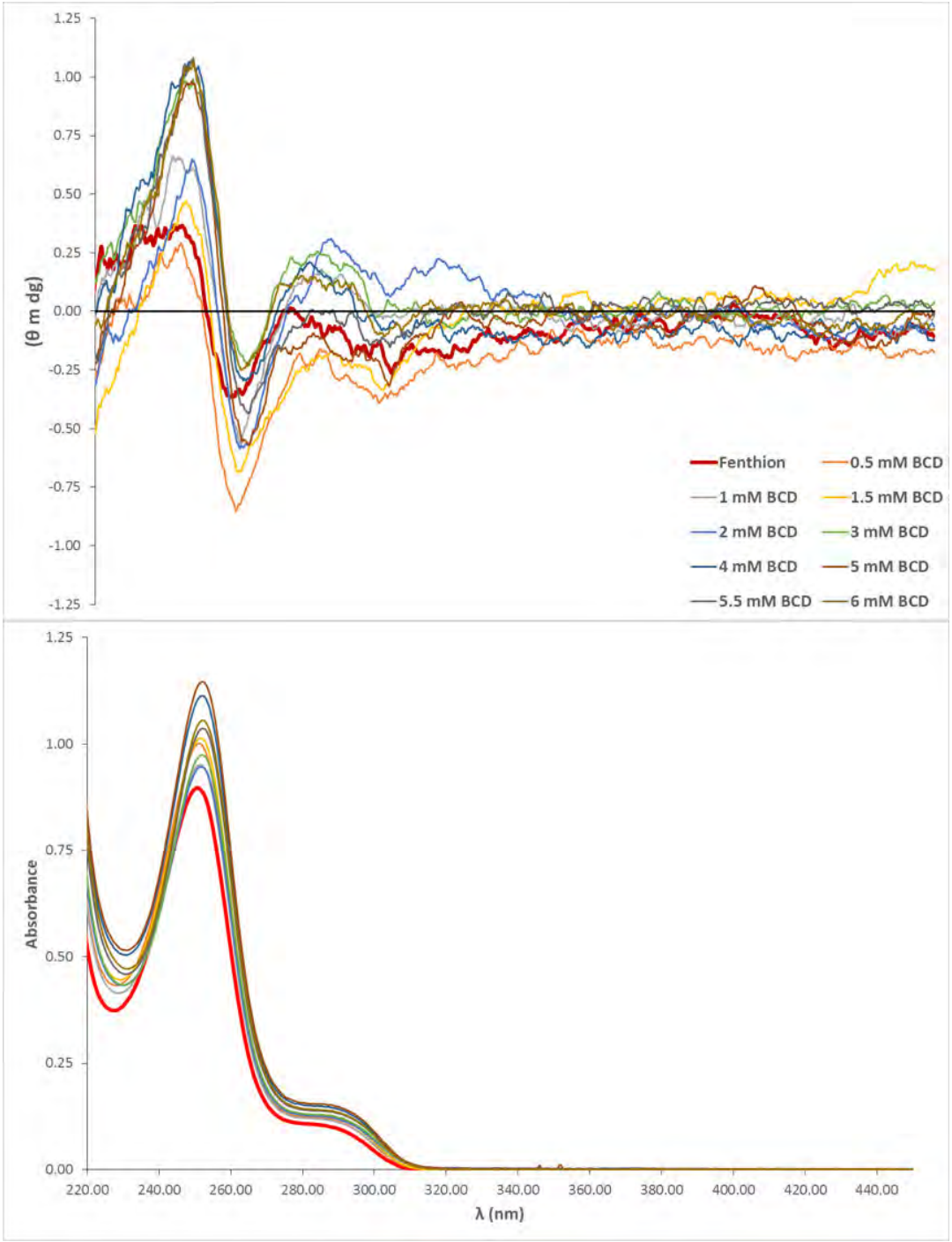

Figure 4.1: ICD (top) and UV-Vis spectra (bottom) of β-CD with fenthion in 2 % 1,4-dioxane solutions

The signal measured in the ICD spectrum is ellipticity. This is a measure of the degree to which linearly polarised light becomes elliptically polarised when passed through a circular dichroic sample. While observable changes, with β-CD concentration, are present in the absorbance and ellipticity signal they are erratic and follow no known profile. The changes indicate that there is an interaction between β-CD and fenthion in solution. As the profile for the changes in the observed signals could not be found it was not possible to calculate the binding constants for this

interaction. It is possible that there is more than one type of interaction between β-CD and fenthion occurring in solution, making calculations problematic. Without a well-defined mode of inclusion it is not possible to calculate the binding constants.

OTHER CYCLODEXTRINS

Further ICD experiments were performed with several cyclodextrins in order to observe the relative strengths of the respective interactions with the fenthion molecule. The cyclodextrins α-CD, β-CD, γ-CD, TRIMEB, DIMEB and TRIMEA were tested with fenthion. Experiments with the native cyclodextrins were performed at cyclodextrin concentrations of 10 mM. However, due to the limited supply of the derivatised cyclodextrins the experiments were carried out using concentrations of 5, 2.5 and 1 mM for TRIMEB, DIMEB and TRIMEA respectively.

The changes in the ICD signals are presented in Table 4.2. These changes are clearly visible in the ICD spectra in Figure 4.2, where a signal change can be seen when fenthion is combined with each of the cyclodextrins. From the similarities in the profile one can infer that the mode of interaction between fenthion and each of the cyclodextrins is similar. The solid-state data for these complexes, presented in forthcoming sections, show the inclusion of the chromophores in the cyclodextrin cavities. If the mode of inclusion is similar in solution then the observed changes in the ICD spectra are indicative of a negative Cotton effect. The negative Cotton effect observed in all the spectra indicates that the orientation of the transition dipole of fenthion is perpendicular to the axis of symmetry of the cyclodextrins.

Table 4.2: Induced circular dichroism signals for various cyclodextrins with fenthion in solution

Cyclodextrin	[Cyclodextrin] (mM)	λ_{ICD} (nm)	Signal
α-CD	10	242	Positive
		258	Negative
β-CD	10	247	Positive
		262	Negative
γ-CD	10	241	Positive
		262	Negative
TRIMEB	5	240	Positive
		259	Negative
DIMEB	2.5	246	Positive
		262	Negative
TRIMEA	1	245	Positive
		258	Negative

During the experiments the concentration of fenthion was kept constant. The changes in signal strength with changing cyclodextrin point to variations in the strength of interaction with each cyclodextrin. Normalising for concentration, the strengths of the interactions between fenthion and the various host molecules are in the order DIMEB > TRIMEA > TRIMEB > β-CD > γ-CD > α-CD.

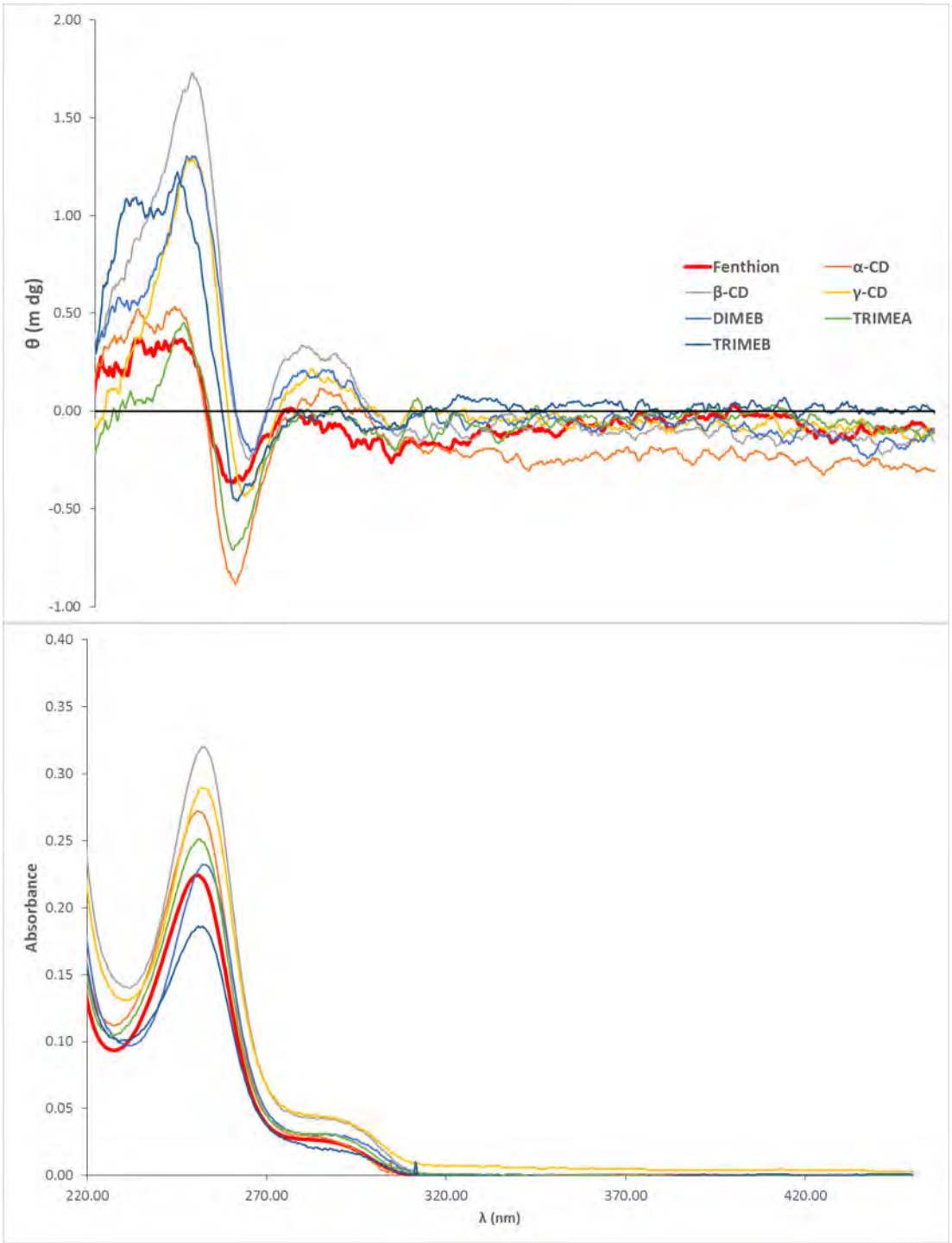

Figure 4.2: ICD (top) and UV-Vis spectra of various cyclodextrins with fenthion in 2 % 1, 4-dioxane solutions

The binding strength trend outlined above has also been observed with the fenthion analogue fenitrothion.[2–4] The profiles observed for α-CD, β-CD, γ-CD and DIMEB with fenitrothion and fenthion are similar, while those for TRIMEA and TRIMEB are inverted. In the solid-state the complexes TRIMEB/fenthion and TRIMEB/fenitrothion are isostructural.[5] However, the solid-state structures of TRIMEA/fenthion and TRIMEA/fenitrothion differ significantly. The TRIMEA/fenitrothion complex has a 2:1 host-guest stoichiometry[6] while the TRIMEA/fenthion complex has a 1:1 stoichiometric ratio (detailed below). The ICD spectra indicate that the complexes TRIMEA/fenthion and TRIMEA/fenitrothion differ in solution as well as in the solid-state. The TRIMEB/fenthion and TRIMEB/fenitrothion complexes, while similar in the solid-state, must have differing modes of inclusion in solution. The profiles of the signals further imply that that the modes of interaction of these guest molecules with α-CD, β-CD, γ-CD and DIMEB are similar for both fenthion and fenitrothion.

While it is possible to use ICD and UV-Vis spectroscopy to investigate association constants, to do so requires a well determined mode of inclusion. In the case of the β-CD complex the data did not fit any of the established models generally used in these calculations. For the remaining complexes the association constants were not investigated due to the limited supplies of the derivatised cyclodextrins. Therefore, ICD and UV-Vis spectroscopy were used as qualitative techniques to describe the presence of complexes in solution.

PART 2 – COMPLEXATION IN THE SOLID-STATE

Fenthion was included in three cyclodextrin host molecules in the solid-state. The cyclodextrins successfully forming inclusion complexes with fenthion were β-CD, TRIMEA and TRIMEB. The results of the experiments performed on the complexes obtained are presented in this section of the chapter.

β-CYCLODEXTRIN/FENTHION

The investigation of the inclusion complex of β-CD with fenthion was problematic. The production of the inclusion complex did not give rise to a crystal suitable for a high quality single crystal data collection. Therefore, the results presented pertaining to the structure of the inclusion complex provide only an overview of the structural features. An in depth analysis of the structural details and interactions would not be reliable due to the poor quality of the refined single crystal model.

The inclusion complex of fenthion in β-cyclodextrin will be referred to as BCDFEN.

COMPLEX PREPARATION

The BCDFEN complex was prepared *via* co-precipitation. One drop of the fenthion oil (23 mg, 0.0823 mmol) was added to an aqueous solution (4 cm^3) containing an equimolar quantity of β-cyclodextrin (93 mg, 0.0823 mmol). The mixture was stirred at an elevated temperature of approximately 50 °C for 6 hours and then filtered through a 0.45 μm nylon filter into a clean vial. The filtered product was allowed to cool slowly in a Dewar™ flask over several days and large, block-like crystals were observed.

CONFIRMATION OF STOICHIOMETRY

The stoichiometry of the complex was confirmed *via* NMR spectroscopy. Crystals from the co-precipitation preparation were dissolved in DMSO-d_6 for analysis by ^{1}H-NMR spectroscopy. The labelling schemes of the β-CD glucopyranose subunit and fenthion are presented in Figure 4.3. Integration of the C-H_1 proton signal of β-CD was used as the reference integral. The C-$H_{1a,b,c}$ and C-$H_{9a,b,c}$ methyl protons of fenthion were integrated and together these showed a β-CD to fenthion ratio of 2:1. The integration values and NMR spectrum are presented in Table 4.3 and Figure 4.4 respectively.

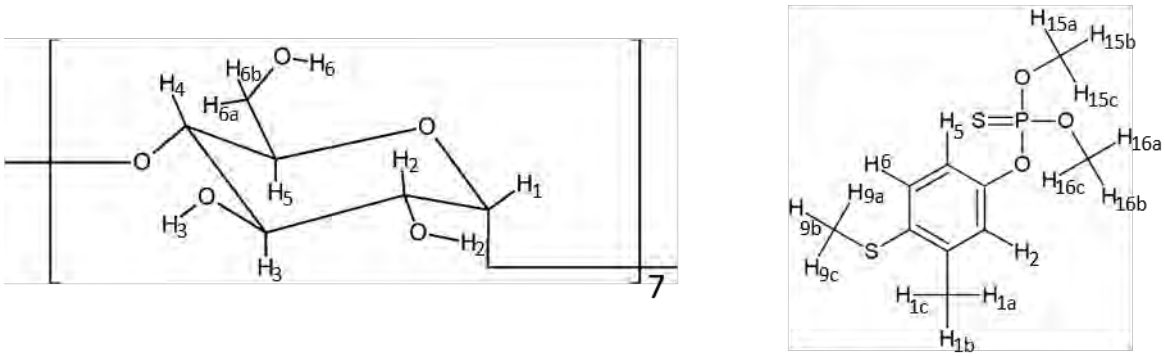

Figure 4.3: Proton labelling of β-CD glucopyranose subunits (left) and fenthion (right)

Table 4.3: Integrals and assignment of host and guest protons used for stoichiometric confirmation

Proton	**δ (ppm)**	**Integration**		**Experimental/ Theoretical**
		Experimental	Theoretical	
β-cyclodextrin				
C-H_1	4.87	14‡	14	1
O-H_6	4.46	13.11	14	0.94 ≈ 1
Fenthion				
C-$H_{1a,b,c}$	2.30	3.05	3	1.02 ≈ 1
C-$H_{9a,b,c}$	2.49	3.04	3	1.01 ≈ 1
C-$H_{15a,b,c}$ + C-$H_{16a,b,c}$	3.87, 3.82	5.62	6	0.94 ≈ 1
C-H_5 + C-H_6	7.06	2.04	2	1.02 ≈ 1

‡*Reference Integral*

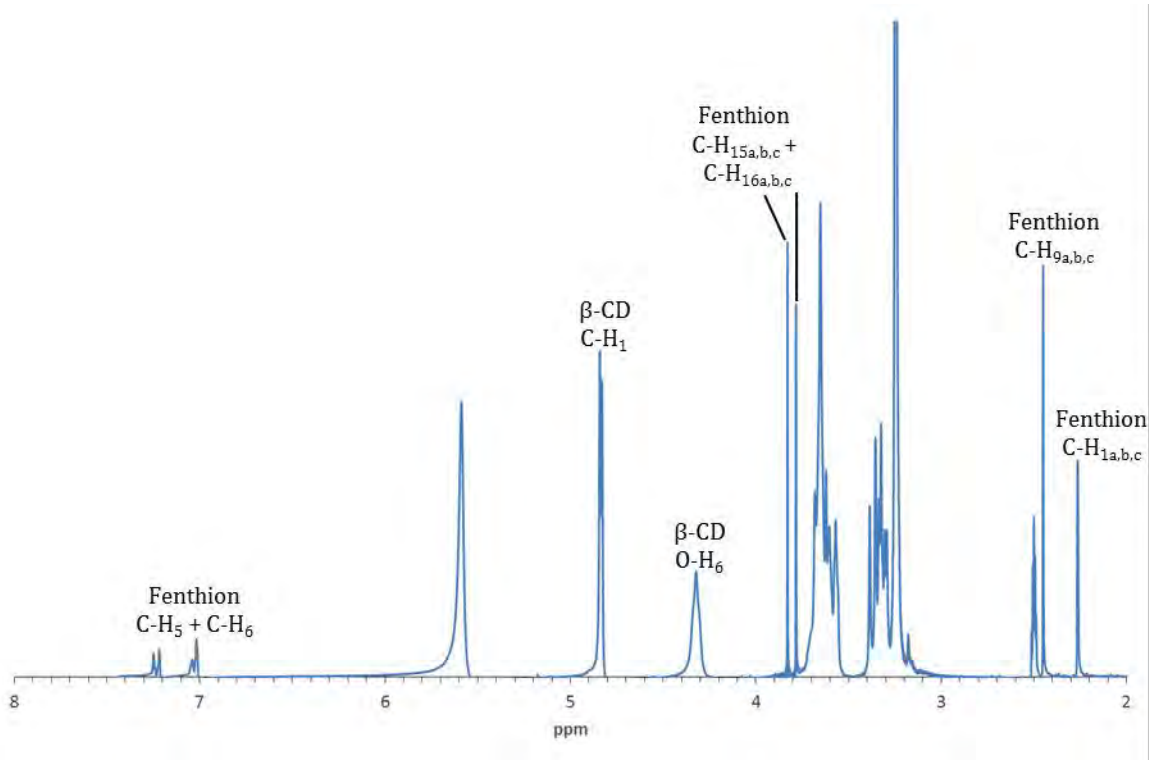

Figure 4.4: NMR spectrum of BCDFEN crystals in DMSO-d_6 to determine the stoichiometric ratio

THERMAL ANALYSIS

Thermal analysis comprising DSC, TGA and HSM were performed on single crystals of BCDFEN with a 2:1 stoichiometry. The TGA and DSC traces are shown in Figure 4.5. It was found that the complex had a water loss of 14.1 ± 0.7 % (n = 2) equating to approximately 24 water molecules per inclusion complex unit.

The TGA trace shows an immediate mass loss from room temperature to 90.0 ± 7.1 °C due to the expulsion of water from the complex. This is corroborated by both the DSC trace and the HSM images (Figure 4.6) where a broad solvent loss endotherm is seen and bubbles begin to appear respectively. A large mass loss representing decomposition of the complex begins at 203.2 ± 4.5 °C. The DSC trace shows an endotherm characteristic of decomposition in the same region. The HSM images at 280 °C show a clearly degraded crystal.

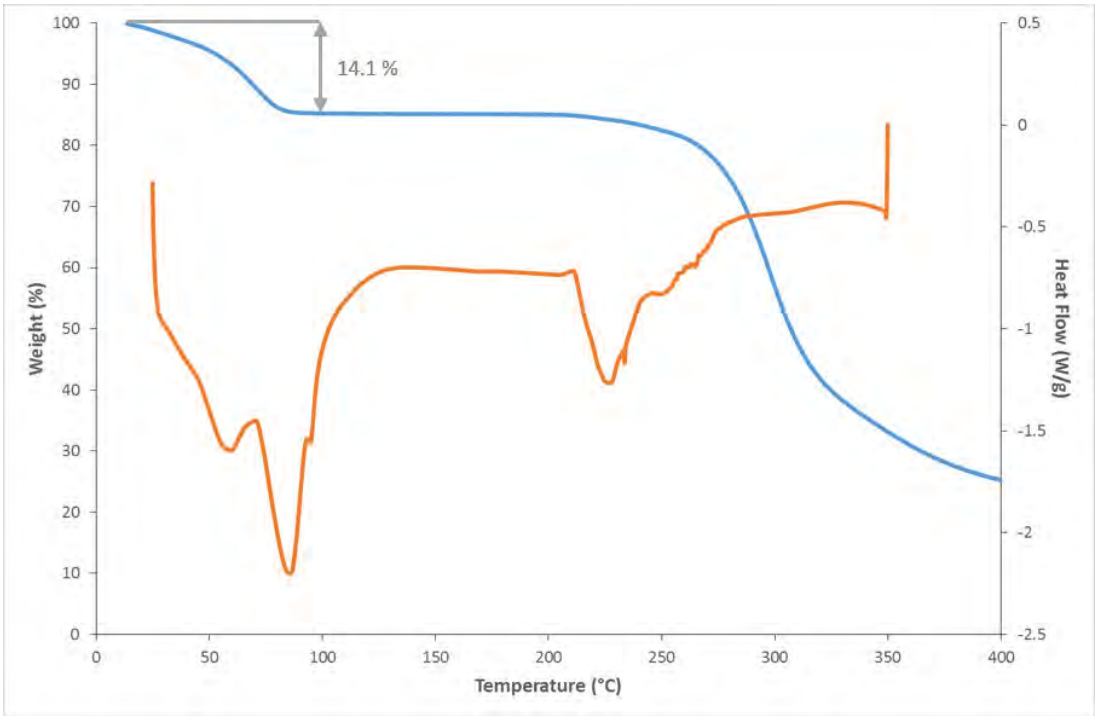

Figure 4.5: Representative TGA (blue) and DSC (orange) traces for BCDFEN

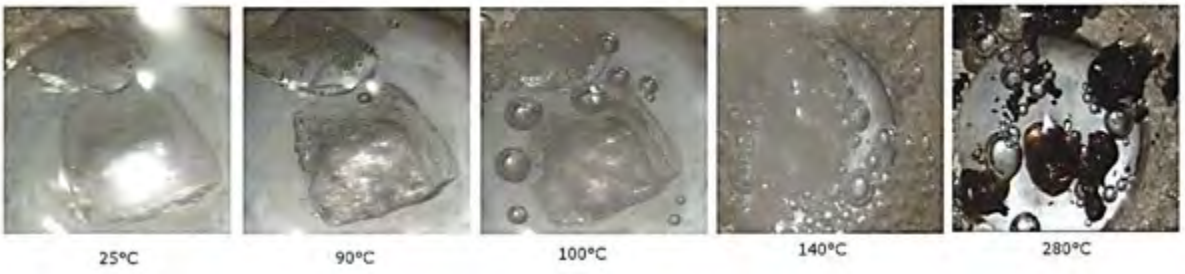

Figure 4.6: Hot stage micrographs showing the BCDFEN complex at various stages of heating

CRYSTAL STRUCTURE ANALYSIS

DATA COLLECTION AND SPACE GROUP DETERMINATION

The single crystal intensity data were collected on a Bruker Apex Duo II diffractometer. The X-ray diffraction pattern was determined to have $\bar{1}$ Laue symmetry, indicating a triclinic space group. As β-cyclodextrin is chiral the only choice was the space group P1. The data collection was performed at 100 ± 2 K.

STRUCTURE SOLUTION AND REFINEMENT

The program SAINT[7] was used in data reduction and unit cell refinement. The asymmetric unit comprises two β-CD molecules, one fenthion molecule and 21.7 waters of crystallisation. The positions of the host atoms were determined by isomorphous replacement.[8] The atomic coordinates of the rigid backbone structure of an isostructural complex were used as a trial model. After a CSD[9] search for suitable candidates, the β-CD inclusion complex of N-acetyl-L-phenylalanine (refcode: AGAZOX)[9,10] was selected from the 33 isostructural complexes. The backbones of the β-CD molecules of the two structures have similar atomic co-ordinates. The differences in the magnitudes of the unit cell dimensions are Δa: 0.038 Å; Δb: 0.056 Å; Δc: 0.041 Å; Δα: 0.38°; Δβ: 0.36° and Δγ: 0.04°.

The rigid backbone used for isomorphous replacement consisted of the non-hydrogen atoms of the glucose rings. The primary -OH groups were excluded in the rigid backbone trial model due to their conformational flexibility. Subsequent electron density difference maps were used to locate the remaining non-hydrogen atomic co-ordinates. The glucopyranose subunits were labelled A1 through A7 and B1 through B7 for the respective β-CD molecules. Once the hydrogen atoms were located in the difference Fourier map they were assigned using a riding model with a U_{iso} value 1.2 to 1.5 times that of the parent atom.

A total of 21.7 water molecules of crystallization per complex unit were located in the crystal structure, in good agreement with the TGA data (24 water molecules). Sixteen of these water molecules were located with full occupancy. Twelve of the oxygen atoms were refined anisotropically, while the remaining showed unrealistic thermal ellipsoids, and were therefore refined isotropically. To determine the *s.o.f.s* of the partially occupied water molecules the U_{iso} values for the fully occupied counterparts were averaged. The U_{iso} values of the partially occupied waters were then fixed to this value and the *s.o.f.s* allowed to vary freely. Once the occupancies converged, these values were fixed and the U_{iso} values allowed to vary freely. Combined, the partially occupied waters summed to 5.7 water molecules.

Table: 4.4: Crystallographic data for the single crystal X-ray structure of BCDFEN

Chemical formula	$2(C_{42}H_{70}O_{35})\cdot(C_{10}H_{15}O_3PS_2)\cdot 21.7(H_2O)$
Molar Mass (g mol^{-1})	2912.22
Crystal system	Triclinic
Space group	P1
Unit cell parameters	
a (Å)	17.852(8)
b (Å)	15.334(7)
c (Å)	15.431(7)
α (°)	103.134(8)
β (°)	113.029(8)
γ (°)	99.227(8)
Volume ($Å^3$)	3636(3)
Z	1
$Density_{calcd}$ (g cm^{-3})	1.322
μ [MoKα] (mm^{-1})	0.156
F (000)	1 524
Temperature (K)	100(2)
Crystal size (mm)	0.15×0.13×0.05
Range scanned θ (°)	2.0 – 24.9
Index ranges	h: -21, 21; k: -18, 18; l: -18, 18
ϕ and ω scan angle (°)	0.5
Dx (mm)	50
Total number of reflections	56 328
Number of independent reflections	24 176
Number of reflections with I > 2σ(I)	12 453
R_{int}	0.0656
R_1 [I > 2σ(I)]	0.1208
wR_2	0.3384
S	1.22
Number of parameters	1 538
Number of reflections omitted	76
Parameters a, b in	a = 0.2000; b = 0
$w = 1/[\sigma^2(F_O^2)+(aP)^2+(bP)]$	
$(\delta/\sigma)_{mean}$	0.039
Δρ excursions (e $Å^{-3}$)	-1.418; 2.187

MODELLING OF THE FENTHION

Initially one guest molecule was modelled; however, large residual electron density peaks surrounding the fenthion molecule indicated the presence of a second image of the molecule. Two guest molecules could not be present simultaneously due to their close proximity, thus indicating disorder. During modelling it was found that the disordered components of the fenthion molecule shared several atoms, namely P11, O13 and C16 (Figure 4.7) of the phosphorothioate moiety. All other atoms were found to be disordered over two positions due to the presence of a rotamer. The angle S14A-P11-S14B arises from the rotamer and is 89.5°. The two guest components were assigned and refined with site-occupancy factors of *x* and *1-x*. The final value of *x* was found to be 0.530(14). Once the occupancy of the fenthion components converged it was decided that the U_{iso} values of each component be assigned as free variables. The relative orientation of the disordered components is shown in Figure 4.7.

During refinement of the structure it was necessary to apply appropriate restraints to the phosphorothioate moiety bonds. The bond lengths of the guest molecule in the complex β-CD/fenitrothion[4] were used to obtain reasonable DFIX restraints to apply to the bonds in fenthion.

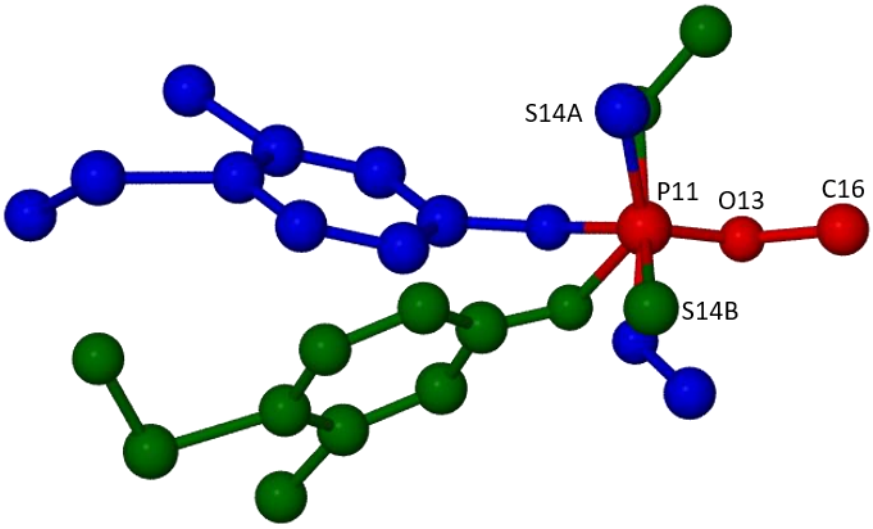

Figure 4.7: Disorder of the fenthion guest molecule with the major component in blue, the minor component in green and the common atoms in red. Hydrogen atoms have been omitted for clarity.

GEOMETRIC ANALYSIS OF THE BCDFEN STRUCTURE

The asymmetric unit comprises a hydrated 2:1 host-guest inclusion complex. This is shown in Figure 4.8 (water molecules excluded). The numbering scheme of the host and guest molecules are presented in Figure 4.9.

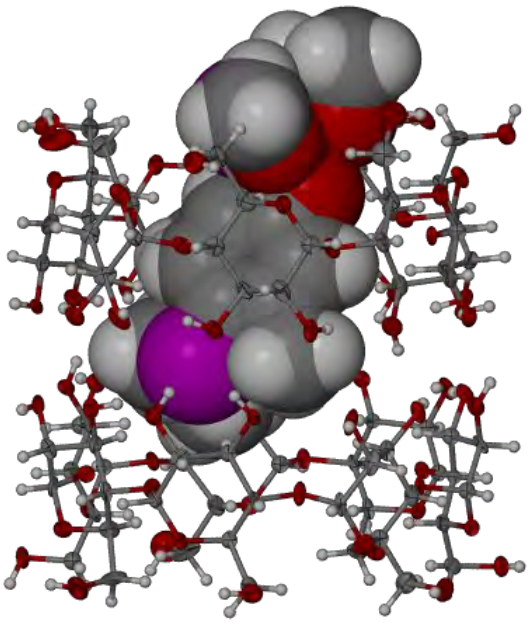

Figure 4.8: The asymmetric unit of the complex BCDFEN (water molecules excluded). Thermal ellipsoids for the host atoms are drawn at the 50% probability level and the guest atoms are drawn in space-filling mode

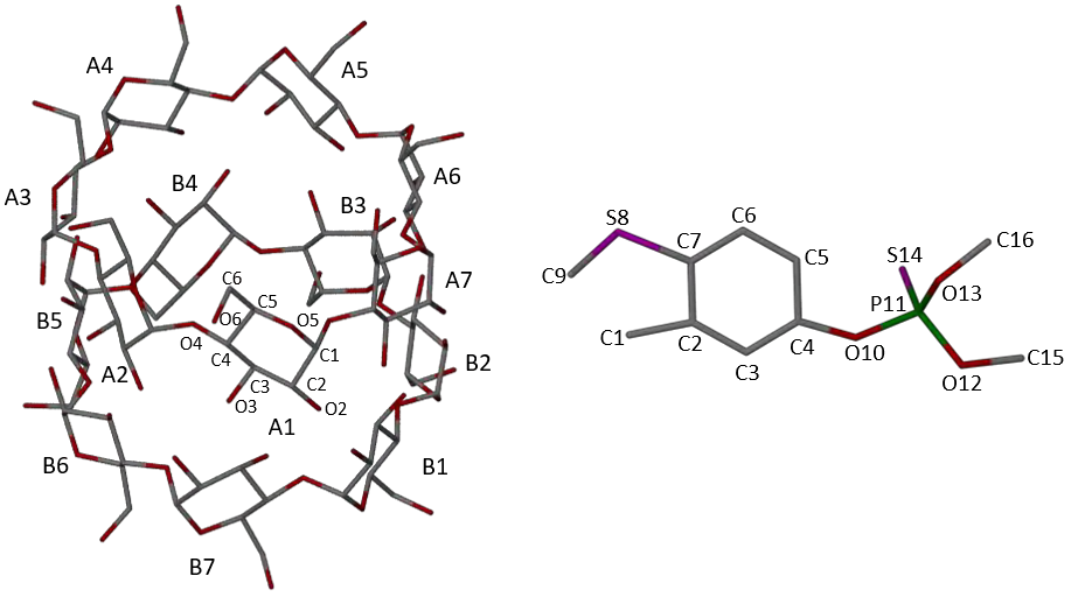

Figure 4.9: Numbering scheme of the glucopyranose rings (left) and the guest molecule (right)

HOST CONFORMATION

The data presented below can be seen in detail in Appendix C. The range of values presented below provides an indication of the geometry of the cyclodextrin host molecules.

The primary torsion angle, ω, is a measure of the O5-C5-C6-O6 dihedral angle. This angle indicates the orientation of the C6-O6 bond, and hence whether this bond is directed towards, or away from, the host cavity. All the primary C6-O6 substituents, other than that of A7, are directed away from the cyclodextrin cavities. The primary hydroxyl group directed towards the cavity has an ω angle of 59°. The substituents that are directed away from the cyclodextrin cavities have torsion angles that fall within the range $-69° \leq \omega \leq -54°$.

The geometric parameters *l*, *D* and ϕ all fall within a narrow range for each cyclodextrin. This indicates that both cyclodextrins maintain a 'round' shape. The ranges of these values are: $4.894 \text{ Å} \leq l \leq 5.218 \text{ Å}$, $4.287 \text{ Å} \leq D \leq 4.478 \text{ Å}$ and $125.7° \leq \phi \leq 131.5°$ for the cyclodextrin labelled A and $4.997 \text{ Å} \leq l \leq 5.079 \text{ Å}$, $4.342 \text{ Å} \leq D \leq 4.405 \text{ Å}$ and $126.9° \leq \phi \leq 129.6°$ for the cyclodextrin labelled B. The circular shape of the cyclodextrins is maintained by the hydrogen bonds O3(n+1)-H···O2.

The tilt angles τ_2 are all positive indicating that the primary ends of the cyclodextrins are oriented inwards, i.e. towards the centre of the cavity. The angle formed between the O4 mean planes of the two β-CD host molecules is 1.0(3)°, which shows that they are almost parallel.

GUEST INCLUSION AND CONFORMATION

The fenthion molecule is disordered over two positions within the cyclodextrin cavity where the major component has a *s.o.f* of 0.530(14). The disordered components share three atoms, namely P11, O13 and C16, as seen in Figure 4.7.

The two disordered components are positioned such that their phosphorothioate moiety is at the primary rim of the cyclodextrin cavity of the host designated A, as shown in Figure 4.10a. The methoxy groups of the phosphorothioate moiety protrude slightly from the primary rim of the cavity. The fenthion molecule extends only slightly into the secondary end of the cyclodextrin molecule B. A large void remains in the second cyclodextrin cavity (Figure 4.11); however, this void is not large enough to accommodate a second guest molecule.

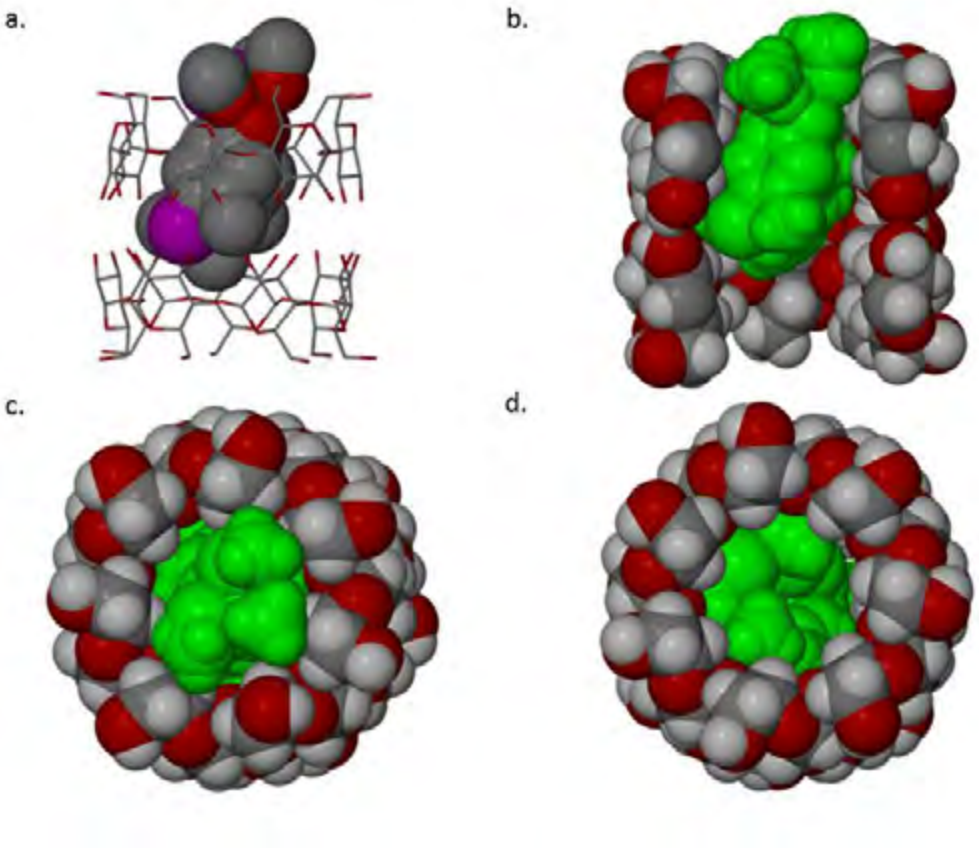

Figure 4.10: a. Relative positions of the disordered fenthion molecule in the β-CD dimer; b. cross-sectional view of the complex; c. view from the primary rim of host molecule A and d. view from the primary rim of host molecule B

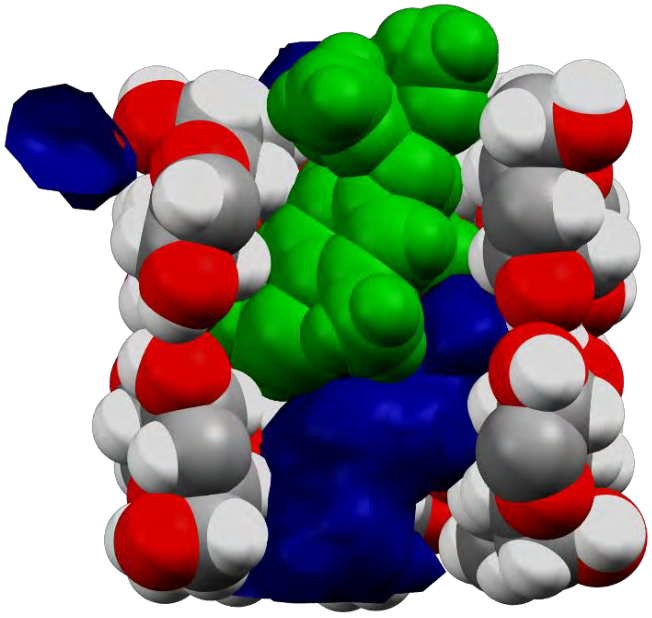

Figure 4.11: Cross sectional view showing void space (blue) relative to the fenthion guest (green)

INTRA- AND INTERMOLECULAR INTERACTIONS

HOST INTERACTIONS

Various hydrogen bonds were identified in the complex host molecules. Both intra- and intermolecular interactions are observed. The intramolecular hydrogen bonds identified were the O3(n+1)-H···O2n interactions which stabilise the 'round' conformation of the host molecules. These hydrogen bonds have O···O donor to acceptor distances ranging from 2.72 Å to 2.86 Å.

The two cyclodextrin molecules are linked by inter-host hydrogen bonds. Four hydrogen bonds are responsible for linking the dimeric host system. These occur between the O3n atoms on the respective cyclodextrins.

Sixteen hydrogen bonds were identified between the β-CD dimers; ten of these are of the type O-H···O while the remaining six are weak C-H···O interactions. Of these, only one is between layers while the remaining hydrogen bonds link the β-CD dimers within a given layer.

The parameters of the above hydrogen bonds are available in Appendix C.

GUEST INTERACTIONS

Only one identifiable interaction between the host and guest molecules is present in the structure. This interaction is between the minor component of the disordered guest and the host. The interaction is the C3B-H···O4A5 weak hydrogen bond with C···O distance of 3.47(5) Å and a hydrogen bond angle of 148°. The association of fenthion and β-CD is primarily due to van der Waals forces and hydrophobic interactions.

Present in each fenthion component is one weak C-H···S intramolecular interaction between the C1-H and S8 atoms. The major component has a C1···S8 distance of 2.55(8) Å while the minor component has a distance of 2.75(8) Å. The hydrogen bonding angles (C1-H···S8) for the major and minor components are 122° and 113° respectively.

CRYSTAL PACKING

The complex BCDFEN comprises two β-cyclodextrin molecules in a head-to-head dimeric arrangement. Within the cavity formed there is a partially disordered fenthion molecule. The dimers stack to form channels parallel to the *a*-axis. The water molecules present in the BCDFEN structure can be found in the interstitial spaces between these channels. The channels and water molecules are visible in Figure 4.12 where one can see the inclusion of the guest within the cyclodextrin structures.

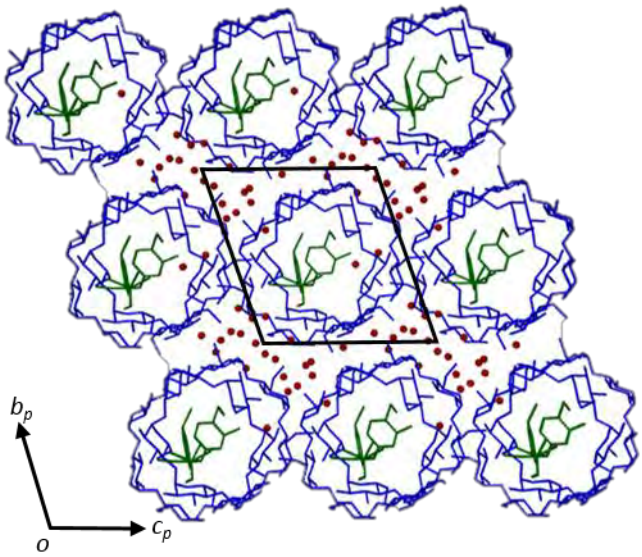

Figure 4.12: Packing diagram of the BCDFEN complex viewed along [1 0 0]

As is common amongst β-CD complexes that crystallise in the space group P1 the packing motif is classified as 'intermediate-type packing'. The layers of the β-CD dimers are essentially parallel where the angle between subsequent O4n least-squares mean planes is 1.0°. In this arrangement the O4n centroids are offset by approximately 6 Å (R_A = 6.042 Å and R_B = 6.055 Å) between layers. The offset of these layers is clear from Figure 4.13. The 'cage-like' term used by Saenger[11] is justified as this large offset causes the cyclodextrin cavities, and by extension the included guests, to be isolated from one another.

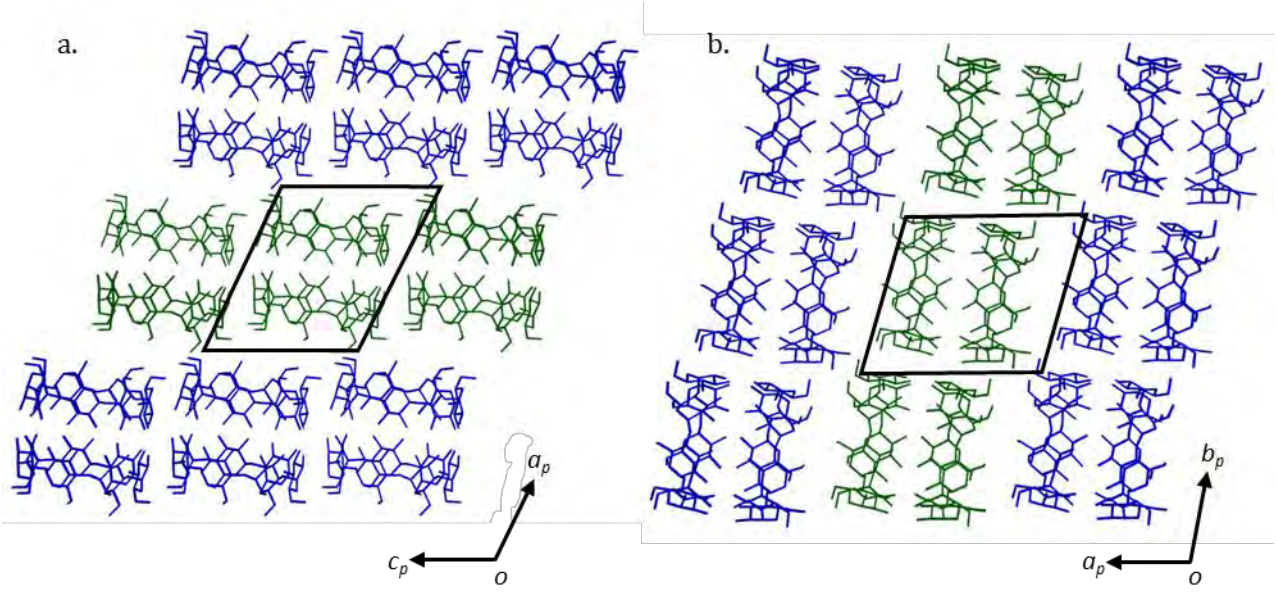

Figure 4.13: Packing diagram of the β-CD host molecules of the BCDFEN complex viewed along a. [0 1 0] and b. [0 0 1]

The section on structure solution and refinement explained the choice of the complex β-CD/(N-acetyl-L-phenylalanine) (refcode: AGAZOX)[9,10] for use in isomorphous replacement. Figure 4.14 shows the good match of the atomic co-ordinates of the host molecule backbones.

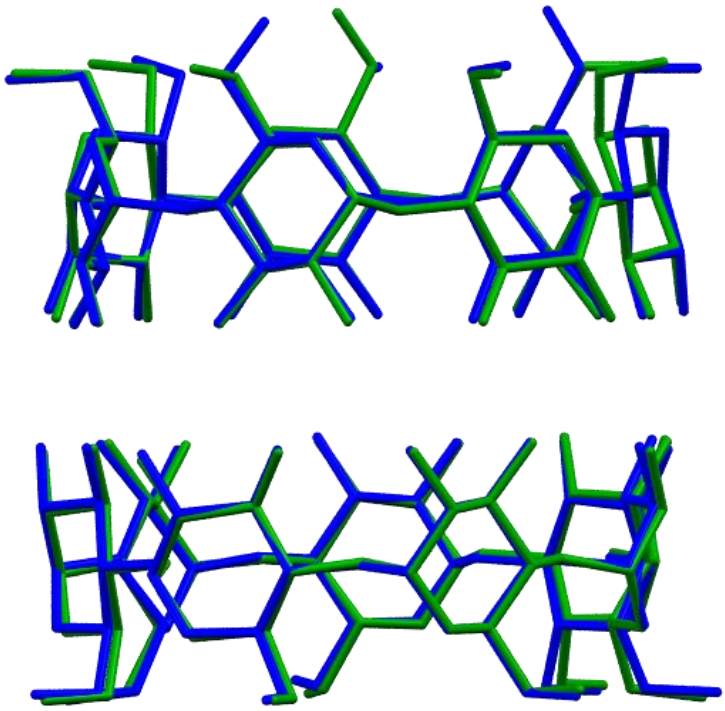

Figure 4.14: Overlay of AGAZOX (green) and BCDFEN (blue) host molecules

TRIMEA/FENTHION

The inclusion complex of fenthion with TRIMEA will be referred to as TMAFEN.

COMPLEX PREPARATION

The complex was prepared *via* co-precipitation, during which TRIMEA (101.2 mg; 0.0826 mmol) was weighed into a vial and dissolved to make a 3 cm^3 aqueous solution. A drop of fenthion (23 mg; 0.0826 mol) was added to the vial and the solution stirred at 4 °C for 3 to 4 hours. The mixture was then filtered through a 0.45 µm nylon filter into a clean vial and left to crystallise in a 60 °C oven. Small colourless block-like crystals appeared after 3 days.

CONFIRMATION OF STOICHIOMETRY

The complex stoichiometry was confirmed by NMR spectroscopy. Crystals obtained by co-precipitation were dissolved in DMSO-d_6 for analysis by ^{1}H-NMR spectroscopy. Labelling of the protons on the methylated glucopyranose subunits of TRIMEA and fenthion are shown in Figure 4.15. The integration of the C-H_1 proton on TRIMEA was used as the reference integral. Integration of the C-$H_{1a,b,c}$, C-$H_{15a,b,c}$ and C-$H_{16a,b,c}$ methyl protons were integrated for fenthion and showed a stoichiometric ratio of 1:1 for TMAFEN. The table of integration values and the NMR spectrum can be found in Table 4.5 and Figure 4.16 respectively.

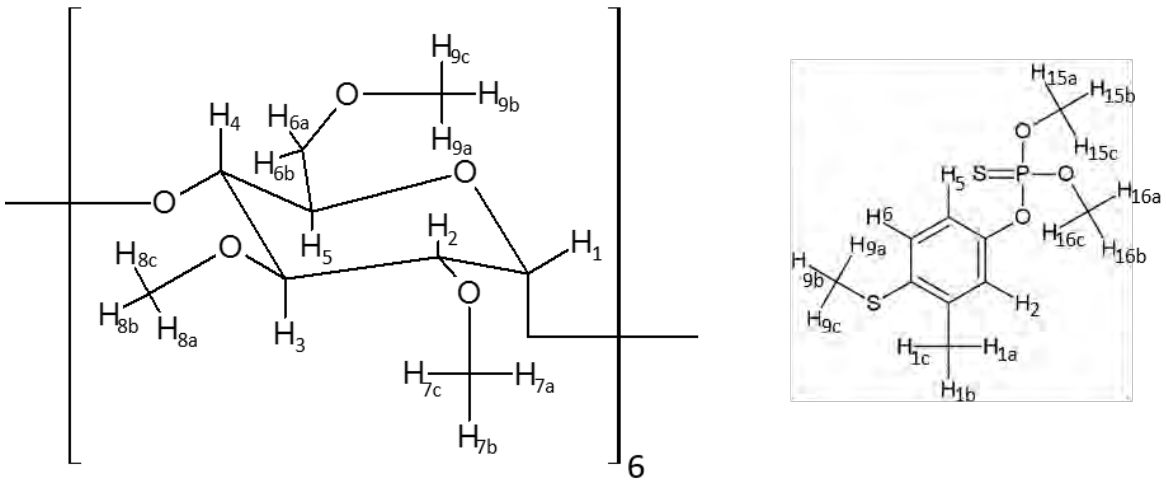

Figure 4.15: Proton labelling of TRIMEA methylated glucopyranose subunits (left) and fenthion (right)

Table 4.5: NMR spectroscopy proton assignment and integration of TMAFEN

Proton	δ (ppm)	Integration		Experimental/ Theoretical
		Experimental	Theoretical	
TRIMEA				
C-H_1	5.01	6.00‡	6.00	1
C-$H_{9a,b,c}$	3.27	17.99	18	0.99 ≈ 1
C-$H_{7a,b,c}$	3.41	17.78	18	0.99 ≈ 1
Fenthion				
C-$H_{1a,b,c}$	2.29	2.90	3	0.97 ≈ 1
C-$H_{15a,b,c}$ + C-$H_{16a,b,c}$	3.82, 3.87	5.76	6	0.96 ≈ 1

‡*Reference Integral*

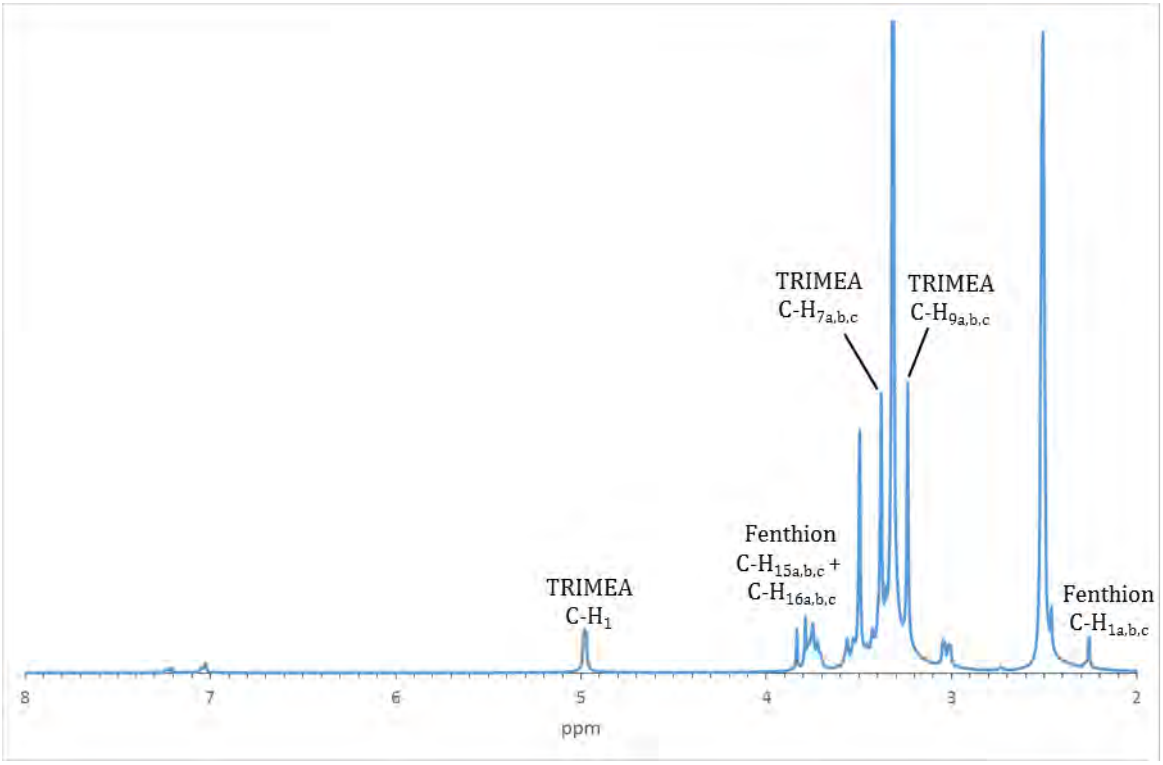

Figure 4.16: NMR spectrum of TMAFEN in DMSO-d_6 to determine the stoichiometric ratio

THERMAL ANALYSIS

The TGA trace of the TMAFEN complex (Figure 4.17) shows a mass loss of 0.5 ± 0.1 % (n = 2) from room temperature to 109.1 ± 5.9 °C, interpreted as the loss of 0.4 ± 0.1 of a water molecule. There is no endotherm relating to the mass loss of the partially occupied water molecule due to the negligible thermal energy relating to this event. The DSC trace shows two endotherms coinciding with the second and third mass losses in the TGA trace. The second endotherm is consistent with melting followed by a mass loss in the TGA trace. The HSM images (Figure 4.18) corroborate the above interpretation. At 100 °C some bubbling, indicative of solvent loss, is observed. At 230 °C the crystals have clearly melted with some further bubbling. In the micrograph taken at 300 °C, the decomposed cyclodextrin is clearly visible.

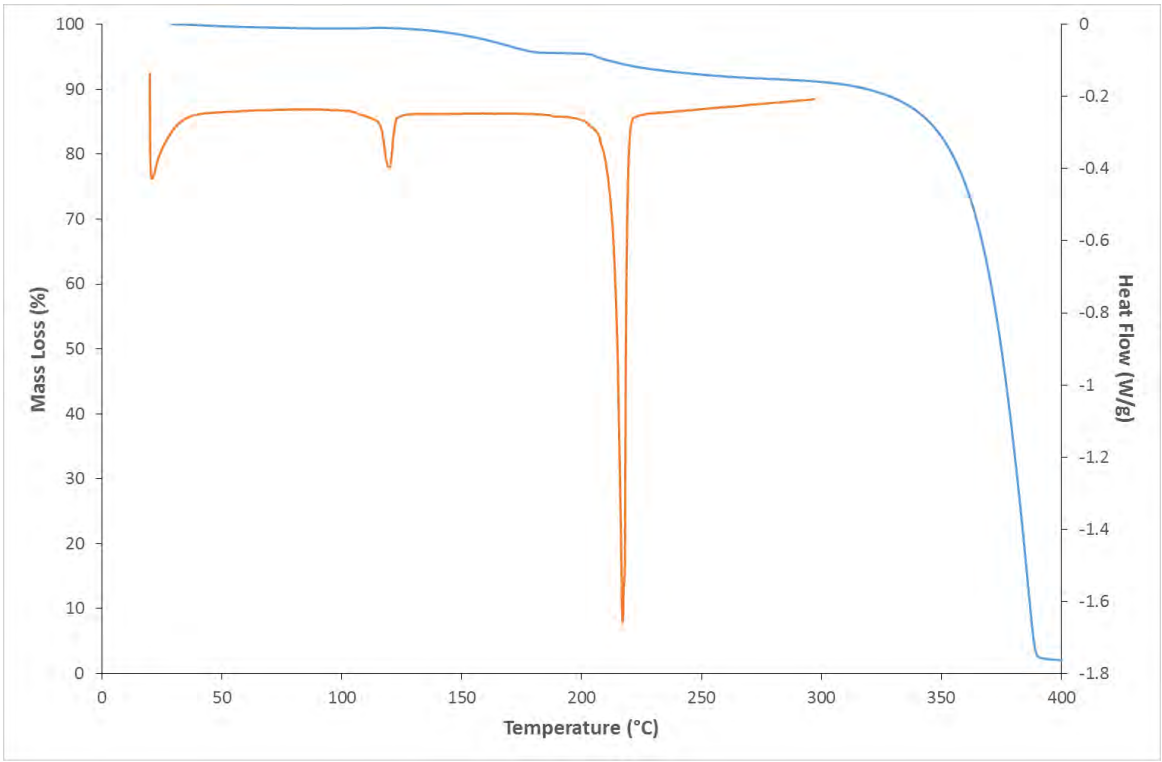

Figure 4.17: Representative TGA (blue) and DSC (orange) traces for TMAFEN

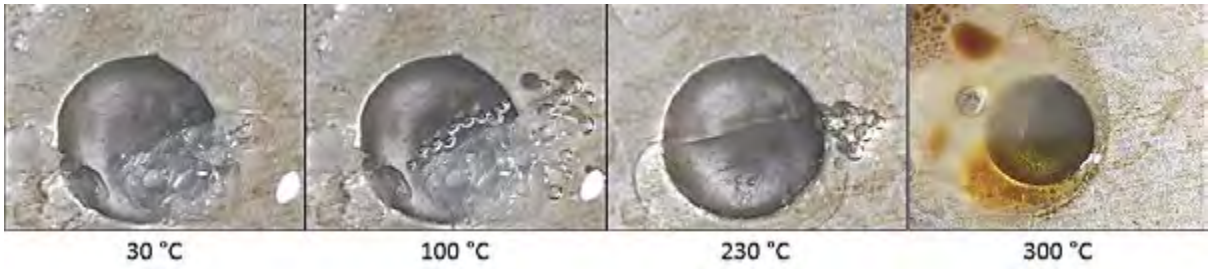

Figure 4.18: Hot stage micrographs showing the TMAFEN complex at various stages of heating

CRYSTAL STRUCTURE ANALYSIS

DATA COLLECTION AND SPACE GROUP DETERMINATION

The intensity data were collected using a Bruker Kappa Apex II DUO diffractometer. The Laue symmetry was determined to be 2/m indicating the monoclinic crystal system. The conditions limiting reflections were *hkl: none, h0l: none, 0k0: k = 2n*. These conditions indicate the space groups $P2_1$ or $P2_1/m$, but since the host molecule is chiral the correct space group $P2_1$ was chosen for the analysis. The asymmetric unit contains one fenthion molecule, one TRIMEA molecule and a partial water molecule.

STRUCTURE SOLUTION AND REFINEMENT

Table 4.6 shows the crystallographic data and data-collection parameters. The program SAINT[7] was used for unit cell refinement and data reduction. SADABS[12] was used to correct absorption using the multi-scan method. A search of the CSD[9] was undertaken, but no suitable structures were found for isomorphous replacement. The structure was then solved using SHELXD,[13] employing *ab initio* methods. Once a reasonable solution was found with SHELXD the host molecule atoms were assigned and the structure was refined using SHELXL.[13] The glucopyranose subunits were labelled with the suffixes G1 – G6.

Disordered methyl groups on TRIMEA were modelled by allowing the *s.o.f.s* to vary by assigning the major component variable *x* and the minor component *1-x* and the atoms were refined isotropically. The C7 methyl group on residue G6 and the O6-C9 methoxy substituent on residue G5 were found to be disordered with the major components having *s.o.f.s* 0.58(1) and 0.51(1) respectively. All ordered atoms were treated anisotropically.

The complete fenthion molecule was found to be disordered over two positions. The *s.o.f.s* were linked to free variables, as in the case of the methoxy groups above. The major component was refined to have a *s.o.f.* of 0.71(1). Once the hydrogen atoms were located in the difference Fourier map they were placed in idealised positions using a riding model. The temperature factors in the riding model were 1.2 to 1.5 times those of their parent atoms.

From the residual electron density in the structure, a water molecule with partial occupancy was located at the primary rim of the cyclodextrin cavity. The occupancy of the water molecule was determined from the TGA trace and set as 0.4. With this occupancy the U_{iso} value was found to be 0.17(1) $Å^2$. The large relative error in the TGA mass loss makes exact estimation of the *s.o.f.* problematic. As no other evidence for the occupancy of the water molecule is available it is possible that the occupancy has been overestimated and therefore the U_{iso} value remains large.

Table 4.6: Crystallographic data and data-collection parameters for TMAFEN

Chemical Formula	$C_{54}H_{94}O_{30}{\cdot}C_{10}H_{15}O_3PS_2{\cdot}(H_2O)_{0.4}$
Crystal system	Monoclinic
Molar Mass (g mol^{-1})	1493.53
Space group	$P2_1$
Unit cell parameters	
a (Å)	11.2135(6)
b (Å)	22.9575(12)
c (Å)	15.4666(9)
α (°)	90.0
β (°)	104.238(1)
γ (°)	90.0
Volume (Å^3)	3860.4(4)
Z	2
Density$_{calcd.}$ (g cm^{-3})	1.285
μ [MoKα] (mm^{-1})	0.173
F (000)	1 592
Temperature (K)	173(2)
Crystal size (mm)	0.25×0.30×0.43
Range scanned θ (°)	1.4 – 27.2
Index ranges	h: -14, 14; k: -29, 29; l: -19, 19
ϕ and ω scan angle (°)	0.50
Dx (mm)	40
Total number of reflections	57 806
Number of independent reflections	17 099
Number of reflections with I > 2σ(I)	15 158
R_{int}	0.022
R_1 [I > 2σ(I)]	0.0469
wR_2	0.1154
S	1.024
Number of parameters	900
Number of reflections omitted	14
Parameters a, b in	a = 0.0582; b = 2.2093
w = 1/[σ^2(F_O^2)+(aP)^2+(bP)]	
$(\delta/\sigma)_{mean}$	<0.001
Δρ excursions (e Å^{-3})	-0.67; 0.72

MODELLING OF THE FENTHION GUEST MOLECULE

Initially the guest was easily modelled after the early refinements of the host molecule. After preliminary assignment of the guest molecule several large electron density peaks remained around the phosphorothioate moiety. Several of the remaining fenthion atoms had unacceptably large thermal parameters, suggesting that the molecule was disordered. From the X-ray data, a second component was modelled. The guest components, labelled with suffixes A and B, were refined with global *s.o.f.s*. of *x* and *1-x*. The value of *x* refined to 0.71(1) for the major component, A. Two distance restraints were applied to the thioester moiety of the minor component. The thioester and phosphorothioate moieties of the major and minor components required FLAT restraints to maintain reasonable geometry. The hydrogen atoms were placed in idealised positions, with U_{iso} values of 1.2 to 1.5 times that of the parent atom, after they were located in the difference Fourier map. The partial hydrogen atoms of the water molecule were not found in the difference Fourier map and are not included in this structure.

GEOMETRIC ANALYSIS OF TMAFEN

The asymmetric unit of the inclusion complex TMAFEN comprises one host and one guest molecule and a water molecule with partial occupancy. The asymmetric unit is shown in Figure 4.19. The numbering schemes for the guest and host molecules are shown in Figure 4.20.

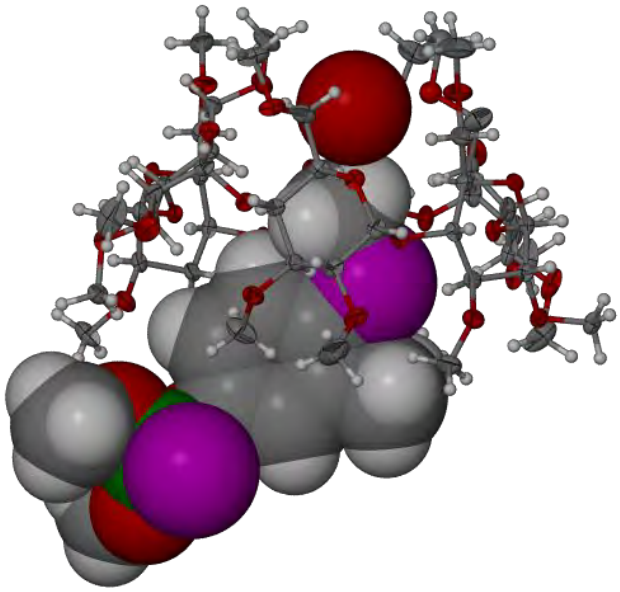

Figure 4.19: The asymmetric unit of the complex TMAFEN. Thermal ellipsoids for the host atoms are drawn at the 50% probability level and the guest and water atoms are drawn in space-filling mode. The minor disorder components have been omitted for clarity

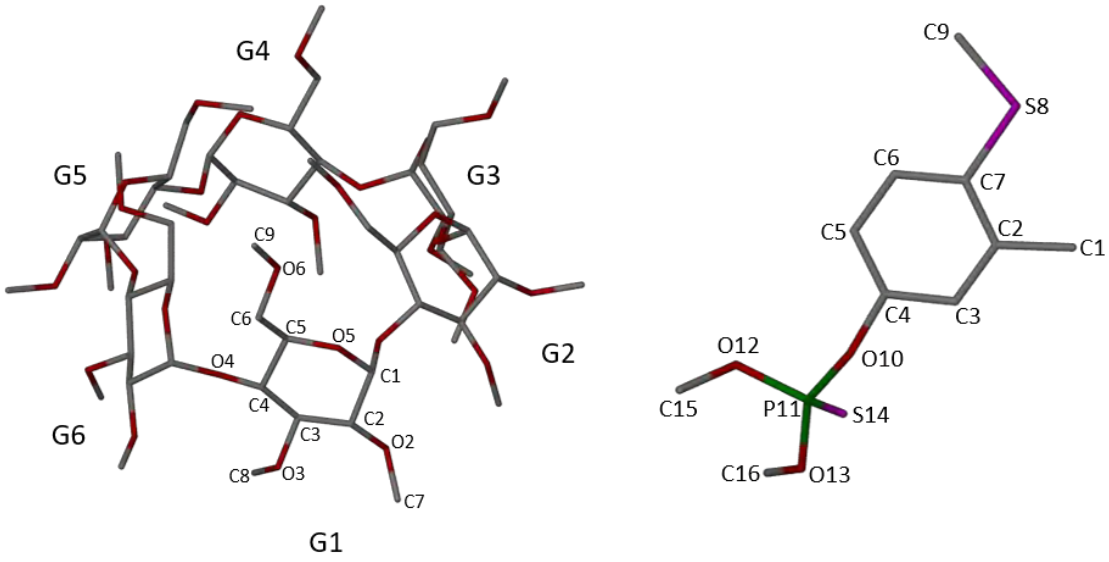

Figure 4.20: Numbering scheme of the glucopyranose rings (left) and the guest molecule (right). The minor component is not shown here for clarity. The major component is designated by the suffix A and the minor component by the suffix B

HOST CONFORMATION

The torsion angles of the primary methoxy substituents, ω, are listed in Table 4.7. From these values it was found that four of these groups are directed towards the cyclodextrin cavity and the G3 and G6 groups are directed outwards. When these data are combined with the τ_2 tilt angles listed in Table 4.8 one can conclude that the primary end of the TRIMEA cavity is closed off, restricting access from this end of the cyclodextrin.

Table 4.7: Torsion angles (ω) for TMAFEN

Glucose Residue	ω (°)‡
G1	69.8
G2	71.6
G3	-70.4
G4	74.4
G5	55.1
G6	-71.3

‡*Mean e.s.d. 0.4°*

Tables 4.8 and 4.9 show the geometric parameters for TMAFEN and uncomplexed TRIMEA (refcode: TEVCEC)[9,14] respectively. The TRIMEA molecules in these crystal structures are conformationally similar. However, the geometric parameters show that the host molecule in TMAFEN has a slightly elliptically distorted O4n hexagon compared to TEVCEC:

3.952 Å ≤ *l* ≤ 4.533 Å, 4.172 Å ≤ *D* ≤ 4.421 Å and 109.8° ≤ ϕ ≤ 126.5°. The corresponding parameters for TEVCEC are 4.041 Å ≤ *l* ≤ 4.375 Å, 4.095 Å ≤ *D* ≤ 4.469 Å and 116.1° ≤ ϕ ≤ 122.8°.

The inclusion of fenthion in the TMAFEN complex causes the distortion of the hexagon. However, the included portion of fenthion is not parallel to the elliptical distortion of the cavity (Figure 4.21). The aromatic plane of fenthion forms an angle of approximately 60° to the long axis of the ellipse. The O4G2···O4G5 distance, parallel to the thiomethyl group, is 8.463(3) Å. The longest transannular distance, 8.942(3) Å and the shortest, 7.937(4) Å (O4G1···O4G4 and O4G3···O4G6 respectively) are inclined at approximately 60° to the O4G2···O4G5 transannular line. This shows that the planar portion of the guest is not included parallel to the longest distortion of the hexagon. The view from the primary end of the cyclodextrin cavity (Figure 4.21) illustrates the distortion. The large tilt angle observed for glucopyranose subunit G2 is caused by the steric hindrance arising from the protrusion of the fenthion phosphorothioate moiety. This has the effect of shortening the O4G2···O4G5 and O4G3···O4G6 transannular distances.

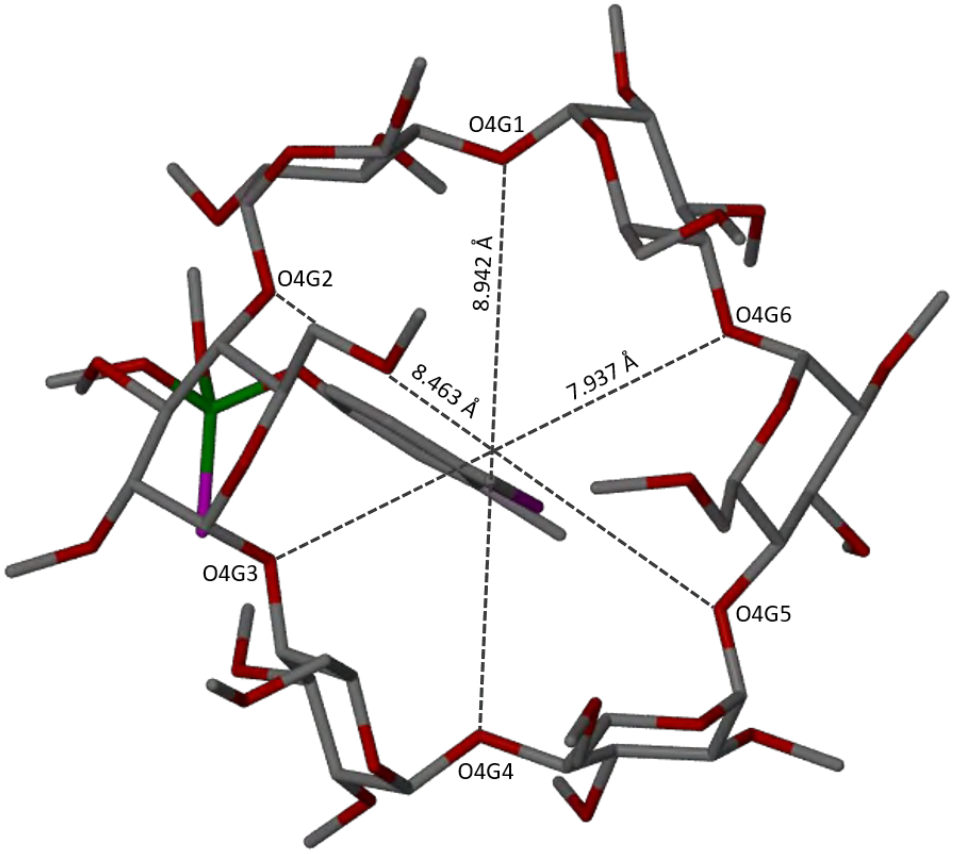

Figure 4.21: View from the primary end of TMAFEN illustrating the O4Gn transannular distances

The tilt angles, τ_2, are similar in TMAFEN and TEVCEC, having ranges 6.4° ≤ τ_2 ≤ 40.4° and 9.0° ≤ τ_2 ≤ 42.4°, respectively. These large tilt angles close off the primary end of the cavity giving the TRIMEA molecules a 'bowl' shape rather than the usual torus seen in native cyclodextrins.

The conformational similarity of the TRIMEA molecules in TMAFEN and TEVCEC can be seen in Figure 4.22. The primary ω torsion angles in TMAFEN further show that the methoxy substituents close off this end of the cyclodextrin cavity.

In TMAFEN, the methyl substituents on the O2 atoms of all the glucose subunits are directed outwards from the cavity while those on the O3 substituents are directed inwards. The alternating arrangement of the O2Gn and O3Gn methoxy groups is most likely due to the steric hindrance that occurs between the methyl groups attached to these atoms. To compensate for the steric hindrance the τ_2 angles increase to maximise the distance between methoxy substituents on the secondary end of the cavity; this has the additional effect of narrowing the primary end of the cavity.

Table 4.8: Geometric parameters for the host molecule in the complex TMAFEN

Residue	l (Å)	D (Å)	Φ (°)	d (°)	α[a] (Å)	D_3[b] (Å)	τ_2[c] (°)
G1	4.533	4.229	121.0	-12.1	-0.373	3.431	6.4
G2	4.213	4.202	126.5	23.3	0.030	3.325	40.4
G3	3.952	4.260	112.0	-11.3	0.355	3.332	10.7
G4	4.442	4.172	119.8	-10.7	-0.381	3.356	10.2
G5	4.249	4.292	125.3	21.5	0.023	3.180	34.1
G6	4.018	4.421	109.8	-10.1	0.347	3.825	27.1

[a] mean e.s.d: 0.013 Å; [b] mean e.s.d: 0.004 Å; [c] mean e.s.d: 0.1°

Table 4.9: Geometric parameters for uncomplexed TRIMEA (refcode: TEVCEC)[9,14]

Residue	l (Å)	D (Å)	Φ (°)	d (°)	α (Å)	D_3[a] (Å)	τ_2 (°)
G1	4.255	4.132	117.6	-17.8	0.352	3.441	12.1
G2	4.322	4.095	122.8	26.5	0.131	3.429	42.4
G3	4.041	4.433	117.4	-7.8	-0.487	3.510	9.0
G4	4.222	4.112	116.1	-16.8	0.364	3.598	17.2
G5	4.375	4.230	122.0	25.9	0.112	3.309	38.7
G6	4.083	4.469	116.2	-6.8	-0.472	3.332	9.8

[a] mean e.s.d: 0.006 Å

The e.s.d. values for α and τ_2 were not available from the publication[14]

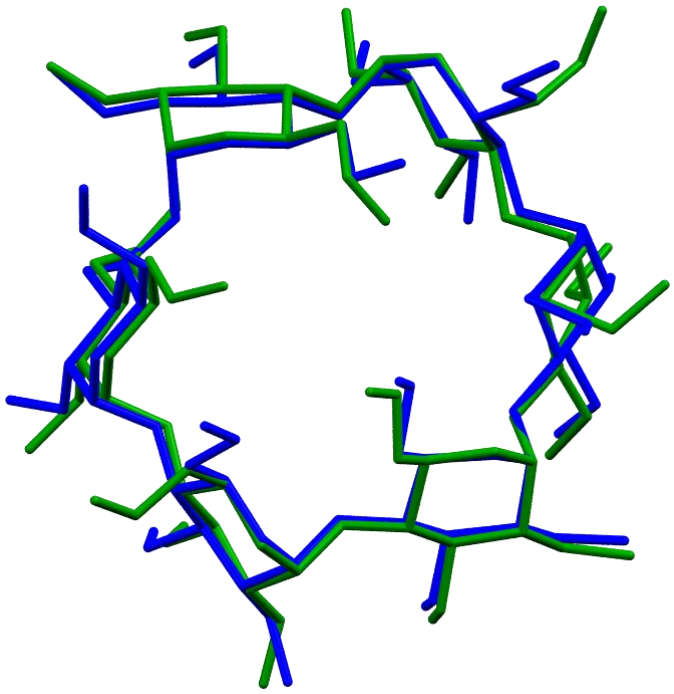

Figure 4.22: Overlay of TEVCEC (green) and TMAFEN (blue) host molecules

GUEST INCLUSION

The inclusion of fenthion in the complex TMAFEN will be described using the major component due to the similarity in atomic co-ordinates of the two disordered components. As shown in Figure 4.19 the thiomethyl portion of fenthion is included within the TRIMEA cavity. The aromatic and phosphorothioate moieties extend into the interstitial spaces between cyclodextrin molecules. The tilt angles of the glucopyranose subunits, combined with the primary methoxy substituent of the TRIMEA molecule close off the cavity, isolating the thiomethyl group from the external environment. The penetration of the thiomethyl group is minimal as indicated by the fact that the methyl only extends 0.037 Å above the O4Gn least-squares plane. Meanwhile, the sulfur atom is located 1.501 Å below the same plane and only 0.281 Å above the secondary oxygen atom (O2 and O3) least-squares plane.

The guest molecule fenthion is disordered over two positions with the major component having a *s.o.f.* of 0.71(1). The respective aromatic planes of the major and minor components intersect at 5.0(1)°. Both the major and minor components include in the same manner and occupy almost overlapping atomic coordinates, except for the phosphorothioate moiety, as can be seen in Figure 4.23.

Figure 4.23: Disorder of the fenthion guest molecule (major component: blue, minor component: green) viewed perpendicular (left) and parallel (right) to the aromatic planes

The selected torsion angles shown in Table 4.10 illustrate the differences in the major and minor component conformations. As can be seen from the torsion angle S14-P11-O10-C4 the major component is in a (-)-*gauche* conformation while the minor component is in the (+)-*gauche* conformation. The remaining substituents of fenthion remain in similar conformations in the major and minor components. The phosphorothioate groups of both components are in a tetrahedral arrangement about the phosphorus atom. In the minor component the tetrahedral arrangement is slightly distorted with the O10B-P11B-O12B angle being only 99.8(7)°. The angles O12B-P11B-S14B and O13B-P11B-S14B were found to be 114.2(5)° and 112.4(5)° respectively.

Table 4.10: Selected torsion angles (°) for the major and minor components

Torsion Angle	Major	Minor
O10-C4-C5-C6	-171.7(6)	-179(1)
S8-C7-C6-C5	179.8(6)	175(1)
C1-C2-C3-C4	-179.9(7)	-171(1)
S14-P11-O10-C4	-37.7(5)	66(1)

INTRA- AND INTERMOLECULAR INTERACTIONS

HOST INTERACTIONS

Unlike the host cyclodextrins β-CD and DIMEB, TRIMEA is fully methylated and as such has no hydroxyl groups available for hydrogen bonding. There are eight intramolecular interactions within the host molecule, all of the type C-H···O. These have D···A distances ranging from 2.782(4) Å to 3.152(5) Å and D-H···A angles from 101° to 140°.

There are three inter-host interactions that occur during packing of the crystal structure. There is no classical hydrogen bonding present in this structure and the inter-host interactions are of the C-H···O type. These hydrogen bonds are listed in Table 4.11 below.

Table 4.11: Inter-host interactions of TMAFEN

Interaction	D···A (Å)‡	D-H···A (°)	Symmetry Operator
C2G3-H···O5G1	3.315	170	*(2-x, 1/2+y, 1-z)*
C9G3-H···O3G1	3.373	139	*(2-x, 1/2+y, 1-z)*
C2G4-H···O6G6	3.322	150	*(2-x, 1/2+y, 2-z)*

‡*Mean e.s.d.: 0.004 Å*

GUEST INTERACTIONS

Two hydrogen bonding interactions of the form C-H···O occur between the guest and host molecules, namely C5A-H···O2G1 and C3A-H···O5G2‡ (‡ = *1+x, y, z*). The first occurs within the asymmetric unit while the second occurs with a translated TRIMEA molecule The D···A distances are 3.271(7) Å and 3.328(6) Å and the D-H···A angles 148° and 171° respectively.

WATER INTERACTIONS

The water molecule with partial occupancy is in a position indicative of hydrogen bonding with the host molecule. As the hydrogen atoms were not located in the difference Fourier map the interactions were determined from short intermolecular contacts. The water oxygen atom was found to be 2.89(2) Å from O6G2 and 2.86(3) Å from O7G5. These values are less than the sum of the respective van der Waals radii indicative of hydrogen bonding. The angle O6G2···OW1···O7G5 is 102.1(7)°, which is close to the H-O-H angle of 104.5° typically found for water molecules.

CRYSTAL PACKING

The TMAFEN complex crystallises in a column type arrangement in space group $P2_1$. The complexes pack in a head-to-tail arrangement along the *a*-axis. The columns are then arranged anti-parallel to one another along both the *b*- and *c*-axes. The inter-host interactions listed in Table 4.11 show the three non-classical hydrogen bonds that stabilise the close interaction of the columns. The anti-parallel columns are shown in Figure 4.24. The aromatic and phosphorothioate moieties of the fenthion guest molecule are located in interstitial spaces due to the diminutive size of the TRIMEA cavity; this is shown in the stereo diagram Figure 4.25.

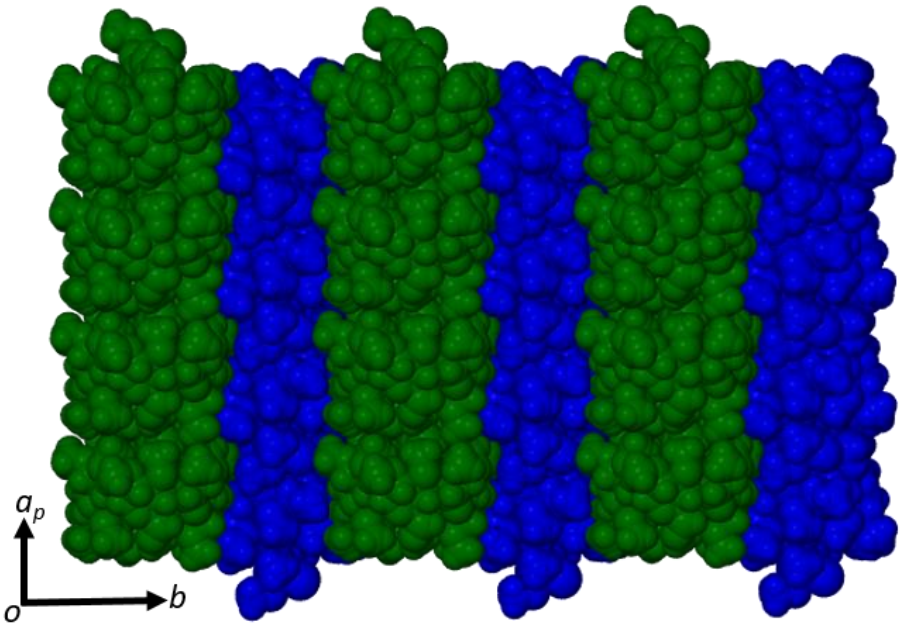

Figure 4.24: Packing diagram down the c-axis showing the anti-parallel columns of TMAFEN

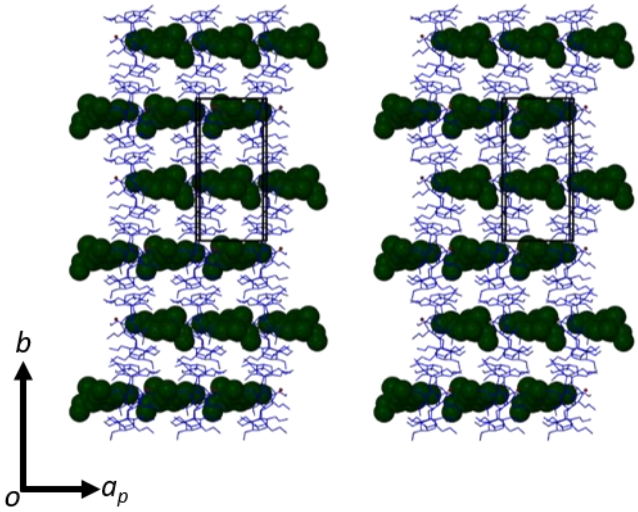

Figure 4.25: Stereo diagram illustrating the arrangement of the phosphorothioate moiety of fenthion in the interstitial spaces between TRIMEA molecules

COMPARATIVE PXRD

The PXRD trace (Figure 4.26) for the bulk sample shows good agreement with the pattern calculated from the refined X-ray crystal structure of the complex. The slight differences in the 2θ angles result from the powder diffraction pattern having been collected at room temperature while the single crystal intensity data were collected at 173(2) K. When the crystal is cooled there are angular shifts in peak positions, most likely resulting from anisotropic contraction of the unit cell.

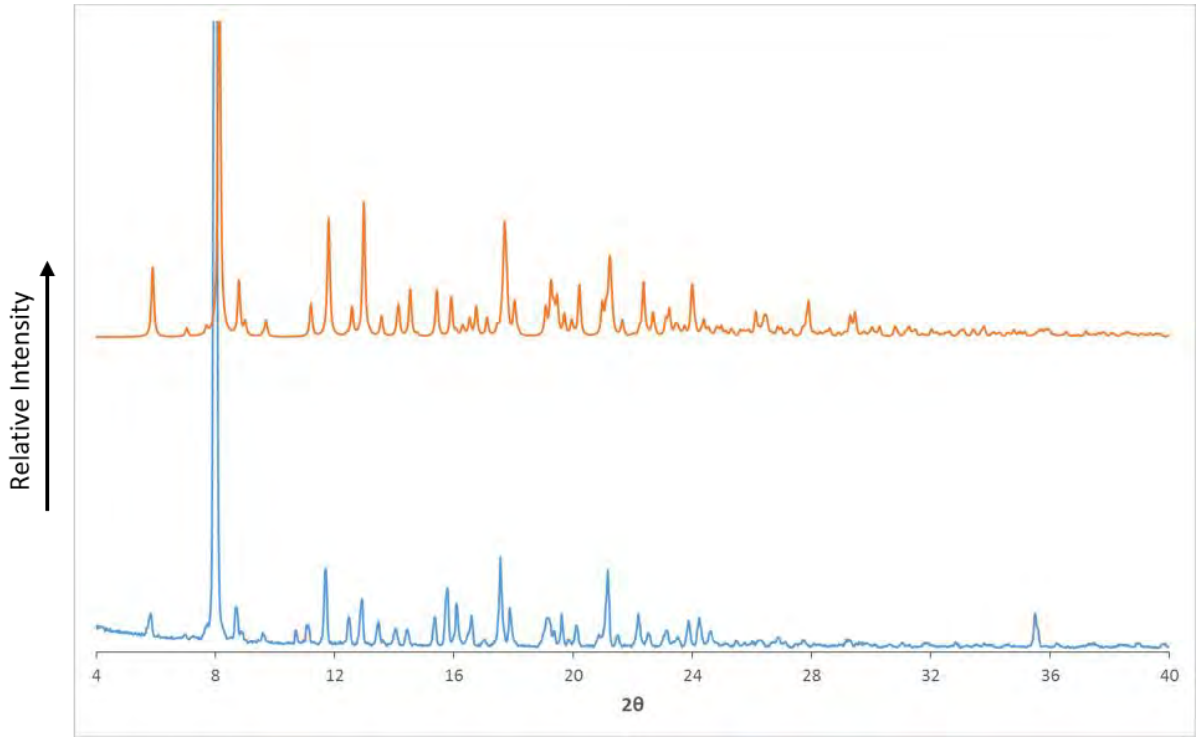

Figure 4.26: The PXRD trace recorded for the bulk sample (blue) and the computed PXRD pattern based on the single crystal X-ray structure of TMAFEN (orange)

TRIMEB/FENTHION

COMPLEX PREPARATION

The complex TMBFEN was prepared *via* a co-precipitation experiment. To perform this, TRIMEB (118 mg; 0.0826 mmol) was weighed into a vial and dissolved in 3 cm^3 MilliQ water. This solution was cooled to 4 °C and a drop of fenthion (23 mg; 0.0826 mmol) was added to the solution and stirred for several hours. The solution was then heated to 40 °C and stirred for another hour. The solution was then cycled several times between 4 °C and 40 °C for half an hour in an attempt to determine the point at which the largest amount of the complex was in solution. At this point the solution was filtered into a clean vial through a 0.45 µm nylon filter. This was then left to crystallise in a 60 °C oven and plate-like crystals were obtained after four days.

ASSESSMENT OF STOICHIOMETRY

The stoichiometry of the complex was confirmed by thermal analysis. The TGA trace (Figure 4.27) showed a mass loss of 15.9 ± 0.7 % (n = 2) from 122.3 ± 0.9 °C to 217.2 ± 0.5 °C. This equated to a host-guest ratio of 1:1 (calculated mass loss = 16.3 %). No solvent loss was observed for this complex indicating that there is no water present in the complex.

THERMAL ANALYSIS

In the TGA trace, no mass loss occurs until 122.3 ± 0.9°C (n = 2) indicating that there is no water present in the structure. The DSC trace also shows no thermal events over this range. At 152.4 ± 0.1 °C (n = 2) there is the onset of a melting endotherm in the DSC that coincides with a 15.9 ± 0.7 % (n = 2) mass loss in the TGA. This mass loss correlates with the loss of fenthion from a 1:1 complex. This would imply that upon melting, the fenthion guest is released from the complex. There is no other thermal event over the range of the DSC trace. In the TGA trace, there is a large mass loss indicative of decomposition starting at 299.6 ± 5.0 °C. The same behaviour can be seen in the HSM images (Figure 4.28).

The hot stage micrographs show the melt onset at 144 °C and the complex is completely melted at 155 °C, which corroborates the interpretation of the TGA and DSC traces.

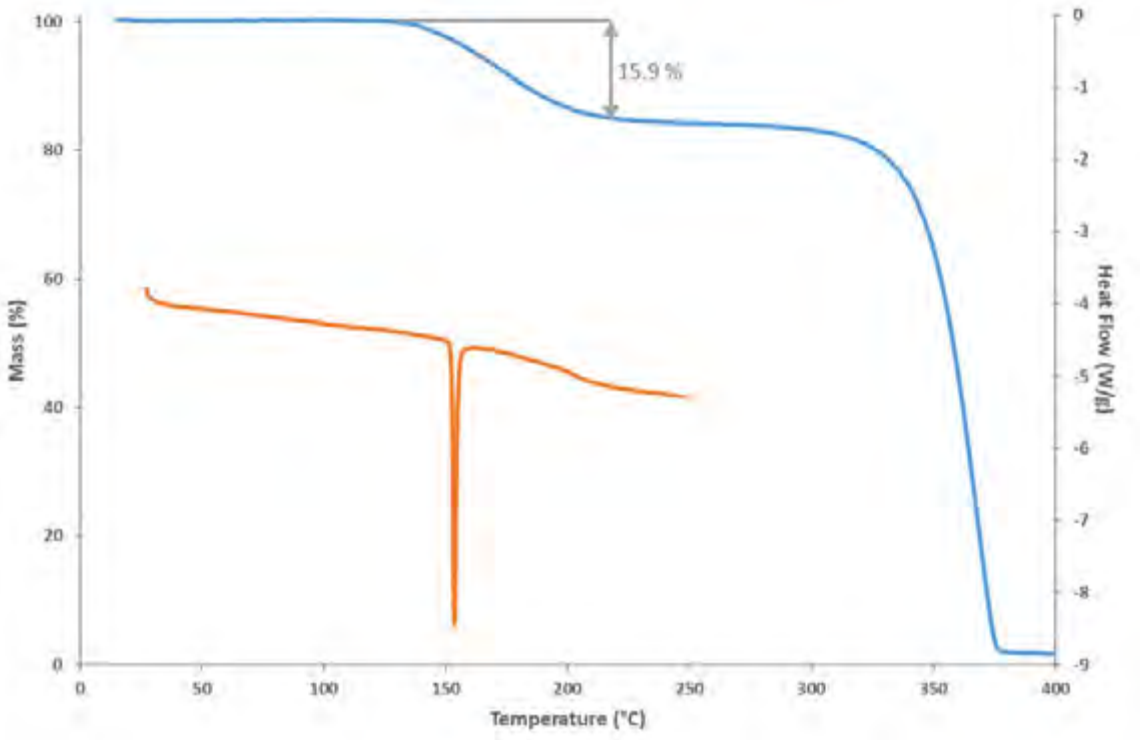

Figure 4.27: Representative TGA (blue) and DSC (orange) traces for TMBFEN

Figure 4.28: Hot stage micrographs showing the TMBFEN complex at various stages of heating

CRYSTAL STRUCTURE ANALYSIS

DATA COLLECTION AND SPACE GROUP DETERMINATION

The intensity data were collected on a Bruker Kappa Apex II DUO diffractometer. It was found that the crystal system is orthorhombic, as indicated by the *mmm* Laue symmetry of the X-ray diffraction pattern. Systematic absences were investigated and the space group was identified as $P2_12_12_1$. The conditions limiting reflection were *hkl:* none, *h00: h = 2n, 0k0: k = 2n, 00l: l = 2n* confirming the assignment. The asymmetric unit contains a 1:1 TMBFEN complex.

STRUCTURE SOLUTION AND REFINEMENT

The software program SAINT[7] was used in data reduction and unit cell refinement. Absorption corrections were performed using the multi-scan method employed by SADABS.[12] The asymmetric unit of TMBFEN is made up of one host molecule and one fenthion molecule. No water molecules are present in the structure. The position of the host atoms was determined using the isomorphous replacement method.[8] A search of the CSD[9] resulted in twelve isostructural TRIMEB inclusion complexes. The complex of TRIMEB with *p*-iodophenol (refcode: CAMPIP)[9,15] was deemed the most suitable due to the similarities in the host atomic co-ordinates and unit cell parameters ($|\Delta a|$ = 0.0873 Å, $|\Delta b|$ = 0.203 Å, $|\Delta c|$ = 0.714 Å). The O6, C7, C8 and C9 atoms of each subunit were not included in the trial model, as these residues are flexible within structures. The glucopyranose subunits were labelled using the notation G1 - G7. Two groups are disordered in the host structure, namely the C9G3 and C7G6 methyl groups. They are disordered over two positions and were assigned *s.o.f.s* of *x* for the major component and *1-x,* where *x* is linked to a free variable. The values of *x* refined to 0.66(3) and 0.52(5) for C9G3 and C7G6 respectively. The hydrogen atoms were placed in idealised positions using a riding model. The isotropic temperature factors were 1.2 - 1.5 times those of the parent atoms. All ordered non-hydrogen atoms were treated anisotropically. The data were collected at 100 ± 2 K. The crystallographic data for the TMBFEN complex are presented in Table 4.12.

Table 4.12: Crystallographic data and data-collection parameters for TMBFEN

Chemical formula	$C_{63}H_{112}O_{35}{\cdot}C_{10}H_{15}O_3PS_2$
Molar mass (g mol^{-1})	1707.83
Crystal system	Orthorhombic
Space group	$P2_12_12_1$
Unit cell parameters	
a (Å)	15.084(2)
b (Å)	21.164(3)
c (Å)	27.491(3)
α = β = γ (°)	90.0
Volume (Å^3)	8776.5(18)
Z	4
Density$_{calcd}$ (g cm^{-3})	1.292
μ [MoKα] (mm^{-1})	0.165
F (000)	3664
Temperature (K)	100(2)
Crystal size (mm)	0.298 × 0.12 × 0.054
Range scanned θ (°)	1.5 ≤ θ ≤ 25.1
Index ranges	h: -9, 17; k: -25, 25; l: -32, 32
ϕ and ω scan angle (°)	0.50
Dx (mm)	50
Total number of reflections	73 047
Number of independent reflections	15 526
Number of reflections with I > 2σ(I)	11 248
R_{int}	0.075
R_1 [I > 2σ(I)]	0.0530
wR_2	0.1190
S	1.013
Number of parameters	1 052
Number of reflections omitted	11
Parameters a, b in	a = 0.0686; b = 3.8356
w = 1/[σ^2(F_0^2)+(aP)^2+(bP)]	
$(\delta/\sigma)_{mean}$	<0.001
Δρ excursions (e Å^{-3})	-0.61, 0.62

MODELLING OF THE FENTHION GUEST MOLECULE

After initial refinement of the trial model and assignment of the remaining host atoms, several large electron density peaks were observed in the cyclodextrin cavity. These were assigned as the guest atoms. After their identification in the Fourier difference map hydrogen atoms were placed in idealised positions with temperature factors 1.2-1.5 those of the parent atoms. No disorder was observed in the guest structure and no restraints were required during refinement. All non-hydrogen atoms were treated anisotropically for fenthion.

GEOMETRIC ANALYSIS OF TMBFEN

The asymmetric unit of TMBFEN comprises one TRIMEB molecule with a fenthion molecule included in the host molecule. The asymmetric unit can be seen in Figure 4.29. The numbering schemes of the host and guest are presented in Figure 4.30.

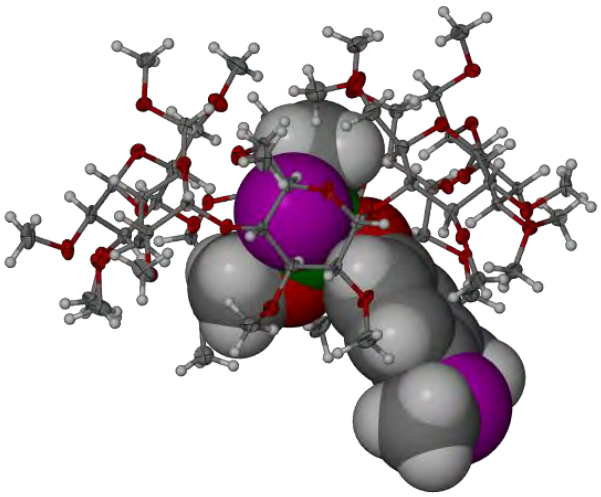

Figure 4.29: The asymmetric unit of the complex TMBFEN. Thermal ellipsoids for the host atoms are drawn at the 50% probability level and the guest atoms are drawn in space-filling mode.

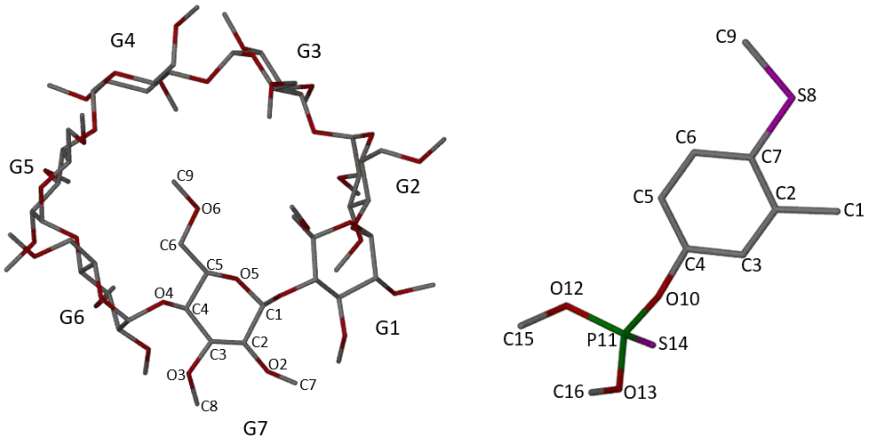

Figure 4.30: Numbering scheme of the glucopyranose rings (left) and the guest molecule (right)

HOST CONFORMATION

The torsion angles, ω, of the primary methoxy groups G3, G5 and G7 show that they are directed towards the cavity of the cyclodextrin. The remaining primary methoxy groups are directed outwards. The groups that are positioned towards the centre of the cavity create a 'lid' at the primary end of the cavity. This closes off this side of the cyclodextrin. This 'lid' conformation is evident in Figure 4.31c.

Table 4.13: Torsion angles (ω) for TMBFEN

Glucose Residue	ω (°)‡
G1	-73.0
G2	-79.4
G3	70.1
G4	-72.4
G5	73.1
G6	-67.1
G7	70.4

‡*Mean e.s.d. 0.5°*

In a manner analogous to the TMAFEN structure, the secondary methoxy groups alternate their orientation towards and away from the cyclodextrin cavity: the O2Gn-C7Gn groups are all directed away from the cavity while the O3Gn-C8Gn groups are directed towards the cavity. This alternating arrangement most likely occurs to minimise the steric hindrance between the large methyl groups. The tilt angles, τ_2, are distributed over a large range to further compensate for this steric hindrance.

The geometric parameters of the TMBFEN inclusion complex are presented in Table 4.14. As can be seen from the large range of tilt angles ($12.7° \leq \tau_2 \leq 42.8°$) the cyclodextrin is in a distorted, saddle-like conformation. This is further shown by the large deviations of the O4 atoms from the O4n mean plane ($|0.007|$ Å $\leq \alpha \leq |0.567|$ Å) and the large torsion angles involving the O4 atoms ($-21.4° \leq d \leq 23.9°$).

A search of the CSD[9] showed that this structure is isostructural with twelve TRIMEB inclusion complexes, and is most similar to the inclusion complex of TRIMEB with fenitrothion[5,6].

There are three known structures of uncomplexed TRIMEB hydrates (CSD refcodes: HEZWAK,[9,16] WAGLOG[9,17] and WAGLUM[9,17]). WAGLOG ($TRIMEB \cdot 3H_2O$) has been selected for the principal comparison with TMBFEN as these cyclodextrins have similar geometric parameters, as shown in Tables 4.14 and 4.15.

The WAGLOG and TMBFEN host molecules show relatively little difference between their geometric parameters. The tilt angles of the two TRIMEB molecules show similar ranges where TRIMEB in TMBFEN has τ_2 angles ranging from 12.9° to 42.8°, while the range in WAGLOG is somewhat larger, from 4.3° to 66.5°. The difference is likely due to the inclusion of fenthion limiting the ability of the glucopyranose subunits to tilt to the same extent as in the hydrated structure. The 'round' shape of the TRIMEB cavities is only slightly distorted as evidenced by the relatively small range of parameter *l* (TMBFEN: 4.666 Å ≤ *l* ≤ 5.211 Å and WAGLOG: 4.673 Å ≤ *l* ≤ 5.485 Å). The distortion is less pronounced in the TMBFEN inclusion complex than in WAGLOG.

The other TRIMEB hydrates show much greater distortion from the 'round' shape of the cyclodextrin cavity, especially HEZWAK (HEZWAK: 3.933 Å ≤ *l* ≤ 5.947 Å and WAGLUM: 4.591 Å ≤ *l* ≤ 5.496 Å). The vastly different conformation of HEZWAK, having a glucopyranose ring in the $^4C_1$ arrangement, gives rise to the large differences in geometric parameters to the other TRIMEB structures. All three of the TRIMEB hydrates show varying degrees of 'self-inclusion', not present in the TMBFEN structure.

Table 4.14: Geometric parameters of TMBFEN

Residue	l (Å)	D (Å)	Φ (°)	d (°)	α[a] (Å)	D_3[b] (Å)	τ_2[c] (°)
G1	5.174	4.421	124.0	0.6	0.567	3.817	36.4
G2	5.163	4.429	131.9	-21.4	-0.321	3.476	12.7
G3	4.826	4.289	129.3	4.2	-0.355	3.246	34.5
G4	4.911	4.479	124.0	19.6	0.408	3.098	28.5
G5	5.211	4.268	123.6	-12.9	0.237	3.395	16.5
G6	5.081	4.508	137.9	-17.2	-0.529	3.458	12.9
G7	4.666	4.258	121.1	23.9	-0.007	3.347	42.8

[a] mean e.s.d.: 0.002 Å; [b] mean e.s.d.: 0.005 Å; [c] mean e.s.d.: 0.1°

Table 4.15: Geometric parameters of TRIMEB·(3H_2O) (refcode: WAGLOG)[9,17]

Residue	l (Å)	D (Å)	Φ (°)	d (°)	α (Å)	D_3 (Å)	τ_2 (°)
G1	4.722	4.413	112.4	3.1	0.799	4.059	42.5
G2	5.485	4.243	135.5	-29.3	-0.369	3.605	9.1
G3	4.808	4.468	126.7	11.3	-0.467	3.318	43.1
G4	4.818	4.420	129.5	10.1	0.484	3.184	27.5
G5	5.037	4.433	117.6	2.7	0.178	3.406	17.1
G6	5.364	4.171	135.3	-39.5	-0.448	3.872	4.3
G7	4.673	4.548	129.5	36.0	-0.178	3.395	66.5

The e.s.d.s were not available from the publication[17]

GUEST INCLUSION

The phosphorothioate moiety of fenthion is deeply embedded within the cyclodextrin cavity. The thiomethyl and methyl substituents of fenthion protrude beyond the secondary rim of the TRIMEB cavity.

The inclusion of fenthion slightly distorts the cyclodextrin from the uncomplexed conformation as seen in the change in the G6 tilt angle. In the inclusion complex the glucopyranose ring is tilted further outwards from the cavity when fenthion is included in the structure. The lack of stabilisation from traditional hydrogen bonding allows the distortions to occur more easily than in the parent β-cyclodextrin host molecule. The mode of inclusion is depicted in Figure 4.31.

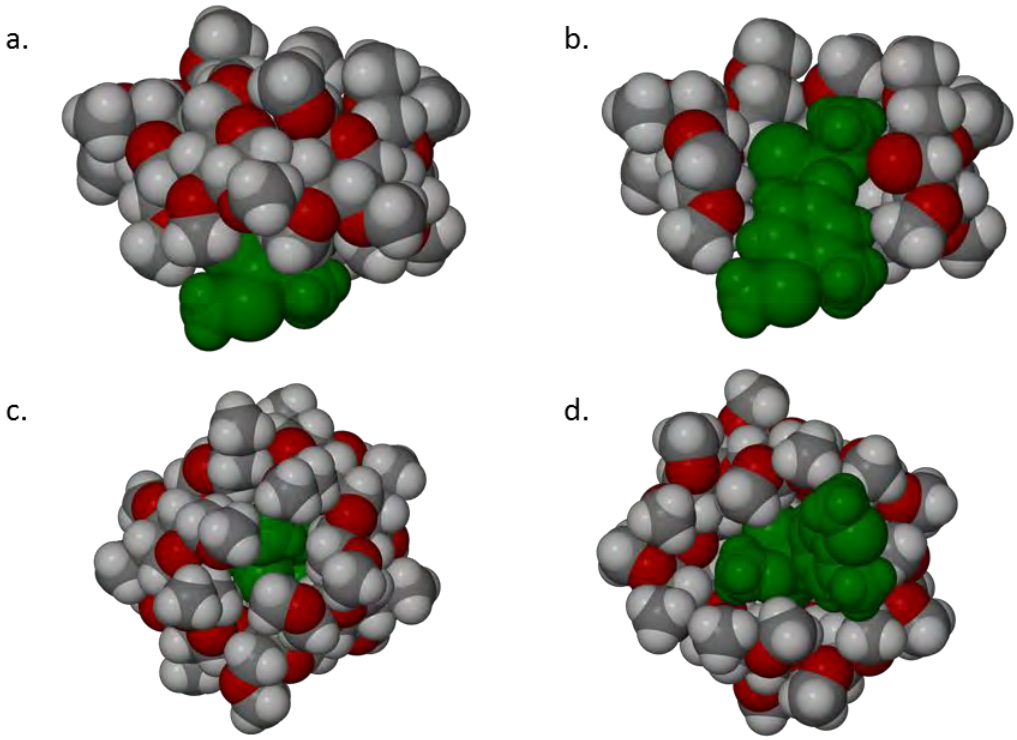

Figure 4.31: Figures showing the inclusion of fenthion in the cyclodextrin cavity. a. protrusion of the thiomethyl moiety from the cavity, b. cut-away cyclodextrin showing the depth of penetration of fenthion, c. view from the primary rim and d. view from the secondary rim

INTRA- AND INTERMOLECULAR INTERACTIONS

The complex TMBFEN does not contain any classical hydrogen bond donors. As a result, weak hydrogen bonds and van der Waals forces are the only intra- and intermolecular interactions in the structure. The cyclodextrin host molecule is stabilised by twenty weak hydrogen bonds. Many of these interactions serve to stabilise the severe tilt angles that occur in TRIMEB inclusion complexes. Four of these occur between C6Gn and O5G(n-1) atoms with a donor to acceptor distance ranging from 3.128(6) Å to 3.194(6) Å. The other major stabilising interactions are the C5Gn-H···O4G(n+1) with D···A distances from 2.772(6) Å to 2.832(6) Å.

There is one intramolecular interaction present within the fenthion guest molecule. This takes place between the C15-H and S14 atoms with the following hydrogen bonding parameters: D···A: 3.329(9) Å, D-H···A: 116°.

There are four host-host interactions, which are listed in Table 4.16. These occur between symmetry-related complex units and aid in stabilising the crystal packing arrangement. There are no hydrogen bonding interactions between the host and guest molecules in the TMBFEN inclusion complex.

Table 4.16: Hydrogen bonding interactions in TMBFEN

Type	Interaction	D···A (Å)	D-H···A (°)	Symmetry Operator
Host-Host	C2G4-H···O6G1	3.383(6)	150	*(3/2-x, 1-y, 1/2+z)*
	C9G1-H···O3G4	3.198(7)	124	*(3/2-x, 1-y, 1/2+z)*
	C9G2-H···O3G7	3.138(8)	120	*(1+x, y, z)*
	C9G4-H···O3G1	3.310(7)	130	*(3/2-x, 1-y, 1/2+z)*

CRYSTAL PACKING

The complex TMBFEN packs in the screw-channel mode. The columns formed comprise monomeric complex units arranged in a head-to-tail manner along the *b*-axis. The O4n least-squares planes of successive TRIMEB molecules are inclined at 9.0° and the O4n centroids are offset by 3.8 Å. The channel that arises is undulating rather than linear due to this incline and offset. The columns pack in an anti-parallel arrangement arising from the 2_1-axes parallel to the crystal *a*- and *c*-axes as shown in Figure 4.32. The columns interact *via* weak hydrogen bonding as outlined in the section on Intra- and Intermolecular Interactions.

Fenthion is deeply embedded in the cyclodextrin cavity, residing close to the 'lid' formed by the primary methoxy substituents. The fenthion molecule is larger than the cyclodextrin cavity and therefore can only be partially included in the cavity. Thus, the thiomethyl moiety of fenthion is

nested in the interstitial spaces created by the arrangement of the host molecules, as can be seen in Figure 4.33.

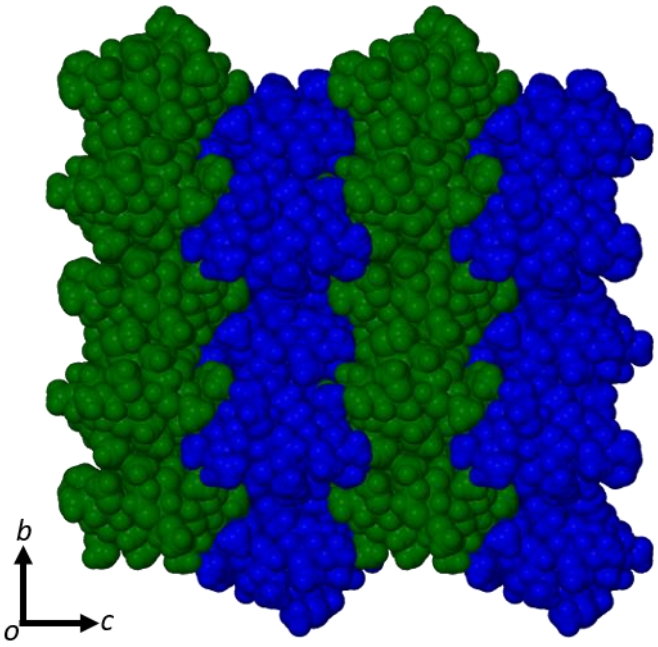

Figure 4.32: Packing of the TMBFEN complex viewed along [1 0 0] highlighting the anti-parallel column arrangement

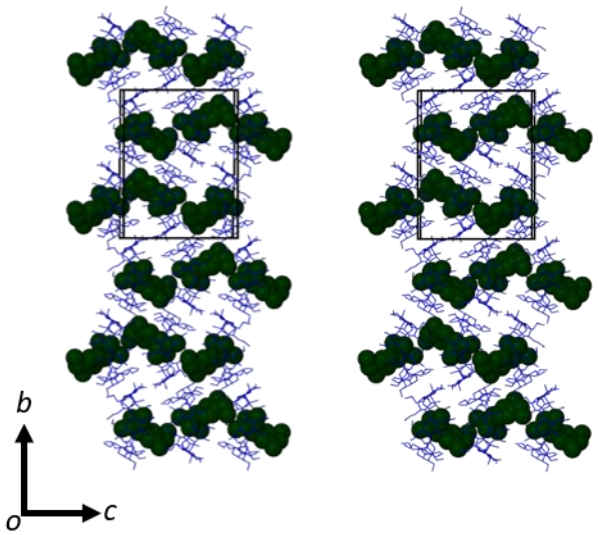

Figure 4.33: Stereo diagram illustrating the arrangement of the thioester moiety of fenthion in the interstitial spaces between TRIMEB molecules

COMPARATIVE PXRD

The PXRD trace (Figure 4.34) calculated from the refined X-ray crystal structure of TMBFEN shows good agreement with the experimental pattern of the bulk samples of the complex. The slight differences in the 2θ peak locations result from the single crystal intensity data having been collected at low temperature, while the powder diffraction data were collected at room temperature. Cooling the sample for single crystal intensity data collection results in an angular shift in the peak positions, most likely due to anisotropic contraction of the unit cell.

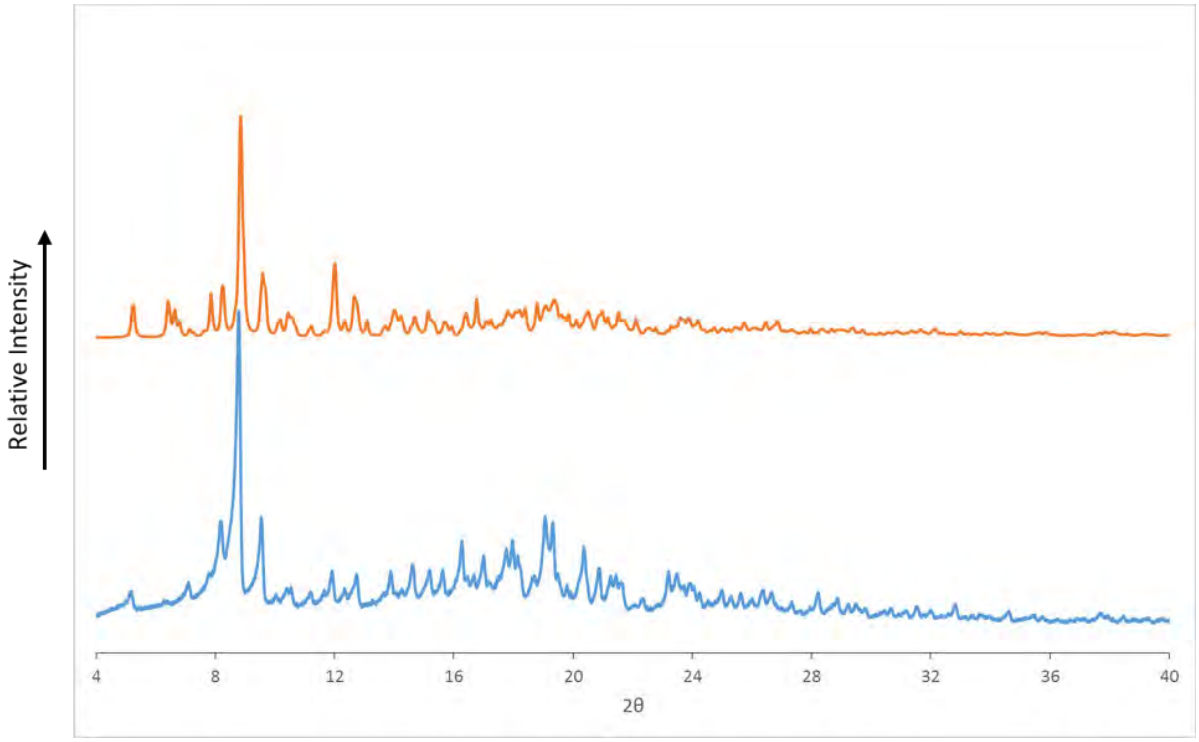

Figure 4.34: The PXRD trace recorded for the bulk sample (blue) and the computed PXRD pattern based on the single crystal X-ray structure of TMBFEN (orange)

In the section describing the structure solution and refinement, the choice of the complex CAMPIP[9,15] for isomorphous replacement was outlined. The differences in the unit cell parameters of CAMPIP and TMBFEN are within reasonable limits for isomorphous replacement ($|\Delta a|$ = 0.0873 Å, $|\Delta b|$ = 0.203 Å, $|\Delta c|$ = 0.714 Å). The backbones of the TRIMEB molecules occupy similar atomic co-ordinates, as shown in Figure 4.35. The differences in the atomic co-ordinates were not significant enough to cause any issues in structure refinement. The packing arrangements of the two complexes are similar, as shown in Figure 4.36. Differences arise in atomic co-ordinates during packing due to the differences in unit cell parameters.

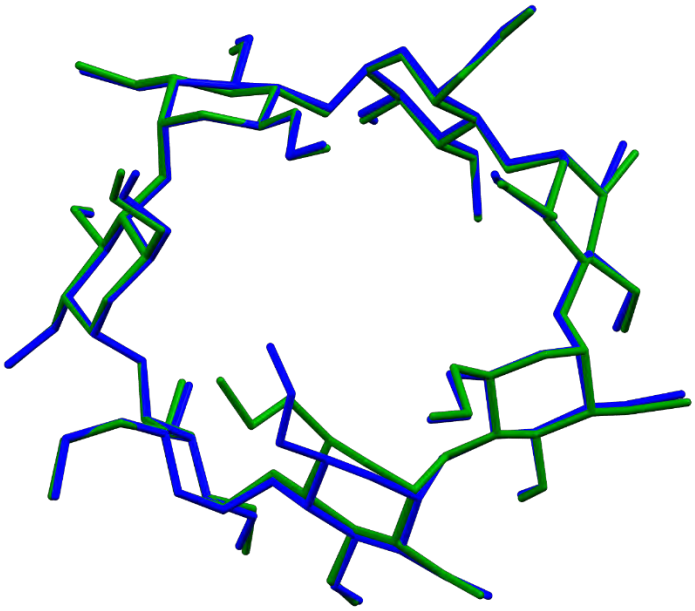

Figure 4.35: Overlay of CAMPIP (green) and TMBFEN (blue) host molecules

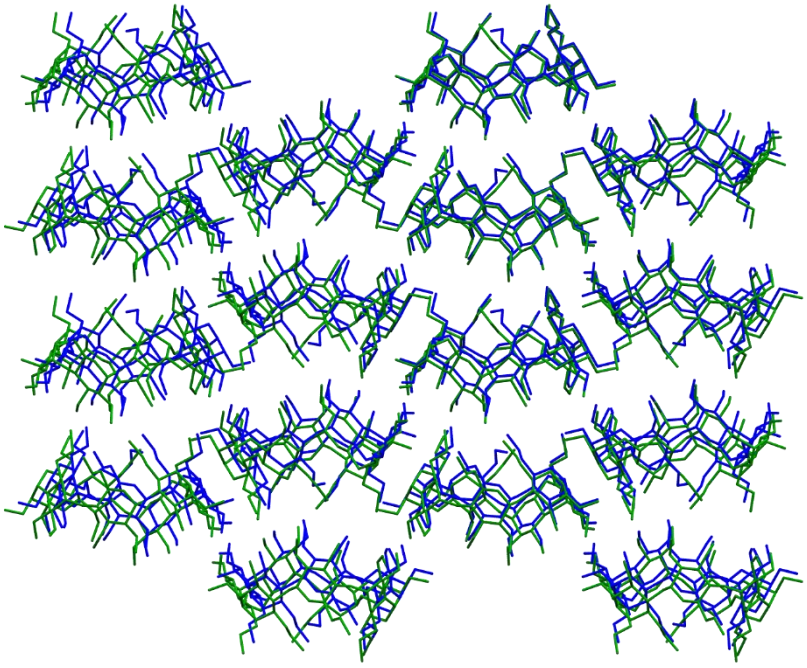

Figure 4.36: Overlay of packed CAMPIP (green) host and TMBFEN (blue) host molecules viewed along the [1 0 0] direction

THERMOGRAVIMETRIC ASSESSMENT OF KINETIC PARAMETERS FOR COMPLEX DISSOCIATION

The complex TMBFEN was presented in a journal article by Cruickshank *et al*. (including the author of the present thesis as a co-author) based on a study performed in the Centre for Supramolecular Chemistry Research (UCT).[5] The complex is isostructural with two other TRIMEB complexes presented in the same paper [TRIMEB/fenitrothion (TMBFENT) and TRIMEB/acetochlor (TMBACE)]. The structural similarities among the three complexes are illustrated in the stereo diagrams viewed from a common direction in Figure 4.37.

The inclusion of the phosphorothioate moiety in TMBFENT and TMBFEN occurs in a similar manner. This moiety is deeply embedded in each of these complexes positioned close to several methoxy groups at the primary rim. The location of the aromatic portions of fenitrothion and fenthion are similar in their respective TRIMEB complexes. In the TMBACE complex the guest positioning is different whereby the aromatic moiety is fully encapsulated by the host molecule.

The TGA traces of the three complexes all display two-step mass losses where the first corresponds to the loss of a single guest molecule being released from the inclusion complex. The second mass loss is attributed to host decomposition. The DSC traces show that the guest loss and fusion of the complex partially overlap with the loss of the guest beginning before the fusion event.

The kinetics of guest loss upon heating was investigated by isothermal and non-isothermal methods for these three complexes. The isothermal results were used to determine the mechanism of guest release, while both methods were used to determine the activation energies of guest loss for each of the complexes. The kinetics results are explained in further detail below.

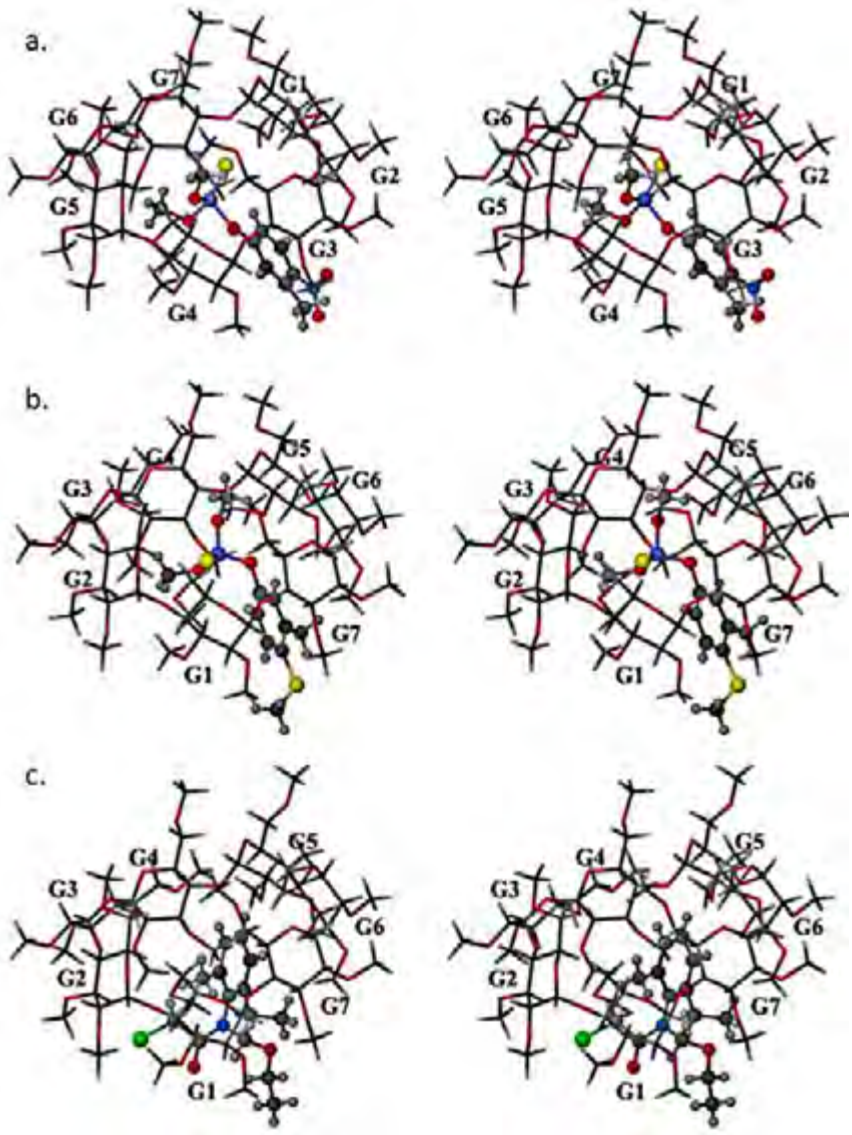

Figure 4.37: Stereoviews of the complexes a. TMBFENT, b. TMBFEN and c. TMBACE with host residue numbering to illustrate structural similarities. Reproduced from Cruickshank et al. (2013).[5]

ISOTHERMAL METHOD

The kinetics of a solid-state process at a constant temperature is represented by two expressions:

Expression 4.1:

$$\frac{\delta\alpha}{\delta t} = kf(\alpha)$$

Expression 4.2:

$$g(\alpha) = kt$$

In these expressions, α is the fractional mass loss $[(m_t - m_0)/(m_\infty - m_0)]$ at reaction time *t*, *k* is the rate constant and $f(\alpha)$ and $g(\alpha)$ are functions describing the reaction mechanism.

In solid-state kinetics it is common that more than one model can be used to describe a particular process. The F1 model, based on the apparent order of a reaction in solution, does not have the same significance in the solid-state. The mechanism of first-order reactions in the solid-state involves random nucleation and growth of such sites that does not extend beyond individual crystallite nucleation sites. The activation energies presented in Table 4.17, obtained from this model for the three complexes, are not statistically different, suggesting that the kinetics of melting and guest release is not dependent on the complex structure.

The second model is the 3D model, which applies to diffusion-limited reactions that take place at a phase interface between TRIMEB and the inclusion complex. As the guest dissociates it diffuses towards the crystal surface and then desorbs from the surface. Using this model one can conclude that the guest release kinetics are dependent on the physical properties or structure of the complexes. This was deduced from the statistically different activation energies of the three complexes (Table 4.17).

Table 4.17: Activation energies determined from isothermal experiments for the TRIMEB/guest complexes

Complex	**Activation Energy (kJ mol^{-1})**	
	F1	**3D**
TMBFENT	126 ± 4	114 ± 1
TMBFEN	129 ± 10	109 ± 9
TMBACE	130 ± 13	86 ± 8

The process under study is complicated as there are two simultaneous events occurring, *viz.* complex fusion and guest loss. Even with these complications, the 3D diffusion model appears to

be a reasonable one as it is consistent with the crystal packing arrangements of the complexes. The guest molecules are isolated from one another and there are no directional constraints on their diffusion.

NON-ISOTHERMAL METHOD

The method developed by Ozawa, Flynn and Wall[18,19] was modified to obtain activation energies to compare with those determined *via* the isothermal technique. This is a model-free isoconversional method.

Expression 4.3:

$$\log \beta_\alpha = \log \frac{A_\alpha E_{a\alpha}}{g(\alpha)R} - 2.315 - 0.457 \frac{E_{a\alpha}}{RT_\alpha}$$

In Expression 4.3, β_α is the heating rate, $E_{a\alpha}$ is the activation energy, T_α is the temperature at each conversion level and $g(\alpha)$ is the kinetic model employed. By plotting $\log(\beta_\alpha)$ versus the reciprocal temperature the activation energy could be calculated from the slope of the plot. The activation energies for each complex at a given conversion level are presented in Table 4.18.

Table 4.18: Activation energies obtained at specific conversion levels for the three inclusion complexes

Conversion level (%)	**Activation Energy (kJ mol^{-1})**		
	TMBFENT	**TMBFEN**	**TMBACE**
8	142.9	130.1	185.5
12	158.2	155.3	157.8
16	167.7	160.6	138.0
20	166.8	150.4	123.0
Average	**158 ± 12**	**149 ± 13**	**151 ± 27**

The variation in the activation energies for TMBFENT and TMBFEN shows no trend and the relative errors are less than 10 %. This error is within the conventionally accepted range for isoconversional methods. The decreasing trend in the TMBACE complex activation energies as a function of conversion can be explained by the significantly lower melting point of this complex. Thus the reciprocal temperature values recorded at the 12, 16 and 20 % conversions were lower than the reciprocal fusion temperature of the complex.

FURTHER CONSIDERATIONS RELATING TO THE ABOVE STUDY

There have been several studies investigating the dissociation of a guest molecule from native cyclodextrins. Researchers who investigated the thermal dissociation of benzyl alcohol and cinnamaldehyde from their β-CD inclusion complexes have reported activation energies of 158 and 160 kJ mol^{-1}, respectively.[20,21] The values obtained for the above β-CD complexes are similar to those obtained by the non-isothermal method for TMBFENT, TMBFEN and TMBACE. Furthermore, the guest loss process for these β-CD complexes occurs *via* a diffusion-based mechanism, as proposed for the TRIMEB complex guest losses.

The thermal stabilities of the TMBFENT, TMBFEN and TMBACE complexes assessed in this study show that a relatively high energy barrier exists for the thermal release of these guest molecules from their complexes. This means that the solid-state complexes should remain intact during normal handling and storage of the material. As these pesticides are liquids at room temperature this indicates that their inclusion complexes would be safer to use and easier to transport.

PHASE SOLUBILITY ANALYSIS

Phase solubility analysis is a method to determine the effect of a host compound on the solubility of a guest molecule.

SAMPLE PREPARATION

The phase solubility of fenthion was investigated with five cyclodextrins, namely α-CD, β-CD, γ-CD, hydroxypropyl β-cyclodextrin (HPBCD) and randomly methlylated β-cyclodextrin (RAMEB).

Due to the extremely low aqueous solubility of fenthion,[1] a co-solvent was required. The solvent 1,4-dioxane was determined to be an appropriate medium. Aqueous 2 % (H_2O:dioxane 98:2 v/v) dioxane solutions were found to be sufficient for this study.

Stock solutions of the cyclodextrins were prepared in 2 % dioxane aqueous solutions, then diluted to the desired concentrations and transferred to polytope vials. The vials all contained 5 cm^3 of the cyclodextrin solutions, to which an excess of fenthion was added. The mixtures were stirred at 1000 rpm for 72 hours at a constant temperature of 25 ± 0.5 ℃. Once the mixtures reached equilibrium they were filtered through a 0.45 μm nylon filter. To determine the intrinsic solubility (S_0) of fenthion; a vial was set up in a similar manner, without the cyclodextrin. The absorbance of the filtered solutions were read using UV-Vis spectroscopy. If required, the filtered solutions were diluted to obtain an absorbance between 0.1 and 1. The concentration of fenthion was calculated from the molar absorptivity value obtained from the Beer-Lambert plot.

UV-VISIBLE SPECTROPHOTOMETRY

The calibration curve used to calculate the molar absorptivity of fenthion using the Beer-Lambert law (Expression 4.4) is shown in Figure 4.38.

Expression 4.4

$$A = \varepsilon c l$$

The path length, *l*, was 1 cm; therefore, the expression indicates that the calibration plot is linear. The molar absorptivity, ϵ, is equal to the slope of plot of absorbance versus the fenthion concentration. From the slope it was found that the molar absorptivity is 11838 mol^{-1} dm^3 cm^{-1}.

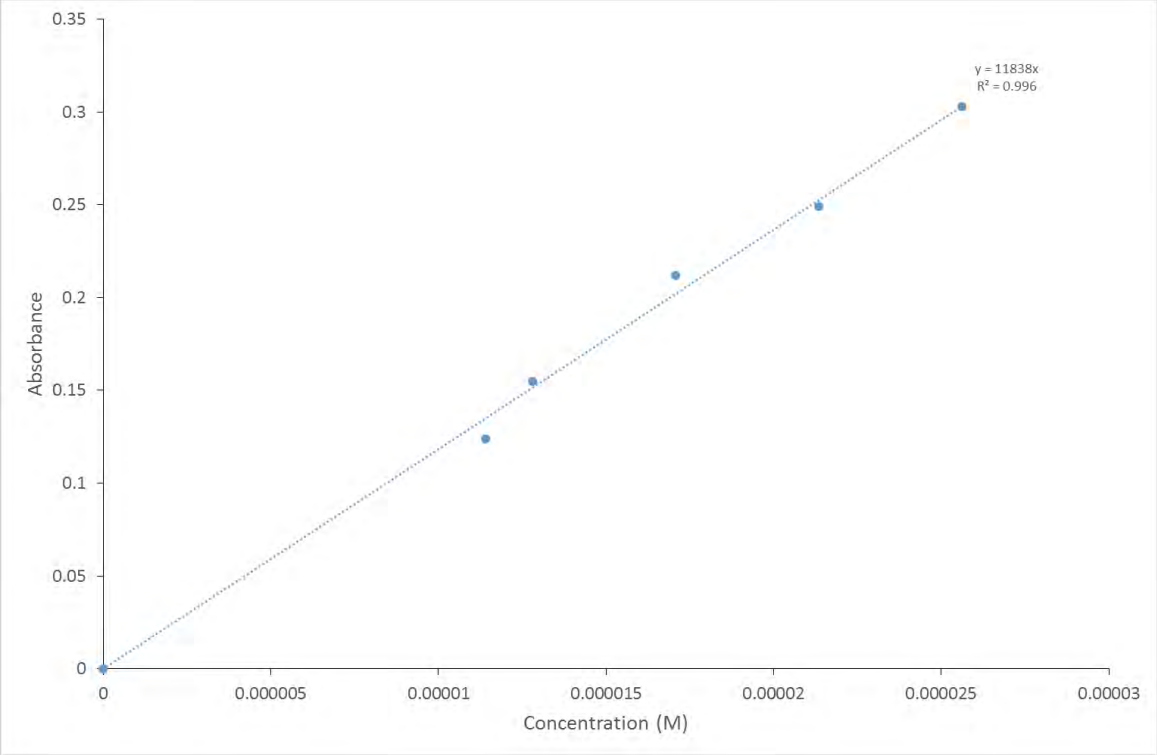

Figure 4.38: Beer-Lambert calibration curve for fenthion in 2% aqueous 1,4-dioxane at 25 °C for λ_{max} = 251.00 nm

PHASE SOLUBILITY

The results of the phase solubility experiments are presented as a function of the apparent solubility of fenthion with increasing cyclodextrin concentration. The profiles are classified as A- or B-type by Higuchi and Connors.[22–24] The profiles described as A-type show linear increases in apparent guest solubility with cyclodextrin concentration. The sub-categories are A_L-, A_P- and A_N-type. The classification A_L-type curves are characterised by linear increases in apparent solubility of the guest while A_P- and A_N-type show deviations from linearity at higher host concentrations. A_P-type plots show a positive deviation while A_N-type show negative deviations, due to changes in the physical nature of the solution. The profiles classified as B-type are the result of formation of partially soluble complexes. There are two B-type sub-categories; B_S and B_L. The B_S-type plot shows an increase in apparent solubility up to a point where the complex precipitates out of solution. The complex formed in B_S-type is generally moderately soluble. In the case of the B_L-type profiles the complex is highly insoluble and precipitates immediately and so there is no initial increase in apparent guest concentration as seen in the B_S-type profile. [22–24]

The experiments of α-CD and γ-CD with fenthion formed insoluble complexes which precipitated out at low cyclodextrin concentrations and were not pursued.

β-CYCLODEXTRIN

A representative phase solubility plot showing the variation in apparent fenthion concentration with increasing β-CD concentration is shown in Figure 4.39. The plot follows B-type behaviour, specifically B_S. This shows an initial linear increase in apparent concentration of fenthion, followed by decrease. The behaviour is most likely due to the BCDFEN complex having low solubility and precipitating at higher β-CD concentrations.[23]

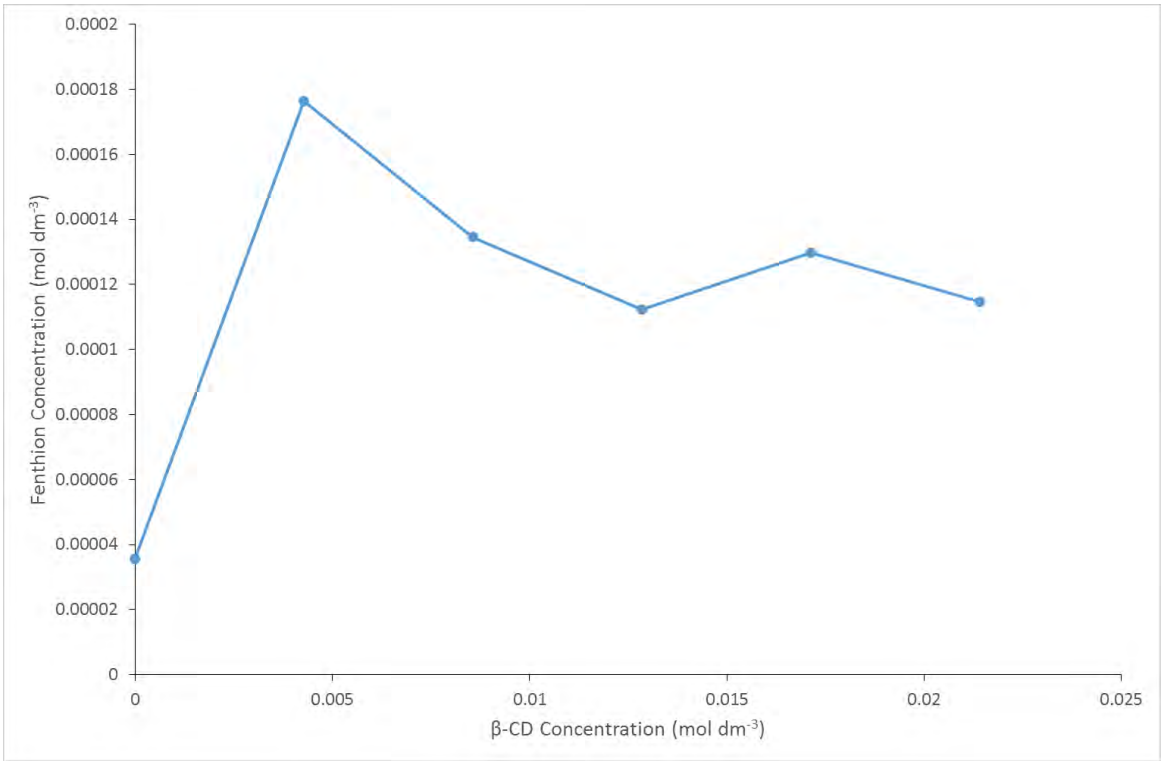

Figure 4.39: Representative phase solubility plot for β-CD with fenthion

From the linear portion of a B_S-type profile it is possible to calculate the binding constant from Expression 4.5 using the initial slope and intrinsic solubility (S_0) measured experimentally.

Expression 4.5:

$$K_{1:1} = \frac{slope}{S_0(1 - slope)}$$

The binding constant for each repeat of the experiment was calculated and the average binding constant was found to be 789 ± 170 M^{-1}. A 5.0-fold increase in the apparent fenthion concentration at a β-CD concentration of 4.3 mM was observed.

HPBCD

The profile of the fenthion phase solubility with HPBCD (Figure 4.40) shows A_N profile. This negative deviation from linearity could be due to several effects. These may be solvent effects altering the bulk properties of the media and/or self-association of the cyclodextrin at high concentrations.[23]

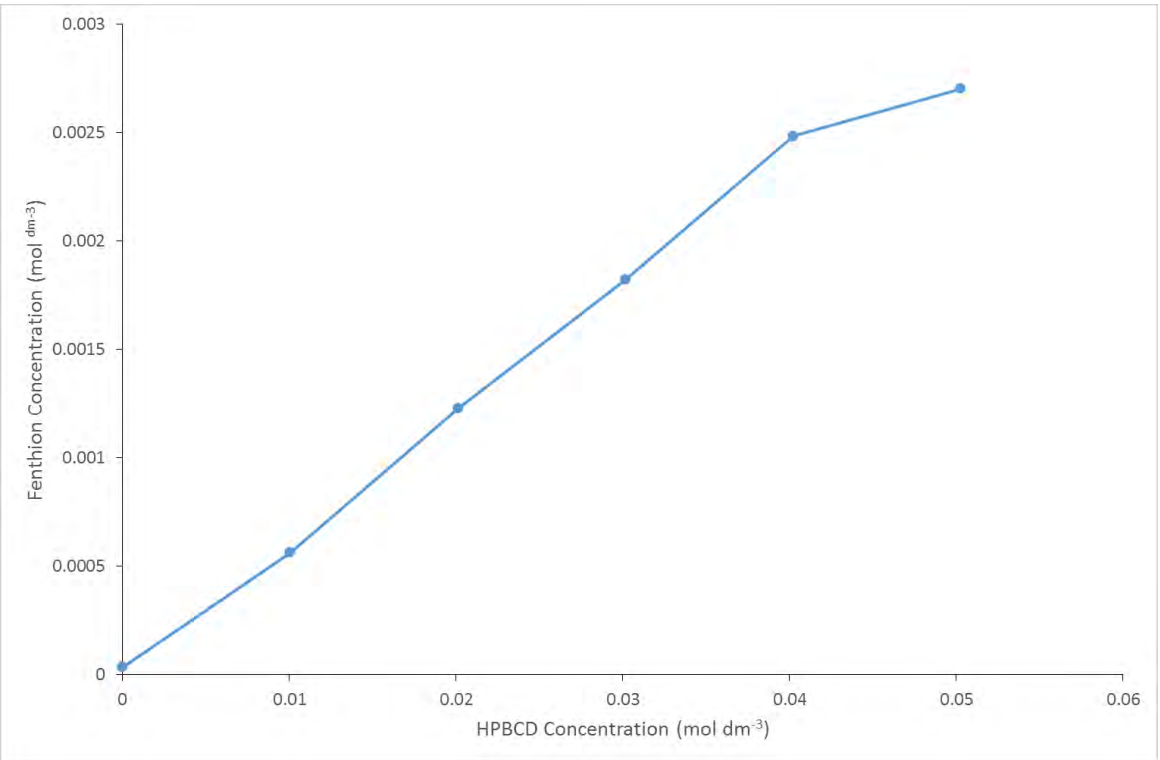

Figure 4.40: Representative phase solubility plot for HPBCD with fenthion

The binding constant for the system could be calculated from Expression 3.5 from the linear portion of the plot. The average binding constant was found to be 1863 ± 26 M^{-1} (n = 2). The binding constants of complexes formed with HPBCD are usually in the order of several thousand M^{-1}. The maximum solubility enhancement due to HPBCD from all experiments was found to be 85.9-fold at a HPBCD concentration of 50.2 mM.

RAMEB

The phase solubility of RAMEB with fenthion was found to follow an A_P profile. This can be seen in Figure 4.41. The positive deviation from linearity suggests the formation of higher order complexes at higher cyclodextrin concentration.[23]

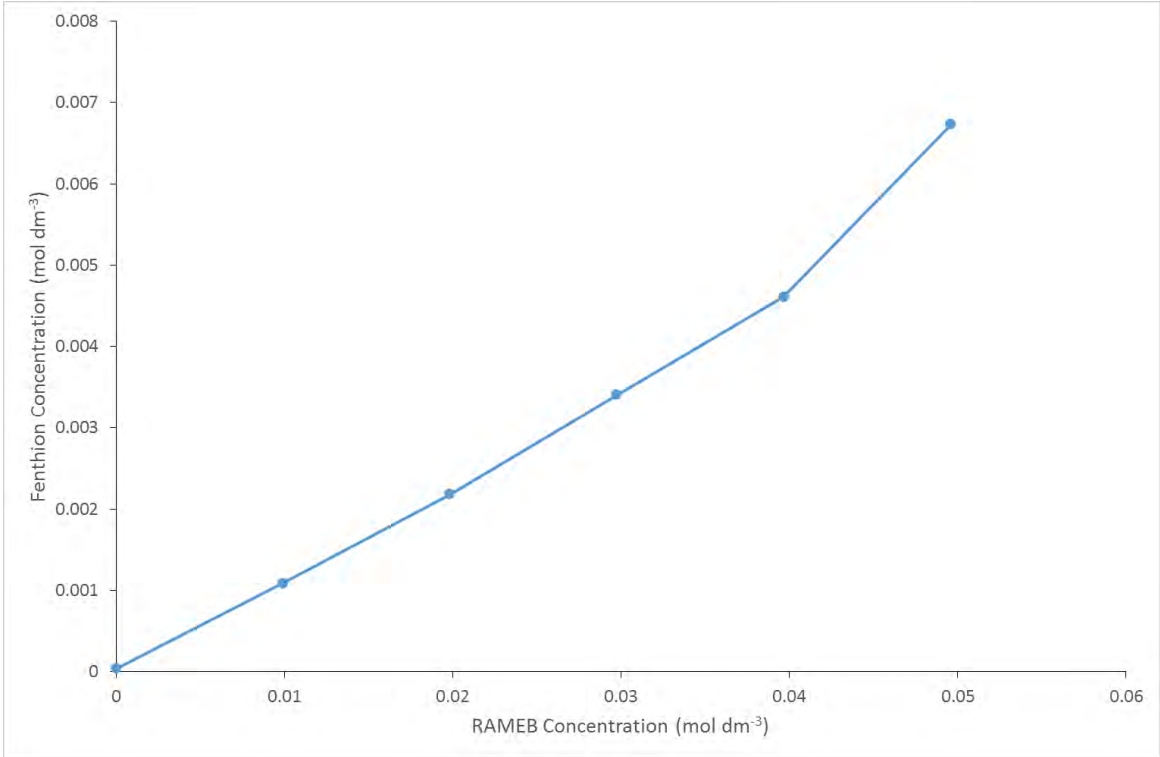

Figure 4.41: Representative phase solubility plot for RAMEB with fenthion

The binding constant was calculated in a similar manner to that of obtained when using HPBCD as host as both systems are of type A. The average binding constant was found to be 3582 ± 106 M^{-1}. It was found that RAMEB increased the apparent solubility of fenthion 189.7-fold at a host concentration of 49.6 mM.

DISCUSSION

INDUCED CIRCULAR DICHROISM

Induced circular dichroism experiments were performed at the Universidad Nacional de Córdoba over the course of two international exchanges. Two sets of experiments were performed, the first with varying concentrations of β-CD to observe changes in the ICD signals due to the cyclodextrin concentrations. The second set was performed with α-CD, β-CD, γ-CD, DIMEB, TRIMEA and TRIMEB to observe differences in the ICD signals with differing cyclodextrins.

The experiments with β-CD showed that fenthion and β-CD interact in solution. The nature of the interaction was assumed to be between the chromophoric moiety of the fenthion molecule and the cyclodextrin cavity. This would indicate that the effect observed in the ICD spectra is a negative Cotton effect. A negative Cotton effect implies that the transition dipole of fenthion is perpendicularly aligned relative to the axis of symmetry of the cyclodextrin cavity. Variations in the absorbance values in the UV-Vis spectra were also observed. These changes further serve to confirm an interaction between fenthion and β-cyclodextrin. These changes were erratic and therefore modelling the stoichiometric ratio in solution was not possible. As the stoichiometric ratio could not be determined it was not possible to confirm the binding constant value between β-CD and fenthion obtained from the phase solubility studies using the ICD technique.

In the experiment performed with the different cyclodextrins it was observed that the ICD profiles were similar. This would imply that the mode of interaction is similar across the cyclodextrins tested. As in the case of β-cyclodextrin above, it would suggest that there is a negative Cotton effect. This indicates that the transition dipole of fenthion is oriented perpendicularly to the axis of symmetry of each of the cyclodextrin cavities.

The differences in the ICD signals with constant fenthion concentration point to a variation in the strength of binding between fenthion and the various cyclodextrins. The relative strengths of interaction, after normalising for cyclodextrin concentration, were found to be:

DIMEB > TRIMEA > TRIMEB > β-CD > γ-CD > α-CD

The same trend has been observed in the complexation of fenitrothion, an analogue of fenthion.[3] The profiles of the ICD signals were similar for α-CD, β-CD, γ-CD and DIMEB, but a different profile was observed for TRIMEA and TRIMEB. These different signals would imply that the modes of interaction are different for fenthion and fenitrothion with TRIMEA and TRIMEB. In the solid-state the complexes TRIMEA with fenitrothion and TMAFEN show different modes of inclusion. TRIMEA/fenitrothion is a complex with a 2:1 host to guest stoichiometric ratio while that of

TMAFEN is 1:1. In the solid-state TMBFEN and TMBFENT are isostructural.[4] This indicates that the modes of association differ in solution.

STOICHIOMETRY AND THERMAL ANALYSIS

The stoichiometries of the BCDFEN and TMAFEN complexes were determined *via* ^{1}H-NMR spectroscopy. The TMBFEN complex stoichiometry was determined by TGA. The BCDFEN complex was found to have a 2:1 stoichiometric ratio and the TMAFEN and TMBFEN complexes a 1:1 ratio.

From the TGA profiles it was determined that BCDFEN and TMAFEN both contain water molecules in their crystal structure. The initial mass loss (14.1 ± 0.7 %) in the BCDFEN TGA trace indicated that the complex contained approximately 24 waters within the asymmetric unit. The protracted mass loss (0.5 ± 0.1 %) in the TMAFEN TGA trace was determined to be due to the presence of 0.4 ± 0.1 of a water molecule in the structure. The TMBFEN complex did not show the presence of any waters of crystallisation in the thermal analysis.

Fenthion occurs as an oil at room temperature, having a melting point of 7.5 °C.[1] The boiling point of fenthion is 90 °C and it is a volatile oil with a vapour pressure of 0.37 mPa at 25 °C.[1] The inclusion in cyclodextrin hosts enables a solid-state formulation of the pesticide. In the BCDFEN and TRIMEA complexes the guest is released only upon decomposition. In TMBFEN the guest is released from 122.3 ± 0.9 °C to 217.2 ± 0.5 °C. It is clear that the thermal stability of fenthion is greatly improved by inclusion in cyclodextrin host molecules. The improvement of the thermal stability and solid formulation would increase the ease of use of the pesticide, as well as facilitating the handling of the product.

CONFORMATIONS OF HOST AND GUEST MOLECULES

In the BCDFEN complex the primary torsion angles, ω, showed that all but one residue (C6A7) point away from the cyclodextrin cavity. The geometric parameters, specifically *l*, *D* and ϕ, of the BCDFEN complex indicate that the host molecules A and B both maintain a 'round' shape. This conformation is maintained by the well-known O2n···H-O3(n+1) hydrogen bonding network at the secondary rim of the cyclodextrins. The tilt angles, τ_2, indicate that the cyclodextrin residues tilt inwards at the primary side. The two independent host molecules are approximately parallel, with their O4n least-squares planes inclined at an angle of 1.0(3)°.

The primary methoxy substituents in the TMAFEN complex form a 'lid' preventing access from this end of the cyclodextrin cavity. This is evident from the torsion angles, ω, where four of the groups are directed towards the centre of the cavity while the G3 and G5 substituents are directed

outwards. The geometric parameters *l*, *D*, and ϕ indicate that the host molecule is slightly distorted into an elliptical conformation. Strong steric repulsion between the secondary methyl groups in TMAFEN causes the glucopyranose subunits to tilt inwards at the primary end. These large tilt angles indicate that the host molecule adopts a 'bowl' configuration.

The torsion angles, ω, of the complex TMBFEN indicate that the primary methoxy groups G3, G5 and G7 are directed towards the cyclodextrin cavity. These three groups form a 'lid' at the primary end of the cavity. The remaining four primary methoxy groups are directed outwards from the cyclodextrin cavity. The O4n atoms of the host molecule, TRIMEB, adopt a 'round' shape and can be seen from the geometric parameters *l*, *D* and ϕ. The tilt angles, τ_2, cover a large range showing that the host molecule adopts a bowl-like configuration. The tilt angles of the trihydrate TRIMEB structure span a larger range that those of TMBFEN.

The conformations of the host molecules of TMAFEN and TMBFEN show several similarities. In both, the primary ends of the cyclodextrin cavities are closed off by the methoxy substituents. The large tilt angles, combined with the primary methoxy groups mean that the hosts have a 'bowl' conformation. The large tilt angles are required to accommodate the steric interference of the methylated secondary substituents. The glucopyranose subunits are able to adopt these large tilt angles as there is no stabilisation from the O2n···H-O3(n+1) hydrogen bonding network that is present in non-derivatised cyclodextrin hosts. The major differences between TMAFEN and TMBFEN occur in the mode of guest inclusion. In TMAFEN, the thioester group of fenthion is included in the cyclodextrin cavity. The phosphorothioate moiety extends into the interstitial spaces between complex subunits. In TMBFEN the mode of inclusion is reversed: the phosphorothioate moiety is in close proximity to the primary end of the cyclodextrin cavity while the thioester group extends beyond the secondary rim of the cyclodextrin into the interstitial spaces between TRIMEB molecules.

The BCDFEN inclusion complex has a very different mode of inclusion to that of TMAFEN and TMBFEN. In BCDFEN the stoichiometry is two β-CD molecules to one fenthion molecule. The fenthion molecule is completely encapsulated within the cyclodextrin dimer. The host molecules both maintain their 'round', symmetrical shape owing to the stabilising presence of the O2n···H-O3(n+1) hydrogen bonding network. These interactions also prevent the glucopyranose subunits tilting inwards.

In two of the inclusion complexes presented here, the fenthion guest is disordered. In BCDFEN the guest is partially disordered over two positions, the two components being rotamers. There are three common atoms in the structure, namely P11, O13 and C16. The rotamer gives rise to an angle of 89.5° between the S14A-P11-S14B atoms in the phosphorothioate groups. In TMAFEN

the whole guest molecule is disordered over two positions. The major and minor components occupy similar atomic co-ordinates and have the same molecular conformation.

INTRA- AND INTERMOLECULAR INTERACTIONS

The three complexes presented here all display various intra- and intermolecular interactions. In the case of the BCDFEN complex there are fourteen O2n···H-O3(n+1) hydrogen bond interactions that maintain the circular shape of the two cyclodextrin molecules. Between the cyclodextrins in the dimer there are four O3An···O3Bn interactions. The dimers interact through sixteen hydrogen bonds. Ten of these are O-H···O hydrogen bonds, with nine linking adjacent dimers within a layer while the remaining interaction is between layers. There are a further six C-H···O weak hydrogen bonds between dimers within layers.

The complexes TMAFEN and TMBFEN both comprise host molecules that are permethylated preventing the formation of classical hydrogen bonds with the hosts. Notably missing is the O2n···H-O3(n+1) hydrogen bonding network found in native and partially methylated cyclodextrins. The TMAFEN complex has sixteen intramolecular host interactions. These interactions are all C-H···O hydrogen bonds with D···A distances ranging from 2.782(4) Å to 3.152(5) Å. The host molecules interact with one another through similar C-H···O hydrogen bonds. The D···A distances for intermolecular host interactions range from 3.315(4) Å to 3.373(4) Å. TMAFEN has one partially occupied water molecule at the primary rim of the cyclodextrin cavity. As the hydrogens could not be modelled the determination of interactions was based on close contact distances, of which there are two. The water molecule interacts with the O6G2 atom of TRIMEA with a close contact distance of 2.89(2) Å. The second interaction is between the water molecule and the minor disorder component of the O6 atom on the G5 residue with a close contact distance of 2.86(3) Å. The angle O6G2-O1W-O6G5 is 102.1(7)°, which is close to the H-O-H angle (104.5°) present in water. The complex TMBFEN has eighteen intramolecular hydrogen bonds, also of the type C-H···O, with donor acceptor distances 2.801(6) Å ≤ D···A ≤ 3.194(6) Å. The intermolecular host interactions are of the same type and there are four such interactions which range from 3.138(8) Å to 3.383(6) Å.

The fenthion molecules in two of the complexes interact with their hosts through various weak molecular interactions. The BCDFEN complex has one weak hydrogen bonding interaction between β-CD and fenthion. The complex TMAFEN has two host-guest interactions. The first (C5A-H···O2G1) is within the asymmetric unit and the second [C3A-H···O5G2‡ (‡:*1+x, y, z*)] occurs between the fenthion molecule and a TRIMEA molecule in the same column. There are no hydrogen bonding interactions between fenthion and the host in the TMBFEN complex. All

remaining host-guest interactions in all three complexes are hydrophobic interactions, owing to the nature of the cyclodextrin cavities.

CRYSTAL PACKING

Of the three inclusion complexes presented here, two are isostructural with other known complexes. The BCDFEN complex was found to be isostructural with the series S. Lubhelwana termed B7.[25] This isostructural series has been shown to have the intermediate packing arrangement where the β-CD complex dimers are slightly offset along their axis of symmetry. In the case of BCDFEN the centroids are offset by approximately 6 Å. The complex TMBFEN crystallises in the isostructural series named BD3 by S. Lubhelwana.[25] This series is characterised by the presence of TRIMEB inclusion complexes packed in anti-parallel head-to-tail columns. These columns are in a screw-channel configuration along the *a*-axis.

The complex TMAFEN was not found to be isostructural to any known cyclodextrin inclusion complex. A comprehensive search of the CSD[9] showed that there are 16 TRIMEA inclusion complexes, 10 of which crystallise in the space group $P2_1$. Nine of these have a similar mode of inclusion to that of TMAFEN, but the packing arrangements of the inclusion complexes differ. The differences in unit cell dimensions also cover a large range of values significantly different from those of the TMAFEN complex. The complex crystallises in the space group $P2_1$ in a column-type arrangement. These columns are made up of head-to-tail complex units arranged parallel to the *a*-axis. The columns are packed anti-parallel along the *b*- and *c*-axes and interact *via* weak hydrogen bonding interactions. The portion of the guest molecule protruding from the cyclodextrin cavity is positioned in the interstitial spaces between complex units.

PHASE SOLUBILITY

Phase solubility experiments of fenthion with α-CD, β-CD, γ-CD, HPBCD and RAMEB were performed. The α-CD and γ-CD systems were not pursued due to precipitation of the complexes at low cyclodextrin concentrations.

The phase solubility experiments with β-CD displayed a B_S-type profile, which is characterised by a linear increase in apparent guest concentration. This initial increase was followed by a decrease in apparent concentration. This is due to the formation of a partially soluble complex that increases the apparent solubility of fenthion. Once the maximum concentration of the complex is reached addition of further β-CD causes the complex to precipitate. The remaining guest is consumed by the addition of any further cyclodextrin, causing further precipitation which decreases the apparent concentration of the guest.[23]

The phase solubility profiles of fenthion with HPBCD and RAMEB both displayed A-type solubility. The phase solubility with HPBCD exhibits A_N behaviour where after an initial linear increase in apparent concentration the profile deviates negatively. There are several explanations for this deviation including changes due to the solution bulk properties and/or self-association of the cyclodextrin at higher concentration.[23] In the case of fenthion with RAMEB, the system shows A_P-type behaviour whereby there is positive deviation from linearity in apparent fenthion concentration. This positive deviation suggests the formation of higher order complexes at elevated cyclodextrin concentrations.

The linear portions of the three systems allowed for calculation of binding constants. The values were found to be 789 ± 170 M^{-1}, 1863 ± 26 M^{-1} and 3582 ± 106 M^{-1} for β-CD, HPBCD and RAMEB respectively. The enhancement factors for these three systems showed improvement of the apparent solubility of fenthion, which has an experimental intrinsic solubility of 3.55×10^{-5} mol dm^{-3}. The solubilisation of fenthion with β-CD was 5.0-fold at 4.3 mM cyclodextrin concentration. The increase in apparent fenthion concentration with HPBCD and RAMEB were were 85.9-fold and 189.7-fold at 50.2 mM and 49.6 mM respectively.

CONCLUSION

Both native and derivatised cyclodextrins have been shown capable of including the organothiophosphate pesticide fenthion, both in solution and in the solid state. Inclusion of this pesticide has allowed the formulation of a solid-state product. The thermal stability of fenthion was also greatly improved *via* cyclodextrin inclusion. The complex TMBFEN was shown to have an energy barrier that prevents the loss of fenthion.[5] The energy barrier is such that guest loss would not occur under normal transport thermal conditions. These factors combined allow one to conclude that use of this pesticide would be both safer and easier when it is included in cyclodextrin host molecules. The solubilisation of fenthion with the cyclodextrins β-CD, HPBCD and RAMEB show promise for an aqueous formulation of the pesticide, eliminating the need for organic solvents.

REFERENCES

1 K. A. Lewis, J. Tzilivakis, D. J. Warner and A. Green, *Hum. Ecol. Risk Assess. An Int. J.*, 2016, **22**, 1050–1064.

2 N. M. Rougier, D. L. Cruickshank, R. V. Vico, S. A. Bourne, M. R. Caira, E. I. Buján and R. H. de Rossi, *Carbohydr. Res.*, 2011, **346**, 322–7.

3 N. M. Rougier, PhD Thesis, Universidad Nacional de Córdoba, 2012.

4 D. L. Cruickshank, PhD Thesis, University of Cape Town, 2011.

5 D. L. Cruickshank, N. M. Rougier, V. J. Maurel, R. H. Rossi, E. I. Buján, S. A. Bourne and M. R. Caira, *J. Incl. Phenom. Macrocycl. Chem.*, 2012, **75**, 47–56.

6 D. Cruickshank, N. M. Rougier, R. V. Vico, R. H. de Rossi, E. I. Buján, S. A. Bourne and M. R. Caira, *Carbohydr. Res.*, 2010, **345**, 141–7.

7 Program SAINT, Version 7.60a, Bruker AXS Inc., Madison, WI, USA, 2006.

8 M. R. Caira, *Rev. Roum. Chim.*, 2001, **46**, 371–386.

9 Cambridge Structural Database and Cambridge Structural Database system, Version 5.37, Cambridge Crystallographic Data Centre, University Chemical Laboratory, Cambridge England, November 2015.

10 J. M. Alexander, J. L. Clark, T. J. Brett and J. J. Stezowski, *PNAS*, 2002, **99**, 5115–20.

11 J. L. Atwood, J. E. D. Davies and T. Osa, Eds., *Clathrate Compounds, Molecular Inclusion Phenomena, and Cyclodextrins*, Springer Netherlands, Dordrecht, 1984.

12 G. M. Sheldrick, Program SADABS, Version 2.05, University of Göttingen, Germany. 2007.

13 G. M. Sheldrick, *Acta Cryst.*, 2008, A**64**, 112–122.

14 T. Steiner and W. Saenger, *Carbohydr. Res.*, 1996, **282**, 53–63.

15 K. Harata, K. Uekama, M. Otagiri and F. Hirayama, *Bull. Chem. Soc. Jpn.*, 1983, **56**, 1732–1736.

16 M. R. Caira, V. J. Griffith, L. R. Nassimbeni and B. van Oudtshoorn, *J. Chem. Soc., Perkin Trans. 2*, 1994, 2071–2072.

17 M. R. Caira, S. A. Bourne, W. T. Mhlongo and P. M. Dean, *Chem. Commun.*, 2004, 2216–7.

18 T. Ozawa, *Bull. Chem. Soc. Jpn.*, 1965, **38**, 1881–1886.

19 J. H. Flynn and L. A. Wall, *J. Polym. Sci. B*, 1966, **4**, 323–328.

20 N. Zhang, J. H. Li, Q. T. Cheng and M. W. Zhu, *Thermochim. Acta*, 1994, **235**, 105–116.

21 J. H. Li, N. Zhang, X. T. Li, J. Y. Wang and S. J. Tian, *J. Therm. Anal. Calorim.*, 1997, **49**, 1527–1533.

22 T. K. Higuchi and K. A. Connors, *Adv. Chem. Instrum.*, 1965, **4**, 212–217.

23 M. E. Brewster and T. Loftsson, *Adv. Drug Deliv. Rev.*, 2007, **59**, 645–66.

24 T. Loftsson and M. E. Brewster, *J. Pharm. Pharmacol.*, 2010, **62**, 1607–1621.

25 S. Lubhelwana, Master's Dissertation, University of Cape Town, 2005.

CHAPTER 5 – ACIPIMOX

This chapter is focused on the formation of multi-component crystalline systems with the antihyperlipidemic agent acipimox. Acipimox is used as an additional treatment in type IIb and type IV hypertriglyceridaemia (high blood levels of triglycerides in the blood stream).[1]

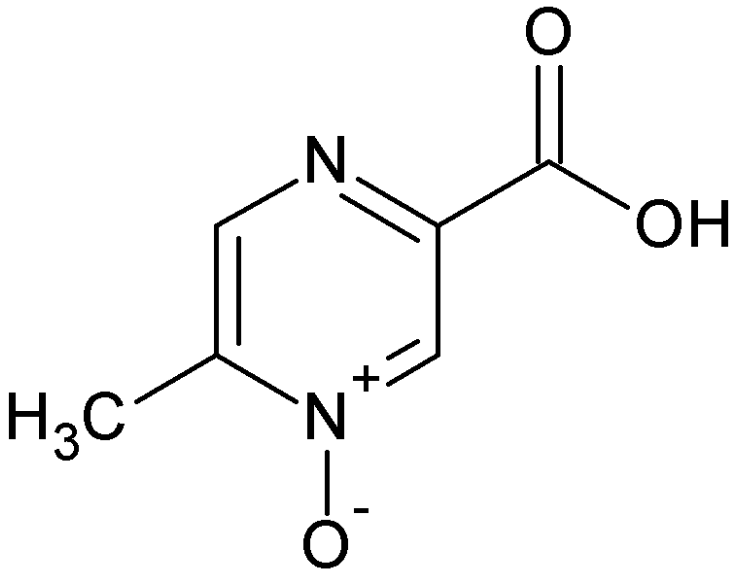

INTRODUCTORY REMARKS

The supramolecular modification of acipimox was investigated through the creation and physicochemical characterisation of multi-component molecular crystalline systems. Many attempts were made with various Generally Recognised as Safe (GRAS) co-former compounds to form co-crystals and other multi-component crystals. Successful multi-component crystalline systems were obtained with only six of these, in the forms of salts, co-crystals and solvates. Screening experiments included dry grinding, liquid-assisted grinding and co-precipitation with acipimox, a GRAS co-former compound and different solvents. Once a successful multi-component crystal was obtained the synthetic procedure was optimised to reproducibly obtain the desired product.

Presented in this chapter are successful attempts at creating multi-component crystalline systems. The co-formers successfully employed were 4-aminobenzamide, 4-aminopyridine, benzamide, isonicotinamide, tranexamic acid and urea. A full list of co-formers used in attempts to form multi-component crystalline systems is available in Appendix D.

ACIPIMOX/4-AMINOBENZAMIDE

The multi-component crystalline system comprising acipimox and 4-aminobenzamide will be referred to as ACPABEN.

SAMPLE PREPARATION

ACPABEN was prepared by both liquid-assisted grinding and co-precipitation. Liquid-assisted grinding was performed by weighing out 10 mg acipimox (0.065 mmol) and 9 mg (0.065 mmol) 4-aminobenzamide. The components were combined in an agate mortar. This mixture was ground together using an agate pestle, with the dropwise addition of isopropanol, for 20 minutes.

To prepare the co-crystal *via* co-precipitation, acipimox (10 mg, 0.065 mmol) was dissolved in 3 cm^3 butan-1-ol. The co-former 4-aminobenzamide (9 mg, 0.065 mmol) was added to this solution and the resulting mixture was stirred at 50 °C for 3 to 4 hours. The resulting solution was then filtered through a 0.45 μm nylon filter into a clean vial and sealed with Parafilm™. The vial was placed on the benchtop to form crystals by slow evaporation. After several days small needle-shaped crystals were observed.

In attempting to form this co-crystal *via* co-precipitation several alcohols were tested as solvents (methanol, ethanol, propan-1-ol, isopropanol and butan-1-ol). These were all successful in forming the desired product. However, only butan-1-ol gave rise to the single crystals required for analysis. Therefore, all analyses were performed on products obtained from butan-1-ol.

STOICHIOMETRY

The stoichiometry of ACPABEN was confirmed using ^{1}H-NMR spectroscopy. Crystals obtained from co-precipitation were dissolved in DMSO-d_6 and analysed using ^{1}H-NMR spectroscopy. The relative integration of the acipimox methyl peak (C-$H_{11a,b,c}$), set as the reference integral, and the 4-aminobenzamide aromatic peaks showed a stoichiometric ratio of 1:1. The proton labelling scheme of each component of the system is shown in Figure 5.1. The integration values and the spectrum are presented below in Table 5.1 and Figure 5.2 respectively.

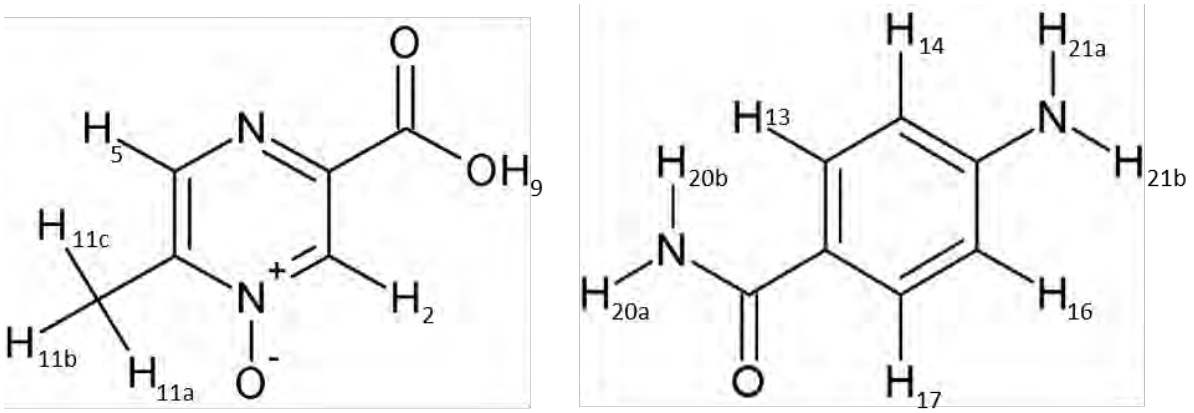

Figure 5.1: Proton labelling of acipimox (left) and 4-aminobenzamide (right)

Table 5.1: Integrals and assignment of component protons used for stoichiometric determination

Proton	**δ (ppm)**	**Integration**		**Experimental/ Theoretical**
		Experimental	Theoretical	
Acipimox				
C-$H_{11a,b,c}$	2.42	3.00‡	3.00	1
C-H_2	8.69	1.01	1	1.01 ≈ 1
C-H_5	8.76	1.01	1	1.01 ≈ 1
4-aminobenzamide				
C-H_{13} + C-H_{17}	6.56	2.05	2	1.03 ≈ 1
C-H_{14} + C-H_{16}	7.61	2.08	2	1.04 ≈ 1

‡*Reference Integral*

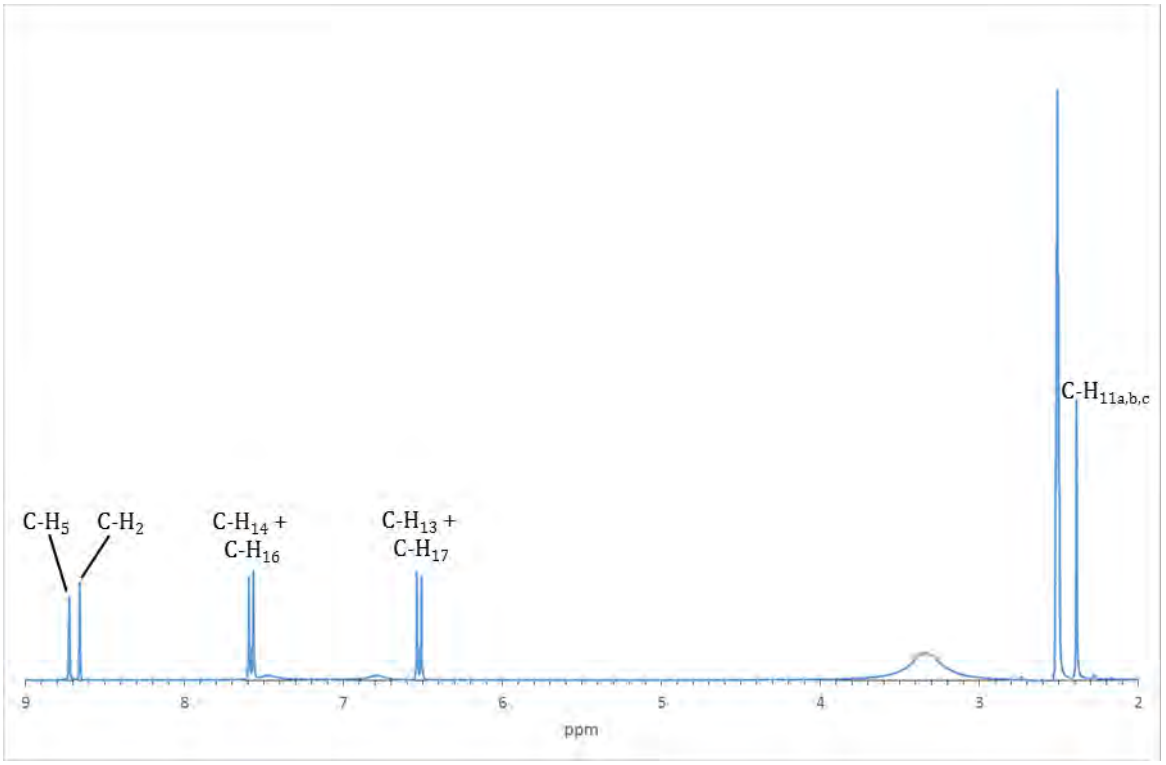

Figure 5.2: ^{1}H-NMR spectrum of ACPABEN in DMSO-d_6 used to determine the stoichiometric ratio

THERMAL ANALYSIS

The thermal analysis of ACPABEN, presented in Figure 5.3, shows that there are no solvent molecules present in the structure. Upon melting at 201.1 ± 0.1 °C (n = 2) a mass loss of 52.8 ± 0.7 % (n = 2) occurs, followed immediately by a second mass loss of 41.0 ± 0.5 %. The first mass loss corresponds to the loss of acipimox (calculated mass loss 53.1 %), while the second is the decomposition of the 4-aminobenzamide component. The DSC trace shows the melting endotherm with no significant heat flow event following. This would indicate that the loss of acipimox and decomposition occur simultaneously with the melting of the co-crystal.

The HSM micrographs (Figure 5.4) provide further evidence for the interpretation of the thermal analysis results. In the micrograph taken at 201 °C, the loss of acipimox is seen in the bubbling. The melting at the edges of crystals, combined with the visible bubbling, confirms the interpretation of simultaneous melting and decomposition. The final micrograph shows the decomposed product.

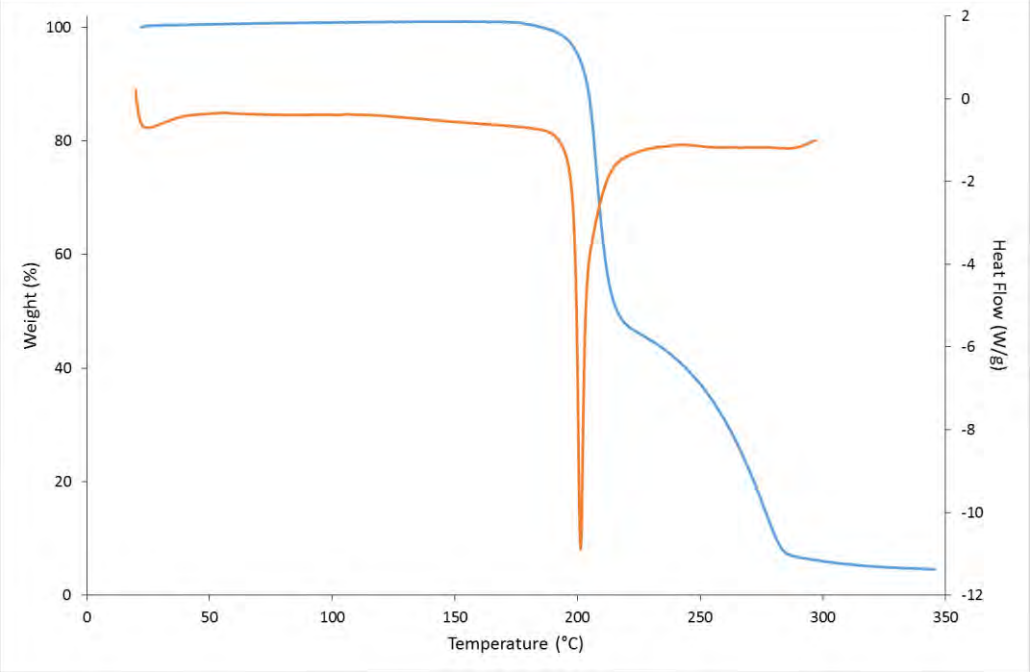

Figure 5.3: Representative TGA (blue) and DSC (orange) traces for ACPABEN

Figure 5.4: Hot stage micrographs showing the ACPABEN crystals at various stages of heating

CRYSTAL STRUCTURE ANALYSIS

DATA COLLECTION AND SPACE GROUP DETERMINATION

Crystal intensity data were collected using a Nonius KappaCCD diffractometer. The program LAYER[2] was used to determine the crystal system and space group of the co-crystal. The crystal system was established as triclinic from the observed Laue symmetry $\bar{1}$. The computer program XPREP[3] was used to determine the space group $P\ \bar{1}$. The program calculated an $|E^2-1|$ value of 1.101, which indicated centrosymmetry.[3] The data collection was performed at 173 ± 2 K.

STRUCTURE SOLUTION AND REFINEMENT

The software program DENZO[4] was used for unit cell refinement and data reduction. The asymmetric unit of ACPABEN comprises one acipimox molecule and one 4-aminobenzamide molecule. The atomic positions were determined using SHELXS, employing direct methods.[5] The atoms were placed at these positions and refined using SHELXL.[5,6] All the non-hydrogen atoms were refined isotropically initially and subsequently anisotropically. The positions of hydrogen atoms were determined from the difference Fourier map and the position of the carboxylic acid proton was found on the acipimox moiety. It was also found that the distinctly different carboxylic bond lengths supported the placement of this atom with C-O bond length values of 1.216(2) Å and 1.302(2) Å. These values are consistent with carboxylic acid bond lengths. No additional proton was located on the amine moiety of 4-aminobenzamide. The two components were present in their neutral state, so the system ACPABEN was therefore designated a co-crystal. Once the determination of the hydrogen atoms was completed they were placed in idealised positions using a riding model with a U_{iso} value 1.2 – 1.5 times that of the parent atom. The crystallographic data and refinement parameters for ACPABEN are presented in Table 5.2.

Table 5.2: Crystallographic data for the single crystal X-ray structure of ACPABEN

Chemical Formula	$C_6H_6N_2O_3 \cdot C_7H_8N_2O$
Molar mass (g mol^{-1})	290.28
Crystal System	Triclinic
Space Group	$P\ \bar{1}$
Unit cell parameters	
a (Å)	6.9367(3)
b (Å)	6.9835(3)
c (Å)	14.7422(9)
α (°)	89.607(2)
β (°)	81.704(3)
γ (°)	63.317(3)
Volume (Å^3)	630.06(6)
Z	2
Density$_{calcd.}$ (g cm^{-3})	1.556
μ [MoKα] (mm^{-1})	0.118
F (000)	304
Temperature (K)	173(2)
Crystal size (mm)	0.31×0.16×0.07
Range scanned θ (°)	1.40 – 28.28
Index ranges	h: -9, 9; k: -9, 9; l: -19, 19
ϕ and ω scan angles (°)	1.0
Dx (mm)	45
Total number of reflections	6 085
Number of independent reflections	3 106
Number of reflections with I > 2σ(I)	2 251
R_{int}	0.0450
R_1 [I > 2σ(I)]	0.0554
wR_2	0.1200
S	1.052
Number of parameters	195
Number of reflections omitted	16
Parameters a, b	a = 0.0764; b = 0.1011
in w = 1/[σ^2(F_0^2)+(aP)^2+(bP)]	
$(\delta/\sigma)_{mean}$	<0.001
Δρ excursions (e Å^{-3})	-0.34; 0.40

MOLECULAR STRUCTURE

The ACPABEN asymmetric unit (Figure 5.5) consists of one acipimox molecule and one 4-aminobenzamide molecule. These two components are hydrogen bonded through the supramolecular synthon between the acipimox carboxylic acid and the 4-aminobenzamide amide group.

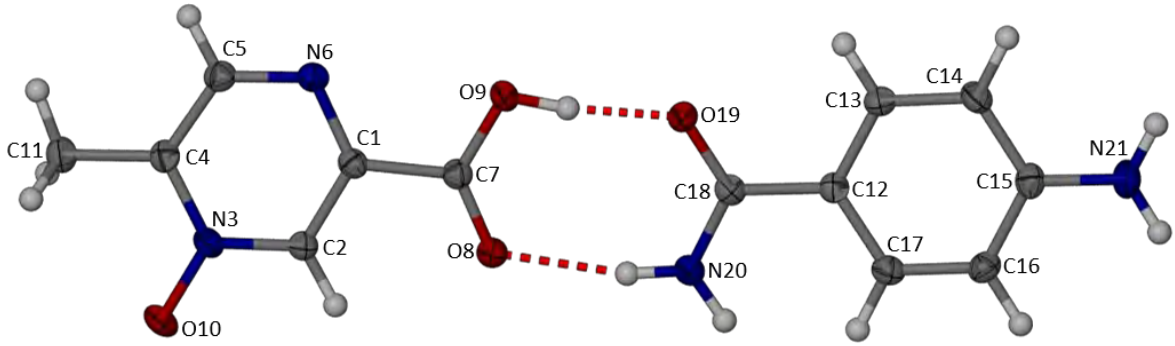

Figure 5.5: The asymmetric unit of the co-crystal ACPABEN with numbering scheme of acipimox (left) and 4-aminobenzamide (right). Thermal ellipsoids are drawn at the 50 % probability level

HYDROGEN BONDING

Both components are present in their neutral state. Within this crystal structure there are two hydrogen bonding synthons, shown in Figure 5.6. One is the carboxylic acid – amide synthon characterised by the $R_2^2(8)$ ring. The second hydrogen bond is that between the pyrazine oxide group of acipimox and the primary amine of 4-aminobenzamide. When these two hydrogen bonding synthons are combined an infinite ribbon is formed, denoted as a C(15) chain. Thus the hydrogen bonding network, N, can be denoted by the graph set notation N = C(15) $R_2^2(8)$. The infinite ribbons are shown in Figure 5.7.

The infinite ribbons interact with adjacent ribbons *via* three C-H···O hydrogen bonds which aid in stabilising the overall structure of the co-crystal. The hydrogen bonding parameters are presented in Table 5.3. As the hydrogen atoms are placed in geometrically idealised positions, the values of the D-H and H···A distances are omitted. The idealised positions of the hydrogen atoms mean that *e.s.d.* values are not available for the hydrogen bond angles. This applies to all crystal structure analyses reported in this chapter. There is one intramolecular interaction, C2-H···O8, which occurs in the acipimox molecule.

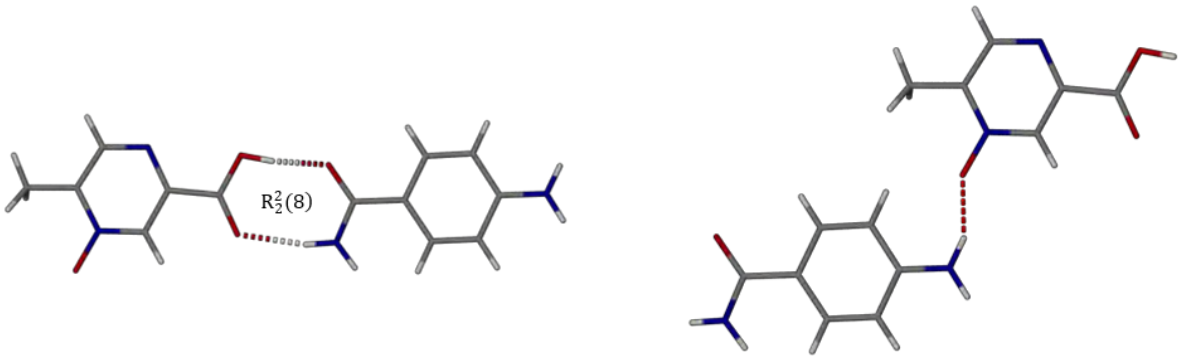

Figure 5.6: Hydrogen bonding motifs showing the carboxylic acid – amide synthon (left) and the pyrazine oxide – amine (right) synthons

Table 5.3: Hydrogen bonding parameters for hydrogen bonds in ACPABEN

Hydrogen Bond Label	D-H···A	D···A (Å)	Angle (°)	Symmetry Operator
1	O9-H···O19	2.529(2)	172	(*x, y, z*)
2	N20-H···O8	2.792(2)	164	(*x, y, z*)
3	N21-H···O10	2.935(2)	143	(*1+x, y, -1+z*)
4	C2-H···O8	2.663(2)	100	(*x, y, z*)
5	C5-H···O8	3.186(2)	139	(*1+x, y, z*)
6	C11-H···O10	3.465(2)	158	(*1-x, 2-y, 2-z*)
7	C17-H···O9	3.400(2)	166	(*1+x, y, z*)

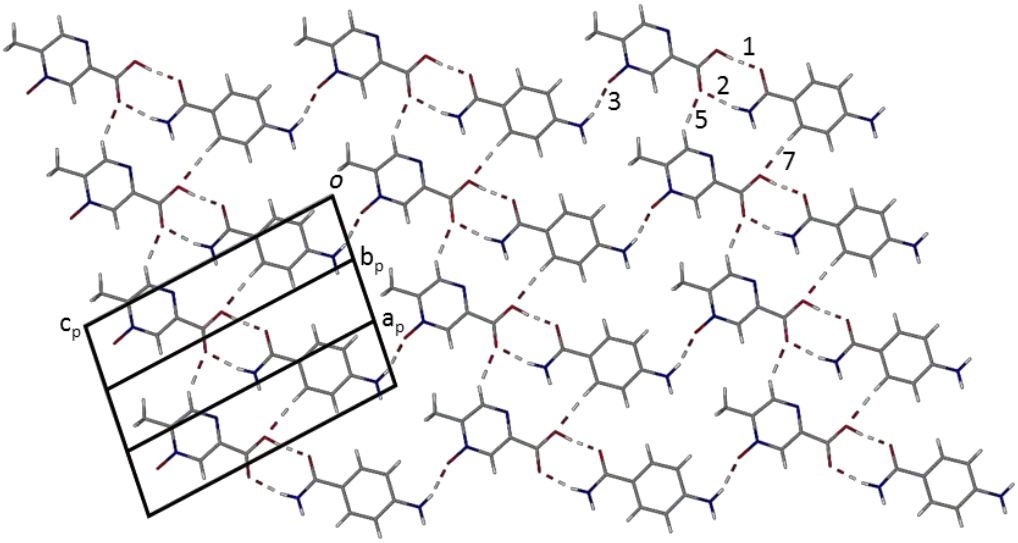

Figure 5.7: Infinite ribbons formed by the hydrogen bonding network N_1 = C(15) $R_2^2(8)$ linked by C-H···O hydrogen bonds (5, 7). The intramolecular hydrogen bonds labelled 4 and 6 in Table 5.3 have been omitted for clarity

CRYSTAL PACKING

As described in the section above, the pair comprising acipimox and 4-aminobenzmide of the asymmetric unit link through a hydrogen bond to form infinite ribbons which propagate horizontally in Figure 5.7. These ribbons are hydrogen bonded to one another by the intermolecular C-H···O weak hydrogen bonds to form layers. The layers interact through π-π stacking interactions between the aromatic ring of acipimox and that of 4-aminobenzamide with centroid-to-centroid distances less than 5 Å.[7] Relevant data are presented in Table 5.4. The centroids of the aromatic rings are offset by approximately 1.6 Å and the angle of intersection between the aromatic least-squares planes is 1.83(6)° in both interactions.

Table 5.4: π-π interaction parameters

Ring Interaction	Centroid Distance (Å)	Symmetry Operator
Cg(A)···Cg(B)	3.719(1)	(*-x, 2-y, 1-z*)
Cg(A)···Cg(B)	3.604(1)	(*1-x, 1-y, 1-z*)

Cg refers to the centroid of a ring and the symmetry operator in column 3 refers to the second Cg listed in column 1
Ring A: C1-C2-N3-C4-C5-N6
Ring B: C12-C13-C14-C15-C16-C17

The crystal packing can be seen in Figure 5.8 where the layers formed through π - π stacking are clearly visible.

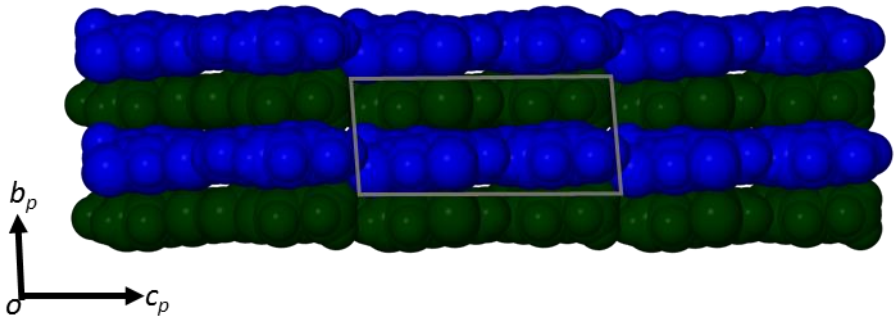

Figure 5.8: Packing of the ACPABEN co-crystal viewed along [1 0 0] highlighting the layers formed through π - π stacking

COMPARATIVE PXRD

The experimental PXRD pattern of the bulk samples of ACPABEN shows good agreement with the pattern calculated from the refined single crystal structure of the co-crystal. Cooling the crystal for intensity data collection results in anisotropic contraction of the unit cell. As the bulk sample PXRD pattern was collected at room temperature this results in slight differences in the angular positions of the peaks.

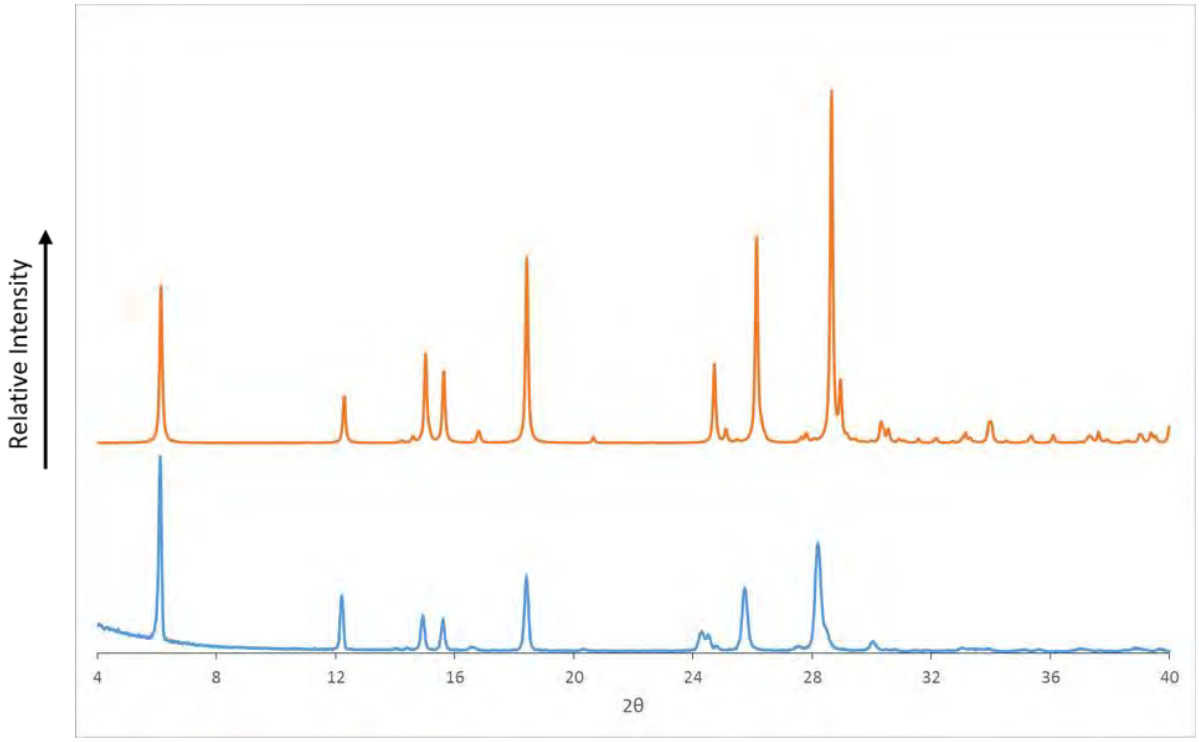

Figure 5.9: The PXRD trace recorded for the bulk sample (blue) and the computed PXRD pattern based on the single crystal X-ray structure of ACPABEN (orange)

INFRARED SPECTROSCOPY

The refined single crystal structure of ACPABEN showed the position of the carboxylic acid proton on the acipimox molecule. As no proton transfer took place, ACPABEN was designated a co-crystal. Infrared spectroscopy was performed to determine whether the spectrum of ACPABEN was in accordance with this designation. By close inspection of characteristic peaks, the presence of relevant functional groups could be observed. A second purpose of recording FTIR spectra was to investigate the use of infrared spectroscopy as a rapid identification method for the co-crystal. This was done by observation of characteristic absorption peaks as well as direct comparison with the API and co-former spectra.

The infrared spectrum of ACPABEN (Figure 5.10) shows a signal characteristic of a carboxylic acid carbonyl peak at 1685 cm^{-1}. A second characteristic peak distinctive of carboxylic acids, the C-O stretching peak, at 1274 cm^{-1}, was also observed in the FTIR spectrum. The presence of these peaks indicates that no proton transfer took place from the carboxylic acid of acipimox during the formation of ACPABEN. This supports the designation of this crystalline system as a co-crystal.

A second purpose of using FTIR spectroscopy was to investigate this technique as a possible means of rapid identification of the co-crystal ACPABEN in future batches of the material. The peaks present at 3408 cm^{-1} and 3449 cm^{-1} are indicative of the presence of an O-H group (as part of a carboxylic acid moiety) and a hydrogen bonded primary amine. It was not possible to unambiguously assign these peaks, as the absorption peaks for these functional groups are known to occur in the same region.

The comparison of the co-crystal spectrum with the spectra of the starting materials could also be used to confirm the formation of a new phase. Differences in signal positions of functional groups in the component and multi-component system spectra will serve to identify a new phase. A shift in the position of the carbonyl carboxylic acid peak from 1701 cm^{-1} in the acipimox spectrum to 1685 cm^{-1} in that of ACPABEN is observed. A similar shift is seen for the N-H signal at 3462 cm^{-1} in the 4-aminobenzamide spectrum to either 3449 cm^{-1} or 3408 cm^{-1} in the ACPABEN spectrum. Through intermolecular interactions between the components the profile of the spectrum of the co-crystal differs significantly from those of the starting materials. Therefore, by comparison one can establish unequivocally the formation of a new phase.

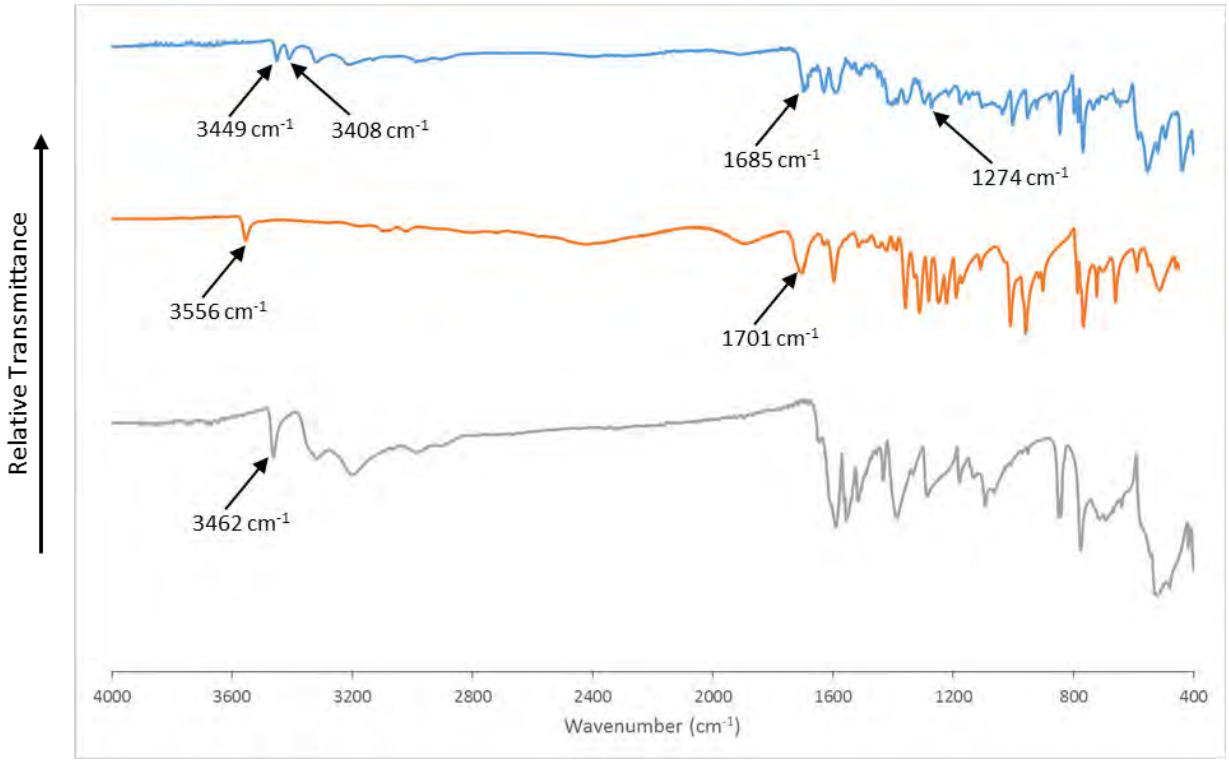

Figure 5.10: FTIR spectra for ACPABEN (blue), acipimox (orange) and 4-aminobenzamide (grey)

ACIPIMOX/4-AMINOPYRIDINE

The multi-component crystalline system of acipimox with 4-aminopyridine has been assigned the codename ACPAPYR.

SAMPLE PREPARATION

The ACPAPYR crystalline system was produced in three ways: two methods rely on mechanochemical action, while the third is production *via* co-precipitation.

Dry grinding and liquid-assisted grinding were the mechanochemical methods employed. Dry grinding was performed by weighing equimolar quantities of acipimox (10 mg, 0.065 mmol) and 4-aminopyridine (6 mg, 0.065 mmol). These were combined in an agate mortar and ground together using an agate pestle for 10 minutes. Liquid-assisted grinding was performed employing the same procedure with the additional step of dropwise addition of isopropanol.

Co-precipitation of ACPAPYR involved dissolving acipimox (10 mg, 0.065 mmol) in 5 cm^3 propan-1-ol and adding an equimolar quantity of 4-aminopyridine (6 mg, 0.065 mmol) to the solution. The resulting mixture was stirred for 2 to 4 hours at 60 °C and then filtered through a 0.45 µm nylon filter into a clean vial. The vial was sealed using Parafilm™ pierced with several holes and allowed to stand on the benchtop to form crystals *via* slow evaporation. Over the course of several days plate-shaped crystals were observed. The precipitate obtained before filtration was found to be the desired product in powder form.

STOICHIOMETRY

The stoichiometry of ACPAPYR was determined using ^{1}H-NMR spectroscopy. The plate-like crystals obtained from co-precipitation were dissolved in DMSO-d_6 and subjected to ^{1}H-NMR spectroscopy. The relative integration of the methyl group of acipimox (set as the reference integral) and the 4-aminopyridine aromatic peaks served to determine a 1:1 stoichiometric ratio. The proton labelling schemes of the two components are shown in Figure 5.11. The integration values and ^{1}H-NMR spectrum are presented in Table 5.5 and Figure 5.12 respectively.

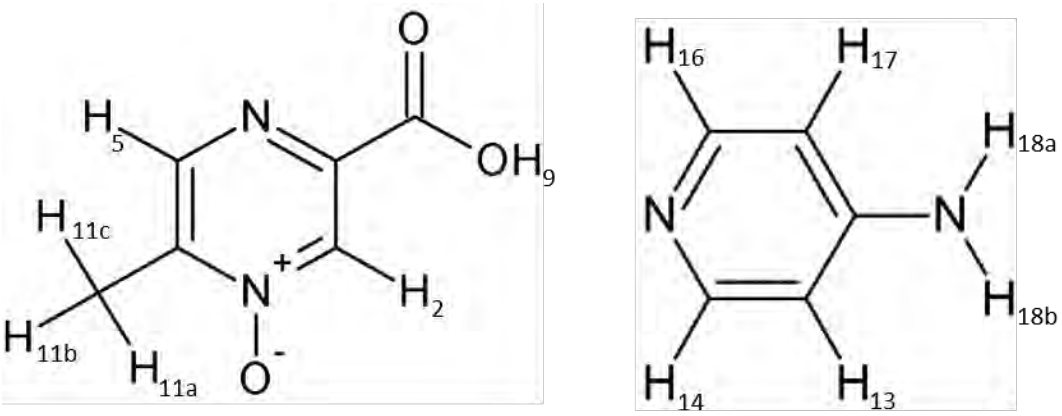

Figure 5.11: Proton labelling of acipimox (left) and 4-aminopyridine (right)

Table 5.5: Integrals and assignment of component protons for stoichiometric determination

Proton	δ (ppm)	Integration		Experimental/ Theoretical
		Experimental	Theoretical	
Acipimox				
C-$H_{11a,b,c}$	2.38	3.00‡	3.00	1
C-H_2	8.55	0.99	1.00	0.99 ≈ 1
C-H_5	8.63	0.98	1.00	0.98 ≈ 1
4-aminopyridine				
C-H_{13} + C-H_{17}	6.78	2.02	2.00	1.01 ≈ 1
C-H_{14} + C-H_{16}	8.16	2.03	2.00	1.02 ≈ 1

‡ *Reference integral*

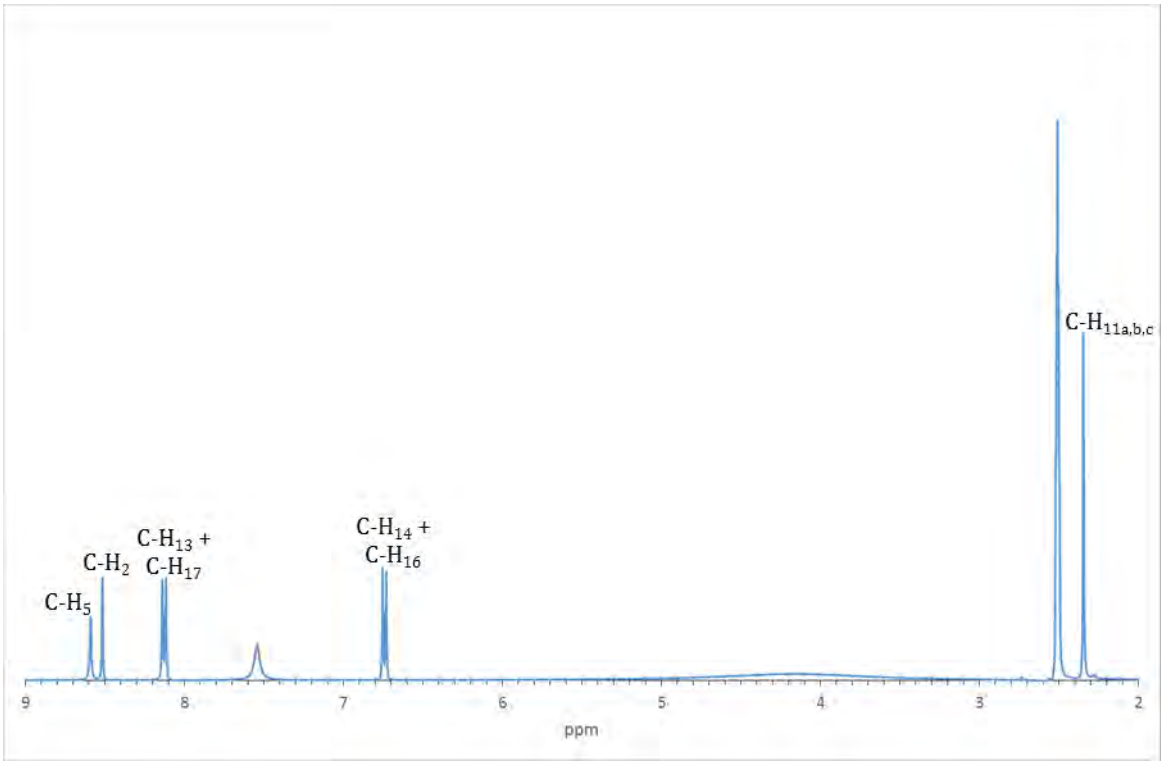

Figure 5.12: ^{1}H-NMR spectrum of ACPAPYR in DMSO-d_6 used to determine the stoichiometric ratio

THERMAL ANALYSIS

Two thermal events present in the DSC trace (Figure 5.13) of ACPAPYR were observed. The first was a small endotherm at 219.4 ± 0.5 °C (n = 2) corresponding to a possible phase change. This is followed by a large endotherm at 246.2 ± 0.9 °C resulting from simultaneous melting and decomposition. This coincides with a large mass loss in the TGA trace (Figure 5.13) with an onset temperature of 233.5 ± 1.2 °C (n = 2). The beginning stages of the decomposition can be seen in the HSM micrograph at 225 °C (Figure 5.14). The micrograph at 250 °C shows the product undergoing rapid and complete decomposition.

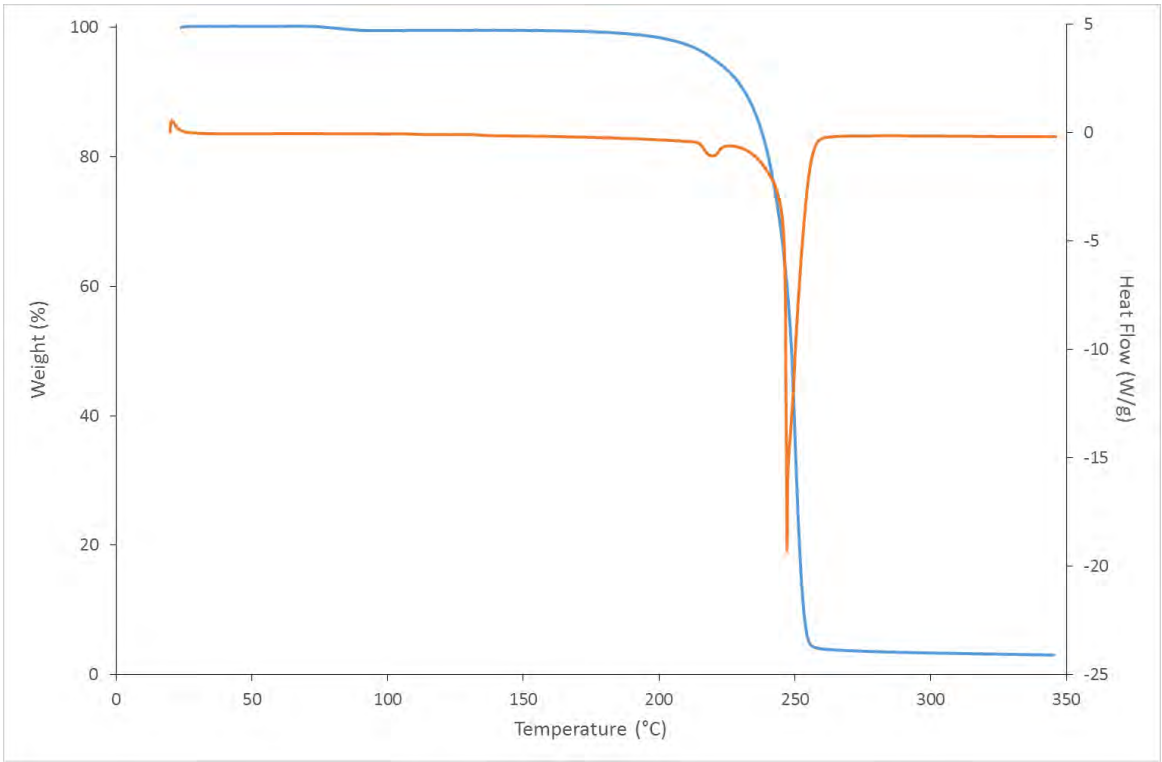

Figure 5.13: Representative TGA (blue) and DSC (orange) traces for ACPAPYR

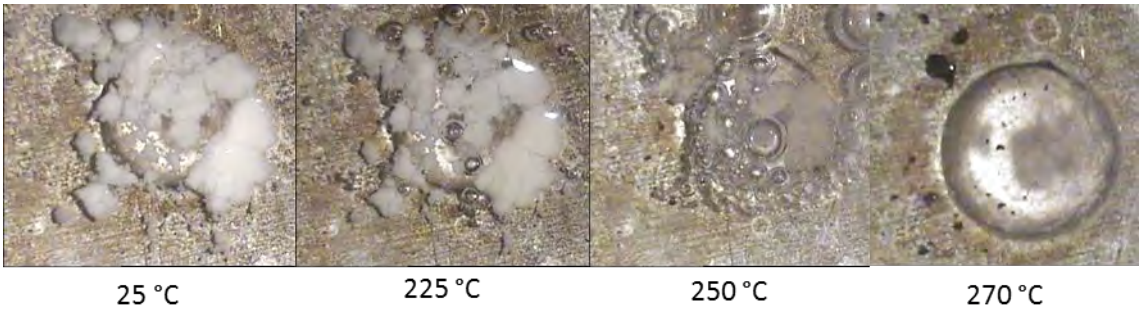

Figure 5.14: Hot stage micrographs showing the ACPAPYR co-crystal at various stages of heating

CRYSTAL STRUCTURE ANALYSIS

The asymmetric unit of ACPAPYR comprises two acipimox moieties and two 4-aminopyridine moieties.

DATA COLLECTION AND SPACE GROUP DETERMINATION

Intensity data were collected using a Bruker KAPPA APEX DUO II diffractometer. The X-ray diffraction pattern was determined to have Laue symmetry $\bar{1}$, indicating the triclinic crystal system. The program XPREP[3] was used to determine the space group and the $|E^2-1|$ value of 1.093 indicated centrosymmetry. The only option was therefore P $\bar{1}$. The crystal exhibited twinning with a BASF factor of 0.40, determined using program Cell_now.[8] The second domain was rotated relative to the first by 178.4° and the approximate twin law applied to convert the data was (-1.000 ~0 ~0)(~0 ~1 ~0)(~0 ~0 1.000) The computer program TWINABS[9] was used to scale the data and for absorption correction. The BASF value refined to 0.322(2) over the course of the structure refinement. The data collection was performed at 173(2) K.

STRUCTURE SOLUTION AND REFINEMENT

The program SAINT[10] was used for unit cell refinement and data reduction. The atomic co-ordinates of the atoms comprising the asymmetric unit were determined using direct methods employed by the program SHELXS.[5] Once the atoms were placed in these presumed positions the latter were refined using SHELXL.[5,6] After several refinement cycles, the HKLF 5 file generated by the program TWINABS was used in subsequent refinement cycles. The non-hydrogen atoms were initially refined isotropically and later anisotropically. The location of the hydrogen atom on the acipimox or 4-aminopyridine moieties was investigated to determine the occurrence of a proton transfer. The location of the hydrogen atom was observed to be on the pyridyl nitrogen atom of the 4-aminopyridine moieties from the Fourier difference map. No carboxylate proton was observed on acipimox. The placement of the hydrogen atom was supported by the similarity in the C-O bond lengths of the acipimox carboxylate functional groups. The values for the first acipimox component were 1.240(2) Å and 1.262(2) Å while the values for the second component were 1.242(2) Å and 1.261(2) Å. These bonds are of length intermediate between single and double bonds. The locations of the hydrogen atoms, with the similarities and values of the bond lengths, indicated unambiguously that the compound is a salt. Once all hydrogen atoms were revealed in the difference Fourier map they were placed in geometrically idealised positions using a riding model, where the U_{iso} values were 1.2 – 1.5 times that of the parent atom. The crystallographic data are presented in Table 5.6.

Due to the twinning problem, a data collection strategy was required where only a hemisphere of the data was collected, leading to zero redundancy. Therefore, the R_{int} value is reported as zero in the cif file. Nevertheless, the solution of the structure is considered of good quality as seen from

the reported R_1 and S values of 0.0441 and 1.048 in Table 5.6. The high level of precision (C-C bond precision 0.0023 Å) further supports the quality of the structure solution.

Table 5.6: Crystallographic data for the single crystal X-ray structure of ACPAPYR

Chemical Formula	$(C_6H_5N_2O_3)^-\cdot(C_5H_7N_2)^+$
Molar mass (g mol^{-1})	248.25
Crystal System	Triclinic
Space Group	$P\ \bar{1}$
Unit cell parameters	
a (Å)	7.3957(15)
b (Å)	11.620(2)
c (Å)	13.020(3)
α (°)	86.51(3)
β (°)	84.62(3)
γ (°)	87.84(3)
Volume (Å^3)	1111.3(4)
Z	4
Density$_{calcd.}$ (g cm^{-3})	1.484
μ [MoKα] (mm^{-1})	0.112
F (000)	520
Temperature (K)	173(2)
Crystal size (mm)	0.17×0.32×0.47
Range scanned θ (°)	1.60 – 28.4
Index ranges	h: -9, 9; k: -15, 15; l: 0, 17
ϕ and ω scan angles (°)	0.50
Total number of frames	2085
Dx (mm)	79.8
Total number of reflections	5 444
Number of independent reflections	5 447
Number of reflections with I > 2σ(I)	4 221
R_{int}	0.000
R_1 [I > 2σ(I)]	0.0441
wR_2	0.1153
S	1.048
Number of parameters	352
Number of reflections omitted	4
Parameters a, b	a = 0.0581; b = 0.1913
in $w = 1/[\sigma^2(F_0^2)+(aP)^2+(bP)]$	
$(\delta/\sigma)_{mean}$	<0.001
Δρ excursions (e Å^{-3})	-0.24; 0.36

MOLECULAR STRUCTURE

The asymmetric unit of ACPAPYR, shown in Figure 5.15, comprises two crystallographically independent hydrogen bonded units. These units are each made up of one acipimox anion and one 4-aminopyridine cation. Each independent ion is designated the suffix A or B. The two components are present in their charged forms. Each acipimox moiety contains a carboxylate group and each 4-aminopyridine counterion has a protonated pyridyl group. The interactions present in this structure will be described in detail below in the section on Hydrogen Bonding.

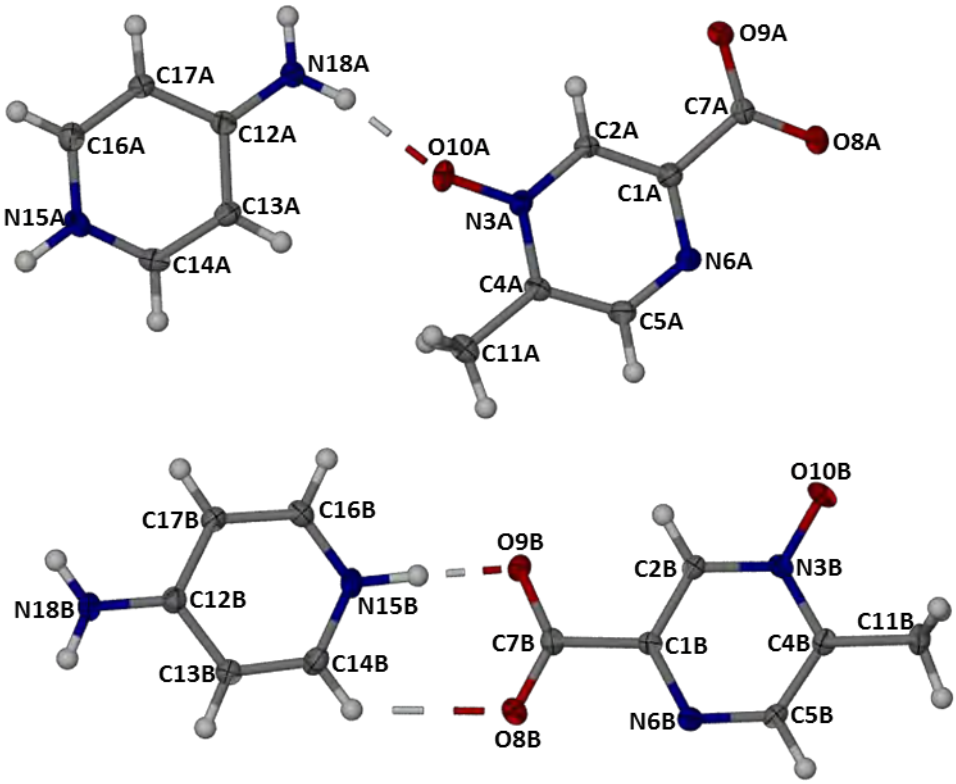

Figure 5.15: The asymmetric unit of the salt ACPAPYR with numbering schemes of acipimox (right) and 4-aminopyridine (left). Thermal ellipsoids are drawn at the 50 % probability level

HYDROGEN BONDING

The multi-component crystalline system ACPAPYR has three hydrogen bonding synthons. The first, shown in Figure 5.16a., is the pyridyl-carboxylate synthon between acipimox and 4-aminopyridine. The second is a bifurcated hydrogen bond with a hydrogen atom of the amine group of 4-aminopyridine as a donor and the pyrazine nitrogen and a carboxylate oxygen of acipimox being acceptors (Figure 5.16b.). Finally the remaining nitrogen of the amine group of 4-aminopyridine participates in a hydrogen bond with the pyrazine oxide moiety of acipimox, as shown in Figure 5.16c.

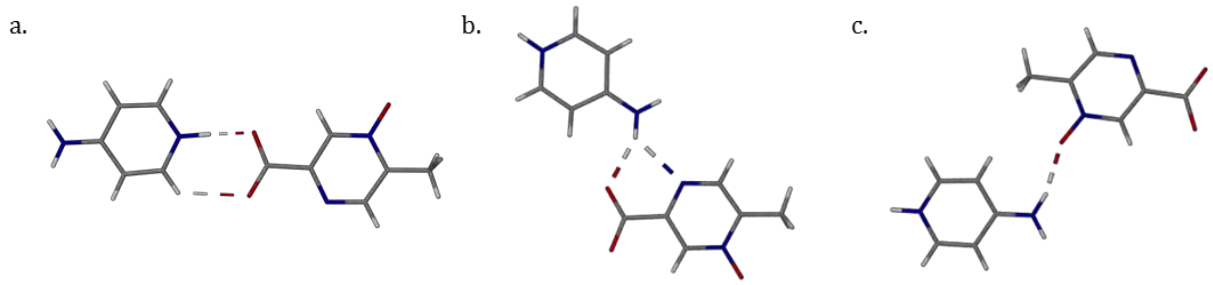

Figure 5.16: Hydrogen bonding synthons present in the ACPAPYR crystal structure

The combination of these hydrogen bonds results in six patterns that link to create an infinite sheet. The first and second patterns have the same connectivity, but are crystallographically independent, $N_1 = R_2^2(7)$ and $N_2 = R_2^2(7)$ (Figure 5.17a.). Similarly, the third and fourth patterns, N_3 and N_4, while crystallographically independent, have the same connectivity, producing $R_1^2(5)$ rings. Finally the patterns $N_5 = R_6^5(28)$ and $N_6 = R_6^5(28)$ are similarly rings with the same connectivity which are crystallographically independent. These six rings are concatenated, sharing common molecular ions, and form infinite sheets that can be seen in Figure 5.17. The hydrogen bonds involved in these patterns are shown in Table 5.7. Two hydrogen bonds, C11A-H···O10A‡ (‡:*1-x, 1-y, 1-z*) and C11B-H···O10B‡ (‡:*-x, 2-y, -z*), aid in stabilising the packing of these infinite sheets into layers.

Table 5.7: Hydrogen bonding interactions present in ACPAPYR

Hydrogen Bond Label	D-H···A	D···A (Å)	Angle (°)	Symmetry Operator
1	N15A-H···O9A	2.631(2)	176	(*x, y, 1+z*)
2	N15B-H···O9B	2.637(2)	177	(*x, y, z*)
3	N18A-H···O10A	2.891(2)	158	(*x, y, z*)
4	N18A-H···O8B	2.966(2)	153	(*1+x, -1+y, z*)
5	N18A-H···N6B	3.072(2)	129	(*1+x, -1+y, z*)
6	N18B-H···O8A	3.003(2)	152	(*x, y, 1+z*)
7	N18B-H···N6A	3.048(2)	130	(*x, y, 1+z*)
8	N18B-H···O10B	2.884(2)	153	(*x, y, 1+z*)
9	C2B-H···O9B	2.727(2)	100	(*x, y, z*)
10	C11A-H···O10A	3.482(2)	165	(*1-x, 1-y, 1-z*)
11	C11A-H···O9B	3.548(2)	171	(*x, y, z*)
12	C11B-H···O10B	3.487(2)	160	(*-x, 2-y, -z*)
13	C14A-H···O8A	3.179(2)	126	(*x, y, 1+z*)
14	C14B-H···O8B	3.207(2)	126	(*x, y, z*)
15	C17A-H···O8B	3.190(2)	138	(*1+x, -1+y, 1+z*)
16	C17B-H···O8A	3.215(2)	138	(*x, y, 1+z*)

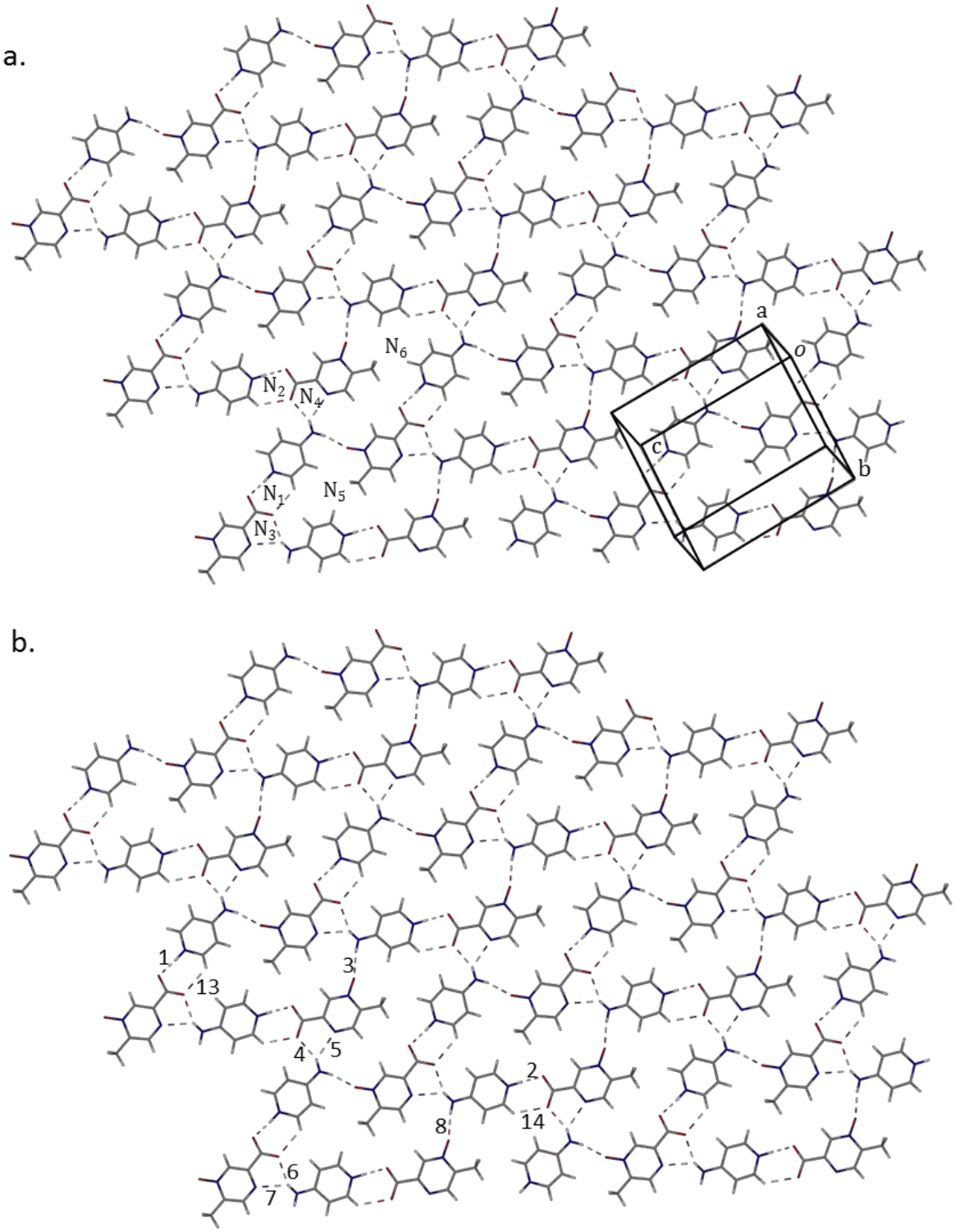

Figure 5.17: Figures showing a. interconnected hydrogen bonding patterns N_1, N_2, N_3, N_4, N_5 and N_6 in the salt ACPAPYR and b. hydrogen bonds involved within the layers (The hydrogen bonds labelled 9, 10, 11, 12, 15 and 16 in Table 5.7 have been omitted for clarity)

CRYSTAL PACKING

The packing of the crystal structure ACPAPYR is formed by layers of concatenated N_1, N_2, N_3, N_4 N_5 and N_6 hydrogen bonding patterns. The layers stack along the *a*-axis and interact *via* two C-H···O hydrogen bonds and π-π stacking. The two hydrogen bonds are C11A-H···O10A‡ (‡:*1-x, 1-y, 1-z*) and C11B-H···O10B‡ (‡:*-x, 2-y, -z*). The π-π stacking takes place between the aromatic rings of acipimox ions and 4-aminopyridine ions. The least-squares planes through the aromatic rings intersect at an angle of 1.6(1)° for the Cg(A)···Cg(C) interactions and 1.8(1)° for the Cg(B)···Cg(D) interactions. The centroids of the aromatic rings are offset by approximately 1.7 Å in each of the four interactions. The data relevant to the π-π stacking are presented in Table 5.8. The close packing of the layers is clearly visible in the diagram shown in Figure 5.18.

Table 5.8: π-π interaction parameters

Ring Interaction	Centroid-centroid Distance (Å)	Symmetry Operator
Cg(A)···Cg(C)	3.752(1)	(1-*x, 1-y, 1-z*)
Cg(A)···Cg(C)	3.781(1)	(*2-x, 1-y, 1-z*)
Cg(B)···Cg(D)	3.793(1)	(*-x, 2-y, 1-z*)
Cg(B)···Cg(D)	3.609(1)	(1-*x, 2-y, 1-z*)

Cg refers to the centroid of a ring and the symmetry operator in column 3 refers to the second Cg listed in column 1

Ring A: C1A-C2A-N3A-C4A-C5A-N6A

Ring B: C1B-C2B-N3B-C4B-C5B-N6B

Ring C: C12A-C13A-C14A-N15A-C16A-C17A

Ring D: C12B-C13B-C14B-N15B-C16B-C17B

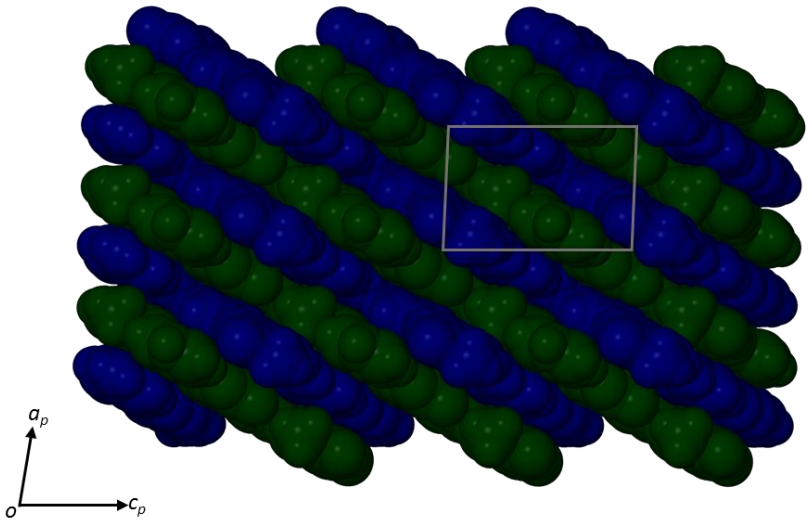

Figure 5.18: Packing of ACPAPYR viewed along [0 -1 0] illustrating the layers formed through π-π stacking and C-H···O interactions

COMPARATIVE PXRD

The PXRD pattern of the bulk material was recorded and compared to the pattern calculated from the refined single crystal data of ACPAPYR. The two patterns show good agreement; however, there are slight differences in the angular positions of peaks between the traces. This is due to the single crystal intensity data having been collected at 173(2) K while the PXRD trace was collected at room temperature. When cooling the crystal for single crystal intensity data, the unit cell parameters undergo contraction and/or expansion, which in turn affects the peak positions of the calculated PXRD trace.

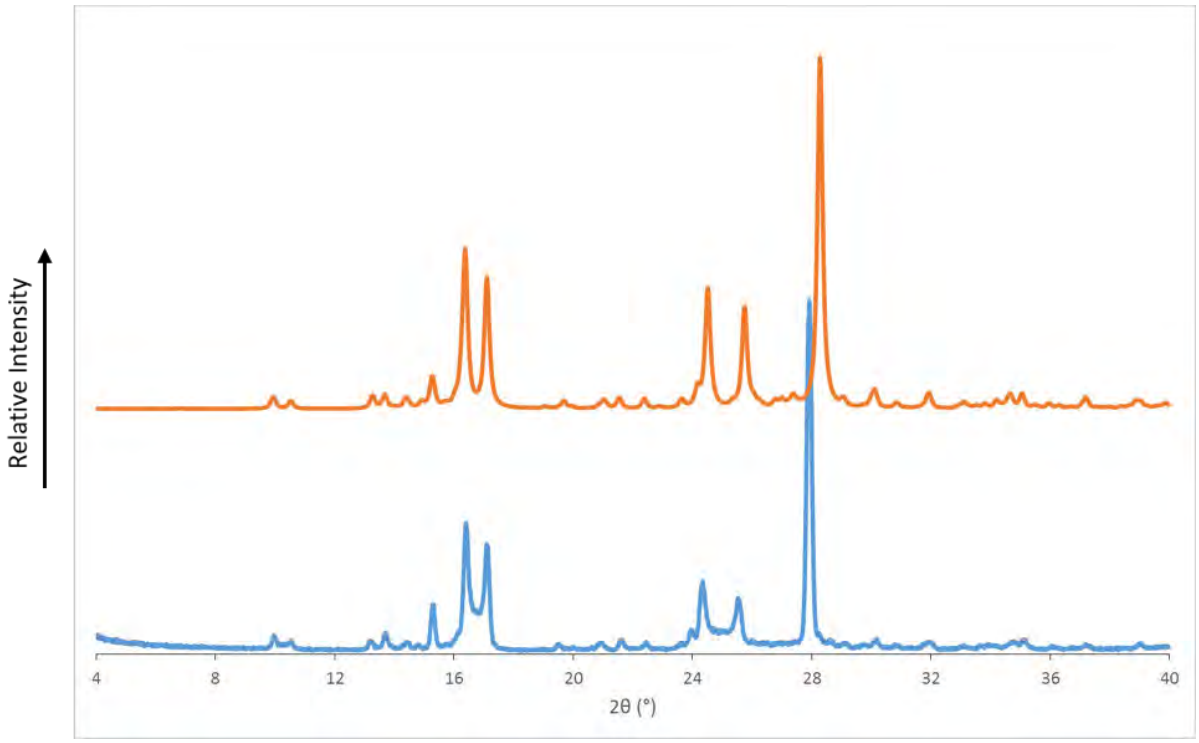

Figure 5.19: The PXRD trace recorded for the bulk sample (blue) and the computed PXRD pattern based on the single crystal X-ray structure of ACPAPYR (orange)

INFRARED SPECTROSCOPY

The position of the proton on the pyridyl nitrogen of 4-aminopyridine was directly observed in an electron-density map during single crystal X-ray analysis of the structure of ACPAPYR. The carboxylic acid proton of acipimox was not present in the structure. This showed that a proton transfer took place during the formation of ACPAPYR, so this crystalline system was designated a salt. Infrared spectroscopy was carried out to determine if the spectrum of ACPAPYR reflected this designation. The presence of relevant functional groups was confirmed by close inspection of the spectrum. Infrared spectroscopy was also used to explore the use of FTIR as a rapid method for identification of the salt. This was done by the observation of characteristic peaks, as well as comparing the spectra of the salt, API and co-former.

Two signals characteristic of carboxylate anions were observed in the FTIR spectrum of ACPAPYR (Figure 5.20) at 1583 cm^{-1} and 1358 cm^{-1}. A slight overlap of the symmetrical stretching peak of the carboxylate ion (1583 cm^{-1}) and the N-H bend (1649 cm^{-1}) of the primary amine of the 4-aminopyridine counterion was observed, but these are distinct enough for the proposed interpretation. The presence of the carboxylate anion absorption peaks indicates the occurrence of a proton transfer, which supports the designation of ACPAPYR as a salt.

Several characteristic peaks are present in the new spectrum, notably the primary amine bend peak at 1649 cm^{-1} and the carboxylate absorption peaks at 1583 cm^{-1} and 1358 cm^{-1}. Another sharp peak at 3371 cm^{-1} and a broad peak from 3052 cm^{-1} to 3224 cm^{-1} indicative of hydrogen bonded amine groups could serve to aid in the identification of ACPAPYR *via* FTIR spectroscopy. By direct comparison of the spectrum of ACPAPYR with those of acipimox and 4-aminopyridine it is clear that a new product has been obtained from these starting materials. The intermolecular interactions between the components give rise to significant differences between the spectra; for example, the disappearance of the carbonyl peak (1701 cm^{-1}) and O-H signal (3554 cm^{-1}) in the acipimox spectrum and the shift in the primary amine group of 4-aminoyridine (3435 cm^{-1}). Therefore, through comparison of the spectra one can unequivocally establish the presence of a new phase and use the spectrum of the product as a reference for identifying the salt ACPAPYR.

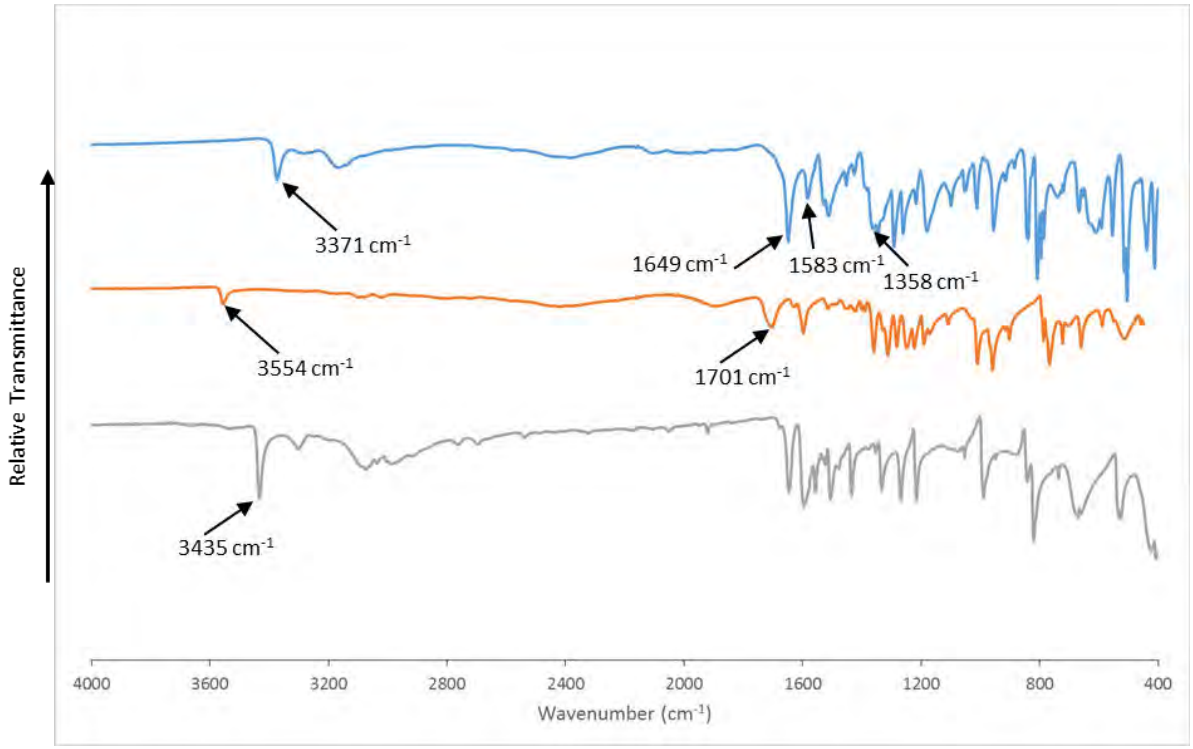

Figure 5.20: FTIR spectra for ACPAPYR (blue), acipimox (orange) and 4-aminopyridine (grey)

ACIPIMOX/4-AMINOPYRIDINE DIHYDRATE

This multi-component crystalline system has been designated the code name ACPAPYR-W.

SAMPLE PREPARATION

This product was prepared *via* co-precipitation. Co-precipitation of ACPAPYR-W was performed by dissolving acipimox (10 mg, 0.065 mmol) in 3 cm^3 propan-1-ol and adding an equimolar quantity of 4-aminopyridine (6 mg, 0.065 mmol). The resulting mixture was stirred for 2 to 4 hours at 60 °C. A drop of water was added to solubilise the remaining suspension and the resulting solution was then filtered through a 0.45 µm nylon filter into a clean vial. The vial was sealed with Parafilm™ pierced with several holes and allowed to stand on the benchtop to form crystals *via* slow evaporation. Over the course of several days large needle-shaped crystals were observed.

STOICHIOMETRY

The stoichiometry of the product was determined using ^{1}H-NMR spectroscopy. The needle-shaped crystals obtained from co-precipitation were dissolved in DMSO-d_6 and subjected to ^{1}H-NMR spectroscopy. The integration of the acipimox methyl protons were used as the reference integral. Integration of this peak and the 4-aminopyridine peaks were used to determine a 1:1 stoichiometric ratio. The proton labelling schemes of the two components are shown in Figure 5.21. The integration values and spectrum are presented in Table 5.9 and Figure 5.22 respectively.

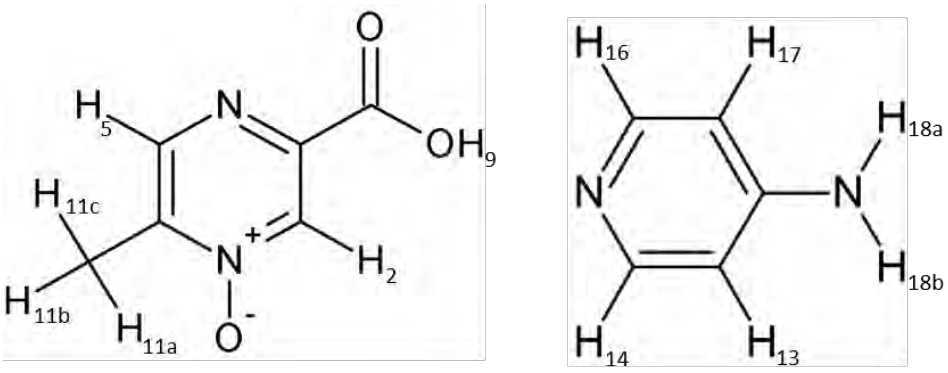

Figure 5.21: Proton labelling of acipimox (left) and 4-aminopyridine (right)

Table 5.9: Integrals and assignment of component protons for stoichiometric determination

Proton	**δ (ppm)**	**Integration**		**Experimental/ Theoretical**
		Experimental	Theoretical	
Acipimox				
C-$H_{11a,b,c}$	2.38	3.00‡	3.00	1
C-H_2	8.54	1.02	1	1.02 ≈ 1
C-H_5	8.62	1.05	1	1.05 ≈ 1
4-aminopyridine				
C-H_{13} + C-H_{17}	6.76	2.18	2	1.09 ≈ 1
C-H_{14} + C-H_{16}	8.15	2.17	2	1.09 ≈ 1

‡ *Reference integral*

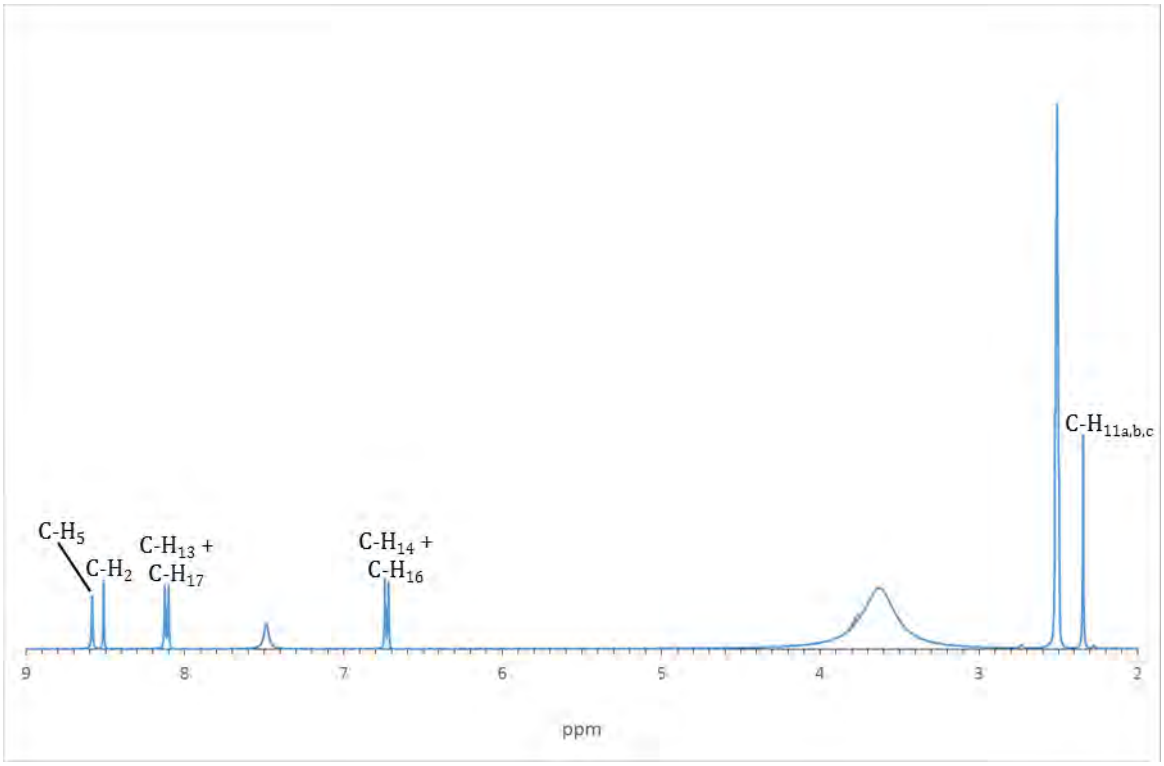

Figure 5.22: ^{1}H-NMR spectrum of ACPAPYR-W in DMSO-d_6 used to determine the stoichiometric ratio of the organic components

THERMAL ANALYSIS

The TGA profile of ACPAPYR-W shows two mass losses. The first, a mass loss of 11.7 ± 0.1 % (n = 2), equates to the loss of two water molecules per formula unit (calculated = 12.7 %). A broad endotherm characteristic of solvent loss is observed in the DSC trace over the same temperature range as the loss of the two water molecules. The second, larger mass loss corresponds to the decomposition of the multi-component crystal. The decomposition occurs simultaneously with melting at 249.2 ± 0.1 °C (n = 2), as is evident from the overlay of the DSC and TGA traces (Figure 5.23). A smaller endotherm at 206.9 ± 0.7 °C was observed in the DSC trace, attributable to a phase change of the dehydrated material. The HSM micrograph (Figure 5.24) at 108 °C shows the loss of the water molecules through bubbling. The decomposition of the resulting system can be seen in the micrograph at 245 °C.

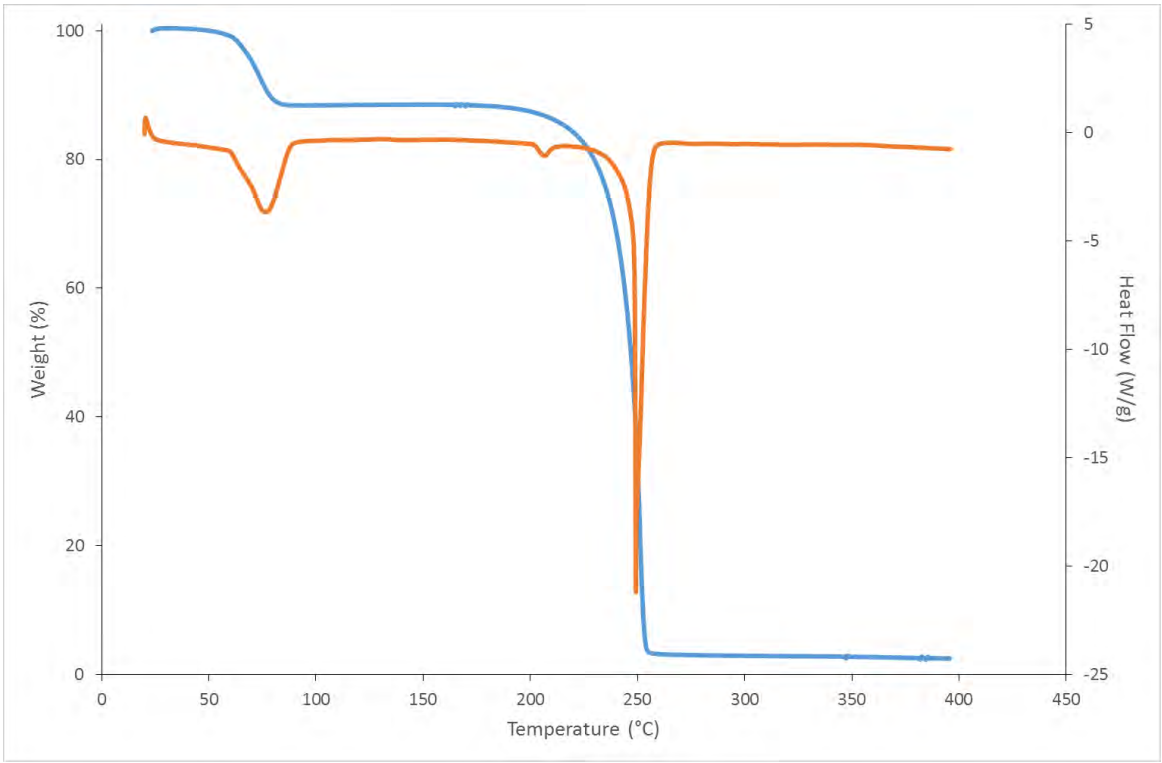

Figure 5.23: Representative TGA (blue) and DSC (orange) traces for ACPAPYR-W

Figure 5.24: Hot stage micrographs showing the ACPAPYR-W crystals at various stages of heating

The removal of water from ACPAPYR-W results in the anhydrous salt ACPAPYR, confirmed from the PXRD trace of the dehydrated material. This conversion was not pursued in detail.

CRYSTAL STRUCTURE ANALYSIS

DATA COLLECTION AND SPACE GROUP DETERMINATION

The crystal intensity data were collected at 173 ± 2 K on a BRUKER APEX II Duo diffractometer. The Laue symmetry was found to be *2/m* indicating that the crystal system is monoclinic. The space group was determined to be $P2_1/c$ by examination of the systematic absences. The conditions limiting reflections to determine the assignment were *hkl: none; h0l: l = 2n; 0k0, k = 2n.*

STRUCTURE SOLUTION AND REFINEMENT

The software program SAINT[10] was used for data reduction and unit cell refinement. The program SADABS,[11] employing the multi-scan method, was used for absorption correction. The asymmetric unit of ACPAPYR-W comprises one acipimox moiety, one 4-aminopyridine moiety and two water molecules. The atomic positions of the components were determined using direct methods in SHELXS.[5] The program SHELXL[5,6] was used to refine the structure isotropically once the atoms were placed in the presumed positions. All non-hydrogen atoms were subsequently refined anisotropically. The location of the hydrogen atoms, observed from the difference Fourier map, was of importance to designate the product as a co-crystal or salt. The presence of a hydrogen atom on the pyridyl nitrogen of 4-aminopyridine, and lack of a proton on the carboxylate ion of acipimox, indicated that a proton transfer had taken place. The absence of a hydrogen atom on the carboxylate moiety of acipimox was supported by the intermediate bond distance of the C-O bonds. The two relevant bonds have bond distances 1.250(2) Å and 1.250(1) Å respectively. As the 4-aminopyridine and acipimox species are charged, the multi-component crystalline system can unequivocally be designated as a hydrated salt. Once the hydrogen atoms were located they were placed in geometrically idealised positions. A riding model was used in which the U_{iso} values are 1.2 to 1.5 those of the parent atoms. The crystallographic data and intensity data-collection parameters are shown in Table 5.10.

Table 5.10: Crystallographic data for the single crystal X-ray structure of ACPAPYR-W

Chemical Formula	$(C_6H_5N_2O_3)^-\cdot(C_5H_7N_2)^+\cdot 2(H_2O)$
Molar mass (g mol^{-1})	284.28
Crystal System	Monoclinic
Space Group	$P2_1/c$
Unit cell parameters	
a (Å)	9.5838(8)
b (Å)	15.2531(13)
c (Å)	9.0906(8)
α (°)	90
β (°)	90.844(2)
γ (°)	90
Volume (Å^3)	1328.7(2)
Z	4
Density$_{calcd.}$ (g cm^{-3})	1.421
μ [MoKα] (mm^{-1})	0.71073
F (000)	600
Temperature (K)	173(2)
Crystal size (mm)	0.46×0.28×0.11
Range scanned θ (°)	2.1 – 27.1
Index ranges	h: -12, 7; k: -19, 16; l: -11, 11
ϕ and ω scan angle (°)	0.50
Total number of frames	1210
Dx (mm)	39.8
Total number of reflections	11 292
Number of independent reflections	2 882
Number of reflections with I > 2σ(I)	2 480
R_{int}	0.0428
R_1 [I > 2σ(I)]	0.0345
wR_2	0.0943
S	1.032
Number of parameters	188
Number of reflections omitted	4
Parameters a, b	a = 0.0513; b = 0.3243
in w = 1/[σ^2(F_0^2)+(aP)^2+(bP)]	
$(\delta/\sigma)_{mean}$	<0.001
Δρ excursions (e Å^{-3})	-0.21; 0.25

MOLECULAR STRUCTURE

The asymmetric unit of ACPAPYR-W, shown in Figure 5.25, contains one acipimox anion, one 4-aminopyridine cation and two water molecules. The proton transfer takes place from the carboxylic group of acipimox to the pyridyl nitrogen of 4-aminopyridine during formation. The two water molecules are hydrogen bonded to the acipimox anion. The intermolecular interactions will be described in further detail in the following section, entitled Hydrogen Bonding.

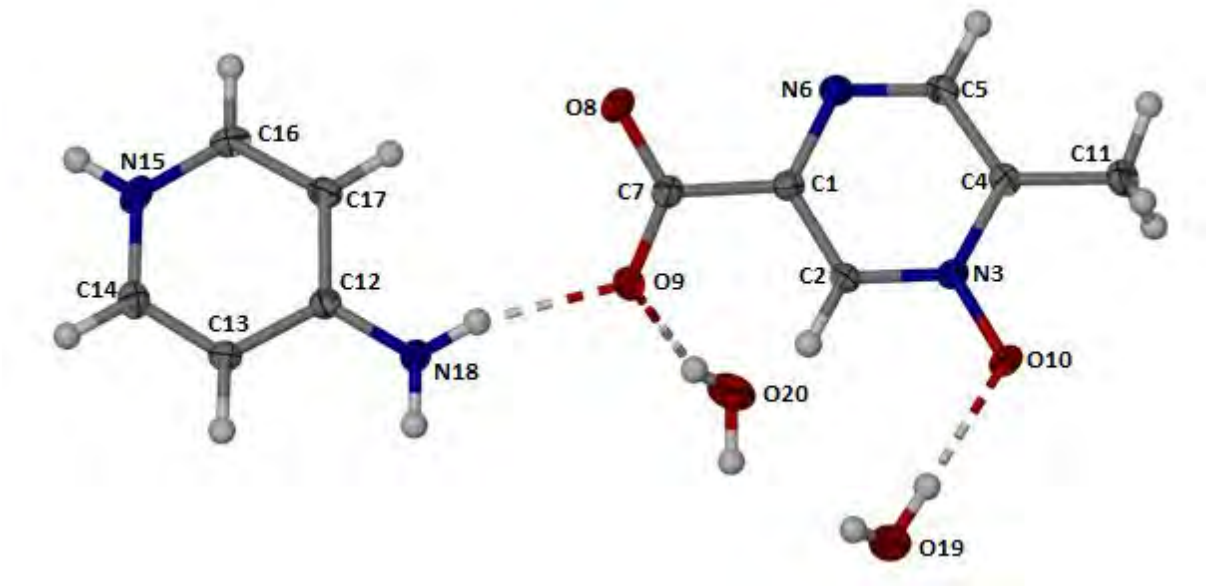

Figure 5.25: The asymmetric unit of the salt ACPAPYR-W with numbering schemes of acipimox (right) and 4-aminopyridine (left). Thermal ellipsoids are drawn at the 50 % probability level

HYDROGEN BONDING

The ACPAPYR-W structure contains several hydrogen bonding patterns. These patterns are assembled from eight hydrogen bonds whose parameters are listed in Table 5.11. Four of these occur directly between the acipimox and 4-aminopyridine molecular ions and the remaining are interactions with the two water molecules. Acipimox acts as an acceptor in all seven classical hydrogen bonds in which this component is involved. The 4-aminopyridine cation acts as the donor for four of these. The water molecules act as donors for the remaining three hydrogen bonds and are involved in hydrogen bonding as both donors and acceptors.

Table 5.11: Hydrogen bonding interactions present in ACPAPYR-W

D-H···A	D···A (Å)	Angle (°)	Symmetry Operator
N15-H···O8	2.781(1)	142	(*1+x, y, -1+z*)
N15-H···N6	3.094(1)	141	(*1+x, y, -1+z*)
N18-H···O10	2.947(1)	172	(*x, y, z*)
N18-H···O9	2.826(1)	164	(*1-x, 1/2+y, 1/2-z*)
O19-H···O10	2.801(1)	178	(*x, y, z*)
O19-H···O8	2.767(1)	169	(*1-x, 1-y, 1-z*)
O20-H···O9	2.923(1)	166	(*x, y, z*)
O20-H···O19	2.801(1)	167	(*1-x, 1-y, -z*)
C5-H···O20	3.450(2)	161	(*x, 3/2-y, 1/2+z*)
C13-H···O19	3.495(2)	169	(*x, y, z*)
C16-H···O20	3.157(2)	149	(*1+x, 3/2-y, -1/2+z*)

The hydrogen bonds form five concatenated hydrogen bonded ring patterns. The first involves interactions among four water molecules and two acipimox anions about a centre of inversion and is described by the graph-set designator $N_1 = R_6^6(22)$. This network N_1 can be seen in Figure 5.26.

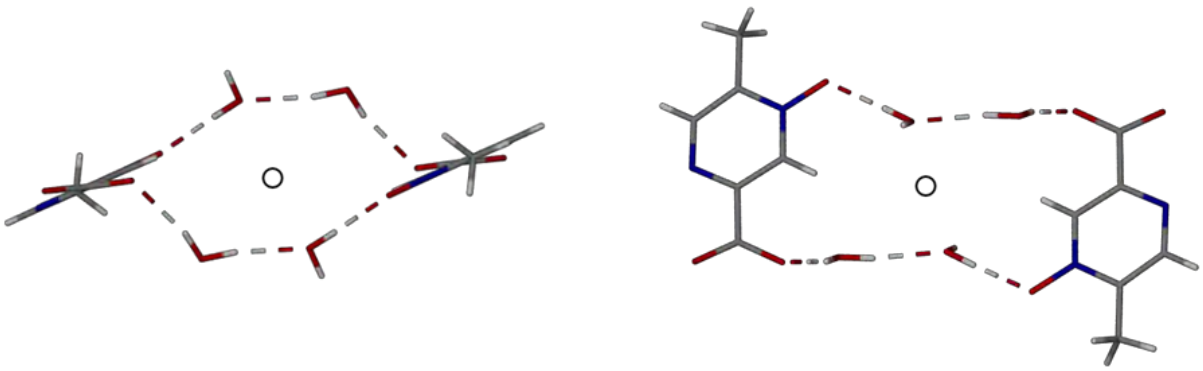

Figure 5.26: Two views of the acipimox anion-water hydrogen bonding scheme in the network $N_1 = R_6^6(22)$ located at an inversion centre

The second pattern takes the form $N_2 = R_6^6(31)$ and involves three acipimox anions and three 4-aminopyridine cations. This is shown in Figure 5.27.

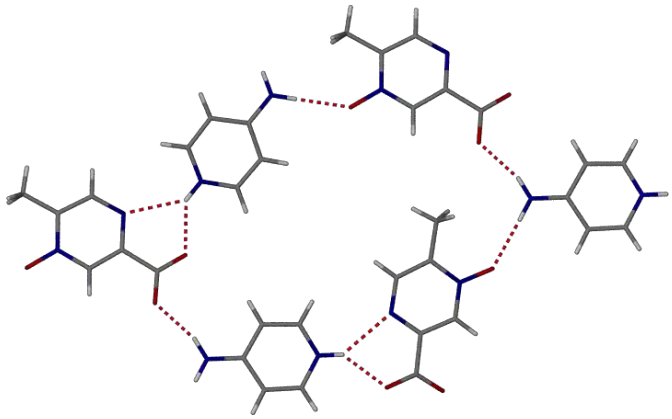

Figure 5.27: Acipimox anions and 4-aminopyridine cations hydrogen bonding to form the pattern $N_2 = R_6^6(31)$

The pattern N_3 comprises a ring with eight hydrogen bond donors and four acceptors, shown in Figure 5.28. This pattern forms about a centre of inversion with four acipimox anions linked through two water molecules and two 4-aminopyridine cations. This pattern is described by the graph-set designator $N_3 = R_8^4(24)$ and is located at a centre of inversion.

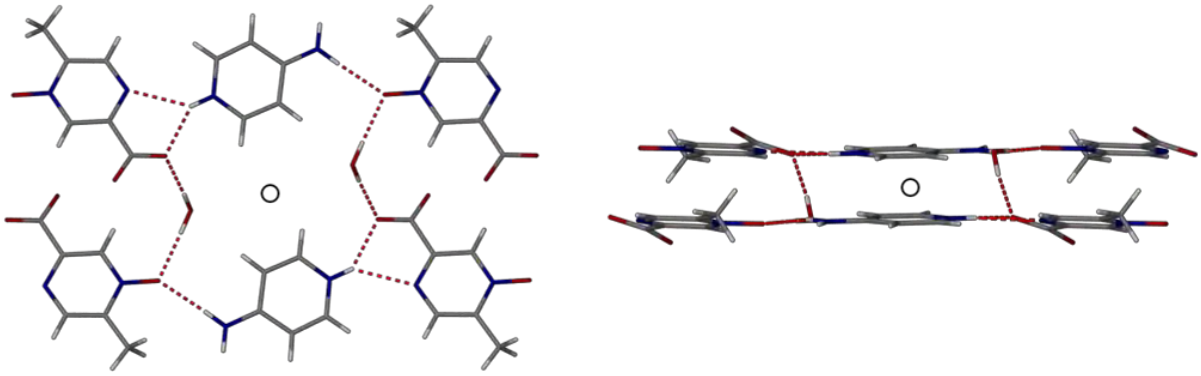

Figure 5.28: Two views of acipimox anions with 4-aminopyridine cations and water hydrogen bonding to form the pattern $N_3 = R_8^4(24)$ about a centre of inversion

The ring $N_4 = R_4^4(18)$ is formed by the interaction between two acipimox anions and two water molecules. This pattern is located on a centre of inversion.

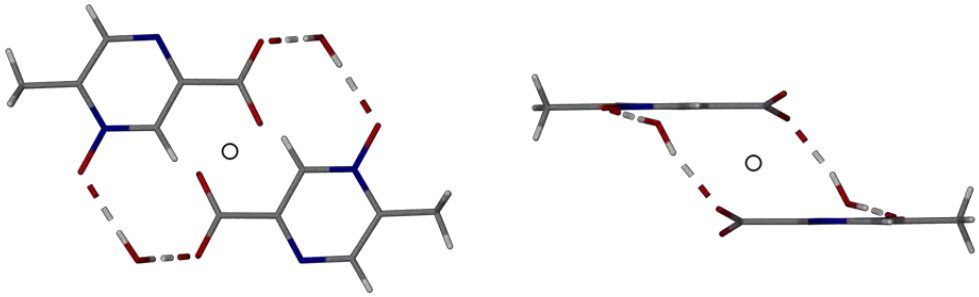

Figure 5.29: Two views of acipimox anions and water molecules hydrogen bonding to form the pattern $N_4 = R_4^4(18)$ about a centre of inversion

The final hydrogen bonded ring occurs between a single acipimox anion and a single 4-aminopyridine counterion. The hydrogen bonding is bifurcated, linking the pyridyl N-H donor to the pyrazine nitrogen and carboxylate anion acceptors. The pattern, $N_5 = R_1^2(5)$, is shown in Figure 5.30.

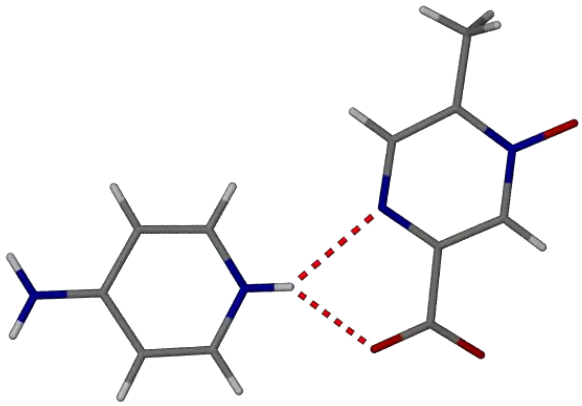

Figure 5.30: The acipimox anion and 4-aminopyridine cation hydrogen bonding to form the pattern $N_5 = R_1^2(5)$ mediated by a bifurcated hydrogen bond

The patterns above concatenate to form a complex hydrogen bonding scheme. The patterns N_2 to N_5 interconnect forming a large, stepped layer. The layers are linked through the N_1 pattern and the interconnectivity of the patterns can be seen in the stereo diagram Figure 5.31.

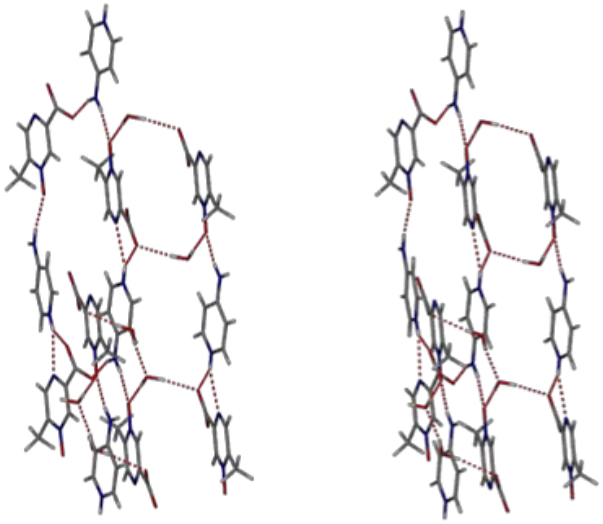

Figure 5.31: Stereo diagram showing the concatenated hydrogen bonding patterns present in ACPAPYR-W

CRYSTAL PACKING

The dihydrate of the acipimox/4-aminopyridine salt packs in layers of concatenated hydrogen bonding patterns N_2 to N_5. These layers are linked to subsequent layers through the hydrogen bonding pattern N_1. The linking of these layers *via* two water molecules in the hydrogen bonding pattern N_1 can be seen in Figure 5.32. The sequential stacking of the stepped layers is more clearly illustrated in Figure 5.33.

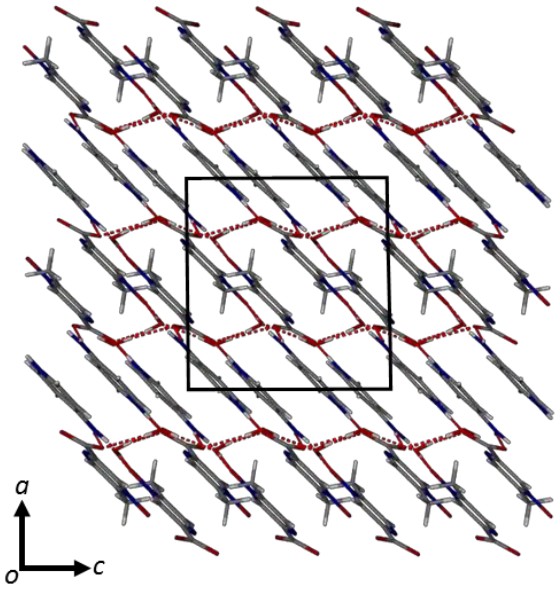

Figure 5.32: Packing of ACPAPYR-W showing layers of concatenated hydrogen bonding patterns linked through the pattern N_1

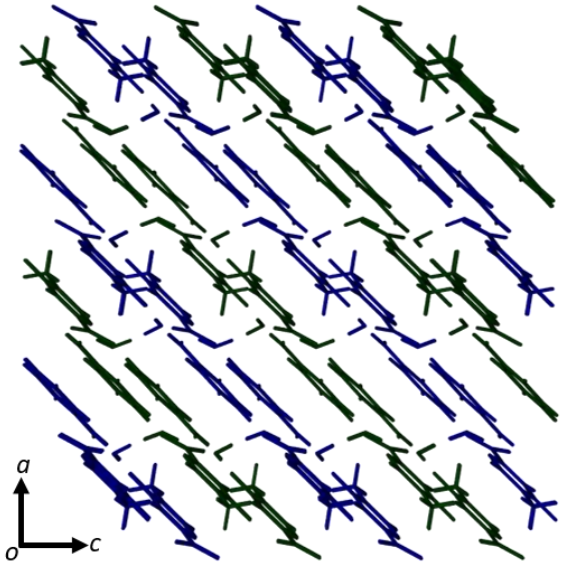

Figure 5.33: Highlighting of the stepped layers in the packing of ACPAPYR-W

COMPARATIVE PXRD

The PXRD pattern obtained from the bulk material (collected at room temperature) shows good agreement with the pattern calculated from the refined single crystal structure [data collected at 173(2) K]. The slight differences in the angular positions of the peaks arise from the differing temperatures of data collection. As the single crystal is cooled, the unit cell undergoes anisotropic contraction, which gives rise to slight angular shifts in the peak positions. The comparative PXRD is shown in Figure 5.34.

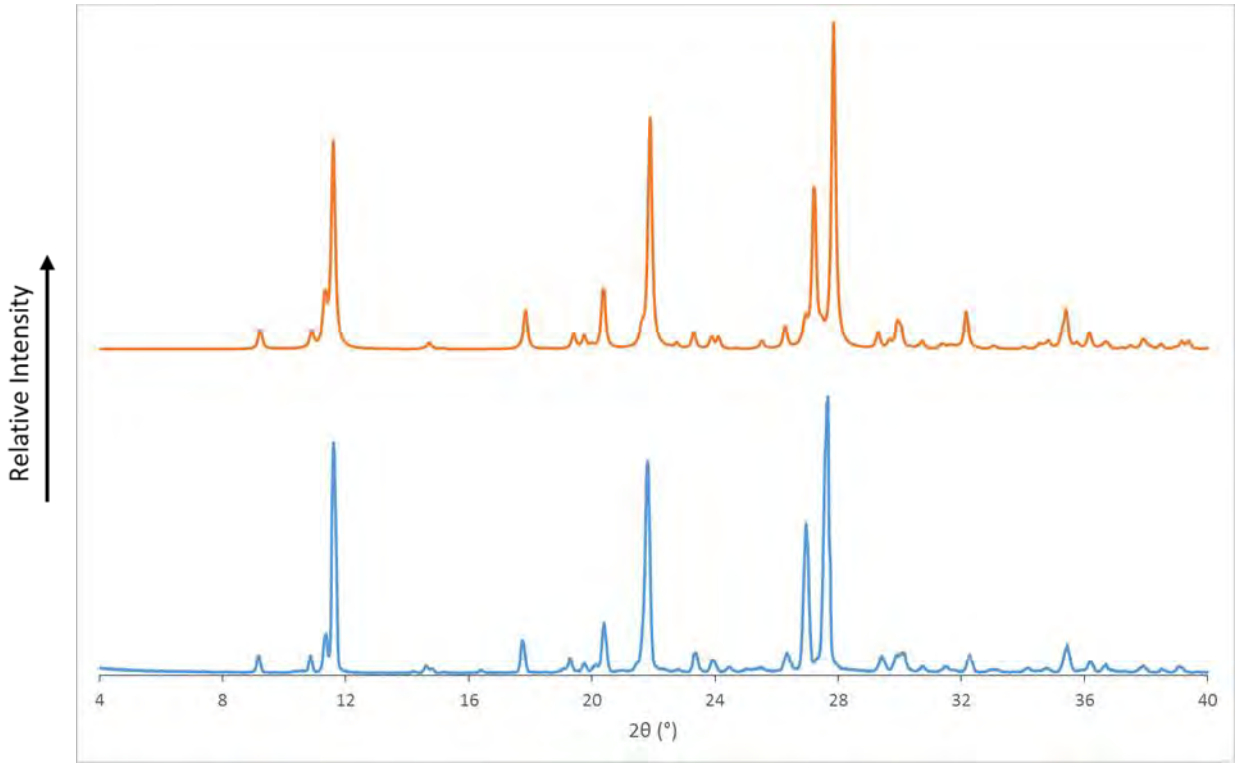

Figure 5.34: The PXRD trace recorded for the bulk sample (blue) and the computed PXRD pattern based on the single crystal X-ray structure of ACPAPYR-W (orange)

INFRARED SPECTROSCOPY

The lack of a proton on the carboxylate group of acipimox and the presence of a proton on the pyridyl nitrogen of the co-former were first observed unequivocally in a difference electron density synthesis during the single crystal X-ray structure determination of ACPAPYR-W. These observations led to the designation of ACPAPYR-W as a salt. As demonstrated previously, FTIR was employed to support the designation and to investigate the applicability of this method to rapid identification of the product.

The infrared spectrum of ACPAPYR-W (Figure 5.35) shows two signals characteristic of carboxylate anions. These signals were observed at 1575 cm^{-1} and 1373 cm^{-1}. The presence of these absorption peaks supports the designation of ACPAPYR-W as a salt. The lack of a signal corresponding to a carboxylic acid carbonyl bond vibration in the region of 1700 cm^{-1} provides further support for the designation.

The formation of a new phase was confirmed by the differences between the ACPAPYR-W spectrum and those of the starting materials. The acipimox spectrum shows an O-H signal at 3554 cm^{-1} and a carboxylic acid carbonyl signal at 1701 cm^{-1} which are not present in the salt spectrum. The counterion has a characteristic sharp amine peak at 3435 cm^{-1}, a feature that is not immediately identifiable in the ACPAPYR-W spectrum. In the ACPAPYR-W spectrum the region from 2951 cm^{-1} to 3486 cm^{-1} is interpreted as overlapping water and hydrogen bonded amine peaks. This region is characteristic of the product. The characteristic signals at 1575 cm^{-1} and 1373 cm^{-1} in the ACPAPYR-W spectrum can be used to rapidly identify the product. The region from 2951 cm^{-1} to 3486 cm^{-1} would further aid in this use of FTIR.

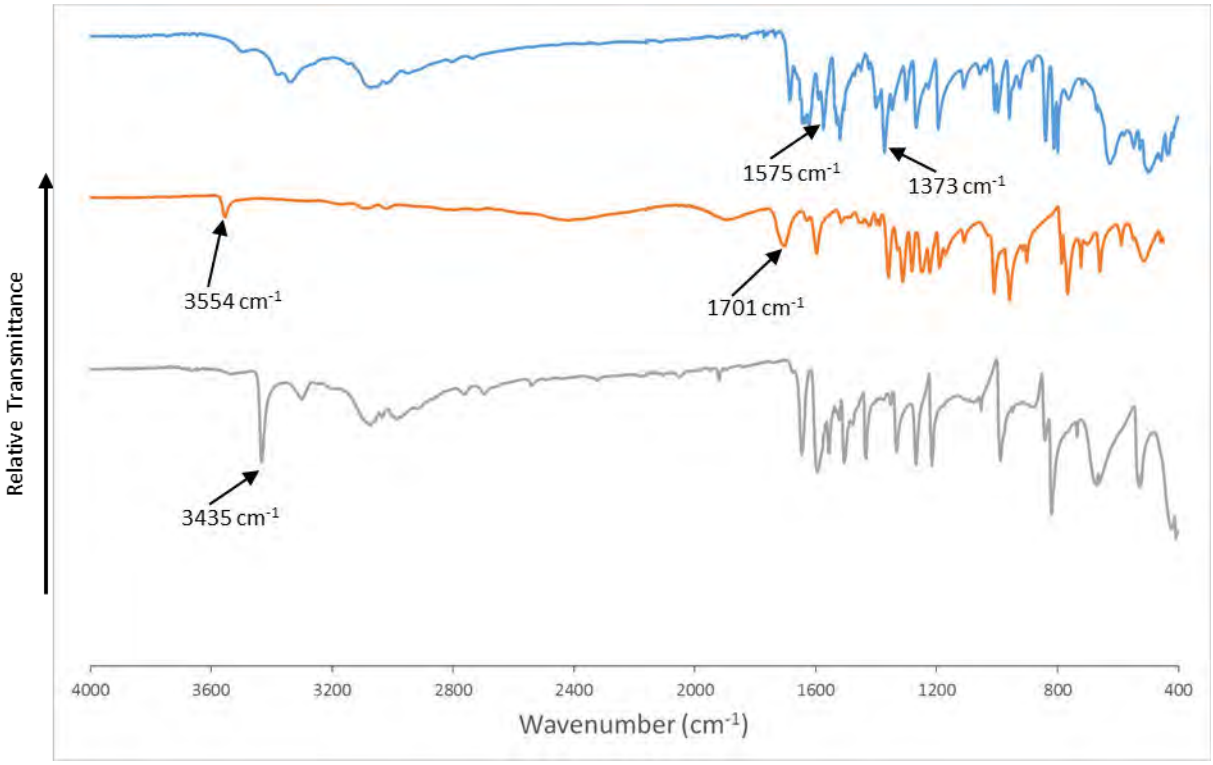

Figure 5.35: FTIR spectra for ACPAPYR-W (blue), acipimox (orange) and 4-aminopyridine (grey)

ACIPIMOX/BENZAMIDE

The multi-component crystalline system formed by acipimox and benzamide will be referred to as ACPBEN.

SAMPLE PREPARATION

The multi-component crystalline system of acipimox and benzamide was prepared in three ways. Two of these methods are mechanochemical in nature, while the third is co-precipitation.

To perform dry grinding and liquid-assisted grinding equimolar quantities of acipimox (10 mg, 0.065 mmol) and benzamide (8 mg, 0.065 mmol) were weighed out. The two compounds were combined in an agate mortar and ground together with an agate pestle for 15 minutes. This constituted the mechanochemical action for dry grinding. Liquid-assisted grinding was performed in the same manner, with the dropwise addition of a 50 % aqueous ethanol solution.

To obtain the product *via* co-precipitation, 10 mg (0.065 mmol) of acipimox was weighed out and dissolved in 3 cm^3 of a 50 % aqueous ethanol solution. An equimolar amount of benzamide (8 mg, 0.065 mmol) was added to the solution and the resulting mixture was stirred at 40 °C for 2 to 3 hours. The resulting solution was then filtered through a 0.45 μm nylon filter into a clean vial and placed on the benchtop to slowly evaporate. Over the course of several days plate-shaped crystals appeared in the solution.

STOICHIOMETRY

The acipimox to benzamide molar ratio was determined using ^{1}H-NMR spectroscopy. Due to the hygroscopic nature of the deuterated solvent DMSO-d_6, it was not possible to use this technique to determine the amount of water in the crystal. The plate-shaped crystals obtained by co-precipitation were dissolved in DMSO-d_6 and subjected to ^{1}H-NMR spectroscopy. The relative integration of the acipimox methyl group protons (set as the reference integral) and the aromatic protons of benzamide served to determine the 1:1 stoichiometric ratio. The proton labelling scheme of the components is shown in Figure 5.36. The integration values are presented in Table 5.12 and the ^{1}H-NMR spectrum is shown in Figure 5.37.

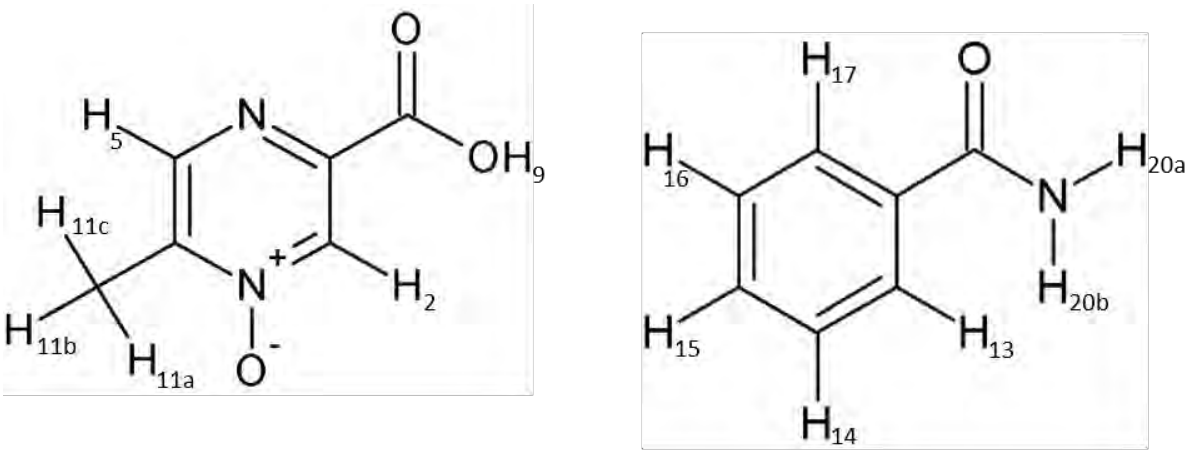

Figure 5.36: Proton labelling of acipimox (left) and benzamide (right)

Table 5.12: Integrals and assignment of component protons for stoichiometric determination

Proton	**δ (ppm)**	**Integration**		**Experimental/ Theoretical**
		Experimental	Theoretical	
Acipimox				
C-$H_{11a,b,c}$	2.38	3.00‡	3.00	1
C-H_2	8.69	1.06	1	1.06 ≈ 1
C-H_5	8.75	1.06	1	1.06 ≈ 1
Benzamide				
C-H_{13} + C-H_{17}	7.91	2.30	2	1.15 ≈ 1

‡ *Reference integral*

It should be noted that the integration of benzamide protons was problematic as the aromatic hydrogens partially overlap the amide hydrogens. However, the signals of C-H_{13} and C-H_{17} are sufficiently distinct for the purposes of stoichiometric ratio determination.

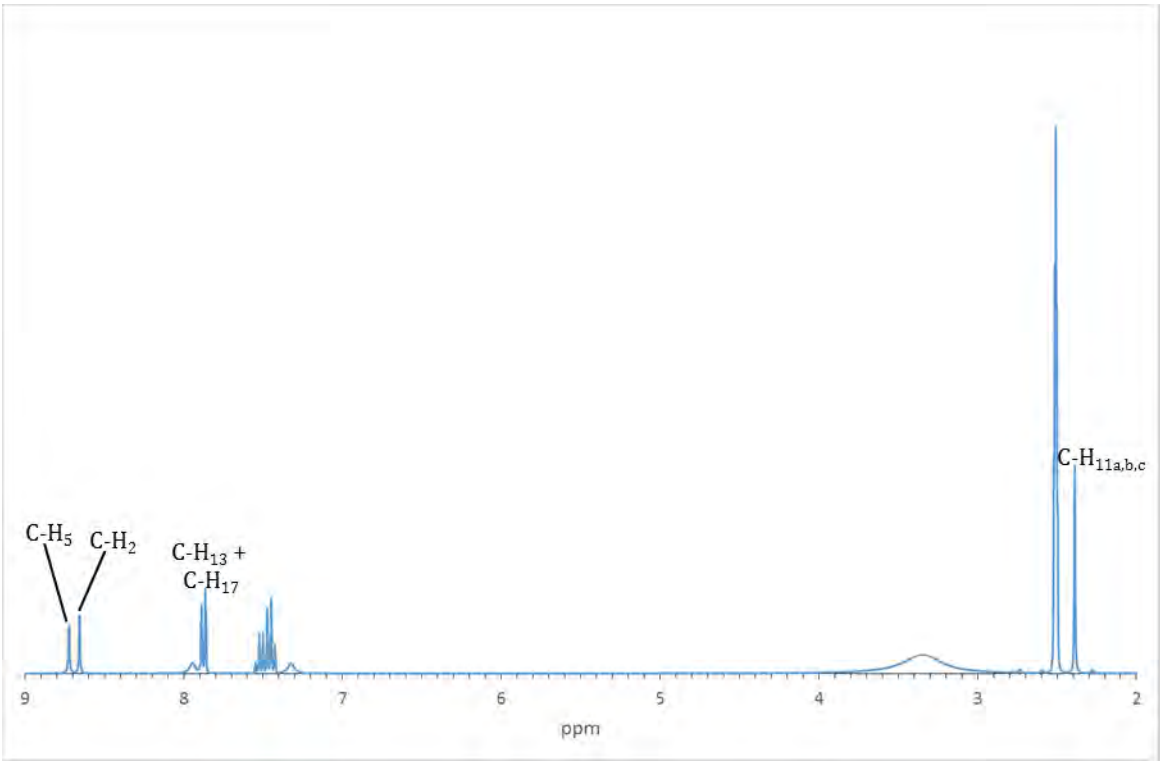

Figure 5.37: ^{1}H-NMR spectrum of ACPBEN in DMSO-d_6 used to determine the stoichiometric ratio

THERMAL ANALYSIS

The TGA profile (Figure 5.38) displays a protracted mass loss of 2.7 ± 0.2 % from 79.1 ± 0.6 °C (n = 2) to 125.0 ± 0.8 °C. This corresponds to the loss of half a water molecule per multi-component crystal unit (calculated = 3.2 %). From 138.9 ± 0.8 °C to 203.8 ± 1.8 °C the TGA trace exhibits a large mass loss resulting from the decomposition of the dehydrated product. The DSC trace for ACPBEN (Figure 5.38) does not have an endotherm corresponding to the loss of the half water molecule as the heat flow for such an event is negligible. The DSC shows a combined melting and onset of degradation endotherm at 133.9 ± 1.3 °C (n = 2) followed immediately by a broad endotherm characteristic of decomposition. The hot stage micrograph at 119 °C (Figure 5.39) shows the opaque crystals resulting from dehydration. The micrograph at 139 °C shows the beginning stages of melting and decomposition. The completely decomposed product can be seen in the micrograph at 233 °C.

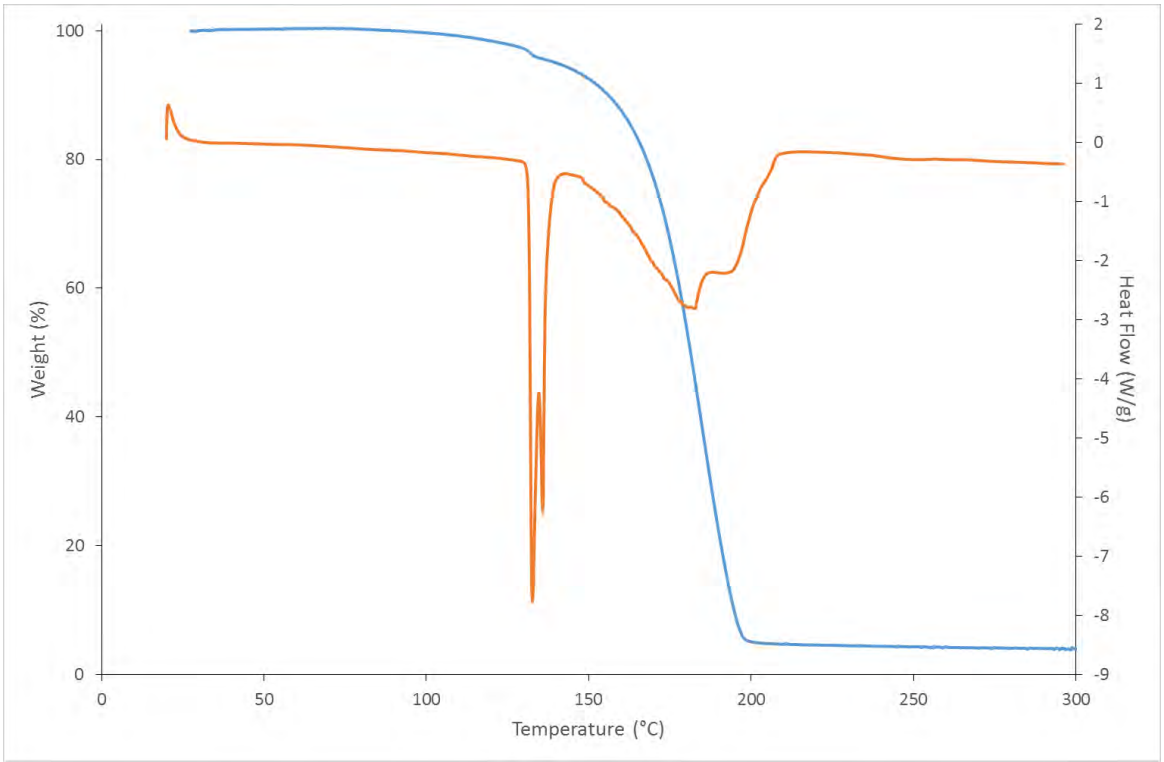

Figure 5.38: Representative TGA (blue) and DSC (orange) traces for ACPBEN

Figure 5.39: Hot stage micrographs showing the ACPBEN crystals at various stages of heating

CRYSTAL STRUCTURE ANALYSIS

DATA COLLECTION AND SPACE GROUP DETERMINATION

The intensity data for the single crystal structure were collected at 173 ± 2 K using a Bruker KAPPA APEX DUO II diffractometer. The crystal system was found to be monoclinic, based on the determined Laue symmetry *2/m*. The conditions limiting possible reflections were as follows: *hkl: h+k = 2n; h0l, l = 2n; (h = 2n); 0k0: (k = 2n),* which indicate the space group C2/*c* (centrosymmetric) or C*c* (non-centrosymmetric). From the value of $|E^2-1| = 0.968$ calculated by the program XPREP[3] centrosymmetry was indicated and hence the former space group was selected for structure solution. This choice was vindicated by the successful structure determination and refinement.

STRUCTURE SOLUTION AND REFINEMENT

Data reduction and unit cell refinement were performed using the software program SAINT.[10] The multi-scan method was used by the absorption correction program SADABS.[11] One acipimox molecule, one benzamide molecule and half a water molecule make up the asymmetric unit of ACPBEN. The atomic co-ordinates were determined by SHELXS[5] employing direct methods. After the atoms were placed in their presumed positions, SHELXL[5,6] was used to refine the structure. All non-hydrogen atoms were initially refined isotropically and later anisotropically. Careful inspection of the position of the carboxylic acid proton of the acipimox moiety was required to investigate the absence of a proton transfer. The hydrogen atom in question was located in the difference Fourier map on the carboxylic acid group of the acipimox molecule. The acipimox and benzamide molecules were both found to be present in a neutral state. This led to the designation of ACPBEN as a co-crystal. The designation was further supported by the distinct C-O bond distances of the carboxylic acid functional group of 1.214(2) Å and 1.311(2) Å. Once all the hydrogen atoms were located in the difference Fourier map, they were placed in idealised positions using a riding model. In the riding model, the U_{iso} values were set as 1.2 to 1.5 times those of the parent atoms.

Table 5.13: Crystallographic data for the single crystal X-ray structure of ACPBEN

Chemical Formula	$C_6H_6N_2O_3 \cdot C_7H_7NO \cdot (H_2O)_{0.5}$
Molar mass (g mol^{-1})	284.27
Crystal System	Monoclinic
Space Group	C2/c
Unit cell parameters	
a (Å)	12.526(7)
b (Å)	7.317(4)
c (Å)	28.394(16)
α (°)	90
β (°)	93.704(11)
γ (°)	90
Volume (Å^3)	2597(3)
Z	8
Density$_{calcd.}$ (g cm^{-3})	1.454
μ [MoKα] (mm^{-1})	0.112
F (000)	1192
Temperature (K)	173(2)
Crystal size (mm)	0.10×0.23×0.35
Range scanned θ (°)	2.9 – 28.3
Index ranges	h: -16, 15; k: -9, 9; l: -37, 37
ϕ and ω scan angle (°)	0.50
Dx (mm)	50.0
Total number of reflections	15 549
Number of independent reflections	3 487
Number of reflections with I > 2σ(I)	2 482
R_{int}	0.0508
R_1 [I > 2σ(I)]	0.0389
wR_2	0.1052
S	1.03
Number of parameters	192
Number of reflections omitted	3
Parameters a, b	0.0498; 1.0975
in w = 1/[$\sigma^2(F_O^2)$+(aP)^2+(bP)]	
$(\delta/\sigma)_{mean}$	<0.001
Δρ excursions (e Å^{-3})	-0.21; 0.30

MOLECULAR STRUCTURE

The asymmetric unit of the co-crystal hemihydrate ACPBEN, shown in Figure 5.40, comprises one acipimox molecule, one benzamide molecule and half a water molecule. The water molecule is located on a crystallographic two-fold rotation axis. In the asymmetric unit the components of the structure interact *via* the carboxylic acid - amide hydrogen bonding synthon. The components are in their neutral state.

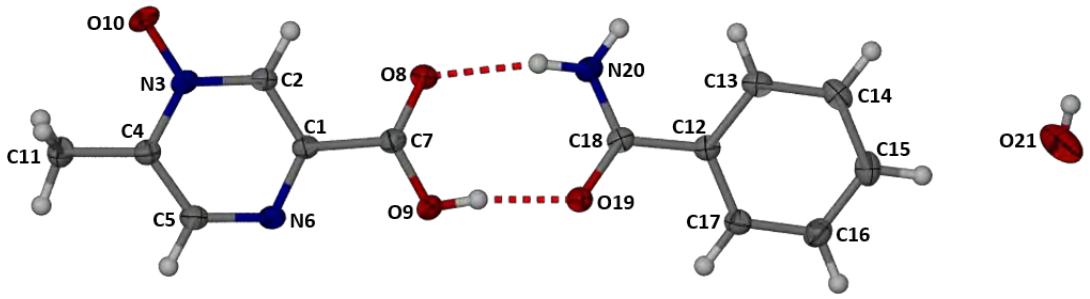

Figure 5.40: The asymmetric unit of the hemihydrated co-crystal ACPBEN with numbering schemes. Thermal ellipsoids are drawn at the 50 % probability level

HYDROGEN BONDING

There are four hydrogen bonds present between the components in this structure. The first two occur in the carboxylic acid – amide synthon between acipimox and benzamide (Figure 5.41a). The third occurs between the amide group of benzamide and the pyrazine nitrogen of acipimox (Figure 5.41b). The fourth hydrogen bond links the pyrazine oxygen atom of acipimox and the water molecule (Figure 5.41c). The hydrogen bonding parameters are shown in Table 5.14.

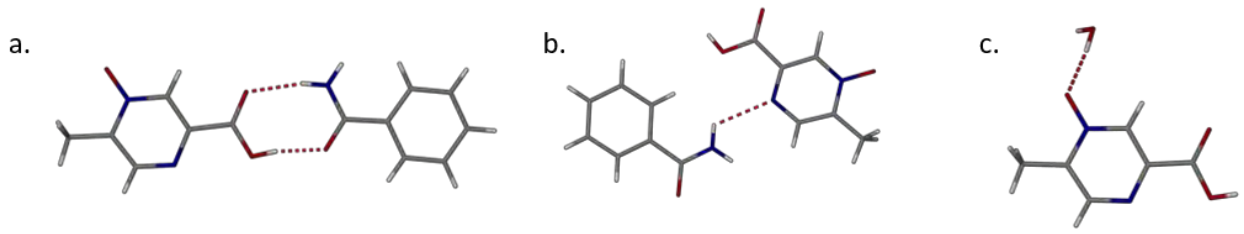

Figure 5.41: Hydrogen bonding synthons present in ACPBEN

Table 5.14: Hydrogen bonding interactions in ACPBEN

D-H···A	D···A (Å)	Angle (°)	Symmetry Operator
O9-H···O19	2.582(2)	170	(*x, y, z*)
N20-H···O8	2.877(2)	166	(*x, y, z*)
N20-H···N6	2.998(2)	117	(*x, -1+y, z*)
O21-H···O10	2.825(2)	174	(*1-x, -1-y, 1-z*)
C5-H···O8	3.258(2)	149	(*x, 1+y, z*)
C11-H···O10	3.266(3)	128	(*3/2-x, 1/2 + y, 3/2-z*)
C15-H···O21	3.386(3)	150	(*x, y, z*)

The hydrogen bonds above form two hydrogen bonding patterns. Figure 5.42 shows the $N_1 = R_2^2(8)$ synthon formed between the carboxylic acid group of acipimox and the amide group of benzamide. The second pattern, N_2, is a large ring created from four acipimox molecules, two benzamide molecules and two water molecules. The water molecules are located on a two-fold rotation axis. This second pattern, $N_2 = R_8^8(34)$, is shown in Figure 5.43.

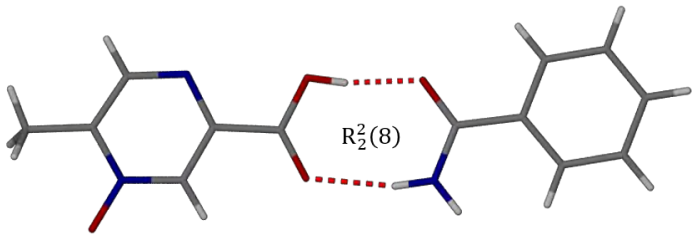

Figure 5.42: The hydrogen bonding synthon, $N_1 = R_2^2(8)$, between acipimox and benzamide in ACPBEN

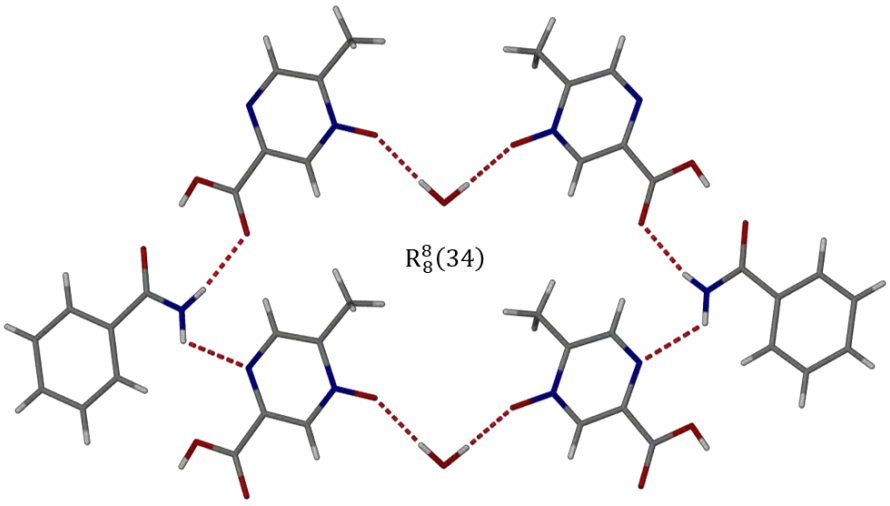

Figure 5.43: The hydrogen bonding pattern, $N_2 = R_8^8(34)$, occurring in ACPBEN

CRYSTAL PACKING

The hydrogen bonding patterns N_1 and N_2 combine to form stepped layers, shown in Figure 5.44a. The stepped nature of the layers is shown in Figure 5.44b. with the water molecules shown linking the N_1 synthon to create the N_2 hydrogen bonding pattern.

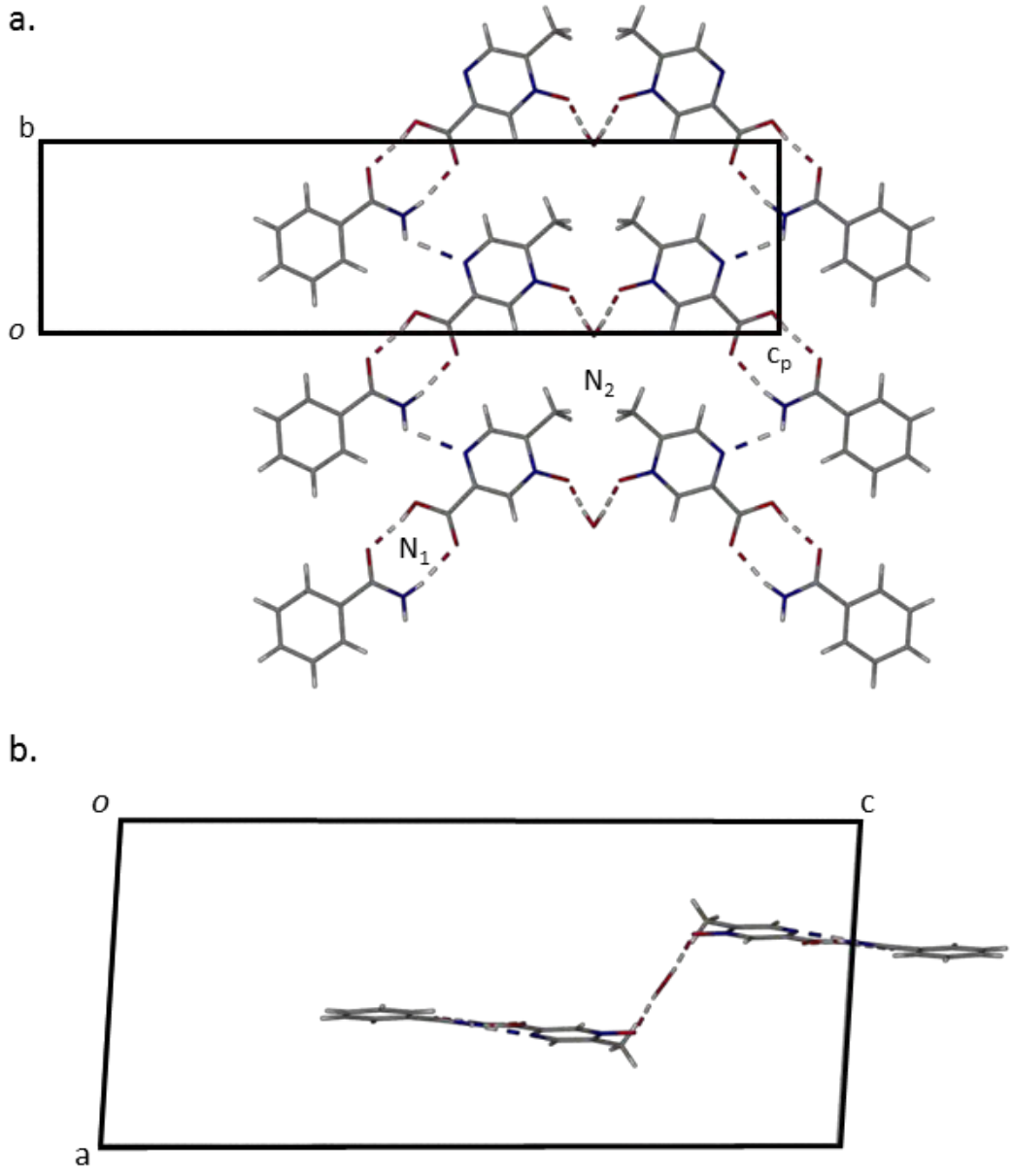

Figure 5.44: The connectivity of the patterns viewed along a. [1 0 0] showing the N_1 and N_2 patterns and b. along [0 1 0] showing the stepped layers linked through the water molecules

The co-crystal ACPBEN forms stepped layers made up of the network N = $R_2^2(8)R_8^8(34)$. These layers interdigitate. The hydrogen bond C5-H···O8 occurs within the layers formed by the network. The interdigitated nature of the hydrogen bonding patterns can be seen in Figure 5.45 and Figure 5.46. The packing of this structure is stabilised by C-H···O hydrogen bonds detailed in

Table 5.14 above. The C5-H···O8‡ (‡: *x, 1+y, z*) hydrogen bonds link the interdigitated layers stacking along the *a*-axis. The C11-H···O10‡ (‡: *3/2-x, 1/2 + y, 3/2-z*) hydrogen bond connects the layers along the *c*-axis.

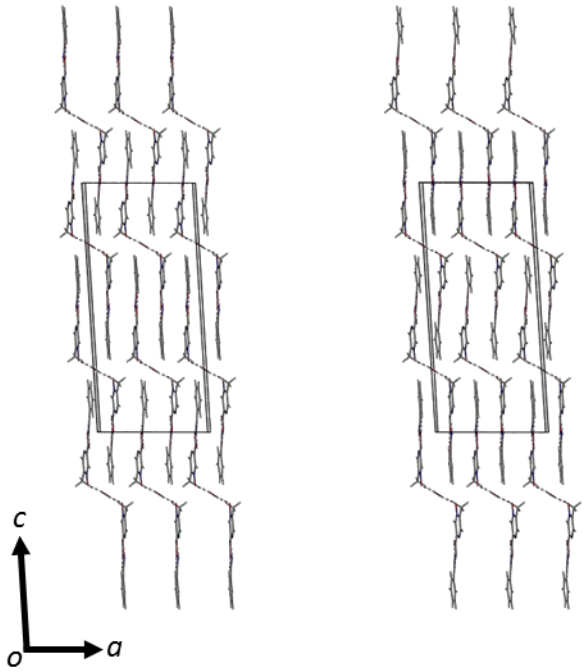

Figure 5.45: Stereo diagram showing the packing of ACPBEN viewed along [0 1 0] featuring the interdigitating stepped layers

The crystal packing is further stabilised by π-π stacking, whose parameters are presented in Table 5.15. The two π-interactions occur between the aromatic rings of acipimox and benzamide. In the π-π stacking interaction labelled 1 in Table 5.15, the centroids are offset by approximately 1.2 Å. The interaction labelled 2 has a centroid-to-centroid offset of approximately 1.5 Å. In both π-π interactions the least-squares planes of the aromatic rings intersect at an angle of 3.2(1)°.

Table 5.15: π-π interaction parameters in ACPBEN

Label	Ring Interaction	Centroid-centroid Distance (Å)	Symmetry Operator
1	Cg(A)···Cg(B)	3.608(2)	(*1-x, -y, 1-z*)
2	Cg(A)···Cg(B)	3.682(2)	(*3/2-x, -1/2-y, 1-z*)

Cg refers to the centroid of a ring and the symmetry operator in column 3 refers to the second Cg listed in column 1

Ring A: C1-C2-N3-C4-C5-N6

Ring B: C12-C13-C14-C15-C16-C17

COMPARATIVE PXRD

The PXRD pattern of the bulk material of ACPBEN was recorded to compare it with that calculated from the refined single crystal structure (Figure 5.46). As the two patterns show good agreement, the conclusion is that the single crystal used for intensity data collection was representative of the bulk material. The slight differences in peak positions are due to the temperatures of data collection, where the experimental PXRD data were collected at room temperature and the single crystal intensity data at 173(2) K. Upon cooling, the unit cell undergoes anisotropic contraction which resulted in slight differences in the location of the peaks.

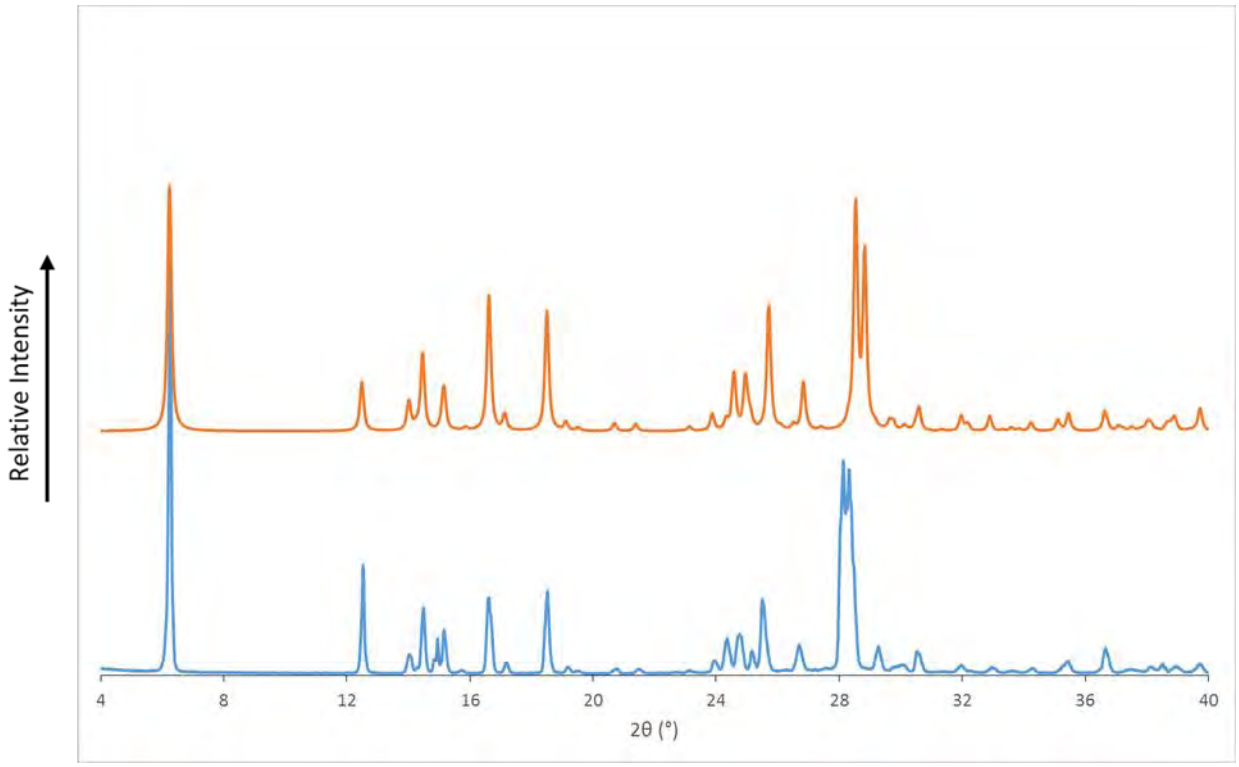

Figure 5.46: The PXRD trace for the bulk sample (blue) and the computed PXRD pattern based on the single crystal X-ray structure of ACPBEN (orange)

INFRARED SPECTROSCOPY

The multi-component crystalline system ACPBEN was designated a co-crystal due to the lack of a proton transfer. This was deduced from the refined single crystal structure. Infrared spectroscopy was used to support this designation and investigated as a rapid identification method for this product. This was performed in a manner similar to previous systems presented in this study.

The infrared spectrum of ACPBEN (Figure 5.47) showed two characteristic signals of a carboxylic acid group. The carbonyl stretch was observed at 1697 cm^{-1} and the C-O-H in plane bend was seen at 1420 cm^{-1}. The peak C-O stretching peak at 1275 cm^{-1} provided further evidence of the presence of the carboxylic acid moiety. Due to the presence of water in the structure, the O-H carboxylic acid group absorbance peak could not be identified. Nevertheless, the presence of the carboxylic acid carbonyl stretching, C-O-H bending and C-O stretching peak signals indicated that no proton transfer took place during the formation of the product. This supports the designation of ACPBEN as a co-crystal.

Rapid identification of ACPBEN by infrared spectroscopy relied on the characteristic carboxylic acid carbonyl and C-O stretching peaks as well as the C-O-H bending peak. The broad spectral region from 3120 cm^{-1} to 3531 cm^{-1}, arising from the overlap of water -OH, the carboxylic acid hydroxyl and amide amine groups, aids in identification of the new crystalline system. By direct comparison with the acipimox and benzamide spectra, the formation of a new phase is evident from the ACPBEN spectrum. The absence of the amine peak from the benzamide spectrum (3361 cm^{-1}) and the hydroxyl peak from acipimox (3554 cm^{-1}) in the ACPBEN spectrum shows the formation of a new phase. The shift in the carboxylic acid carbonyl peak from 1701 cm^{-1} in the acipimox spectrum to 1697 cm^{-1} in the ACPBEN spectrum further supports this assessment. Therefore, by comparison one can conclusively establish the formation of a new phase. The observation of the carboxylic acid signals and the profile of the broad absorption region are characteristic of the ACPBEN co-crystal and can be used for rapid identification of this product.

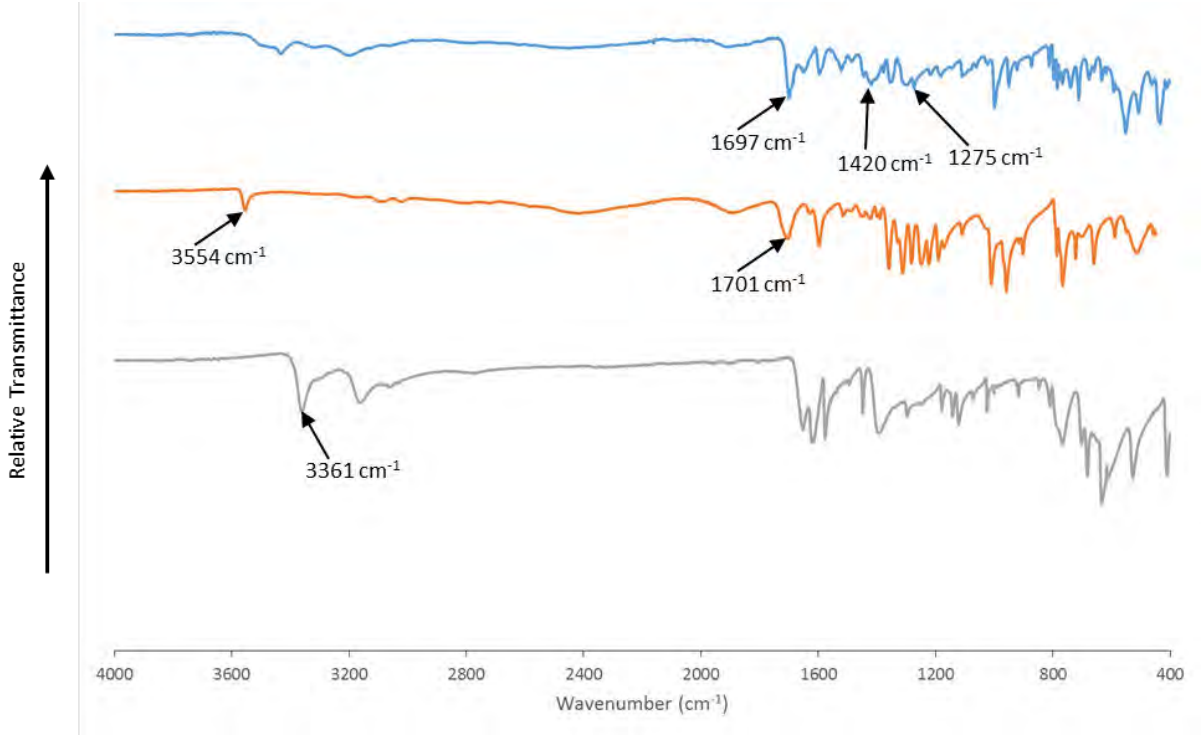

Figure 5.47: FTIR spectra for ACPBEN (blue), acipimox (orange) and benzamide (grey)

ACIPIMOX/ISONICOTINAMIDE

The multi-component crystalline system of acipimox with isonicotinamide will be referred to as ACPISO.

SAMPLE PREPARATION

The multi-component crystalline system ACPISO was synthesised using two methods. The first was dry grinding and the second co-precipitation.

To perform the dry grinding experiment 10 mg of acipimox (0.065 mmol) was combined with an equimolar quantity of isonicotinamide (8 mg, 0.065 mmol) in an agate mortar. These were ground together with an agate pestle for 15 minutes.

To perform the co-precipitation experiment, equimolar quantities of acipimox (10 mg, 0.065 mmol) and isonicotinamide (8 mg, 0.065 mmol) were weighed out. The acipimox was dissolved in 3 cm^3 propan-1-ol and the isonicotinamide was then added to the solution. The resulting mixture was stirred at 40 °C for 2 to 3 hours and then filtered through a 0.45 µm nylon filter into a clean vial and placed on the benchtop to slowly evaporate. Over the course of several days small needle-shaped crystals appeared.

STOICHIOMETRY

^{1}H-NMR spectroscopy was used to determine the stoichiometry of ACPISO. Crystals obtained from co-precipitation were dissolved in DMSO-d_6 and subjected to ^{1}H-NMR spectroscopy. The relative integration of acipimox methyl group protons, set as the reference integral, and the isonicotinamide aromatic peaks were used to determine a 1:1 stoichiometric ratio. The proton labelling schemes of acipimox and isonicotinamide are shown in Figure 5.48. The integration values of the ^{1}H-NMR spectroscopy experiment and spectrum are shown in Table 5.16 and Figure 5.49 respectively.

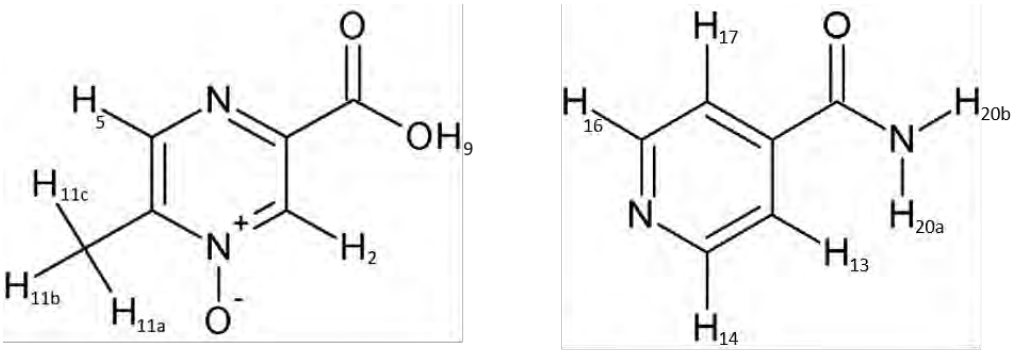

Figure 5.48: Proton labelling of acipimox (left) and isonicotinamide (right)

Table 5.16: Integrals and assignment of component protons for stoichiometric determination

Proton	δ (ppm)	Integration		Experimental/ Theoretical
		Experimental	Theoretical	
Acipimox				
C-$H_{11a,b,c}$	2.42	3.00‡	3.00	1
C-H_2	8.69	0.94	1	0.94 ≈ 1
Isonicotinamide				
C-H_{13} + C-H_{17}	7.80	2.12	2	1.06 ≈ 1
Overlapping Peak				
C-H_5 + C-H_{14} + C-H_{16}	8.75	3.02	3	1.01 ≈ 1

‡ *Reference integral*

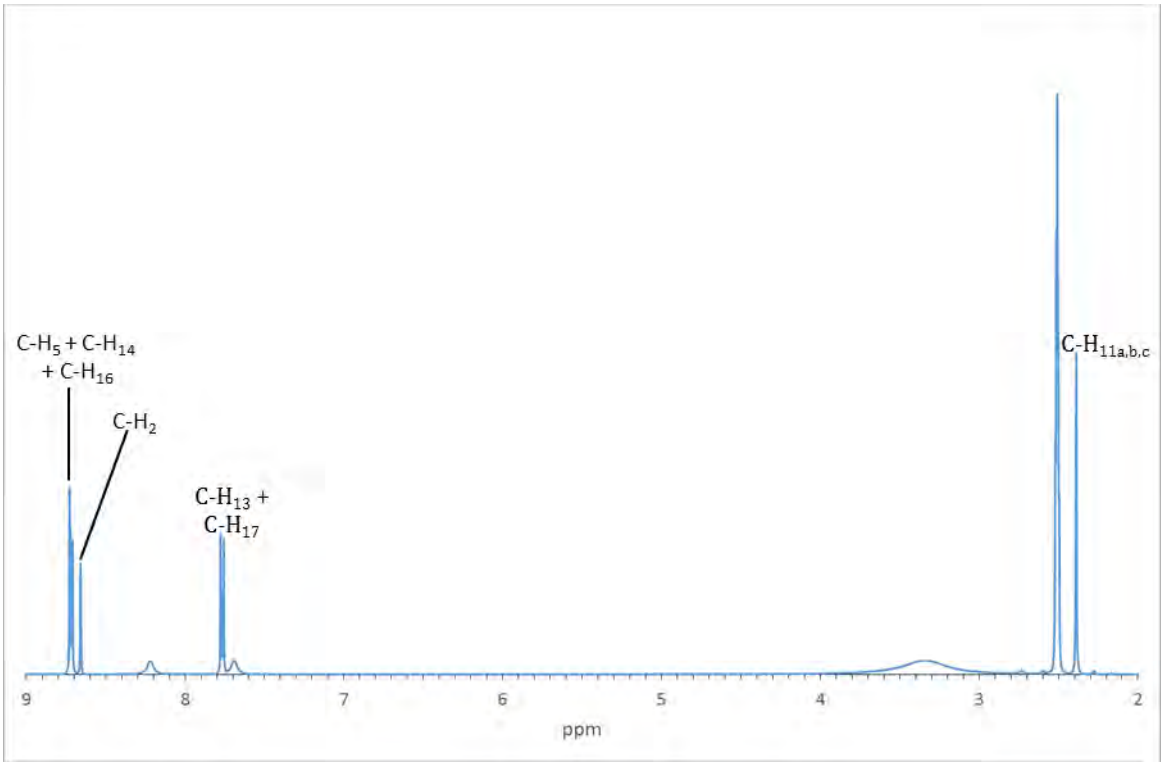

Figure 5.49: ^{1}H-NMR spectrum of ACPISO in DMSO-d_6 used to determine the stoichiometric ratio

THERMAL ANALYSIS

The TGA trace (Figure 5.50) of ACPISO shows no thermal event until 179.1 ± 2.3 °C (n = 2). At this temperature a two-step mass loss occurs. The first is a mass loss of 72.0 ± 0.3 % and the second 24.8 ± 1.6 %. The DSC trace shows an endotherm corresponding to melting at 210.8 ± 0.5 °C (n = 2), occurring simultaneously with decomposition. The HSM micrographs (Figure 5.51) show partial melting at 201 °C and the early stages of decomposition at 210 °C.

A series of detailed micrographs showed melting as the crystal size underwent reduction. It is understood that the liquid phase dissolved into the oil. The lack of deposition of the product on the cover slip as the crystals underwent heating eliminated sublimation as an explanation of the HSM micrographs.

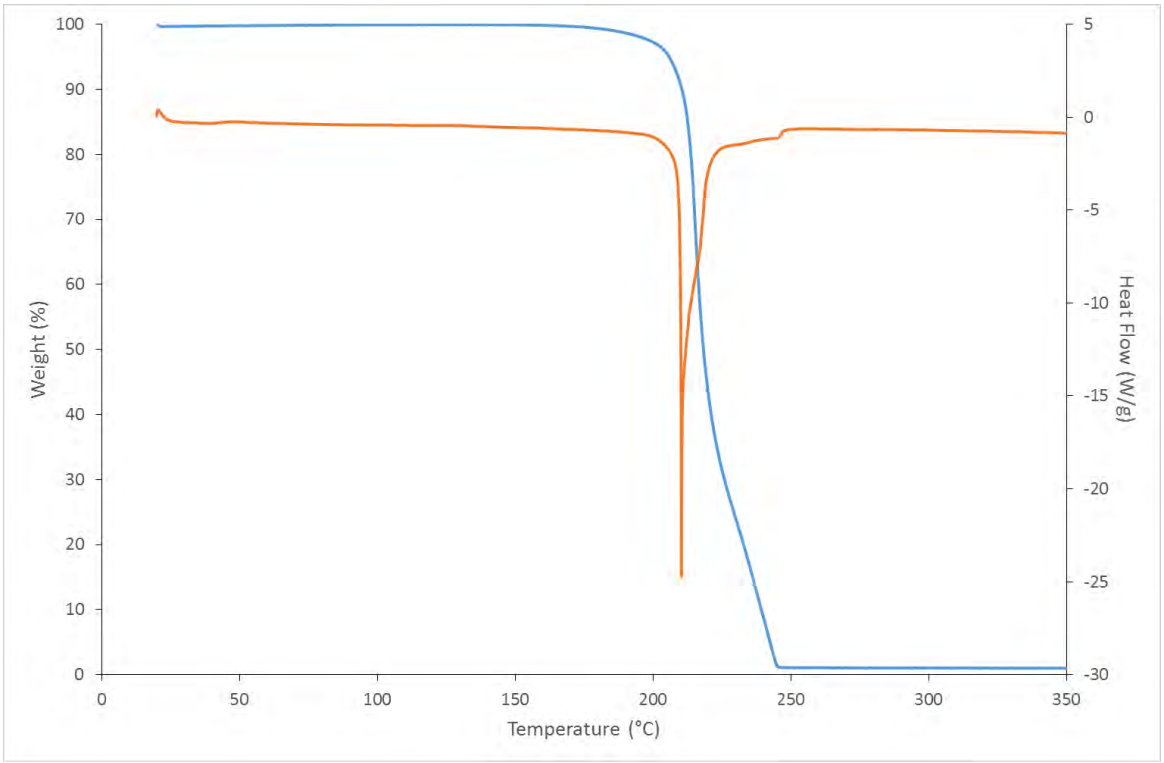

Figure 5.50: Representative TGA (blue) and DSC (orange) traces for ACPISO

Figure 5.51: Hot stage micrographs showing the ACPISO crystals at various stages of heating

CRYSTAL STRUCTURE ANALYSIS

DATA COLLECTION AND SPACE GROUP DETERMINATION

A Bruker KAPPA APEX DUO II diffractometer was used to collect the single crystal intensity data used for the structure determination. The intensity data were collected at 173 ± 2 K. The crystal system was determined to be monoclinic from the Laue symmetry, which was found to be *2/m*. By examination of the systematic absences, namely *hkl: none; h0l: l = 2n+1; 0k0, k = 2n+1*, the space group was uniquely determined to be $P2_1/c$.

STRUCTURE SOLUTION AND REFINEMENT

The software program SAINT[10] was used for data reduction and unit cell refinement. The program SADABS,[11] employing the multi-scan method, was used for absorption correction. The asymmetric unit comprises one acipimox moiety and one isonicotinamide moiety. Direct methods employed by SHELXS[5] were used to locate the atomic co-ordinates. The program SHELXL[5,6] was used to refine the structure isotropically after placing atoms in their postulated positions. All non-hydrogen atoms were subsequently refined anisotropically. Hydrogen atoms were located from the Fourier difference map. Through careful inspection, a hydrogen atom was determined to be positioned on the pyridyl nitrogen atom of isonicotinamide. In addition, the acipimox moiety was devoid of a proton, featuring instead a carboxylate group. This was supported by the similarities in the C-O bond lengths of 1.278(2) Å and 1.235(2) Å. These distances are intermediate between single and double C-O bond lengths. This lead to the deduction that a proton transfer took place during formation of the product and therefore ACPISO was designated a salt. After locating the hydrogen atoms in the difference Fourier map, they were placed in idealised positions using a riding model with U_{iso} values 1.2 to .1.5 times those of the parent atoms. The crystallographic data for ACPISO are presented in Table 5.17 below.

Table 5.17: Crystallographic data for the single crystal X-ray structure of ACPISO

Chemical Formula	$(C_6H_5N_2O_3)^-\cdot(C_6H_7N_2O)^+$
Molar Mass (g mol^{-1})	276.26
Crystal System	Monoclinic
Space Group	$P2_1/c$
Unit cell parameters	
a (Å)	4.1770(5)
b (Å)	12.1709(15)
c (Å)	24.220(3)
α (°)	90
β (°)	92.716(2)
γ (°)	90
Volume (Å^3)	1229.9(3)
Z	4
Density$_{calcd.}$ (g cm^{-3})	1.492
μ [MoKα] (mm^{-1})	0.115
F (000)	576
Temperature (K)	173(2)
Crystal size (mm)	0.11×0.13×0.47
Range scanned θ (°)	1.7 – 27.5
Index ranges	h: -5, 5; k: -15, 15; l: -31, 31
ϕ and ω scan angle (°)	0.5
Dx (mm)	50.0
Total number of reflections	23 463
Number of independent reflections	2 832
Number of reflections with I > 2σ(I)	2 158
R_{int}	0.041
R_1 [I > 2σ(I)]	0.0374
wR_2	0.1049
S	1.026
Number of parameters	182
Number of reflections omitted	4
Parameters a, b	0.0524; 0.4053
in w = 1/[σ^2(F_O^2)+(aP)^2+(bP)]	
$(\delta/\sigma)_{mean}$	<0.001
Δρ excursions (e Å^{-3})	-0.26; 0.22

MOLECULAR STRUCTURE

The asymmetric unit of the salt ACPISO is shown in Figure 5.52. In the asymmetric unit there is one acipimox anion hydrogen bonded to one isonicotinamide cation. The components are in their respective deprotonated and protonated forms. The proton transfer occurs from the carboxylic acid moiety of acipimox to the pyridyl nitrogen of isonicotinamide during formation of the salt. Further intermolecular interactions will be expanded upon in the forthcoming section, entitled Hydrogen Bonding.

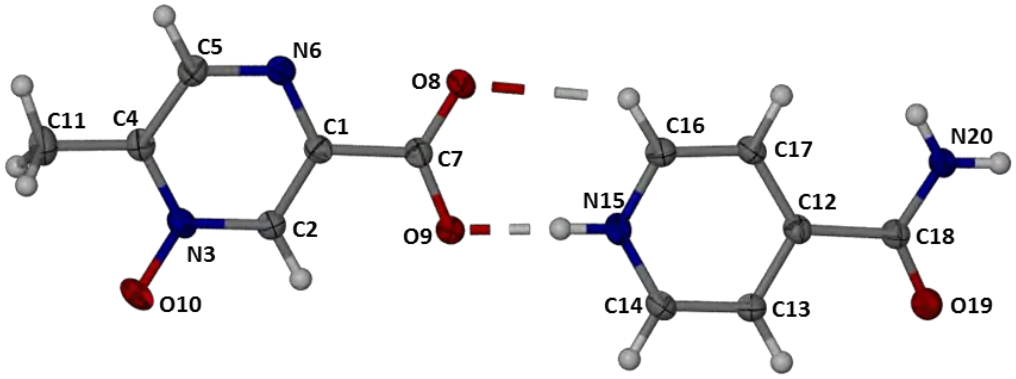

Figure 5.52: The asymmetric unit of ACPISO with numbering scheme of acipimox (left) and isonicotinamide (right). Thermal ellipsoids are drawn at the 50 % probability level

HYDROGEN BONDING

There are three hydrogen bonding synthons present in the ACPISO structure. The first, shown in Figure 5.53a., are the two hydrogen bonds (N-H···O and C-H···O) which link the components of the asymmetric unit. The second, Figure 5.53b., is that between the amide group of the isonicotinamide cation and the carboxylate anion of acipimox. Finally, the third hydrogen bonding synthon is that between two isonicotinamide molecules through an amide–amide hydrogen bonding homosynthon, shown in Figure 5.53c.[12] The hydrogen bonding parameters are listed in Table 5.18.

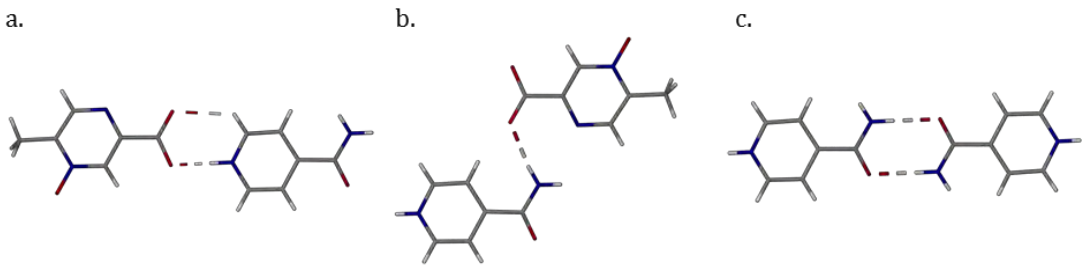

Figure 5.53: Hydrogen bonding synthons between a. carboxylate and aromatic nitrogen and aromatic proton, b. carboxylate and amide and c. amide and amide

The C-H···O hydrogen bonds listed in Table 5.18 are mostly involved in stabilising the packing of ACPISO. Two of these interactions, however, occur within the asymmetric unit. The first is C2-H···O9, an intramolecular interaction within the acipimox anion. The second is C16-H···O8, between isonicotinamide and acipimox in the asymmetric unit, further stabilising the interaction between these ions, as shown in Figure 5.53a. The remaining three C-H···O will be discussed below.

Table 5.18: Hydrogen bonding parameters for ACPISO

D-H···A	D···A (Å)	Angle (°)	Symmetry Operator
N15-H···O9	2.557(2)	173	(*x, y, z*)
N20-H···O19	2.923(2)	163	(*3-x, 2-y, 1-z*)
N20-H···O8	3.032(2)	170	(*2-x, 1-y, 1-z*)
C2-H···O9	2.727(2)	100	(*x, y, z*)
C5-H···O19	3.172(2)	122	(*1+x, -1+y, z*)
C14-H···O10	3.094(2)	137	(*-x, 1/2+y, 1/2-z*)
C16-H···O8	3.236(2)	126	(*x, y, z*)
C17-H···O8	3.253(2)	139	(*2-x, 1-y, 1-z*)

When combined, the synthons described above form three hydrogen bonding patterns. The first occurs between the amide groups of two isonicotinamide cations and is described by the graph set designator $N_1 = R_2^2(8)$, and is shown in Figure 5.54. The second pattern is a larger ring, $N_2 = R_4^2(16)$, comprising two acipimox anions and two isonicotinamide cations and is presented in Figure 5.55. This pattern is assembled from the hydrogen bonds N15-H···O9 and C16-H···O8. These two patterns are each located at centres of inversion. The final pattern (Figure 5.56) is that found in the asymmetric unit. It is described by the graph set designator $N_1 = R_2^2(7)$.

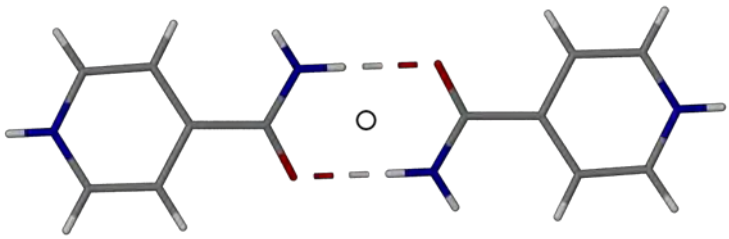

Figure 5.54: Hydrogen bonding pattern, $N_1 = R_2^2(8)$, occurring in ACPISO

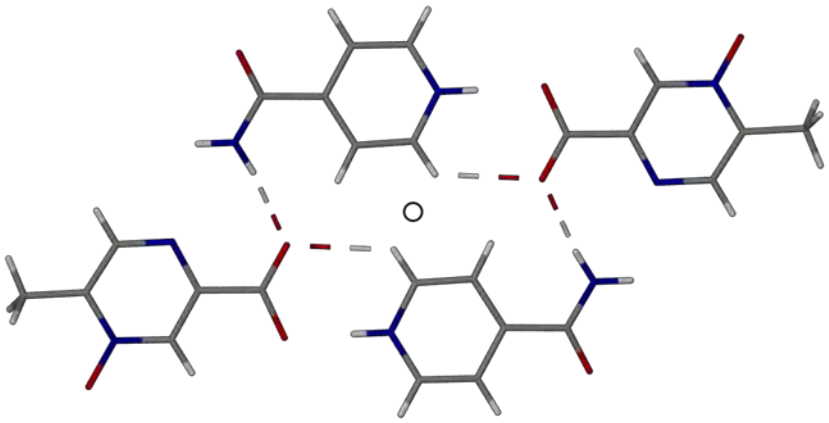

Figure 5.55: Hydrogen bonding pattern, $N_2 = R_4^2(16)$, occurring in ACPISO

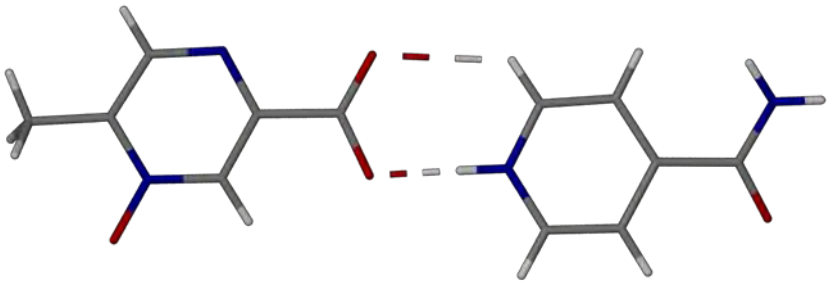

Figure 5.56: Hydrogen bonding pattern, $N_3 = R_2^2(7)$, occurring in ACPISO

CRYSTAL PACKING

The hydrogen bonding patterns above combine to form layers propagating through the network N = $R_2^2(8)R_4^2(16)R_2^2(7)$. The repeating unit of this pattern is shown in Figure 5.57. The layers then stack along the *a*-axis in distinct columns. The columns are related by a two-fold screw axis such that the layers in adjacent columns are inclined at 50.7°. These columns are shown in Figure 5.58 and their inclination is shown in Figure 5.59.

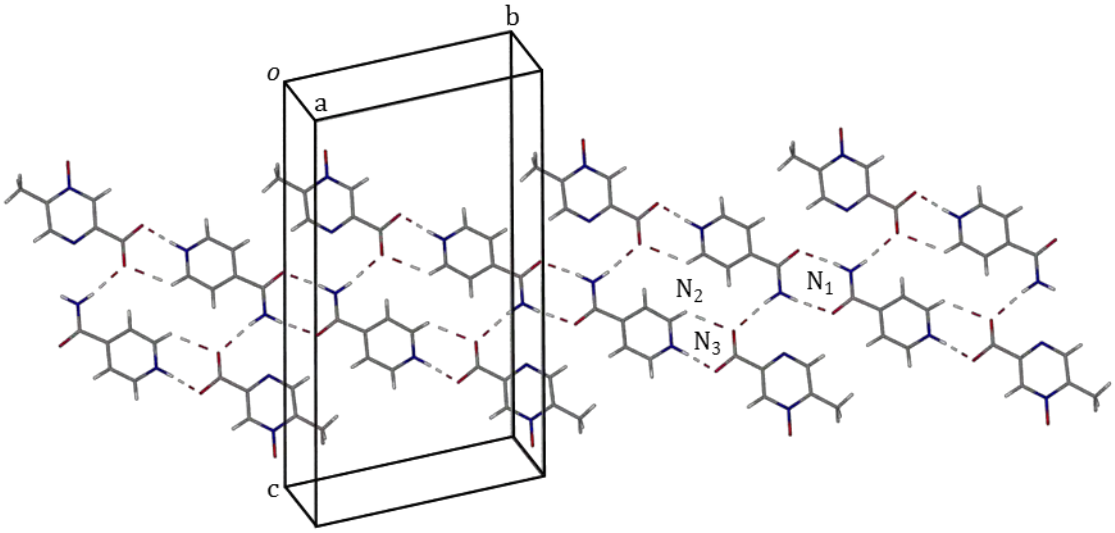

Figure 5.57: Layer formed from combined hydrogen bonding patterns N_1, N_2 and N_3 in ACPISO

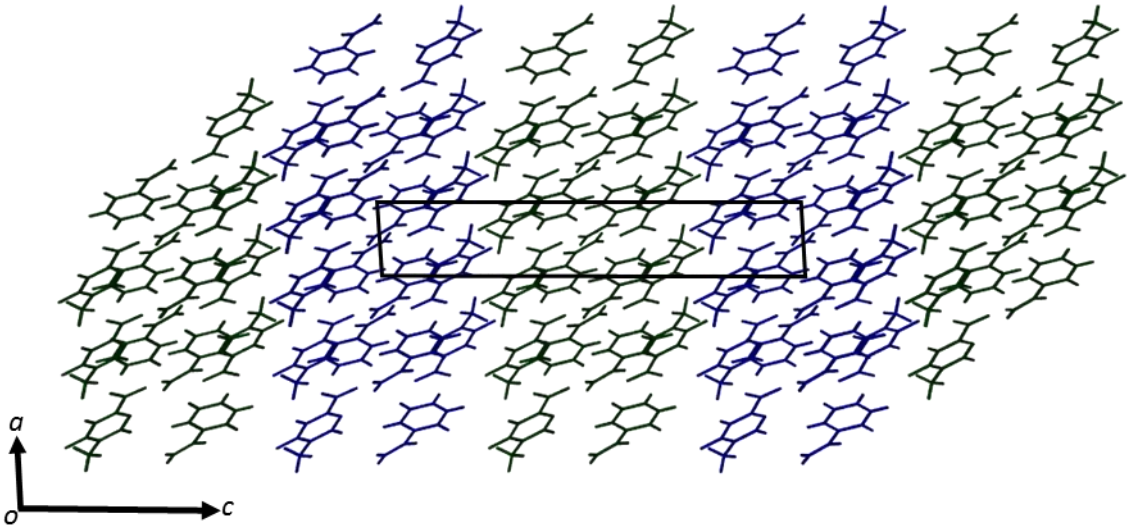

Figure 5.58: Packing of ACPISO viewed along [0 1 0] highlighting the columns in alternating colours

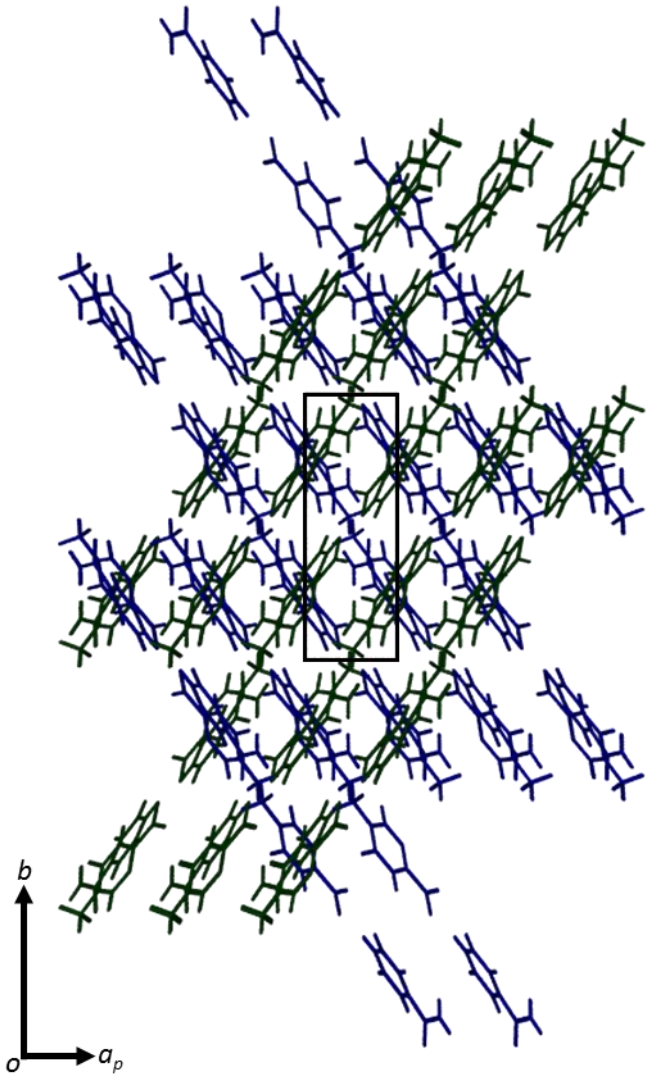

Figure 5.59: Packing of ACPISO viewed along [0 0 1] illustrating the inclination of the columns

As mentioned above, three of the C-H···O hydrogen bonds present in this structure are involved in stabilising the packing. Two of the listed interactions, C5-H···O19ǂ (ǂ: *1+x, -1+y, z*) and C17-H···O8ǂ (ǂ: *2-x, 1-y, 1-z*), occur within columns stabilising the columns and layers. The remaining hydrogen bond, C14-H···O10ǂ (ǂ:*-x, 1/2+y, 1/2-z*), stabilises the interaction between the adjacent columns.

COMPARATIVE PXRD

The bulk material obtained during production of ACPISO was subjected to PXRD analysis. This trace was compared with that calculated from the refined crystal structure. There are slight differences in the locations of the peaks, which result from the temperatures at which the bulk PXRD data (room temperature) and the single crystal structure data [173(2) K] were collected. Upon cooling the unit cell contracts and/or expands, which in turn causes the slight differences in the angular positions of the peaks.

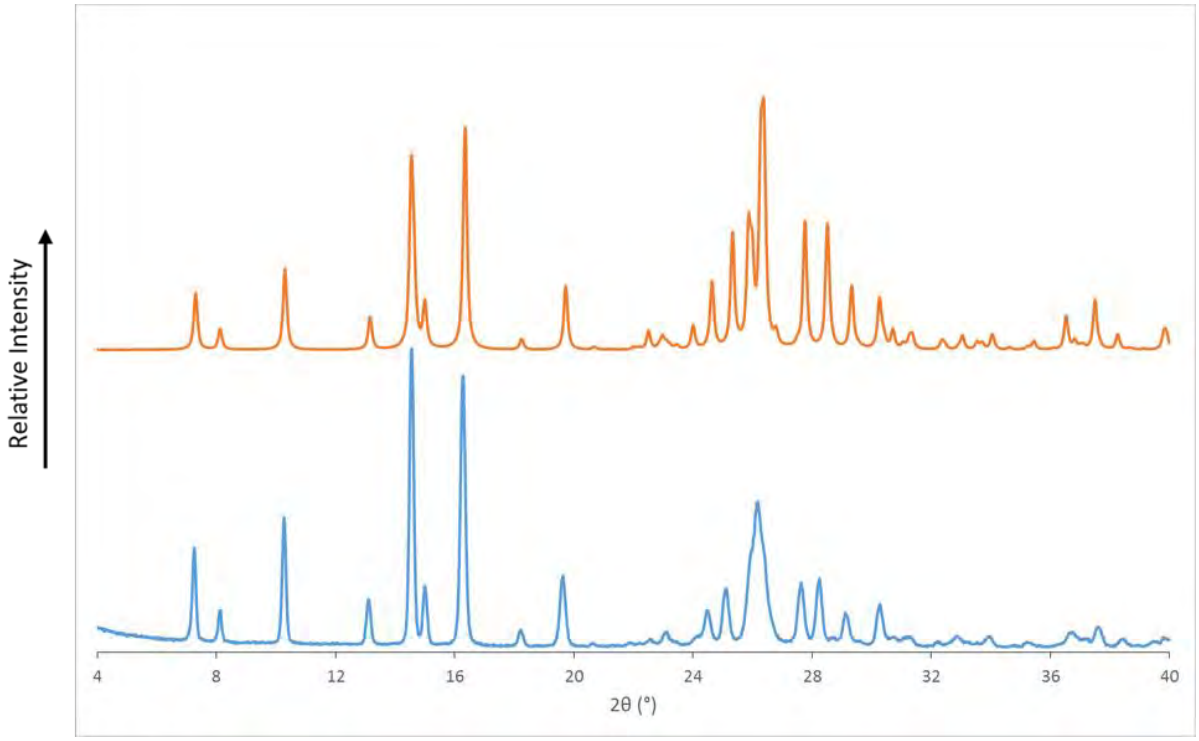

Figure 5.60: The PXRD trace for the bulk sample (blue) and the computed PXRD pattern based on the single crystal X-ray structure of ACPISO (orange)

INFRARED SPECTROSCOPY

The crystal structure of ACPISO showed the position of the proton on the pyridyl nitrogen of the isonicotinamide component. Furthermore, no proton was found on the acipimox carboxylate moiety. As a proton transfer had taken place during formation, ACPISO was designated a salt. Infrared spectroscopy was performed to investigate if the spectrum of ACPISO supported this designation and as a rapid identification method for ACPISO. The methods for these experiments are outlined above for previous multi-component crystalline systems.

The infrared spectrum of ACPISO (Figure 5.61) shows two signals characteristic of a carboxylate anion, the first was seen at 1582 cm^{-1} and the second at 1345 cm^{-1}, representing a C-O stretch. The presence of these peaks indicate that a proton transfer from acipimox has taken place. This supports the designation of ACPISO as a salt.

To identify a new phase the spectrum of ACPISO was compared with those of the starting materials. The O-H signal, 3554 cm^{-1} in the acipimox spectrum, is absent in that of ACPISO. The carboxylic acid carbonyl peak was also observed in the acipimox spectrum (1701 cm^{-1}), but is absent in the product spectrum. The positions of the amide carbonyl signals in the isonicotinamide spectrum (1620 cm^{-1}) and product spectrum (1699 cm^{-1}) aid in distinguishing these spectra. The differences presented here allow one to establish unequivocally the formation of a new phase.

The signals used in determination of proton transfer and differentiating between the product and starting material spectra are characteristic of ACPISO. The broad absorption region from 2919 cm^{-1} to 3418 cm^{-1} representing the hydrogen bonded amine moieties, is a further feature distinctive of this multi-component crystalline system. Therefore, using these signals one can use FTIR as a rapid identification technique for ACPISO.

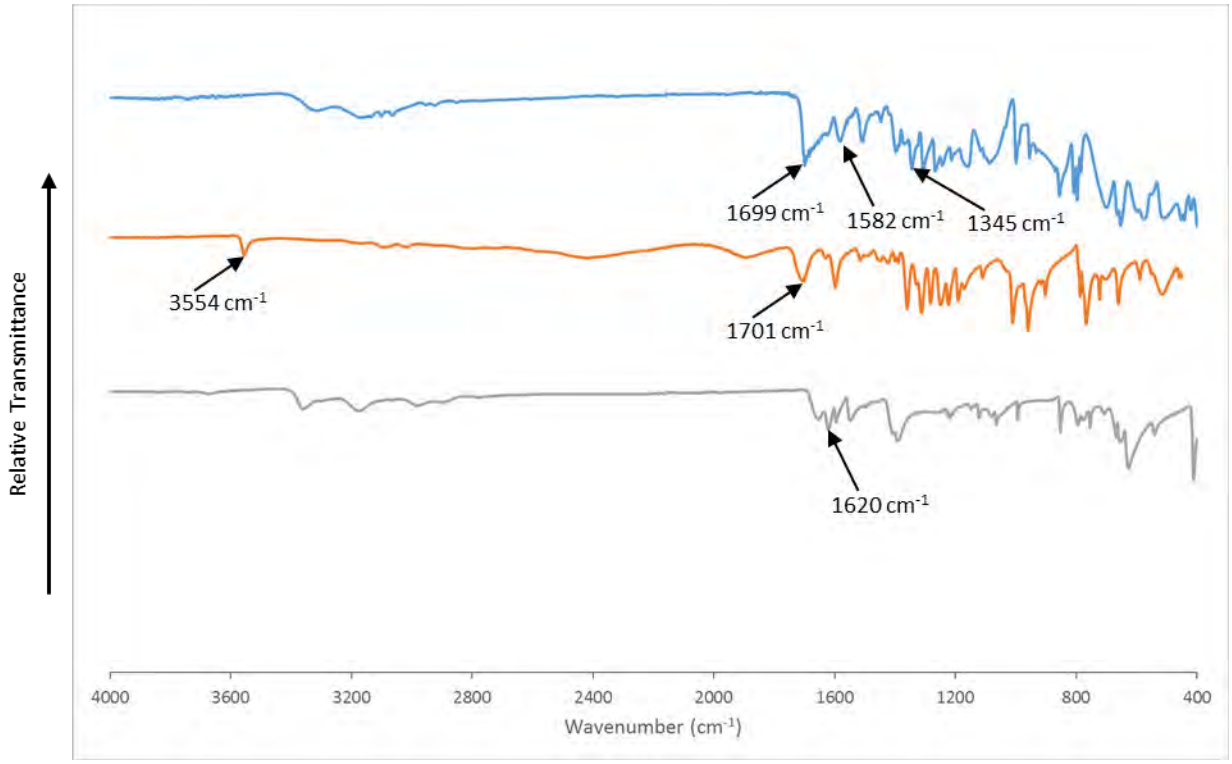

Figure 5.61: FTIR spectra for ACPISO (blue), acipimox (orange) and isonicotinamide (grey)

ACIPIMOX/TRANEXAMIC ACID

The multi-component crystalline system formed between acipimox and tranexamic acid will be referred to as ACPTRA.

SAMPLE PREPARATION

The system was prepared in three ways. The first was dry grinding where acipimox (10 mg, 0.065 mmol) was weighed out and placed in an agate mortar. An equimolar quantity of tranexamic acid (10 mg, 0.065 mmol) was added and the compounds were ground together using an agate pestle for 15 minutes. The second method used to produce ACPTRA was liquid-assisted grinding. In this method the same procedure as dry grinding was used with the dropwise addition of butan-1-ol.

The third method employed was co-precipitation, where 10 mg of acipimox (0.065 mmol) was weighed into a clean vial. The acipimox was then dissolved in 3 cm^3 butan-1-ol and an equimolar amount of tranexamic acid (10 mg, 0.065 mg) was added to this solution. The resulting mixture was stirred at 50 °C for 3 hours and then filtered through a 0.45 µm nylon filter into a clean vial. This was then left to stand on the benchtop until needle-shaped crystals were observed. The precipitate formed before filtration was determined to be a powdered form of the desired product. Single crystals were required for the analyses performed below.

STOICHIOMETRY

The stoichiometric ratio of ACPTRA was determined *via* ^{1}H-NMR spectroscopy. Crystals resulting from co-precipitation were dissolved in DMSO-d_6 and subjected to ^{1}H-NMR spectroscopy. The relative integration of the acipimox methyl moiety, set as the reference integral, and the C-$H_{21a,b}$ protons of tranexamic acid were used to determine a stoichiometric ratio of 1:1. The proton labelling of acipimox and tranexamic acid are shown in Figure 5.62 while the integration values are presented in Table 5.19 and the spectrum in Figure 5.63. The signals for the protons C-H_2 and C-H_5 overlap, therefore their integration was considered together.

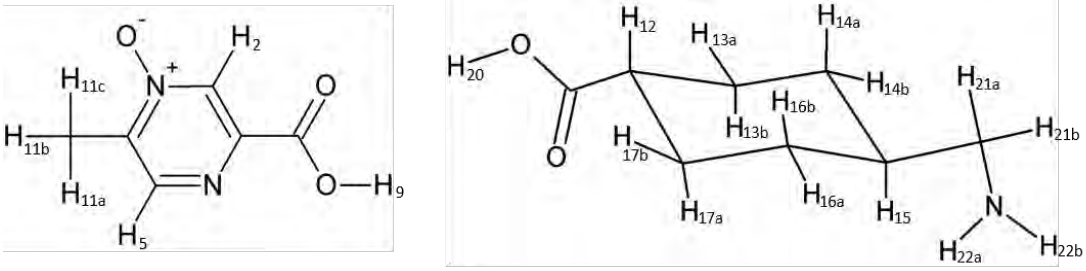

Figure 5.62: Proton labelling of acipimox (left) and tranexamic acid (right)

Table 5.19: Integrals and assignment of component protons for stoichiometric determination

Proton	**δ (ppm)**	**Integration**		**Experimental/ Theoretical**
		Experimental	Theoretical	
Acipimox				
C-$H_{11a,b,c}$	2.37	3.00‡	3.00	1
C-H_2 + C-H_5	8.49, 8.55	2.08	2.00	1.04 ≈ 1
Tranexamic Acid				
C-$H_{21a,b}$	2.70	1.98	2.00	0.99 ≈ 1

‡ *Reference integral*

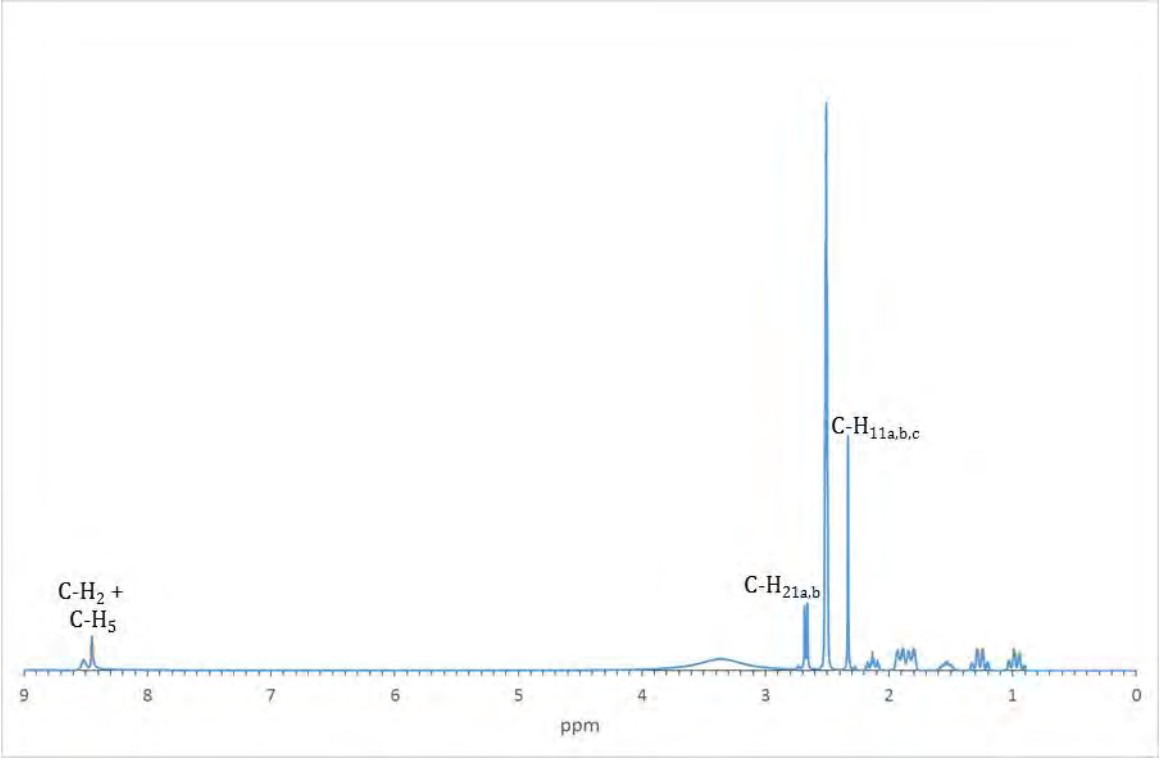

Figure 5.63: ^{1}H-NMR spectrum of ACPTRA in DMSO-d_6 used to determine the stoichiometric ratio

THERMAL ANALYSIS

The absence of thermal events in the initial stages of the thermal analysis of ACPTRA indicates that no solvent molecules are present in the sample. One major thermal event occurs from 214.0 ± 1.3 °C (n = 2) in the TGA trace (Figure 5.64). This is interpreted as the initial stages of decomposition. This event is followed by a slow continuous mass loss resulting from the continued decomposition of ACPTRA. The DSC trace (Figure 5.64) shows only one endotherm at 241.5 ± 0.2 °C (n = 2) corresponding to the simultaneous melting and decomposition of the multi-component crystalline system. The hot stage micrographs in Figure 5.65 at 247 °C show the melting and decomposition of the sample, corroborating the interpretation of the TGA and DSC profiles. The decomposed product can be seen in the HSM micrograph at 260 °C.

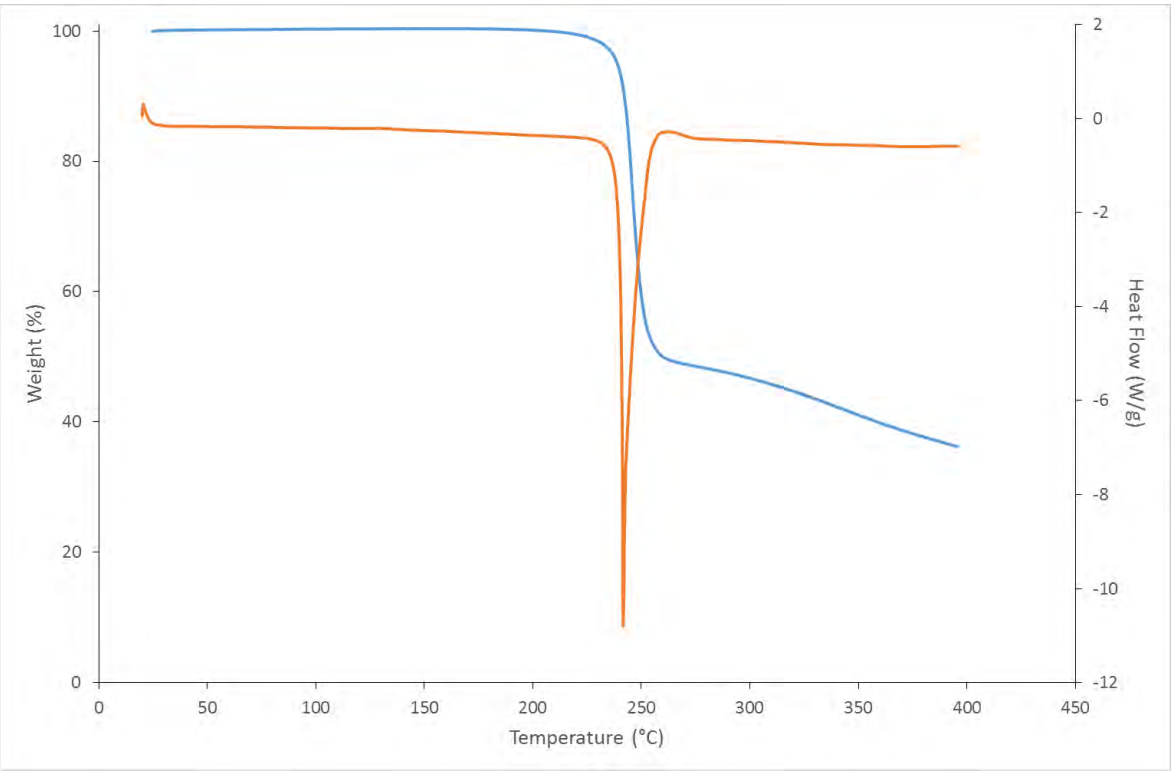

Figure 5.64: Representative TGA (blue) and DSC (orange) traces for ACPTRA

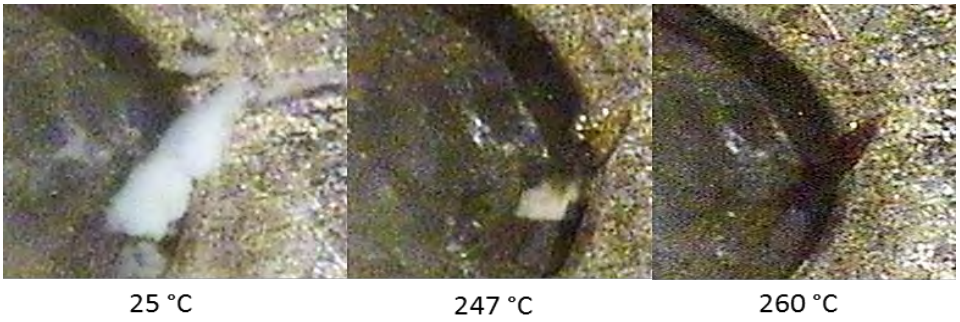

Figure 5.65: Hot stage micrographs showing ACPTRA crystals at various stages of heating

CRYSTAL STRUCTURE ANALYSIS

DATA COLLECTION AND SPACE GROUP DETERMINATION

A Bruker KAPPA APEX DUO II diffractometer was used to collect the single crystal intensity data at 173 ± 2 K. The crystal system was determined using the computer program LAYER.[2] The triclinic crystal system was determined from the observed Laue symmetry $\bar{1}$. Centrosymmetry of the crystal was deduced from the value of $|E^2-1|$ = 1.034 for the intensity data (program XPREP[3]) and hence the space group P $\bar{1}$ was assigned.

STRUCTURE SOLUTION AND REFINEMENT

Data reduction and unit cell refinement were performed using the program SAINT.[10] The intensity data were corrected for absorption by the multi-scan technique employed in the program SADABS.[11] The atomic co-ordinates were located by direct methods using SHELXS.[5] Once the atoms were placed in their presumed positions SHELXL[5,6] was used to refine the structure. All non-hydrogen atoms were initially refined isotropically and subsequently refined anisotropically. Tranexamic acid is known to exist as a zwitterion in its pure state and as an ammonium ion $(-NH_3)^+$ when present in a salt.[13,14] Close inspection of the Fourier difference map revealed the proton on the tranexamic acid carboxyl group. The absence of a hydrogen atom on the carboxylate anion of acipimox confirmed the occurrence of a proton transfer during formation of the product. Further evidence of a proton transfer was provided by the similarities in the C-O bond lengths of the acipimox carboxylate group. The values are 1.243(1) Å and 1.249(1) Å, and are intermediate between single and double carbon-oxygen bonds. The location of the proton on the tranexamic acid carboxyl group provides unequivocal proof of a proton transfer, leading to the designation of ACPTRA as a salt. Once the remaining hydrogen atoms were located in the Fourier difference map they were placed in idealised positions using a riding model with U_{iso} values 1.2 to 1.5 times those of the parent atoms. The asymmetric unit of ACPTRA comprises one deprotonated acipimox molecule (i.e. an anion) and one protonated tranexamic acid molecule (i.e. a cation). The crystallographic data for this structure are presented in Table 5.20.

Table 5.20: Crystallographic data for the single crystal X-ray structure of ACPTRA

Chemical Formula	$(C_6H_5N_2O_3)^-\cdot(C_8H_{16}NO_2)^+$
Molar mass (g mol^{-1})	311.34
Crystal System	Triclinic
Space Group	P $\bar{1}$
Unit cell parameters	
a (Å)	6.9663(14)
b (Å)	9.5250(19)
c (Å)	12.154(2)
α (°)	79.27(3)
β (°)	84.99(3)
γ (°)	70.49(3)
Volume (Å^3)	746.6(3)
Z	2
Density$_{calcd.}$ (g cm^{-3})	1.385
μ [MoKα] (mm^{-1})	0.106
F (000)	332
Temperature (K)	173(2)
Crystal size (mm)	0.08×0.13×0.41
Range scanned θ (°)	1.7 – 28.4
Index ranges	h: -9, 9; k; -12, 12; l: -16, 16
ϕ and ω scan angle (°)	0.50
Total number of frames	2835
Dx (mm)	47.24
Total number of reflections	13 715
Number of independent reflections	3 701
Number of reflections with I > 2σ(I)	3 382
R_{int}	0.027
R_1 [I > 2σ(I)]	0.0367
wR_2	0.1041
S	1.032
Number of parameters	202
Number of reflections omitted	10
Parameters a, b	a: 0.0580, b: 0.769
in w = 1/[σ^2(F_0^2)+(aP)^2+(bP)]	
$(\delta/\sigma)_{mean}$	<0.001
Δρ excursions (e Å^{-3})	-0.26, 0.33

MOLECULAR STRUCTURE

The asymmetric unit of ACPTRA, shown in Figure 5.66, comprises one acipimox anion and one tranexamic acid cation. During the formation of this product a proton transfer from the carboxylic acid moiety of acipimox to the carboxylate group of tranexamic acid occurs. There are several hydrogen bonding interactions between the ions that will be expanded upon in the Hydrogen Bonding section.

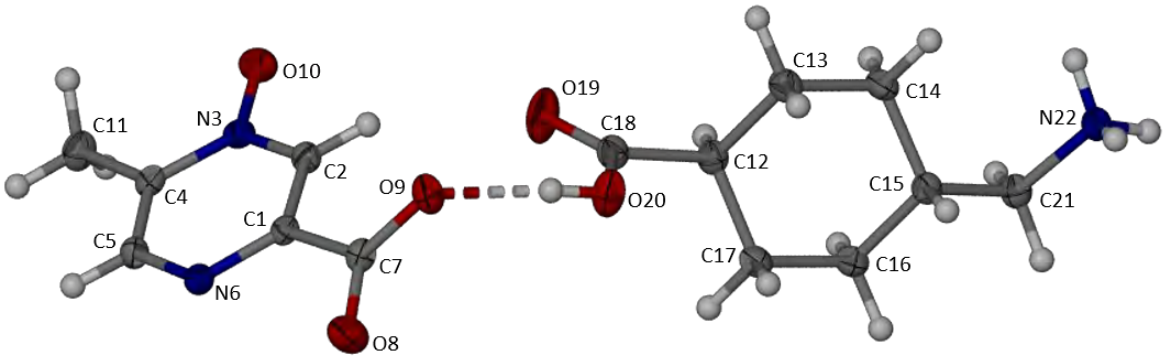

Figure 5.66: The asymmetric unit of the salt ACPTRA with numbering scheme of acipimox (left) and tranexamic acid (right). Thermal ellipsoids are drawn at the 50 % probability level

HYDROGEN BONDING

There are four hydrogen bonding synthons present in the organic salt ACPTRA. All the hydrogen bonds involve acipimox anions and the tranexamic acid counterions. The first involves the tranexamic acid carboxylic acid and the acipimox carboxylate anion (Figure 5.67a.). The second interaction links the ammonium cation of tranexamic acid to the pyrazine oxide group of acipimox, seen in Figure 5.67b. The third synthon, in Figure 5.67c., is an interaction of the carboxylate anion of acipimox and the ammonium cation of tranexamic acid. The final hydrogen bond, Figure 5.67d., is an interaction of the ammonium cation of tranexamic acid with the aromatic nitrogen of acipimox. The hydrogen bonding parameters are presented in Table 5.21.

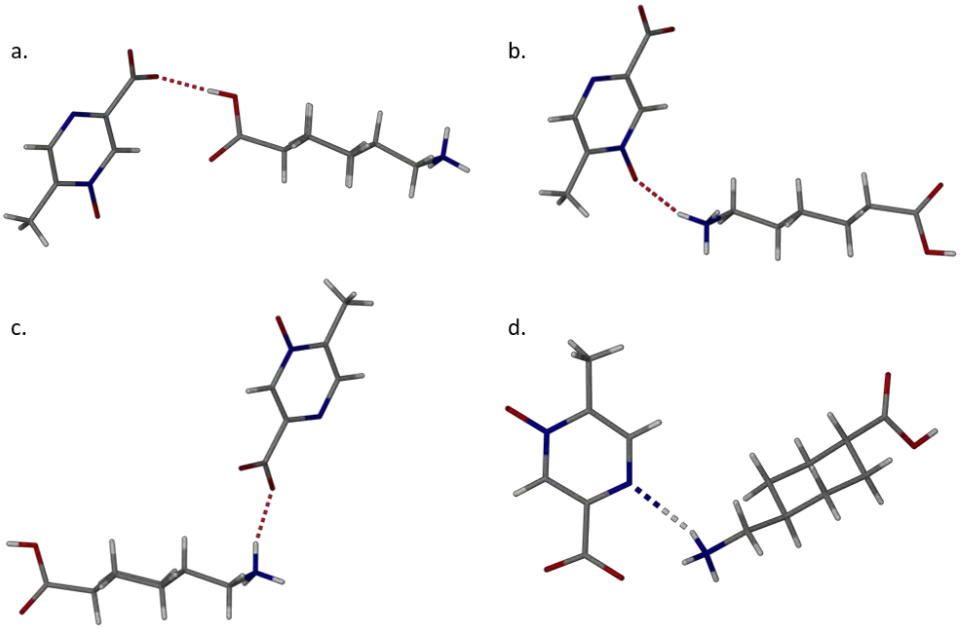

Figure 5.67: Hydrogen bonding synthons present in ACPTRA

Table 5.21: Hydrogen bonding parameters in ACPTRA

D-H···A	D···A (Å)	Angle (°)	Symmetry Operator
O20-H···O9	2.639(1)	176	(*x, y, z*)
N22-H···O8	2.738(1)	163	(*1-x, 2-y, -z*)
N22-H···N6	3.063(1)	142	(*1+x, y, -1+z*)
N22-H···O10	2.797(1)	158	(*2-x, 1-y, -z*)
C2-H···O19	3.312(2)	151	(*x, y, z*)
C14-H···O10	3.481(2)	150	(*1-x, 1-y, -z*)
C21-H···O19	3.422(2)	173	(*2-x, 1-y, -z*)

Each acipimox anion is hydrogen bonded to four tranexamic acid counterions (Figure 5.68a.) through the four hydrogen bonds above. Each of the tranexamic acid cations is hydrogen bonded to four acipimox anions through the same four hydrogen bonds (Figure 5.68b.).

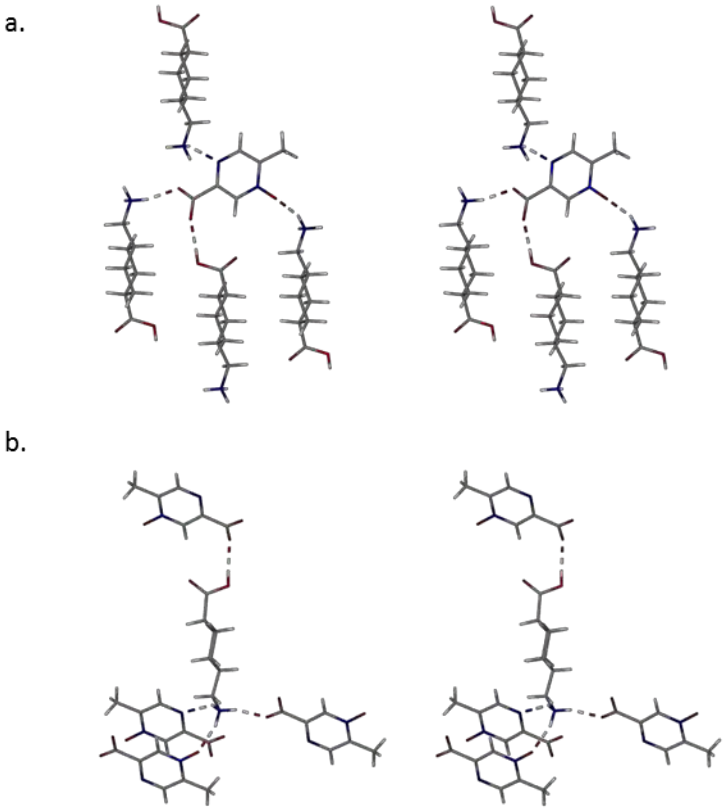

Figure 5.68: Stereo diagrams highlighting the a. four tranexamic acid cations hydrogen bonding to a single acipimox anion and b. four acipimox anions bonding to a single tranexamic acid counterion

These hydrogen bonds between acipimox and tranexamic acid form four hydrogen bonding patterns. Each of the patterns is described by a graph-set designator as a hydrogen bonded ring. Each of these rings comprises two acipimox anions and two acipimox cations.

The first of these patterns, $N_1 = R_4^4(26)$, involves two acipimox anions and two tranexamic acid cations. The latter are linked through the carboxylate anions of two acipimox counterions. The carboxylate group of each acipimox anion acts as an acceptor of hydrogen atoms from a carboxylic acid and ammonium cation of the respective tranexamic acid ions. The hydrogen bonding pattern, N_1, is located at a centre of inversion and is shown in Figure 5.69.

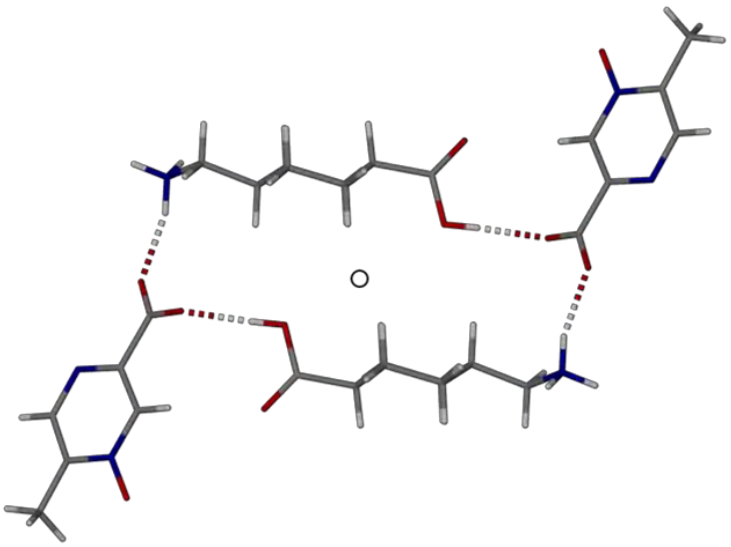

Figure 5.69: Hydrogen bonding pattern $N_1 = R_4^4(26)$ in ACPTRA

The second ring pattern comprises two acipimox anions linked through the ammonium cations of two tranexamic acid counterions. The ammonium cation hydrogen bonds with the pyrazine oxide and aromatic nitrogen groups of inversion-related acipimox anions. The ring is described by the graph-set designator $N_2 = R_4^4(16)$ and is located at a centre of inversion, shown in Figure 5.70.

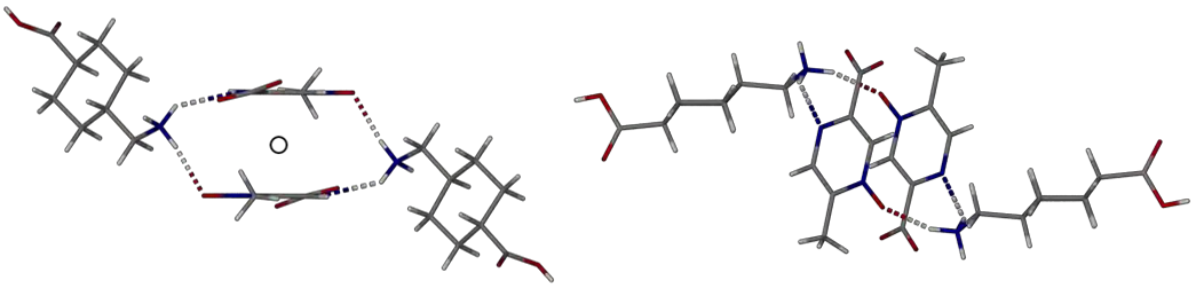

Figure 5.70: Two views of the hydrogen bonding pattern $N_2 = R_4^4(16)$ in ACPTRA

The hydrogen bonding pattern $N_3 = R_4^4(14)$ is similar to N_2 as it too comprises two acipimox anions linked through the ammonium cations of two tranexamic acid cations. The ammonium ion of each tranexamic acid cation acts as hydrogen bond donors to the aromatic nitrogen and the carboxylate anion of the two acipimox ions. This hydrogen bonding pattern can be seen in Figure 5.71, where it is also shown that it lies at a centre of inversion.

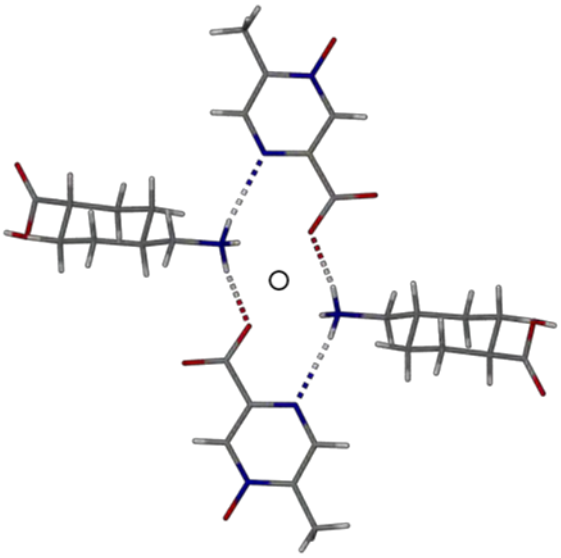

Figure 5.71: Hydrogen bonding pattern $N_3 = R_4^4(14)$ in ACPTRA

The final hydrogen bonding pattern $N_4 = R_4^4(32)$ is the largest, involving two acipimox anions and two tranexamic acid counterions. The carboxylate group of each acipimox anion acts as a hydrogen bond acceptor to the carboxylic acid group of a tranexamic acid cation. The ammonium cation of each tranexamic acid ion is hydrogen bonded to the pyrazine oxide of an acipimox anion. The pattern is located at a centre of inversion and is shown in Figure 5.72.

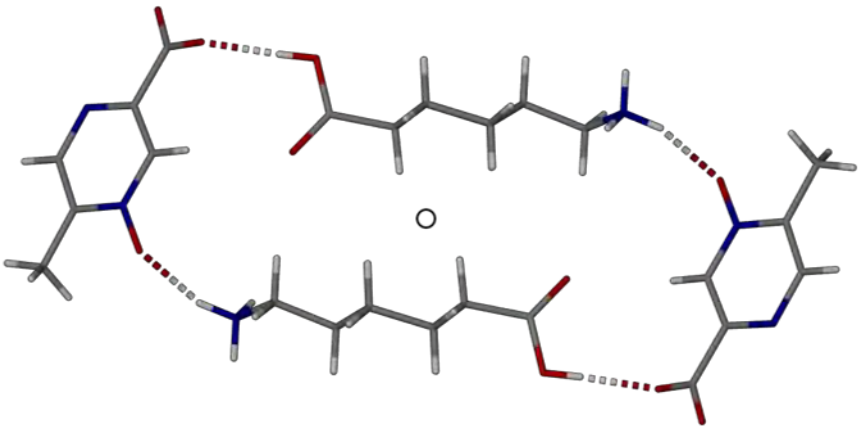

Figure 5.72: Hydrogen bonding pattern $N_4 = R_4^4(32)$ in ACPTRA

These four hydrogen bonding patterns concatenate to form the overall network $N = R_4^4(26)\ R_4^4(16)\ R_4^4(14)\ R_4^4(32)$. Each of the patterns described above is adjacent to a neighbouring hydrogen bonding ring. The overall network is illustrated in the stereo diagram in Figure 5.73.

Two of the C-H···O hydrogen bonds listed in Table 5.21 above serve to stabilise the interaction between the networks. The C2-H···O19‡ (‡: *x*, *y*, *z*) and C14-H···O10‡ (‡: *1-x*, *1-y*, *-z*) H-bonds are interactions between acipimox anions and tranexamic acid counterions, while the C21-H···O19‡ (‡: *2-x*, *1-y*, *-z*) interaction involves two tranexamic acid cations.

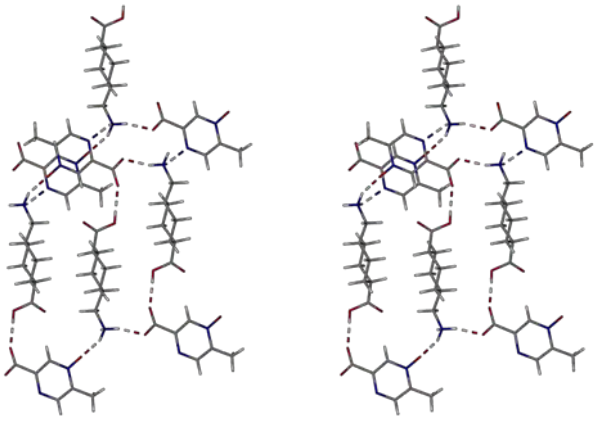

Figure 5.73: Stereo diagram showing the hydrogen bonding network present in ACPTRA

CRYSTAL PACKING

The hydrogen bonding network propagates along the *c*-axis forming layers. The layers are hydrogen bonded to subsequent layers along the *b*-axis. The hydrogen bonding pattern N_1 is responsible for linking these layers. The layers and hydrogen bonding can be seen in Figure 5.74a. A consequence of this packing pattern is that the acipimox anions form columns which stack along the *a*-axis. The tranexamic acid cations are arranged in columns stacking along the *b*-axis. The acipimox anion and tranexamic acid cation columns can be seen in Figure 5.74b., where the hydrogen atoms have been omitted for clarity.

The packing of the structure is further stabilised by two non-classical hydrogen bonds in the structure. The hydrogen bond C14-H···O10‡ (‡: *1-x*, *1-y*, *-z*) occurs within the layers stabilising this arrangement. The hydrogen bond C21-H···O19‡ (‡: *2-x*, *1-y*, *-z*) links the layers, stabilising their packing. The overall structure is further stabilised by π-π stacking, which is expanded upon below.

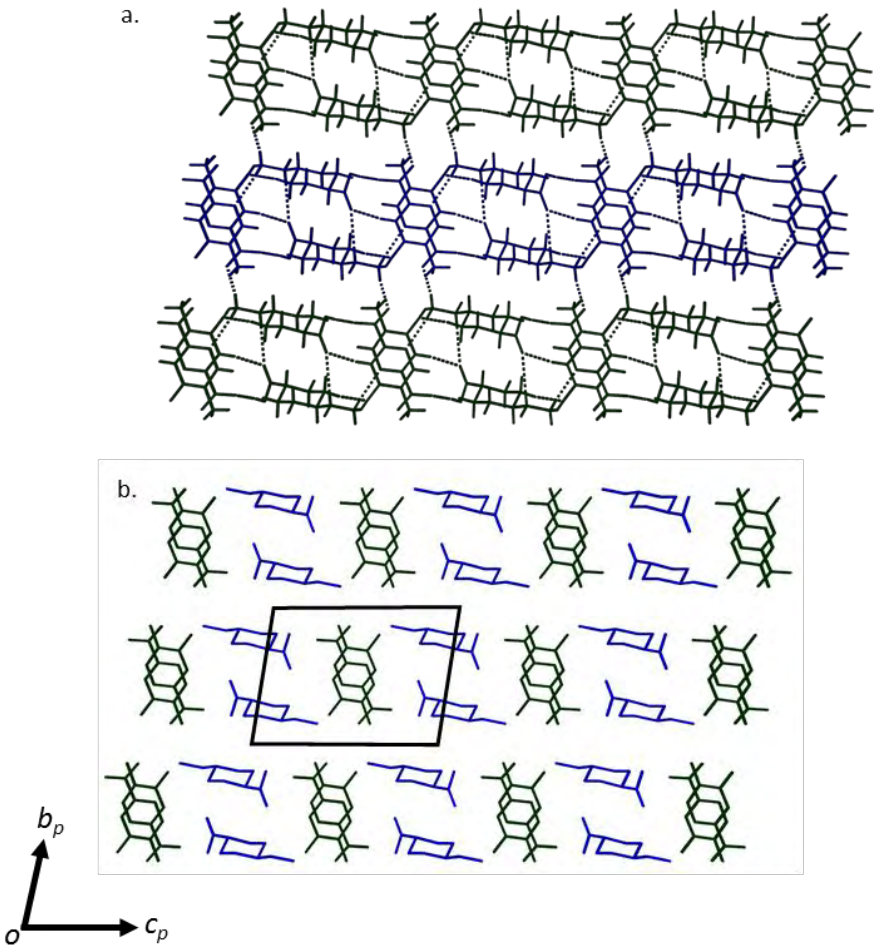

Figure 5.74: Packing of the salt ACPTRA highlighting a. the layers of the network N, linked through the hydrogen bonding pattern N_1 with alternating layers in blue and green and b. the columns of acipimox anions (green) and tranexamic acid cations (blue) with hydrogen atoms omitted for clarity

The π-π stacking takes place between the aromatic rings of inversion-related acipimox anions in the columns along the *a*-axis. There are two such interactions, the first having a centroid-to-centroid distance of 3.581(1) Å with the centroids offset by approximately 1.4 Å. The acipimox aromatic rings in the second π-π stacking interaction have centroids that are offset by a small distance of approximately 0.9 Å. The centroid-to-centroid distance is 3.636(1) Å. The least-squares planes of the acipimox aromatic anion rings in each of these interactions are parallel because the respective ring-pairs are both inversion-related. The relevant data for the π-π stacking in ACPTRA are presented in Table 5.22.

Table 5.22: π-π interaction parameters in ACPTRA

Ring Interaction	Centroid-centroid Distance (Å)	Symmetry Operator
Cg(A)···Cg(A)	3.581(1)	(*-x, 1-y, 1-z*)
Cg(A)···Cg(A)	3.636(1)	(*1-x, 1-y, 1-z*)

Cg refers to the centroid of a ring and the symmetry operator in column 3 refers to the second Cg listed in column 1

Ring A: C1-C2-N3-C4-C5-N6

COMPARATIVE PXRD

The data for the PXRD trace were collected at room temperature, while the data for the single crystal structure were collected at 173(2) K. The PXRD patterns of the bulk sample of ACPTRA and the pattern calculated from refined single crystal data show good agreement, with slight differences in the angular positions of the peaks. This indicates that the single crystal of ACPTRA is representative of the bulk material. The slight differences in peak locations are due to the anisotropic contraction of the unit cell upon cooling for the single crystal structure data collection.

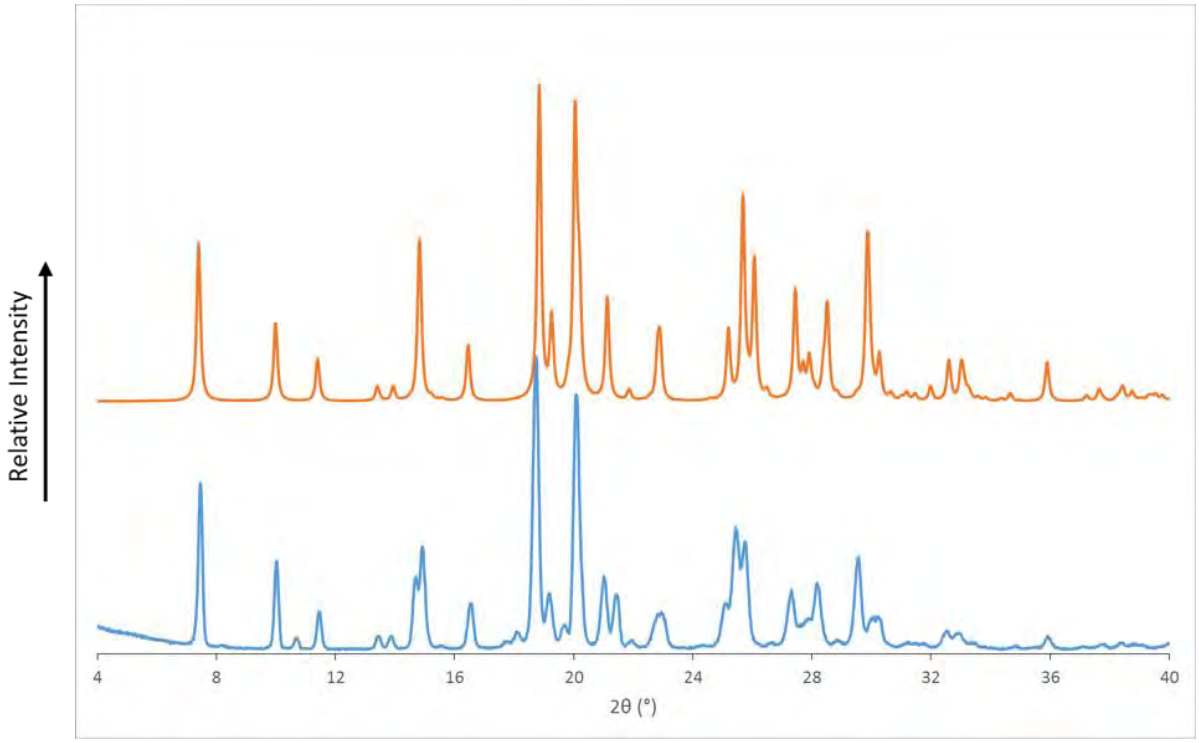

Figure 5.75: The PXRD trace for the bulk sample (blue) and the computed PXRD pattern based on the single crystal X-ray structure of ACPTRA (orange)

INFRARED SPECTROSCOPY

The designation of ACPTRA as a salt was established from the position of a proton on the carboxylic acid group of tranexamic acid. This was observed from the refined single crystal structure. Infrared spectroscopy was performed to investigate whether the spectrum of ACPTRA supported this designation. FTIR was also investigated for its use as a rapid identification method for the product. These investigations were performed as for previous structures.

From the infrared spectrum (Figure 5.76) of ACPTRA the presence of both a carboxylic acid and carboxylate anion were observed. The signals at 1705 cm^{-1} and 1268 cm^{-1} are characteristic of a carboxylic acid carbonyl group and C-O stretching respectively. The signals for the carboxylate anion can be seen at 1579 cm^{-1} and 1369 cm^{-1}. As pure tranexamic acid exists as a zwitterion[13] and acipimox possesses a carboxylic acid group, it is not possible to confirm the presence of a proton transfer from infrared spectroscopy alone.

To investigate the use of FTIR as a rapid method for identifying ACPTRA, first the formation of a new phase was investigated. This was done by comparison of the ACPTRA spectrum with the spectra of the starting materials. Differences were observed in the carbonyl absorbance peaks at 1705 cm^{-1} and 1701 cm^{-1} in the ACPTRA and acipimox spectra respectively. The signals of the carboxylate anion functional groups in the ACPTRA and tranexamic acid signals showed variation in their positions. The carboxylate signals were observed at 1579 cm^{-1} and 1369 cm^{-1} in the ACPTRA spectrum and at 1531 cm^{-1} and 1379 cm^{-1} in the tranexamic acid spectrum. An O-H group signal, present in the acipimox spectrum (3554 cm^{-1}), overlaps with the broad region from 3241 cm^{-1} to 2404 cm^{-1} in the ACPTRA spectrum. This broad absorption is indicative of hydrogen bonded amine and hydroxyl groups. The peaks used in an attempt to confirm a proton transfer would serve to identify ACPTRA.

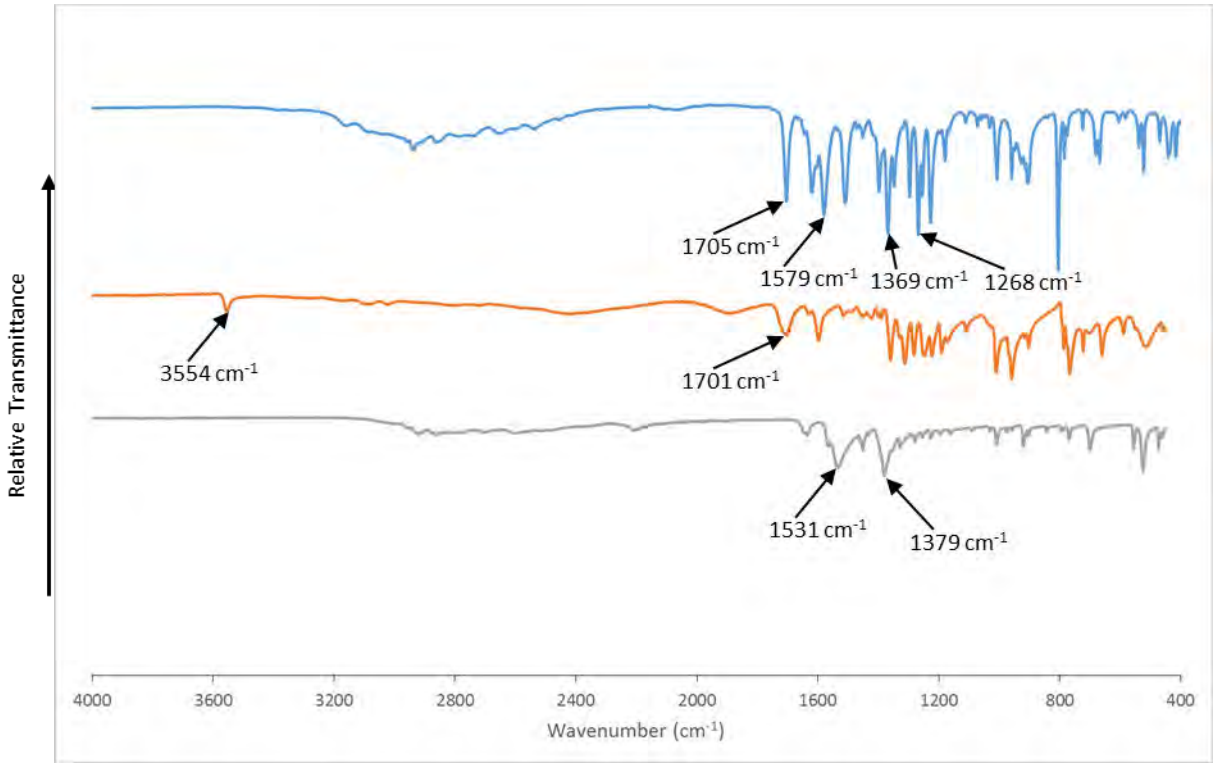

Figure 5.76: FTIR spectra for ACPTRA (blue), acipimox (orange) and tranexamic acid (grey)

ACIPIMOX/TRANEXAMIC HYDRATE

The hydrated multi-component crystalline system of acipimox and tranexamic acid will be referred to as ACPTRA-W.

SAMPLE PREPARATION

This system was prepared *via* co-precipitation. Acipimox (10 mg, 0.065 mmol) was weighed out and dissolved in 3 cm^3 butan-1-ol. An equimolar quantity of tranexamic acid (10 mg, 0.065 mmol) was added to the solution. The resulting mixture was stirred for 2 – 3 hours at 50 °C, at which point a few drops of Milli-Q water were added to the resulting solution. The solution was then filtered through a 0.45 μM nylon filter into a clean vial. The vial was then left to stand on the benchtop for several days until plate-shaped crystals were observed.

STOICHIOMETRY

^{1}H-NMR spectroscopy was used to determine the stoichiometry of ACPTRA-W. Several crystals obtained from co-precipitation were dissolved in DMSO-d_6 and ^{1}H-NMR spectroscopy was performed on the sample. The relative integration of the acipimox methyl group, set as the reference integral, and the tranexamic acid C-H_{21} proton peaks were used to determine a 1:1 stoichiometric ratio. The proton labelling schemes of acipimox and tranexamic acid are shown in Figure 5.77, while the integration values are presented in Table 5.23. The spectrum is shown in Figure 5.78.

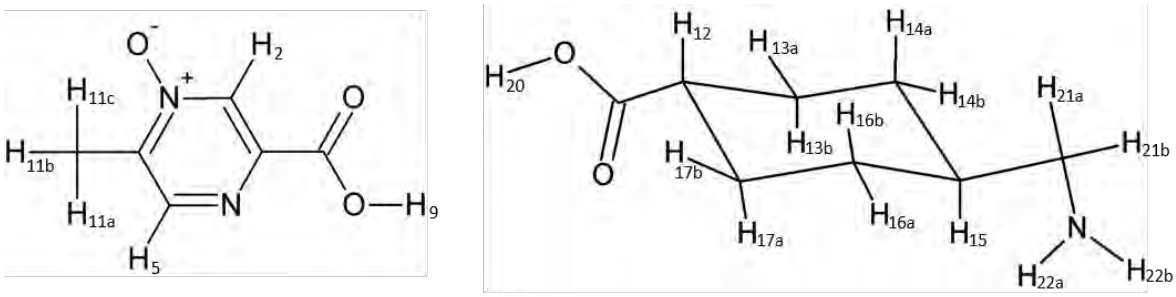

Figure 5.77: Proton labelling of acipimox (left) and tranexamic acid (right)

Table 5.23: Integrals and assignment of component protons for stoichiometric determination

Proton	δ (ppm)	Integration		Experimental/ Theoretical
		Experimental	Theoretical	
Acipimox				
C-$H_{11a,b,c}$	2.36	3.00‡	3.00	1
C-H_2	8.47	1.05	1.00	1.05 ≈ 1
C-H_5	8.53	1.05	1.00	1.05 ≈ 1
Tranexamic Acid				
C-$H_{21a,b}$	2.70	2.04	2.00	1.02 ≈ 1

‡ *Reference integral*

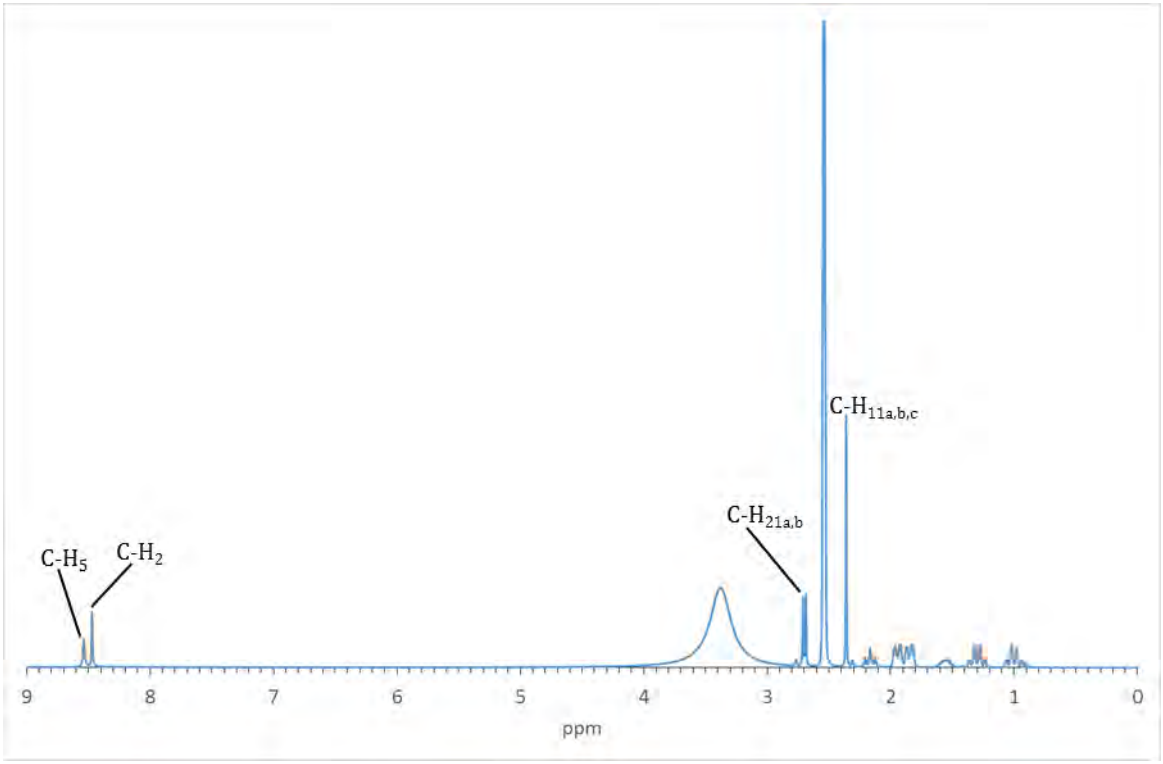

Figure 5.78: ^{1}H-NMR spectrum of ACPTRA-W in DMSO-d_6 used to determine the stoichiometric ratio

THERMAL ANALYSIS

The TGA trace for ACPTRA-W (Figure 5.79) shows a mass loss of 4.5 ± 0.1 % (n = 2) beginning at 76.7 ± 0.6 °C. This mass loss corresponds to the loss of a single water molecule (calculated 5.5 %). The discrepancy between the measured and calculated values was greater than usually observed. Further reference to this point is made in the section entitled Structure Solution and Refinement. A large mass loss of 53.6 ± 2.8 % occurs from 209.6 ± 0.8 °C to 266.0 ± 2.7 °C corresponding to the beginning stages of decomposition of the crystalline system. The mass then continues to decrease as the decomposition continues. The DSC trace shows two endotherms relating to each of the mass losses, the first relating to the loss of water and then at 239.9 ± 1.0 °C (n = 2) corresponding to simultaneous melting and decomposition of the product. The HSM micrographs (Figure 5.80) at 110 °C and 247 °C show the loss of the water and the simultaneous melting and decomposition respectively. The image at 282 °C shows the decomposed product.

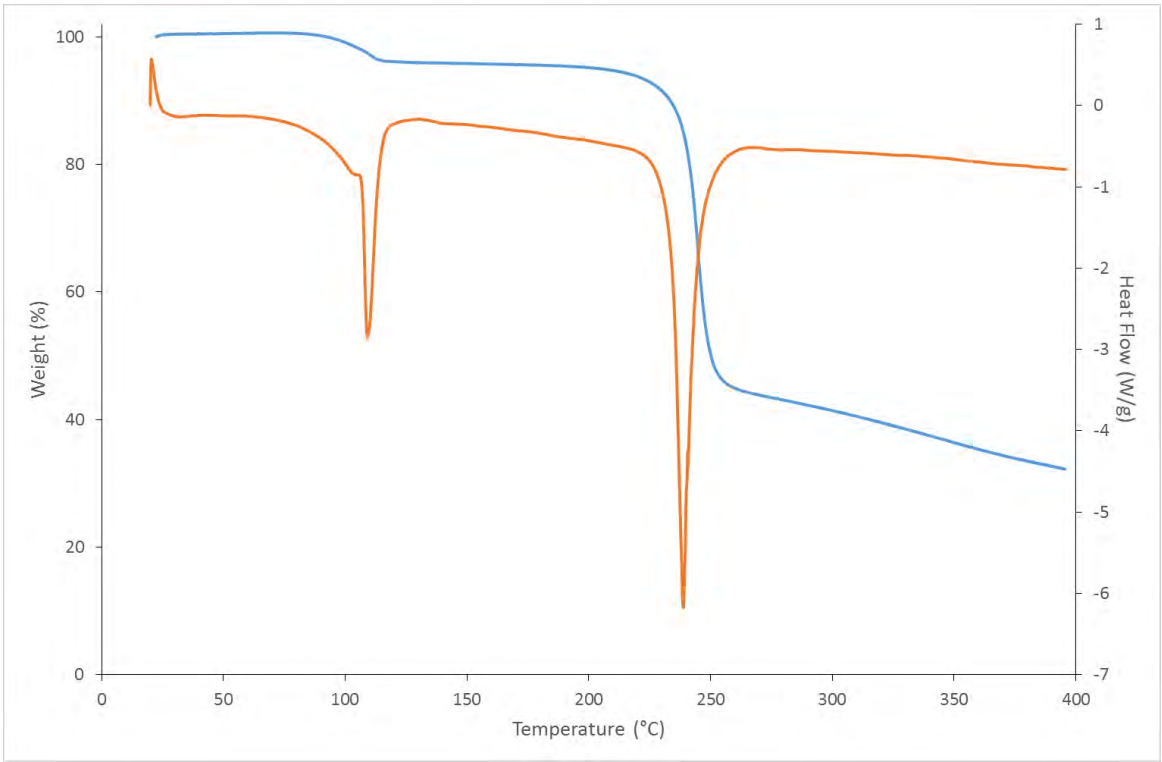

Figure 5.79: Representative TGA (blue) and DSC (orange) traces for ACPTRA-W

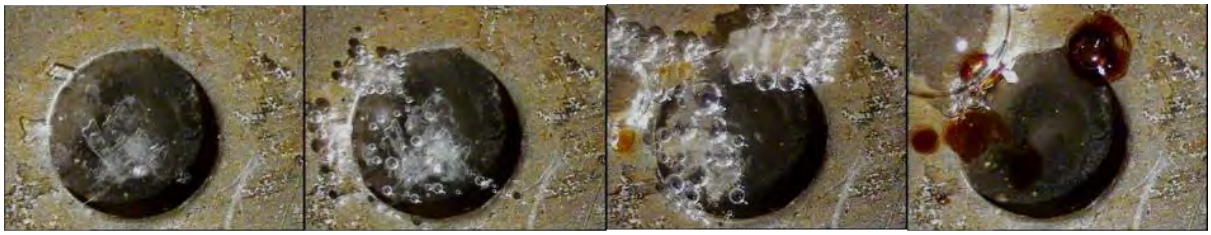

Figure 5.80: Hot stage micrographs showing ACPTRA-W crystals at various stages of heating

The removal of water from the structure through heating gives rise to the anhydrous salt ACPTRA. The dehydrated product was subjected to PXRD analysis to confirm the formation of the anhydrous salt. The conversion from the hydrated ACPTRA-W salt to the anhydrous multi-component crystalline system was not pursued in detail.

CRYSTAL STRUCTURE ANALYSIS

DATA COLLECTION AND SPACE GROUP DETERMINATION

The single crystal intensity data were collected at 173 ± 2 K on a Nonius KappaCCD diffractometer. The computer program LAYER[2] was used to determine the crystal system and space group of ACPTRA-W. The Laue symmetry of $\bar{1}$ indicated that the crystal system was triclinic. The program XPREP[3] was used to determine the space group, where an $|E^2-1|$ value of 1.017 indicated centrosymmetry. The only remaining choice of space group was thus P $\bar{1}$.

STRUCTURE SOLUTION AND REFINEMENT

Data reduction and unit cell refinement were performed using the software program DENZO.[4] The atomic co-ordinates were located by SHELXS[5] employing direct methods. Once the atoms were placed in their presumed positions the program SHELXL[5,6] was used to refine the structure isotropically. The non-hydrogen atoms were subsequently refined anisotropically. Careful inspection of the Fourier difference map revealed the position of a hydrogen atom located on the carboxylic acid group of the tranexamic acid cation. The carboxylate moiety of the acipimox anion lacked the presence of the hydrogen atom. The transfer of the hydrogen atom led to the designation of ACPAPYR-W as a salt. This designation was further supported by the C-O bond lengths of the acipimox carboxylate anion. These bond distances were found to be of intermediate distance between single and double carbon-oxygen bond lengths and are equal within experimental error with values of 1.250(2) Å and 1.257(2) Å. The hydrogen atoms of the water molecule were similarly located. After locating the hydrogen atoms in the Fourier difference map, they were placed in idealised positions using a riding model and refined isotropically with thermal parameters 1.2 to 1.5 times those of the parent atoms.

Due to the discrepancies in the TGA experimental and calculated values for water content, special consideration was given to the oxygen atom of the water molecule in the crystal structure. The oxygen atom of the water molecule was assigned a s.o.f. of 0.81 based on the experimental TGA value. This resulted in an unrealistic U_{iso} value of 0.0202(4) Å^2 compared to the average U_{iso} value of 0.033(3) Å^2 for hydrogen-bonded oxygen atoms. When the s.o.f. of the water oxygen atom was set to unity, the U_{iso} value converged to a physically more reasonable value of 0.0327(3) Å^2, and hence the final model accounted for a full water molecule in the asymmetric unit. It was therefore assumed that the water content had been underestimated in the TGA analysis, possibly due to prior loss of water during sample manipulation.

Table 5.24: Crystallographic data for the single crystal X-ray structure of ACPTRA-W

Chemical Formula	$(C_6H_5N_2O_3)^-\cdot(C_8H_{16}NO_2)^+\cdot H_2O$
Molar mass (g mol^{-1})	329.35
Crystal System	Triclinic
Space Group	P $\bar{1}$
Unit cell parameters	
a (Å)	6.6123(13)
b (Å)	8.4195(17)
c (Å)	15.016(3)
α (°)	93.36(3)
β (°)	102.63(3)
γ (°)	101.14(3)
Volume (Å^3)	795.9(3)
Z	2
Density$_{calcd.}$ (g cm^{-3})	1.374
μ [MoKα] (mm^{-1})	0.108
F (000)	352
Temperature (K)	173(2)
Crystal size (mm)	0.11×0.23×0.47
Range scanned θ (°)	3.0 – 27.5
Index ranges	h: -8, 8; k; -10, 10; l: -19, 19
ϕ and ω scan angle (°)	0.5
Dx (mm)	45
Total number of reflections	6 735
Number of independent reflections	3 612
Number of reflections with I > 2σ(I)	2 697
R_{int}	0.032
R_1 [I > 2σ(I)]	0.0382
wR_2	0.1062
S	1.034
Number of parameters	214
Number of reflections omitted	6
Parameters a, b	a: 0.0493, b: 0.2055
in w = 1/[σ^2(F_0^2)+(aP)^2+(bP)]	
$(\delta/\sigma)_{mean}$	<0.001
Δρ excursions (e Å^{-3})	-0.31, 0.24

MOLECULAR STRUCTURE

The asymmetric unit of the hydrated salt ACPTRA-W (Figure 5.81) comprises one acipimox anion, one tranexamic acid cation and one water molecule. A proton transfer from the carboxylic acid group of acipimox to the carboxylate group of tranexamic acid occurs during synthesis of this crystalline system resulting in salt formation. Both the acipimox anion and the tranexamic acid cation are hydrogen bonded to the water molecule in the asymmetric unit. There are further interactions among the components of this hydrate, which are expanded upon in the Hydrogen Bonding section below.

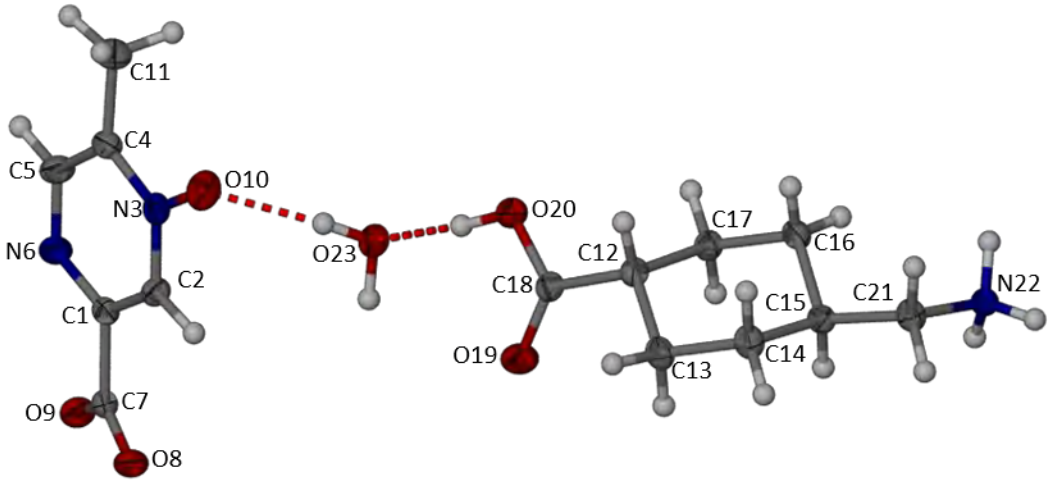

Figure 5.81: The asymmetric unit of ACPTRA-W with the numbering scheme of acipimox (left) and tranexamic acid (right). Thermal ellipsoids are drawn at the 50 % probability level

HYDROGEN BONDING

In the multi-component crystalline system ACPTRA-W there are six hydrogen bonding synthons. Three of these involve the water molecule. The first of these is a hydrogen bond between the water molecule and the pyrazine oxide moiety of acipimox (Figure 5.82a.), while the second is that between the water molecule and a carboxylate oxygen atom of the acipimox anion (Figure 5.82b.). The third hydrogen bond involving the water molecule is that linking it to the carboxylic acid group of the tranexamic acid cation (Figure 5.82c.). The water molecule acts as the donor in the first two hydrogen bonds, while in the third the oxygen of the water molecule is the acceptor.

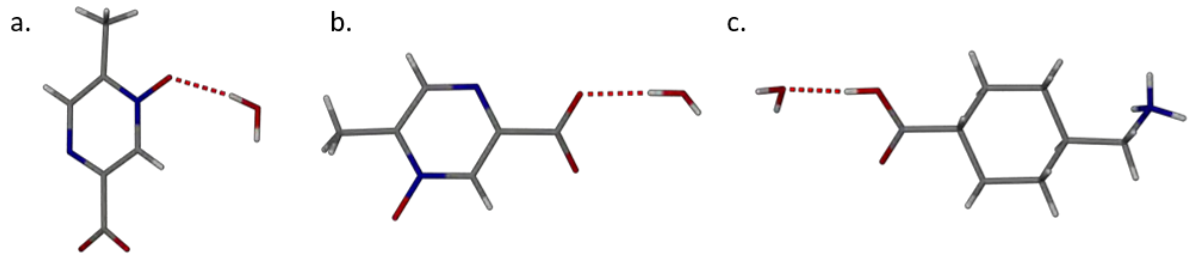

Figure 5.82: Hydrogen bonds in ACPTRA-W involving the water molecule with a. the pyrazine oxide of the acipimox anion, b. a carboxylate oxygen atom of the acipimox anion and c. the carboxylic acid group of the tranexamic acid cation.

The remaining three hydrogen bonding synthons involve the tranexamic cation. The first two occur between the ammonium cation of tranexamic acid and two acipimox anions related by translation along the *a*-axis, both interacting through their carboxylate groups. These hydrogen bonds can be seen in Figure 5.83a. The final hydrogen bonding synthon involves two ammonium cations of tranexamic acid, whereby each of the ammonium groups hydrogen bonds to the carbonyl oxygen of its inversion-related counterpart. In this homosynthon dimer the two moieties hydrogen bond in a head-to-tail manner. This can be seen in Figure 5.83b. The parameters of these hydrogen bonds are presented in Table 5.25.

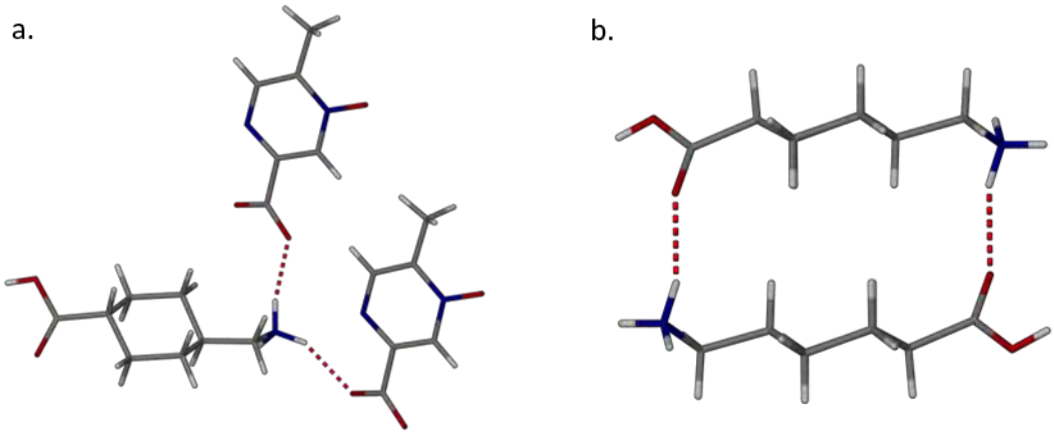

Figure 5.83: Hydrogen bonding interactions between the tranexamic acid cation and a. carboxylate oxygen atoms of two acipimox counterions and b. an inversion-related tranexamic acid cation

Table 5.25: Hydrogen bonding parameters in ACPTRA-W

D-H···A	D···A (Å)	Angle (°)	Symmetry Operator
O20-H···O23	2.597(2)	176	(*x, y, z*)
N22-H···O19	2.851(2)	144	(*-1-x, -y, 1-z*)
N22-H···O8	2.894(2)	153	(*-1+x, y, 1+z*)
N22-H···N6	2.958(2)	124	(*-1+x, y, 1+z*)
N22-H···O9	2.782(2)	161	(*x, y, 1+z*)
O23-H···O8	2.731(2)	174	(*-x, -y, -z*)
O23-H···O10	2.739(2)	169	(*x, y, z*)
C16-H···O23	3.431(2)	159	(*-x, -y, 1-z*)
C21-H···O10	3.344(2)	141	(*-x, 1-y, 1-z*)

When combined, these synthons form four hydrogen bonding patterns. The first, N_1, has graph-set descriptor $R_4^4(18)$. The hydrogen bonds in N_1 involve two acipimox anions linked through two water molecules. The water molecules act as hydrogen bond donors, while the carboxylate anions and pyrazine oxide groups on the acipimox ions act as acceptors. This hydrogen bonding pattern is located on a centre of inversion (Figure 5.84).

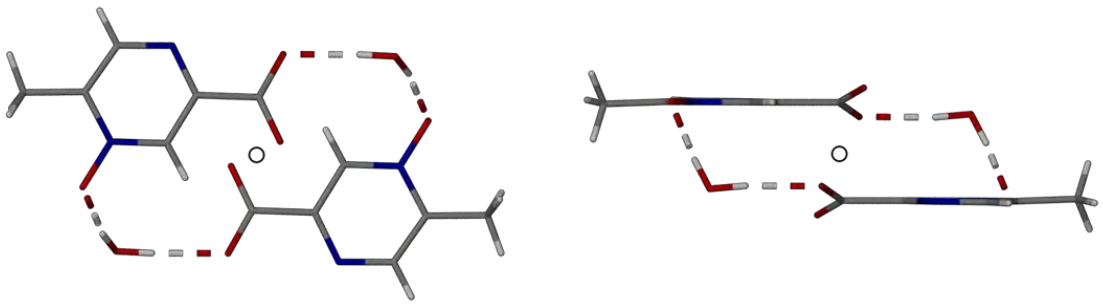

Figure 5.84: Two views of the hydrogen bonding pattern $N_1 = R_4^4(18)$ in ACPTRA-W

The second hydrogen bonding pattern (Figure 5.85) occurs between one tranexamic cation and one acipimox anion. It has the form $N_2 = R_1^2(5)$, where a hydrogen atom of the ammonium group of the tranexamic acid cation forms a bifurcated hydrogen bond with the acipimox anion. The ammonium group acts as the donor with the pyrazine nitrogen and a carboxylate oxygen of the acipimox anion being acceptors.

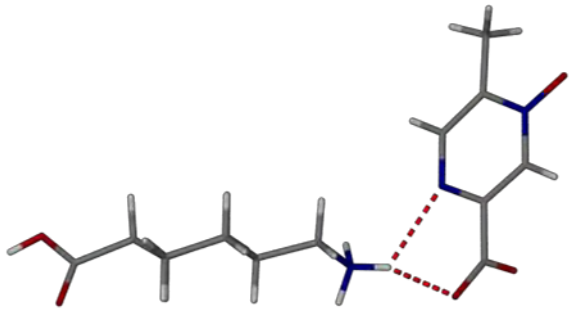

Figure 5.85: Hydrogen bonding pattern $N_2 = R_1^2(5)$ in ACPTRA-W

The third pattern comprises two tranexamic acid cations, one acipimox anion and one water molecule. The tranexamic acid cations hydrogen bond through the ammonium group on the first cation and the carbonyl oxygen on the second. The pattern has the graph-set descriptor $N_3 = R_4^3(10)$ where the ammonium cation of the first tranexamic acid cation hydrogen bonds with the carboxylate anion of the acipimox counterion while the water molecule links the acipimox carboxylate anion to the second tranexamic acid carboxylic acid group (Figure 5.86).

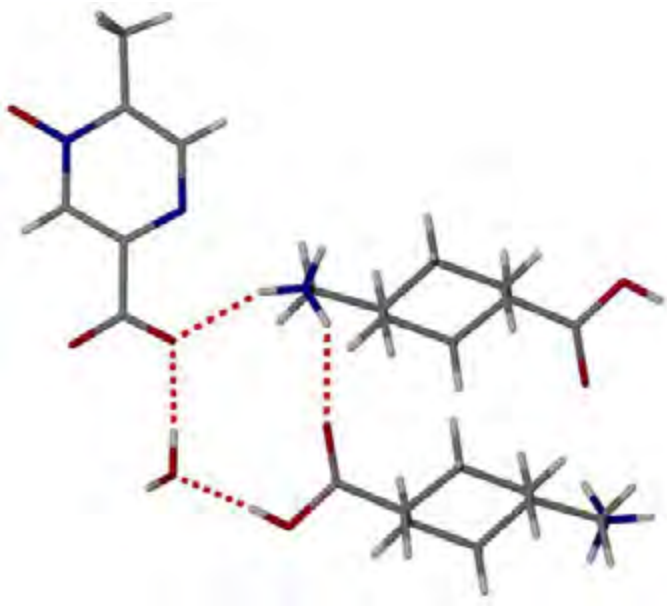

Figure 5.86: Hydrogen bonding pattern $N_3 = R_4^3(10)$ in ACPTRA-W

The final hydrogen bonding pattern comprises two tranexamic cations in a head-to-tail arrangement. The ammonium cation groups act as hydrogen bond donors on each tranexamic acid molecule interacting with the carbonyl oxygens of its inversion-related counterpart. This final pattern has the graph-set descriptor $N_4 = R_2^2(18)$ and is shown in Figure 5.87. The pattern N_4 is located on an inversion centre.

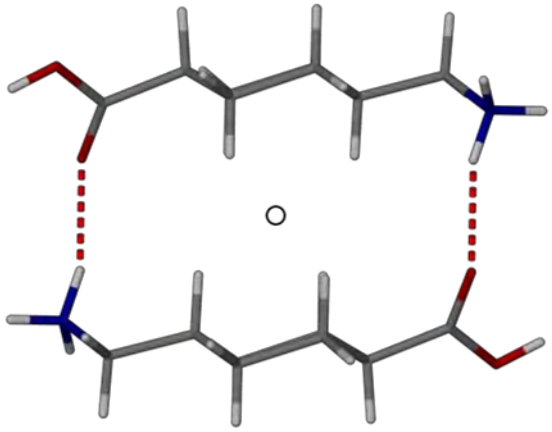

Figure 5.87: Hydrogen bonding pattern $N_4 = R_2^2(18)$ in ACPTRA-W

The hydrogen bond C16-H···O23‡ (‡: *-x, -y, 1-z*) stabilises the position of the water molecule in each of these patterns.

The four hydrogen bonding patterns combine to form a large repeating network, shown in Figure 5.88. The network formed is designated N = $R_4^4(18)R_1^2(5)R_4^3(10)R_2^2(18)$ and can be seen in the stereo diagram (Figure 5.88).

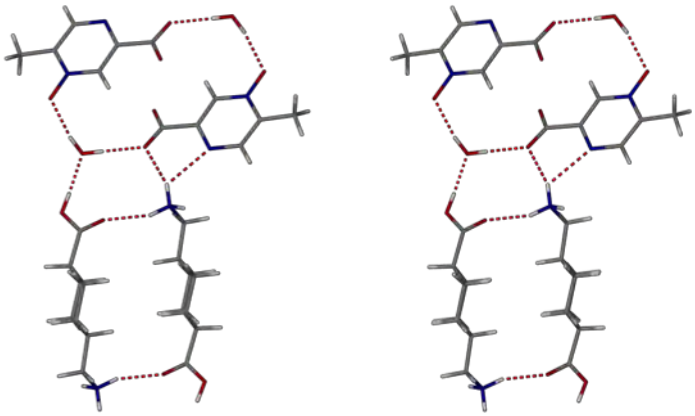

Figure 5.88: Stereo diagram showing repeating network N = $R_4^4(18)R_1^2(5)R_4^3(10)R_2^2(18)$ in ACPTRA-W

CRYSTAL PACKING

The repeating network N forms infinite sheets, which stack along the *b*-axis creating layers (Figure 5.89a. and Figure 5.89b.). They are arranged such that the acipimox anions in adjacent layers are positioned one above another, which can be clearly seen in Figure 5.89c. This pattern is stabilised by a π-π interaction between the aromatic rings of acipimox within the layers. The least-squares planes of the acipimox anion aromatic rings are parallel in the interaction, being related by inversion. The centroids of the aromatic rings are offset by approximately 1.5 Å. Relevant data for the π-π interaction are presented in Table 5.26. The C21-H···O10‡ (‡: *-x, 1-y, 1-z*) hydrogen bond links the adjacent layers and aids in stabilising the structure.

Table 5.26: π-π interaction parameters in ACPTRA-W

Ring Interaction (i to j)	**Centroid-centroid Distance (Å)**	**Symmetry Operator**
Cg(A)···Cg(A)	3.883(1)	(*1-x, 1-y, -z*)

Cg refers to the centroid of a ring and the symmetry operator in column 3 refers to the second Cg listed in column 1
Ring A: C1-C2-N3-C4-C5-N6

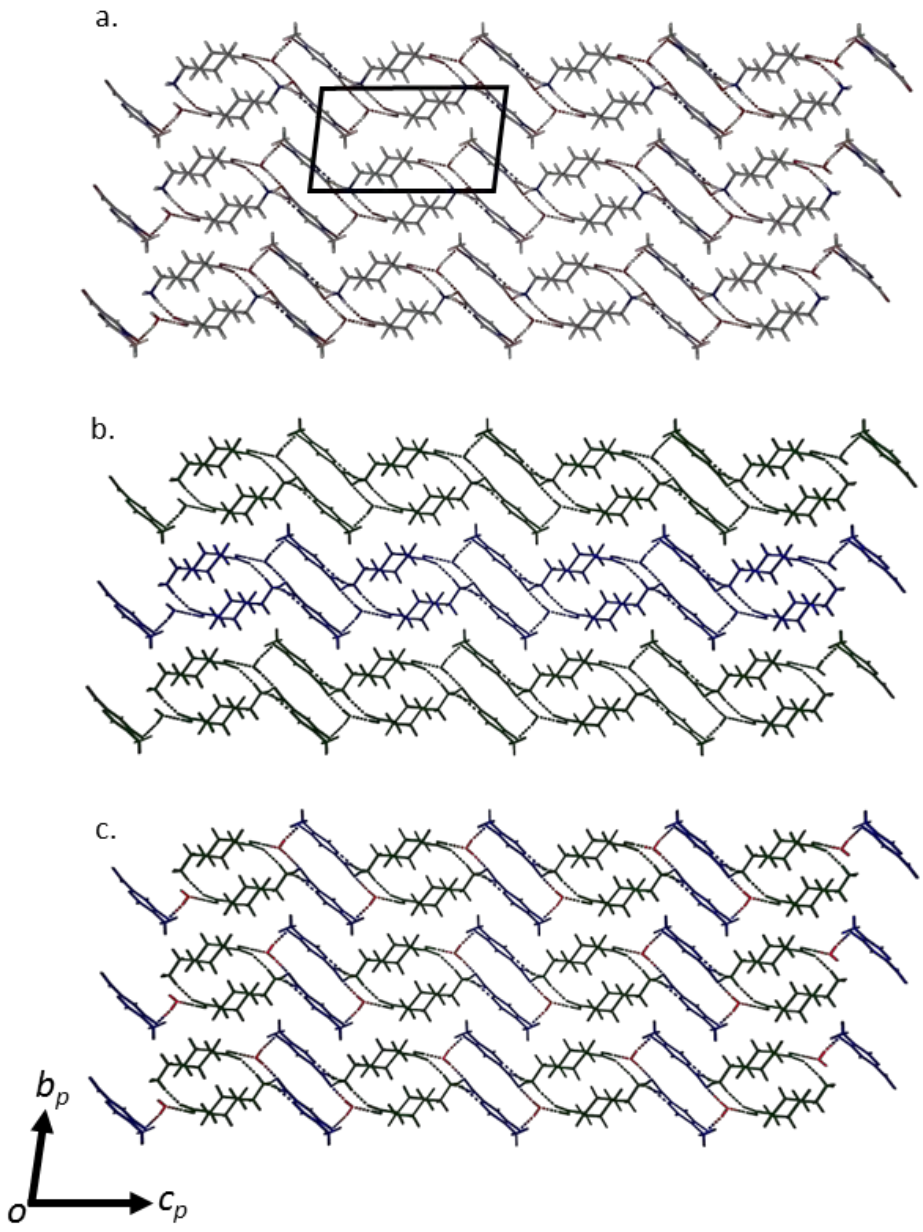

Figure 5.89: Packing diagrams of ACPTRA-W viewed along [1 0 0], a. showing the packing of the networks, b. highlighting the layers formed (indicated by alternating colours), c. showing the stacking of acipimox (blue), tranexamic acid (green) moieties and the water molecules (red)

COMPARATIVE PXRD

The PXRD experimental data were recorded at room temperature and compared with the trace calculated from the refined single crystal structure of ACPTRA-W. There exists a 1:1 correspondence between the angular positions of the peaks in the calculated and experimental traces but there are discrepancies between the intensities of corresponding peaks. This is attributed to preferred orientation of the crystallites of the sample, which is a result of the pronounced plate-like morphology of the crystals (Figure 5.80) persisting in the sample ground for PXRD analysis.

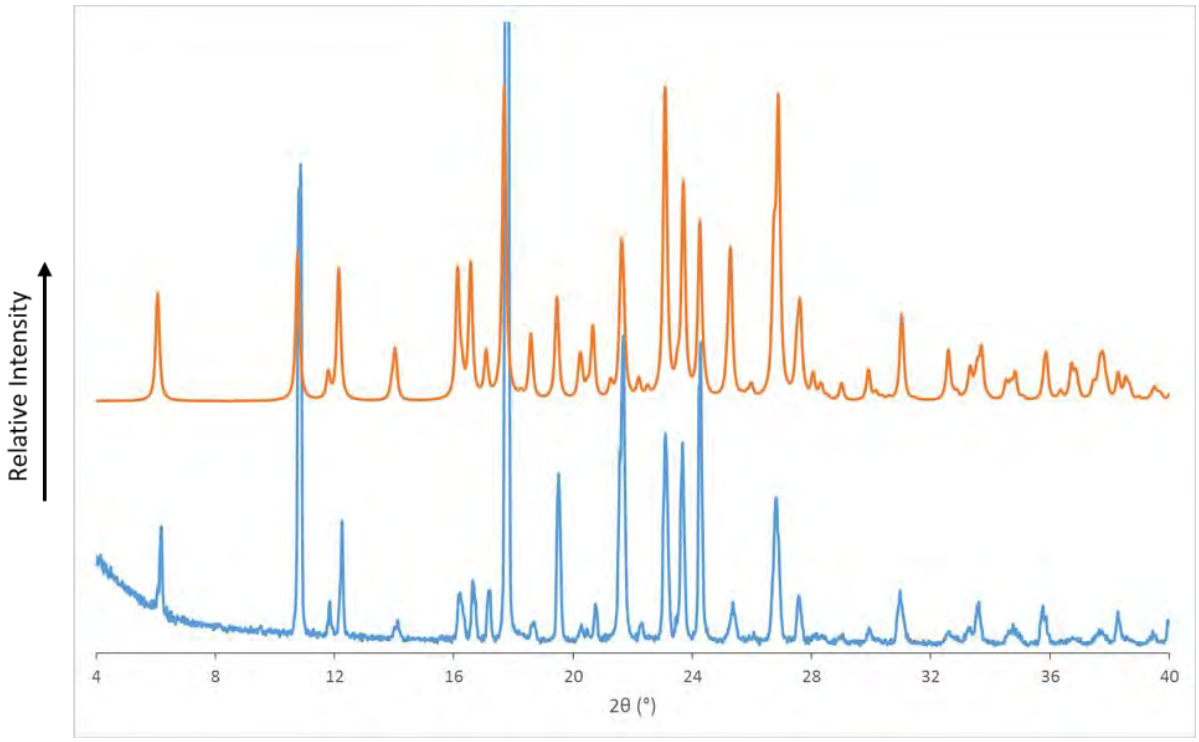

Figure 5.90: The PXRD trace for the bulk sample (blue) and the computed PXRD pattern based on the single crystal X-ray structure of ACPTRA-W (orange)

INFRARED SPECTROSCOPY

The refined single crystal X-ray structure of ACPTRA-W showed the position of the carboxylic acid proton on the tranexamic acid cation. No hydrogen atom was present on the carboxylate anion of the acipimox counterion. As a proton transfer had occurred, ACPTRA-W was designated a salt. Infrared spectroscopy was performed to determine whether the FTIR spectrum of ACPTRA-W supported this designation. As previously, FTIR was investigated as a rapid identification method for the product.

The infrared spectrum of ACPTRA-W (Figure 5.91) shows two signals characteristic of a carboxylate anion at 1568 cm^{-1} and 1374 cm^{-1}. A peak corresponding to the carbonyl carboxylic acid group at 1704 cm^{-1} was also observed in the spectrum. In its pure form, the co-former tranexamic acid exists as a zwitterion,[13] therefore it is not possible to conclusively assign these signals in the infrared spectrum of ACPTRA-W to either acipimox or tranexamic acid. One cannot therefore determine the presence of a proton transfer from FTIR alone.

A second purpose of using FTIR was to investigate this technique as a possible means of rapid identification of ACPTRA-W in future batches. The presence of the peaks presented above can be used for this purpose. Two distinct peaks at 3230 cm^{-1} and 2936 cm^{-1} were observed. However, due the broad absorption band from 3550 cm^{-1} to 2672 cm^{-1} the distinct peaks could not be unambiguously assigned. The comparison of the salt spectrum with the spectra of the starting materials was used to confirm the formation of a new phase. The peak corresponding to the hydroxyl group in the acipimox spectrum (3554 cm^{-1}) is not visible in that of ACPTRA-W. In the product spectrum, the broad absorption band (3550 cm^{-1} to 2672 cm^{-1}) obscures easy identification of a hydroxyl functional group signal. The slight differences in the carbonyl group peak in the two spectra can serve as an additional diagnostic difference. The carboxylate anion absorption peaks in the tranexamic acid spectrum (1531 cm^{-1} and 1379 cm^{-1}) differ from those in the ACPTRA-W spectrum. The differences between the salt spectrum and the spectra of the starting materials allow one to unequivocally establish the formation of the new product and its identity.

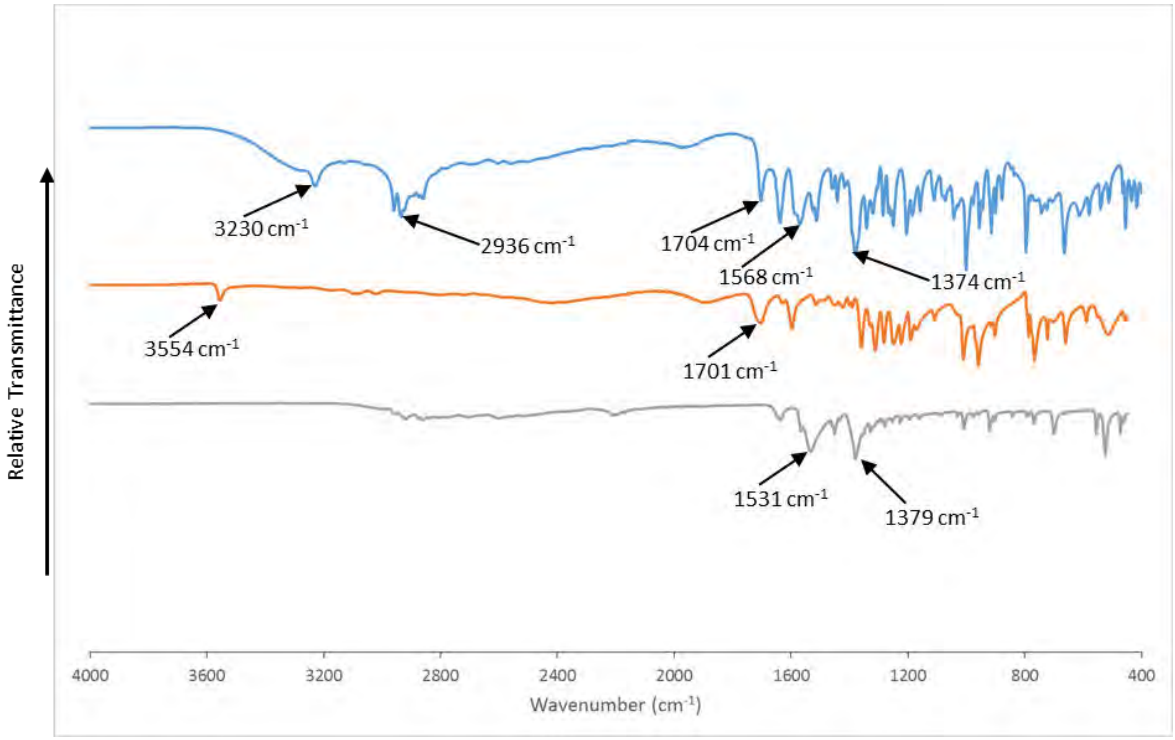

Figure 5.91: FTIR spectra for ACPTRA-W (blue), acipimox (orange) and tranexamic acid (grey)

ACIPIMOX/UREA ACETONITRILE

The crystalline system arising from the components acipimox, urea and acetonitrile shall be referred to as ACPUREA.

SAMPLE PREPARATION

The ACPUREA product was prepared in two ways. The first relied on mechanochemical action while the second was production *via* co-precipitation.

Liquid-assisted grinding required equimolar amounts of acipimox (10 mg, 0.065 mmol) and urea (4 mg, 0.065 mmol) to be weighed out. The compounds were combined in an agate mortar and ground together for 20 minutes using an agate pestle. During manipulation acetonitrile was added in a dropwise fashion.

When producing ACPUREA *via* co-precipitation 10 mg (0.065 mmol) acipimox was weighed into a vial. The acipimox was dissolved in 2.5 cm^3 acetonitrile and an equimolar amount of urea (4 mg, 0.065 mmol) was added to the vial and this mixture stirred at 40 °C for 2 hours. The resulting solution was then filtered into a clean vial through a 0.45 μm nylon filter and left on the benchtop to slowly evaporate. Over the course of 7 – 8 hours small block-shaped crystals appeared in the solution.

STOICHIOMETRY

The stoichiometric ratio of ACPUREA was determined *via* ^{1}H-NMR spectroscopy. Crystals produced by co-precipitation were dissolved in DMSO-d_6. The sample was then subjected to proton NMR spectroscopy. The relative integration of the acipimox methyl functional group (set as the reference integral) and the amine protons of urea were used to determine the stoichiometric ratio as 1:1. Due to the volatile nature of acetonitrile the product partially desolvated during manipulation and therefore the stoichiometry with respect to this component could not be determined through ^{1}H-NMR spectroscopy. The proton labelling diagrams are shown in Figure 5.92. The integration values are shown in Table 5.27 and the spectrum is presented in Figure 5.93.

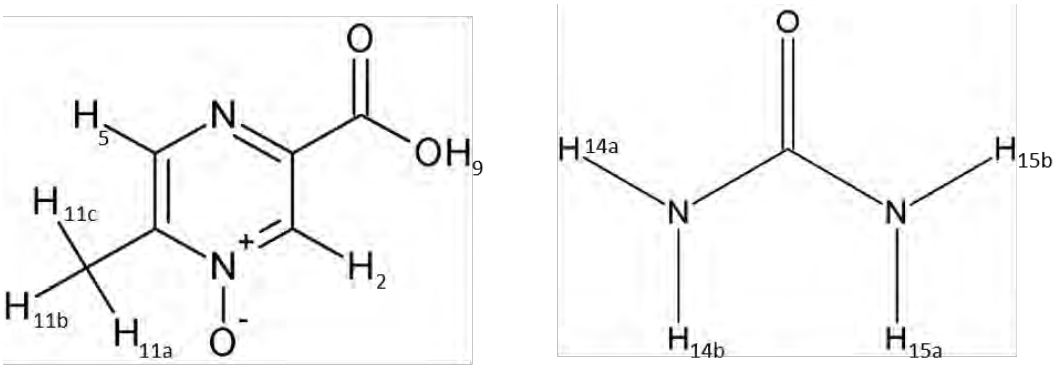

Figure 5.92: Proton labelling of acipimox (left) and urea (right)

Table 5.27: Integrals and assignment of component protons for stoichiometric determination

Proton	δ (ppm)	Integration		Experimental/ Theoretical
		Experimental	Theoretical	
Acipimox				
C-$H_{11a,b,c}$	2.42	3.00‡	3.00	1
C-H_2	8.69	1.02	1.00	1.02 ≈ 1
C-H_5	8.76	1.02	1.00	1.02 ≈ 1
Urea				
N-$H_{14a,b}$ + N-$H_{15a,b}$	5.43	3.82	4	0.96 ≈ 1

‡ *Reference integral*

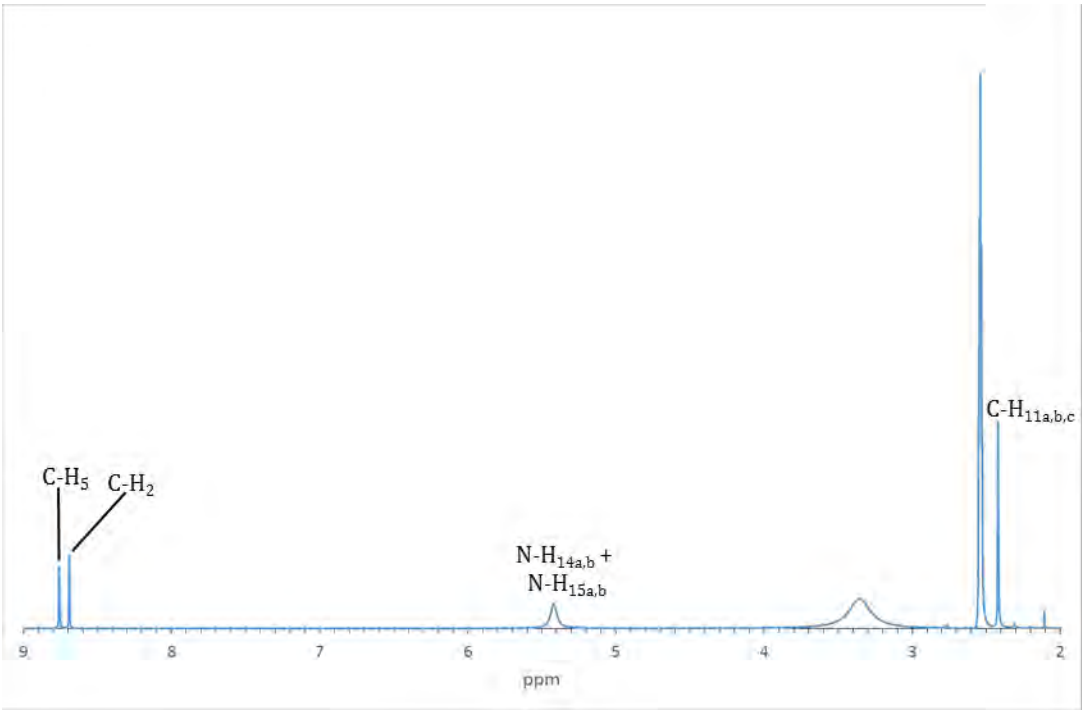

Figure 5.93: ^{1}H-NMR spectrum of ACPUREA in DMSO-d_6 used to determine the stoichiometric ratio

THERMAL ANALYSIS

The TGA profile (Figure 5.94) shows a mass loss between 49.9 ± 2.1 °C and 92.1 ± 0.1 °C (n = 2) of 15.2 ± 0.2 % corresponding to the loss of one acetonitrile molecule from the solvated system (calculated = 16.1 %). The DSC trace displays a corresponding endotherm. The TGA trace then shows a two stage mass loss, beginning at 147.4 ± 1.7 °C where the first mass loss of 20.5 ± 0.9 % corresponds to the loss of one urea molecule (calculated = 23.5 %). This is immediately followed by the decomposition of the remaining acipimox component. In the DSC trace endotherms corresponding to melting immediately followed by decomposition are visible over the same range. The HSM micrograph (Figure 5.95) at 75 °C shows bubbling, indicative of solvent loss. The micrograph at 180 °C shows the beginning stages of decomposition and the final micrograph at 250 °C shows the sample in the final stages of decomposition.

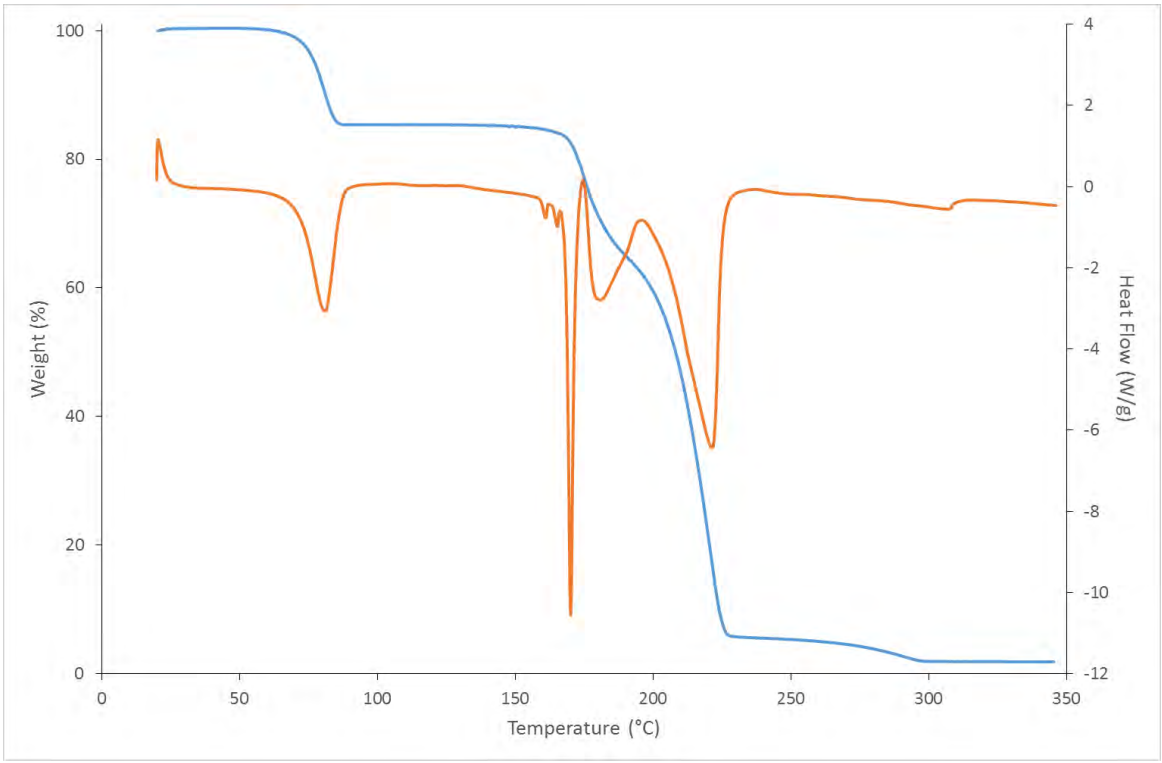

Figure 5.94: Representative TGA (blue) and DSC (orange) traces for ACPUREA

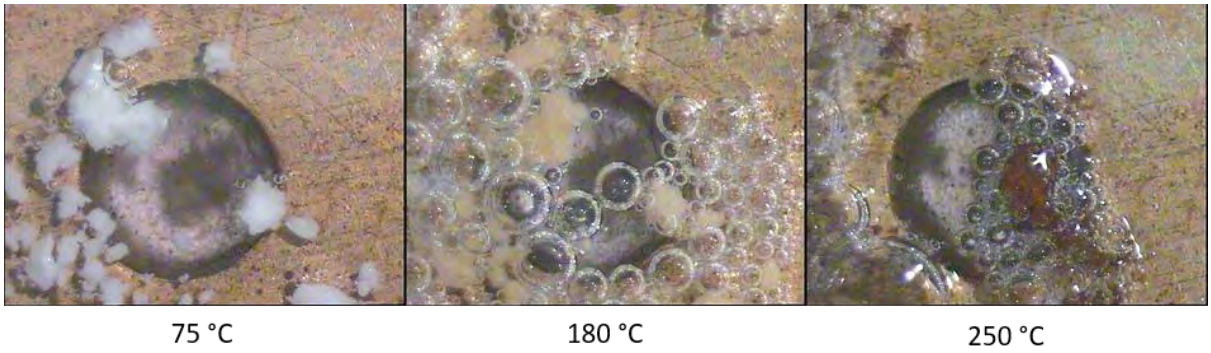

Figure 5.95: Hot stage micrographs showing the ACPUREA multi-component crystalline system at various stages of heating

Based on all the above data, a 1:1:1 stoichiometry for the API·co-former·acetonitrile system was predicted but the states of ionization (or otherwise) of the API and co-former remained to be determined.

CRYSTAL STRUCTURE ANALYSIS

DATA COLLECTION AND SPACE GROUP DETERMINATION

The single crystal intensity data were collected at 173 ± 2 K using a Bruker KAPPA APEX DUO II diffractometer. The computer program LAYER[2] was used to determine the crystal system, the Laue symmetry $\bar{1}$ indicating triclinic symmetry. The $|E^2-1|$ value of 1.035 calculated by program XPREP[3] signified that the structure is centrosymmetric, so the correct choice for the space group was P $\bar{1}$.

STRUCTURE SOLUTION AND REFINEMENT

The computer program SAINT[10] was used to perform the data reduction and unit cell refinement. The absorption corrections were executed by the computer program SADABS[11] employing the multi-scan method. The atomic co-ordinates were located by direct methods using SHELXS,[5]. After placing the atoms in their presumed positions the structure was refined using the program SHELXL.[5,6] The non-hydrogen atoms were initially refined isotropically and later refined anisotropically. The designation of the product as a salt or co-crystal relied on careful examination of the position of the carboxylic acid hydrogen atom. The hydrogen atom in question, revealed in the difference Fourier map, was observed on the carboxylic acid moiety of acipimox. This was supported by the C-O bond lengths of the carboxylic acid group having values of 1.210(2) Å and 1.316(2), which are indicative of a carboxylic acid moiety with a double and single C-O bond, respectively. The acipimox and urea components were thus shown to be in their neutral states. The asymmetric unit of the solvate ACPUREA contains one acipimox molecule, one urea molecule and one acetonitrile molecule. The product ACPUREA was therefore designated a solvated co-crystal. After the remaining hydrogen atoms were located in the difference Fourier map, they were placed in idealised positions using a riding model. The U_{iso} values of these hydrogen atoms were 1.2 to 1.5 times those of the parent atoms. The crystallographic data are available in Table 5.28.

Table 5.28: Crystallographic data for the single crystal X-ray structure of ACPUREA

Chemical Formula	$(C_6H_6N_2O_3)\cdot(CH_4N_2O)\cdot(C_2H_3N)$
Molar mass (g mol^{-1})	255.24
Crystal System	Triclinic
Space Group	P $\bar{1}$
Unit cell parameters	
a (Å)	7.4990(9)
b (Å)	9.4124(12)
c (Å)	9.8814(12)
α (°)	64.714(3)
β (°)	70.679(3)
γ (°)	85.476(3)
Volume (Å^3)	593.53(13)
Z	2
Density$_{calcd.}$ (g cm^{-3})	1.428
μ [MoKα] (mm^{-1})	0.114
F (000)	268
Temperature (K)	173(2)
Crystal size (mm)	0.14×0.26×0.27
Range scanned θ (°)	2.4 – 28.2
Index ranges	h: -9, 7; k; -12, 10; l: -13, 11
ϕ and ω scan angle (°)	0.5
Dx (mm)	37.50
Total number of reflections	8 285
Number of independent reflections	2 866
Number of reflections with I > 2σ(I)	2 200
R_{int}	0.025
R_1 [I > 2σ(I)]	0.0419
wR_2	0.1155
S	1.067
Number of parameters	166
Number of reflections omitted	5
Parameters a, b	a: 0.0539, b: 0.1666
in w = 1/[$\sigma^2(F_0^2)$+(aP)^2+(bP)]	
$(\delta/\sigma)_{mean}$	<0.001
Δρ excursions (e Å^{-3})	-0.28, 0.40

MOLECULAR STRUCTURE

The asymmetric unit of the solvate ACPUREA consists of one acipimox molecule, one urea molecule and one acetonitrile molecule. The asymmetric unit is shown in Figure 5.96. The acipimox and urea components interact through several hydrogen bonds as expanded upon below.

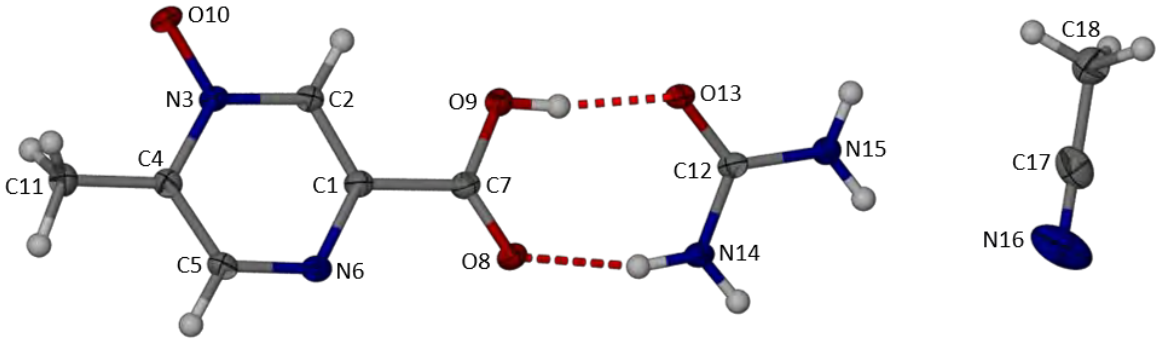

Figure 5.96: The asymmetric unit of ACPUREA with numbering schemes. Thermal ellipsoids are drawn at the 50 % probability level

HYDROGEN BONDING

There are four hydrogen bonding synthons present in the co-crystal ACPUREA. The classical hydrogen bonds involve acipimox and urea. Acetonitrile is only involved in non-classical hydrogen bonding. The first, shown in Figure 5.97a., is the hydrogen bonding synthon linking the carboxylic acid group of acipimox and the amide group of urea. The second is a hydrogen bond of the 'bifurcated acceptor' type, in which both of the H atoms of one amine group of the urea molecule are donated to a common acceptor atom, namely the carbonyl oxygen of acipimox. This hydrogen bond is shown in Figure 5.97b. The third involves a hydrogen atom of the same amine as in the second interaction and the aromatic nitrogen of acipimox acting as the acceptor (Figure 5.97c.). The final hydrogen bond, Figure 5.97d., involves the pyrazine oxide group of acipimox as the acceptor and the second amine of urea as the donor.

Acetonitrile does not participate in classical hydrogen bonding. However, two hydrogen bonds of the form C-H···A occur between acipimox and acetonitrile. The first, C5-H···N16‡ (‡: *-x, 1-y, 1-z*), has one of the aromatic hydrogens of acipimox interacting with the nitrogen group of acetonitrile. The second, C18-H···O10‡ (‡: *-x, 2-y, -z*), links the methyl group of acetonitrile and the pyrazine oxide of acipimox.

The final non-classical hydrogen bond, C2-H···O13‡ (‡: *-x, 2-y, -z*), occurs between acipimox and urea, specifically between an aromatic hydrogen of acipimox and the oxygen atom of urea. The

hydrogen bonding parameters and symmetry operators of all the hydrogen bonds present in this structure can be found in Table 5.29.

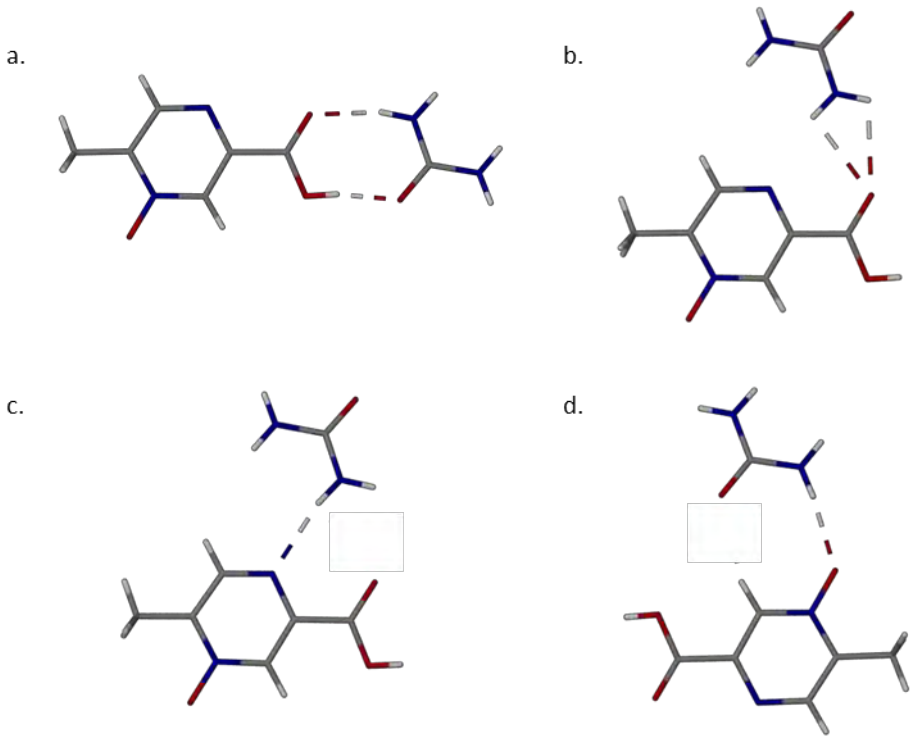

Figure 5.97: Hydrogen bonds present in ACPUREA

Table 5.29: Hydrogen bonding parameters for ACPUREA

D-H···A	D···A (Å)	Angle (°)	Symmetry Operator
O9-H···O13	2.551(2)	171	(*x, y, z*)
N14-H···O8	2.931(2)	153	(*x, y, z*)
N14-HA···O8	2.886(2)	104	(*-x, 1-y, 1-z*)
N14-HB···O8	2.886(2)	100	(*-x, 1-y, 1-z*)
N14-H···N6	3.100(2)	156	(*-x, 1-y, 1-z*)
N15-H···O10	2.912(2)	162	(*-x, 2-y, -z*)
C2-H···O13	3.300(2)	162	(*-x, 2-y, -z*)
C5-H···N16	3.404(3)	168	(*-x, 1-y, 1-z*)
C18-H···O10	3.295(2)	170	(*-x, 2-y, -z*)

Five hydrogen bonding patterns are formed from these hydrogen bonds. The first, $N_1 = R_2^2(8)$, is the hydrogen bonding synthon formed between an amide and a carboxylic acid.[12] This synthon is shown in Figure 5.98. The second pattern is shown in Figure 5.99 and has the designator

$N_2 = R_4^2(14)$ with two acipimox molecules and two urea molecules participating in the hydrogen bonding. This pattern is located at a centre of inversion. The third pattern also involves two acipimox molecules and two urea molecules. In this pattern, $N_3 = R_4^2(8)$, the carbonyl oxygens of the acipimox molecules act as acceptors for two independent amine donors of the urea molecules. This pattern is located at a centre of inversion and can be seen in Figure 5.100. The fourth hydrogen bonding pattern, $N_4 = R_2^2(8)$, involves one acipimox molecule and one urea molecule (Figure 5.101). The final pattern (Figure 5.102) includes an acipimox molecule and a urea molecule and can be described by the graph set $N_3 = R_1^2(5)$.

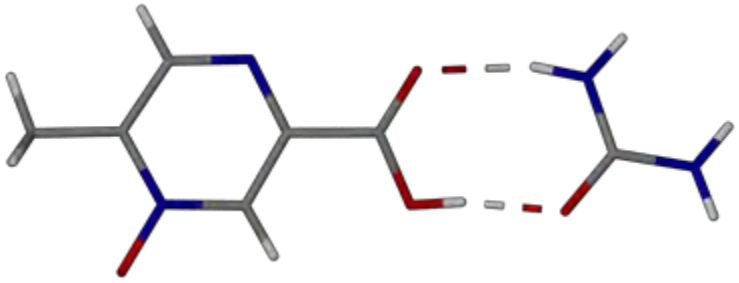

Figure 5.98: Hydrogen bonding pattern $N_1 = R_2^2(8)$ in ACPUREA

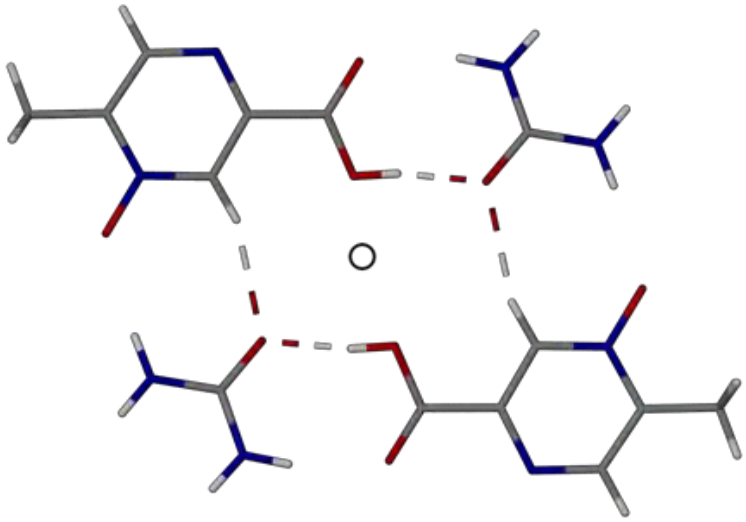

Figure 5.99: Hydrogen bonding pattern $N_2 = R_4^2(14)$ in ACPUREA

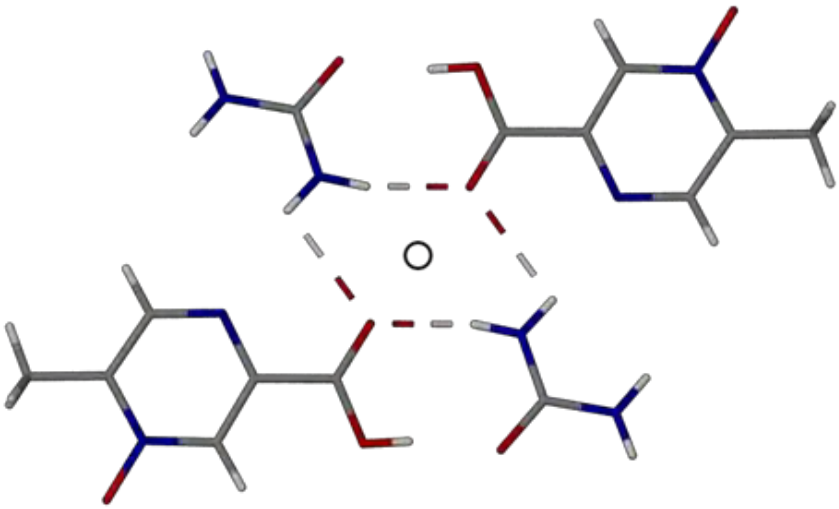

Figure 5.100: Hydrogen bonding pattern $N_3 = R_4^2(8)$ in ACPUREA

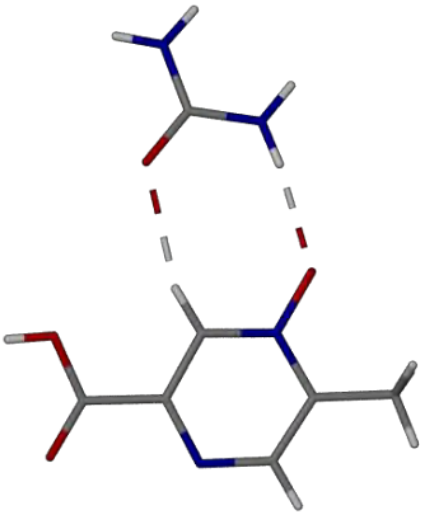

Figure 5.101: Hydrogen bonding pattern $N_4 = R_2^2(8)$ in ACPUREA

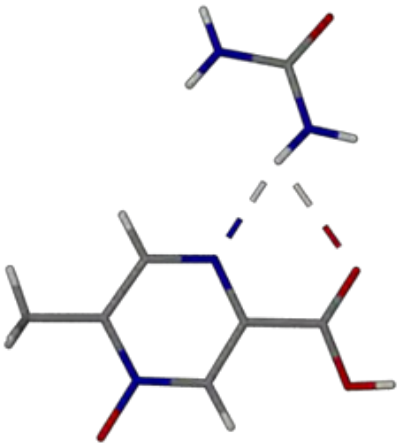

Figure 5.102: Hydrogen bonding pattern $N_5 = R_1^2(5)$ in ACPUREA

The hydrogen bonding patterns $R_2^2(8)$, $R_4^2(14)$, $R_4^2(8)$, $R_2^2(8)$ and $R_1^2(5)$ concatenate to form an overall repeating network, N = $R_2^2(8)R_4^2(14)R_4^2(8)R_2^2(8)R_1^2(5)$, This network forms a ribbon with which acetonitrile only interacts through weak interactions as described above. The ribbon can be seen in Figure 5.103.

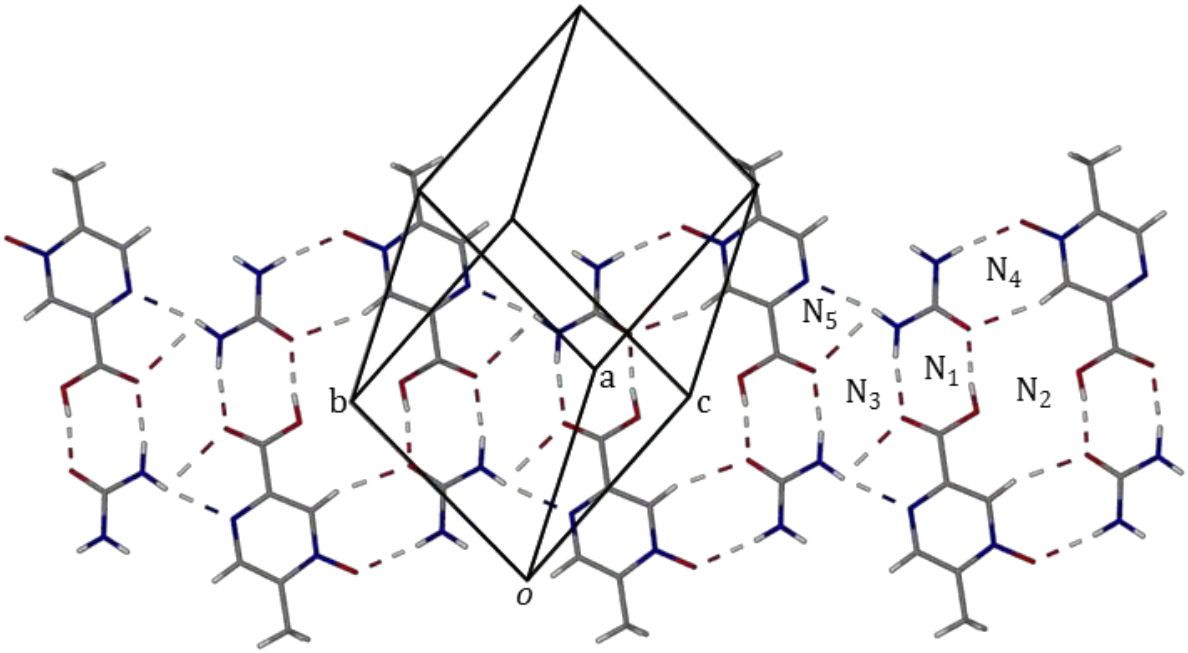

Figure 5.103: Ribbon created through the concatenation of the hydrogen bonding patterns to form the network N = $R_2^2(8)R_4^2(14)R_4^2(8)R_2^2(8)R_1^2(5)$

CRYSTAL PACKING

The structure of ACPUREA packs in repeating ribbons comprising the repeating network described above. These ribbons (Figure 5.104a.) are separated by acetonitrile molecules in the interstitial spaces created as the ribbons propagate horizontally. The ribbons and acetonitrile molecules form layers (Figure 5.104b.) as they pack; however, no interactions were found between the ribbons. No non-classical hydrogen bonds, nor π-π stacking interactions were found between layers in this structure. Therefore, the packing of the structure is stabilised by only van der Waals interactions.

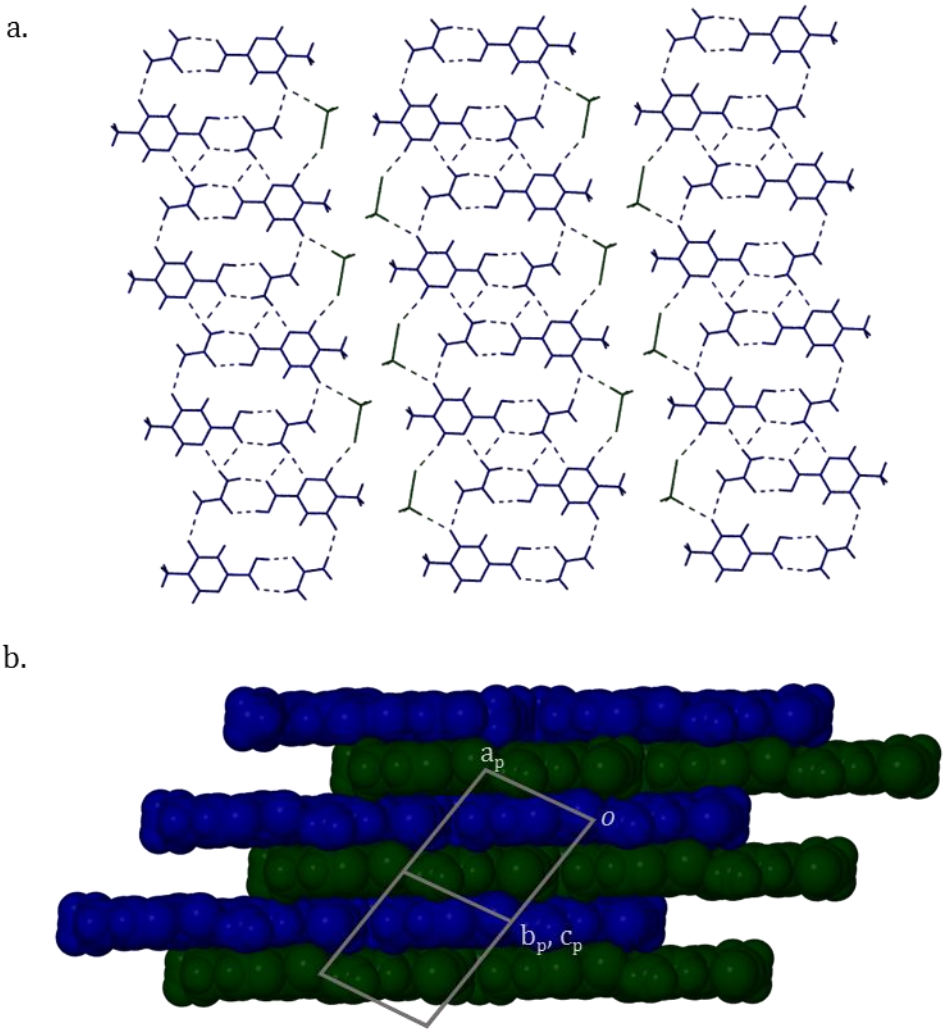

Figure 5.104: Diagram illustrating a. the ribbons of acipimox and urea (blue) with acetonitrile (green) between ribbons and b. the ribbons packed in layers of alternating colours

INFRARED SPECTROSCOPY

The refined crystal structure of ACPUREA showed the position of the carboxylic acid proton on the acipimox molecule. The lack of proton transfer allowed the designation of ACPUREA as a co-crystal. Infrared spectroscopy was performed to determine whether the spectrum of ACPUREA supported the designation as co-crystal. The use of infrared spectroscopy as a rapid identification method of this crystalline system was also investigated.

The infrared spectrum of ACPUREA (Figure 5.105) shows a characteristic signal of a carboxylic acid carbonyl peak at 1738 cm^{-1}. A second characteristic peak of carboxylic acids can be seen at 1271 cm^{-1}, arising from C-O stretching. The presence of these peaks indicates that no proton transfer took place from the carboxylic acid of acipimox during formation of ACPUREA. This supports the designation of this crystalline phase as a co-crystal.

Several differences were observed between the spectra of the starting materials and the spectrum of ACPUREA. The hydroxyl signal in the acipimox spectrum (3554 cm^{-1}) is seen at 3451 cm^{-1} in the spectrum of ACPUREA. A further difference is the position of the carboxylic acid carbonyl signal at 1701 cm^{-1} in the acipimox spectrum and 1738 cm^{-1} in the ACPUREA spectrum. These differences allow one to establish unequivocally the formation of a new phase. A signal at 3175 cm^{-1} in the product spectrum, corresponding to a hydrogen bonded amine, was observed. The signals presented here, along with those used in investigation of a proton transfer, are characteristic of ACPUREA and can be used to rapidly identify the co-crystal. Therefore, FTIR can be used to rapidly determine the formation of a new phase and identify ACPUREA.

Due to its volatile nature, acetonitrile was not observed in the ACPUREA spectrum as the co-crystal desolvated during sample manipulation.

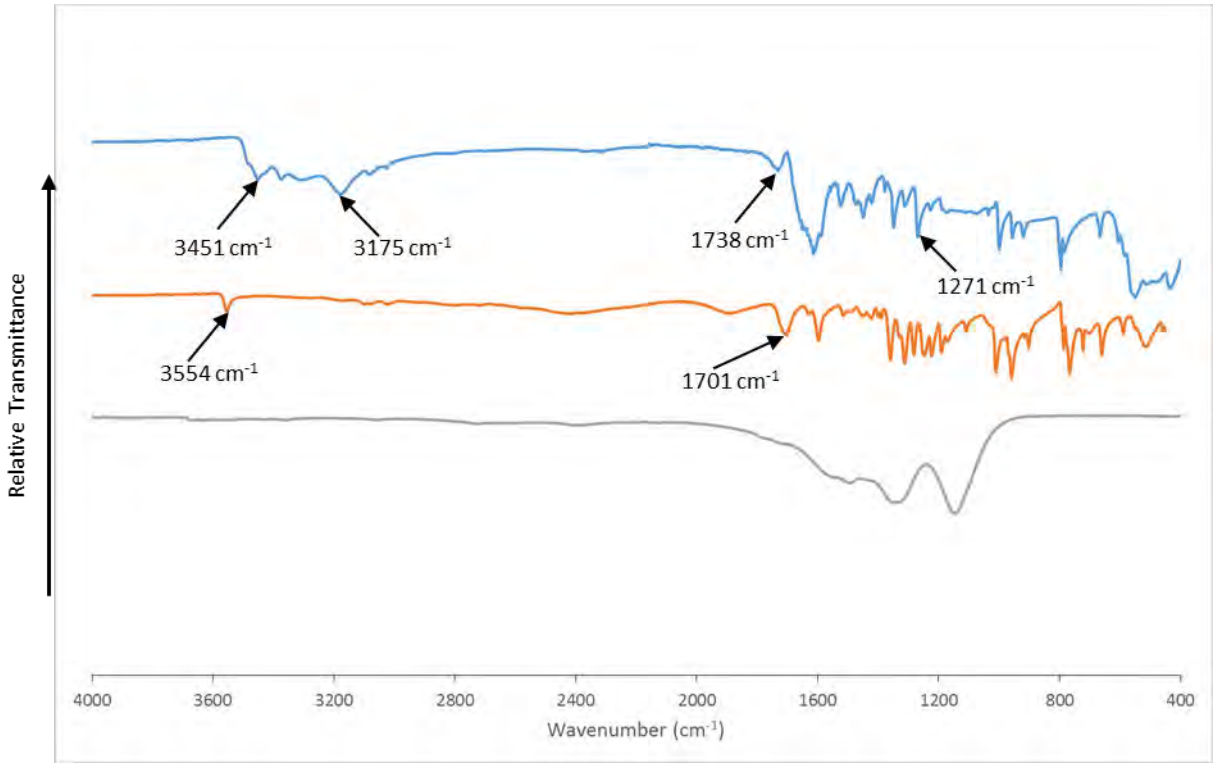

Figure 5.105: FTIR spectra for ACPUREA (blue), acipimox (orange) and urea (grey)

EQUILIBRIUM SOLUBILITY STUDIES

Solubility studies were performed on ACPABEN, ACPAPYR, ACPBEN, ACPISO, ACPTRA and ACPUREA. Attempts were made to produce the two hydrated structures in sufficient quantities, but several issues resulting from scaling up the procedure arose. Therefore, it was not possible to obtain enough sample of ACPAPYR-W and ACPTRA-W, and the solubility studies of these two multi-component systems were therefore not pursued.

SAMPLE PREPARATION

A stock solution of water containing DMSO (99:1 H_2O:DMSO, v/v) was prepared and 1 cm^3 measured into a polytop vial. An excess of the multi-component system was added to the solution and stirred at 500 rpm and a temperature of 25 ± 1 °C for 24 hours. The solutions were then centrifuged at 15 000 rpm for 45 minutes. An aliquot of the supernatant was filtered and 300 µl of this filtered solution was diluted with an equal volume of D_2O. The sample was then analysed *via* ^{1}H-NMR spectroscopy. For each system the process was duplicated. The DMSO concentration was used as an internal standard against which the acipimox concentration could be determined.

Water suppression, using the presaturation pulse program zgpr,[15] was employed to improve the signal-to-noise ratio of the acipimox sample peaks. This was performed by a simple two-pulse experiment where the frequency of water was selectively saturated such that no signal was fully accumulated and a secondary pulse excited the desired resonances. As the DMSO peak was found at 2.71 ppm and the acipimox methyl peak at approximately 2.50 ppm these were sufficiently removed from the H_2O peak to be unaffected by the presaturation pulse. The relative integration of the DMSO peak and the acipimox methyl peak was used to determine the equilibrium concentration of acipimox in each sample. A sample of acipimox was prepared and analysed in the same manner to determine its intrinsic solubility. The NMR spectra, with integration values, can be found in Appendix E.

SOLUBILITY

The concentration of acipimox was determined using the known concentration of DMSO (0.1408 mol dm^{-3}) as an internal standard.

The equilibrium solubility of acipimox in a 1% DMSO aqueous solution at 24 hours was calculated in the following manner. If the concentration of acipimox and DMSO were equal, the methyl peak of acipimox would integrate for 3.00 protons while the methyl signals from DMSO would integrate for 6.00 protons. The ratio of the experimental integration to three protons was used to determine the actual concentration of acipimox. The experimental integration of this peak was found to be

4.79 protons. Therefore, the concentration of acipimox in the equilibrium solution was $\frac{4.79}{3} \times 0.1408 = 0.2249$ mol dm^{-3} (224.9 mM).

The equilibrium concentrations of acipimox in the multi-component system solutions are presented in Table 5.30. The values were calculated by employing the same procedure as described above.

Table 5.30: Equilibrium solubility of acipimox in multi-component system solutions

Multi-component system	Acipimox concentration (mM)	Solubility ratio‡
ACPABEN (co-crystal)	70.7 ± 6.5	0.31
ACPAPYR (salt)	622.2 ± 31.9	2.77
ACPBEN (co-crystal)	85.9 ± 4.4	0.38
ACPISO (salt)	231.9 ± 10.1	1.03
ACPTRA (salt)	330.9 ± 2.1	1.45
ACPUREA (co-crystal)	273.6 ± 4.5	1.22

‡ Defined as (solubility of salt or co-crystal)/(solubility of acipimox) at 25 °C, where denominator = 224.9 mM

From the values in Table 5.30 it is clear that the equilibrium solubility was not increased in all cases. The final acipimox concentration was decreased by the presence of 4-aminobenzamide and benzamide. Each of these decreased the apparent solubility of acipimox to approximately one third the intrinsic solubility value. This may be due to precipitation of the co-crystals over time, or to the co-crystals themselves having relatively poor solubility.

The presence of isonicotinamide in the structure did not change the concentration of acipimox at equilibrium. Tranexamic acid and urea showed slight solubility enhancement of 1.45 and 1.22 respectively. Only ACPAPYR showed a significant increase to the apparent equilibrium solubility of acipimox. This multi-component system showed an apparent increase in acipimox solubility of 2.77-fold.

DISCUSSION

Eight multi-component crystalline systems were presented. These comprised acipimox and each of the following co-formers: 4-aminobenzamide, 4-aminopyridine, benzamide, isonicotinamide, tranexamic acid and urea. Five of the multi-component crystalline systems were organic salts, whereby a proton transfer from the carboxylic acid of acipimox to the co-former occurred during synthesis. In the cases of ACPAPYR and ACPAPYR-W (common co-former 4-aminopyridine) and ACPISO (co-former isonicotinamide) the acceptor of the proton transfer was the co-former pyridyl nitrogen atom. Instead, in the cases of ACPTRA and ACPTRA-W the acceptor was the carboxylate functional group of the co-former tranexamic acid. The remaining three systems, ACPABEN, ACPBEN and ACPUREA (containing the respective coformers 4-aminobenzamide, benzamide and urea) are co-crystals.

Four of the eight systems were solvated. Three of the systems were hydrated. The salt ACPAPYR-W contains two water molecules per acipimox/4-aminopyridine unit, ACPBEN is a hemihydrated structure, while ACPTRA-W contains one water molecule per acipimox/tranexamic acid unit. The solvate ACPUREA contains one acetonitrile molecule per co-crystal unit.

THERMAL ANALYSIS

The antihyperlypidemic agent acipimox has a melting point of 199.7 °C and melting is followed immediately by decomposition. The multi-component crystalline systems produced with acipimox displayed the same behaviour upon heating.

The melting points of the multi-component crystalline systems were investigated by obtaining several DSC traces, using the peak temperatures, to determine the average melting points and standard deviations.

Several of the multi-component crystalline systems raised the melting and decomposition temperature of acipimox. The greatest increase in melting point was seen with the systems ACPAPYR and ACPAPYR-W which have melting and decomposition temperatures of 246.2 ± 0.9 °C and 249.2 ± 0.1 °C respectively. The systems with tranexamic acid have melting and decomposition temperatures greater than that of acipimox, occurring at 241.5 ± 0.2 °C for ACPTRA and 239.9 ± 1.0 °C for ACPTRA-W. Upon heating, the systems ACPAPYR-W and ACPTRA-W dehydrated, converting to the unsolvated species ACPAPYR and ACPTRA respectively. Therefore, the thermal behaviour of the hydrates was identical to that of the unsolvated salts after dehydration. The multi-component crystalline system ACPISO has a marginally higher melting point and decomposition temperature than the API of 210.8 ± 0.5 °C.

The co-crystal ACPABEN was found to have a melting point of 201.1 ± 0.1 °C. The melting point of this co-crystal is only a small increase over that of the untreated API.

Two of the co-crystals showed lower melting and decomposition temperatures relative to untreated acipimox. The co-crystal ACPBEN melted at 133.9 ± 1.3 °C and began to decompose immediately thereafter. In the co-crystal ACPUREA, system began decomposing at 147.4 ± 1.7 °C initially losing the urea component. Once the urea was lost, the remaining component was lost immediately thereafter.

In 2009, Schultheiss and Newman performed a survey of 50 co-crystalline samples and found that 51 % had melting points between those of the components. Of the systems studied, 39% had melting points lower than either of the component melting points, while 6 % had higher melting points than either component melting point and 4 % had a melting point equal to that of one of the components.[16] From the data presented in Table 5.31 it was found that four of the acipimox multi-component crystals have melting points between those of the co-former and acipimox (ACPBEN, ACPTRA-W, ACPTRA and ACPUREA). The remaining systems (ACPABEN, ACPAPYR, ACPAPYR-W and ACPISO) all have melting points higher than both those of acipimox and the respective co-former.

Table 5.31: Melting points of multi-component crystal systems and their co-formers

Multi-component system	Melting Point	Co-former Melting Point[17]
ACPABEN (co-crystal)	201.1(1)	183
ACPAPYR (salt)	246(1)	159.0(5)
ACPAPYR-W (salt)	249.2(1)	159.0(5)
ACPBEN (co-crystal)	134(1)	128(1)
ACPISO (salt)	210.8(5)	156.0(5)
ACPTRA-W (salt)	239(1)	249(4)
ACPTRA (salt)	241.5(2)	249(4)
ACPUREA (co-crystal)	147(2)	132.4(5)

In the second column the values in parentheses represent e.s.d.s calculated from multiple DSC runs
In the third column the values in parentheses represent the uncertainties calculated as combined expanded uncertainties (level of confidence 95 %). No uncertainty value was reported for 4-aminobenzamide.

A search of the literature shows numerous examples of correlations between the melting points of the co-former and those of co-crystals and salts for a given API.[16,18–20] The melting points of the acipimox multi-component crystalline systems and their co-formers are shown in graphical form in Figure 5.106. The general trend is that the co-formers with high melting points tend to produce multi-component crystalline systems with high melting points. Two systems, ACPAPYR and

ACPAPYR-W, are outliers raising the melting point further than expected relative to untreated acipimox.

It is worth noting that the systems which displayed higher melting points than that of pure acipimox are all salts (except ACPABEN with a melting point higher by less than two degrees). This is most likely due to the fact that the interactions between charged species are generally stronger than those between neutral species. It is however difficult to draw conclusions regarding the melting point from the intermolecular interactions alone. Many factors affect melting points, including, but not limited to intermolecular forces, molecular motion in crystals and molecular arrangement. The introduction of numerous components further complicates one's ability to draw conclusions as each component has its own properties which can affect the environment.[16,21]

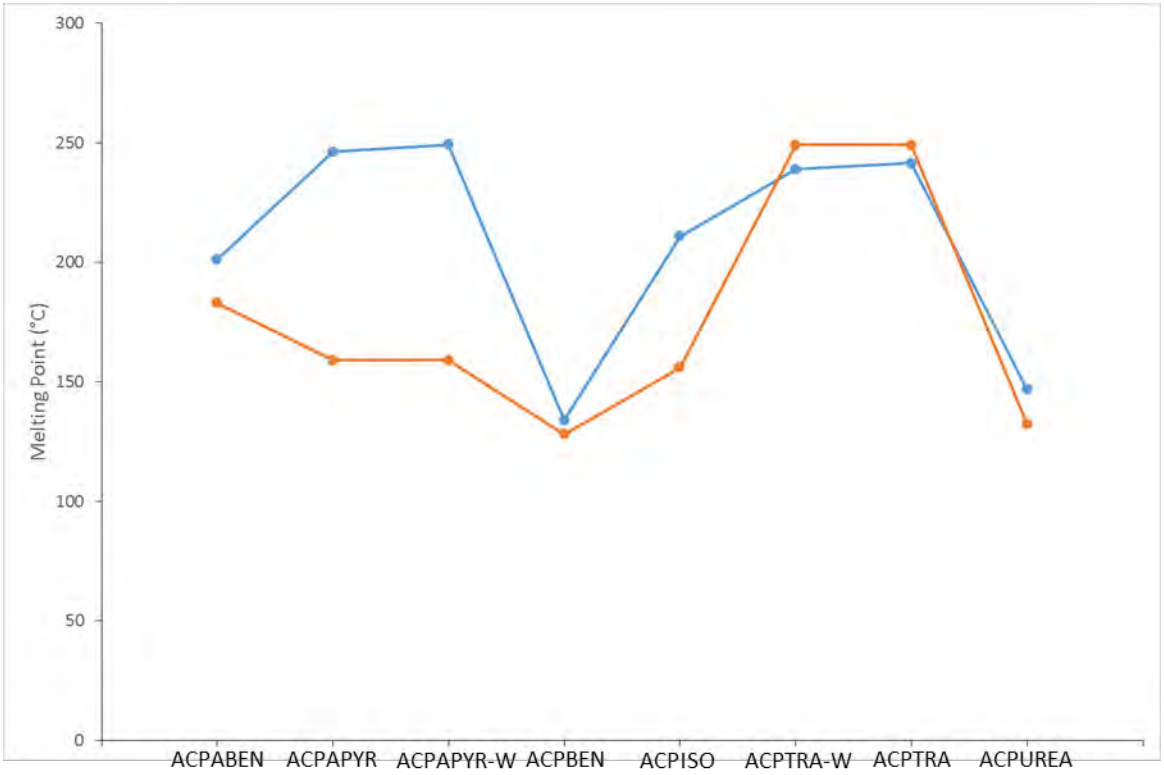

Figure 5.106: Melting point data for acipimox multi-component crystals (blue) and their respective co-formers (orange)

CRYSTAL STRUCTURE ANALYSIS

Five of the multi-component crystalline systems obtained were found to belong to the space group P $\bar{1}$. The remaining three, ACPAPYR-W, ACPBEN and ACPISO crystallise in the space groups $P2_1/c$, C2/c and $P2_1/c$ respectively.

The occurrence of a proton transfer from the carboxylic acid group of acipimox to an appropriate acceptor was observed in five of the eight structures. This was established by careful location of hydrogen atoms in difference Fourier syntheses before assigning idealised geometries. Proton transfers were found to have occurred in ACPAPYR, ACPAPYR-W, ACPISO, ACPTRA-W and ACPTRA. The conformational similarities in the acipimox moieties in the salts and the co-crystals will be treated separately. In the five salts the conformation of the acipimox species is essentially identical, as shown in the overlay of the acipimox anions in Figure 5.107. The structure ACPAPYR contains two independent acipimox anions, designated by the suffixes A and B.

In the salts mentioned above, acipimox anions are approximately planar. The magnitude of the torsion angles N6-C1-C7-O8 and N6-C1-C7-O9 for the carboxylate anions are presented in Table 5.32 to illustrate the similarities. As these structures are all centrosymmetric, only the magnitude of this torsion angle is presented. The absolute values of the torsion angle N6-C1-C7-O8 show it is in a syn-periplanar conformation with little variation in the rotation of the carboxylate moiety during intermolecular interactions. The torsion angle N6-C1-C7-O9 is anti-periplanar in each of the co-crystal structures with similarly little variation.

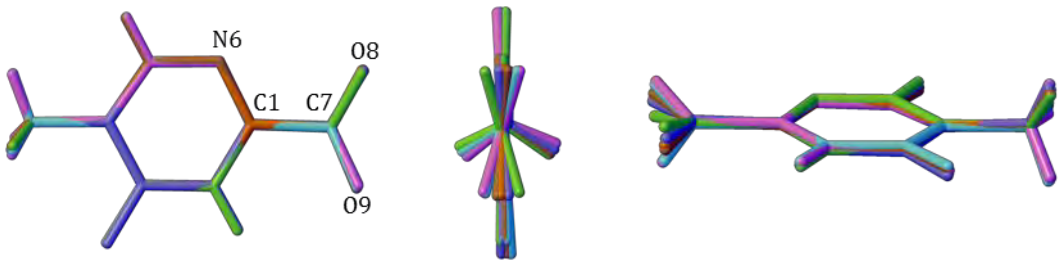

Figure 5.107: Overlay of acipimox molecules from ACPAPYR(A), ACPAPYR(B), ACPAPYR-W, ACPISO, ACPTRA and ACPTRA-W

Table 5.32: The magnitude of the torsion angles N6-C1-C7-O8 and N6-C1-C7-O9

Structure	Torsion angle N6-C1-C7-O8 (°)	Torsion angle N6-C1-C7-O9 (°)
ACPAPYR(A)	2.1(2)	178.2(2)
ACPAPYR(B)	6.1(2)	173.9(1)
ACPAPYR-W	16.5(2)	164.1(1)
ACPISO	3.2(2)	176.4(1)
ACPTRA-W	19.1(2)	160.8(1)
ACPTRA	16.1(1)	163.2(1)

The conformations of the acipimox molecules in the co-crystals are very similar to those of the salts. The overlay of the acipimox molecules from ACPABEN, ACPBEN and ACPUREA illustrates the similarities among the conformations of these molecules. (Figure 5.108). As indicated above, these crystal structures are centrosymmetric, therefore only the magnitude of the torsion angle is presented in Table 5.33. The planarity of the molecules can be seen from the absolute values of the anti-periplanar torsion angle N6-C1-C7-O8 for ACPABEN and ACPBEN and the syn-periplanar conformation of this torsion angle for ACPUREA. The torsion angle N6-C1-C7-O9 is syn-periplanar in the ACPABEN and ACPBEN structures, but is anti-periplanar for the ACPUREA structure. The carboxylic acid group is rotated approximately 180° in ACPUREA relative to ACPABEN and ACPBEN.

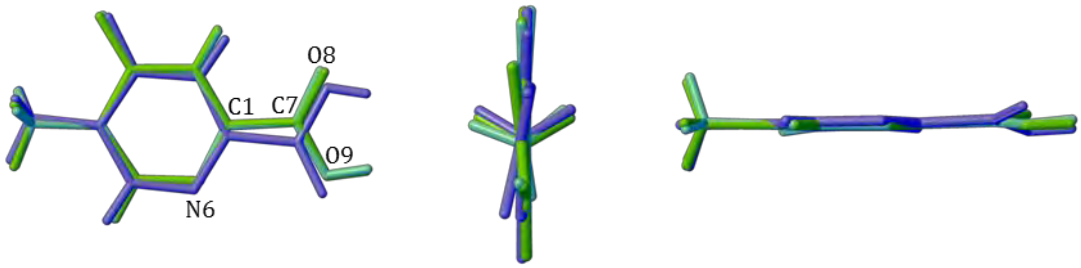

Figure 5.108: *Overlay of acipimox molecules from ACPABEN, ACPBEN and ACPUREA*

Table 5.33: The magnitude of the torsion angles N6-C1-C7-O8 and N6-C1-C7-O9

Structure	Torsion angle N6-C1-C7-O8 (°)	Torsion angle N6-C1-C7-O9 (°)
ACPABEN	176.1(1)	3.0(2)
ACPBEN	174.0(1)	4.8(2)
ACPUREA	9.2(2)	171.3(1)

The carboxylate anions show a greater deviation from planarity than the carboxylic acid groups. The greatest deviation (19.1(2)°) is seen for the salt ACPTRA-W in the torsion angle N6-C1-C7-O8. In comparison the greatest deviation for the co-crystals of the carboxylic acid group is 9.2(2)° for ACPUREA in the torsion angle N6-C1-C7-O8.

HYDROGEN BONDING

There are a total of eight different types of hydrogen bonding synthons (Figure 5.109) present in the eight multi-component crystals. The most common of these is the hydrogen bond between the acipimox pyrazine oxide and an amine group (Figure 5.109a.), occurring in five of the structures. This hydrogen bond can be found in ACPABEN, ACPAPYR, ACPAPYR-W, ACPTRA and ACPUREA. The common carboxylic acid-to-amide synthon (Figure 5.109b.) is found in four of the systems (ACPABEN, ACPBEN, ACPISO and ACPUREA). The amine interaction with the carboxylate ion (Figure 5.109c.) occurs in ACPAPYR-W, ACPISO, ACPTRA-W and ACPTRA. The bifurcated hydrogen between an amine group and the aromatic nitrogen and carboxylate anion of acipimox, shown in Figure 5.109d., is found in ACPAPYR-W, ACPAPYR and ACPTRA-W. The hydrogen bond formed between an amine and the aromatic nitrogen of acipimox, shown in Figure 5.109e., is present in three of the multi-component crystals (ACPBEN, ACPTRA and ACPUREA). The carboxylate anion-pyridyl motif (Figure 5.109f.) is found in the structures ACPAPYR and ACPISO. Two of the hydrogen bonding motifs occur only once. The first, shown in Figure 5.109g., is the hydrogen bond between the carboxylic acid of tranexamic acid and the carboxylate moiety of acipimox in ACPTRA. The second occurs between an amine group on urea and the carbonyl group of the acipimox carboxylic acid in ACPUREA (Figure 5.109h.).

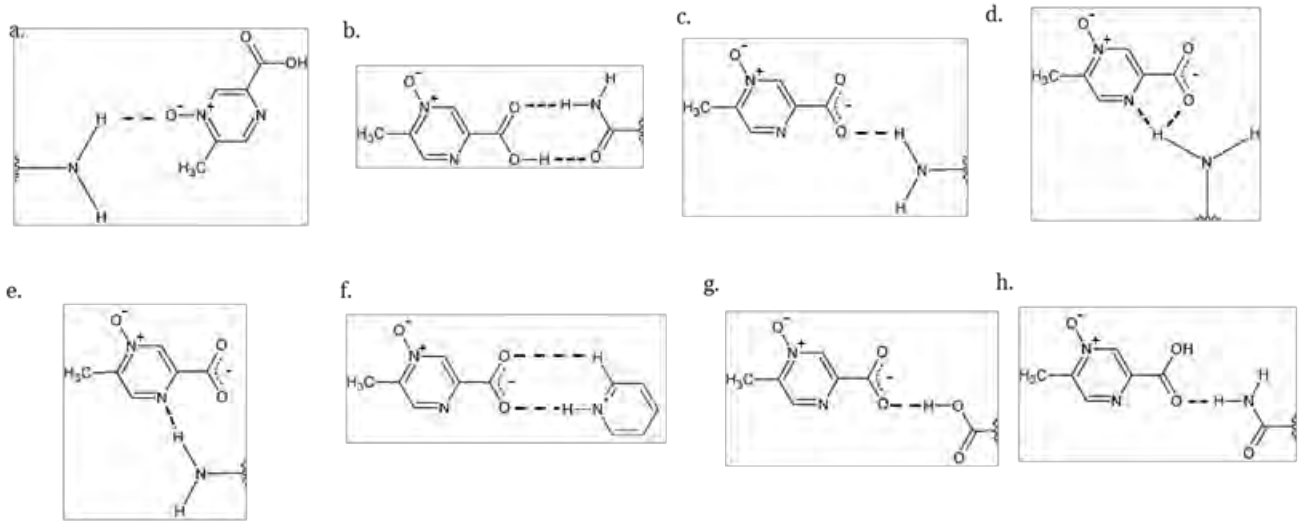

Figure 5.109: Hydrogen bonding motifs present in the multi-component crystal structures formed with acipimox

These hydrogen bonds interact within their respective crystalline systems to form a total of eighteen hydrogen bonding ring patterns. These are summarised in Table 5.34 below. The hydrogen bonding rings contain 5 to 34 atoms. These rings contain between 1 and 8 hydrogen bond donors and 2 to 8 acceptor atoms. It should be noted that the patterns $R_2^2(7)$, $R_6^5(28)$ and $R_1^2(5)$ each occur twice in the system ACPAPYR. While the pairs of these patterns have identical connectivity, they are crystallographically independent.

Table 5.34: Hydrogen bonding patterns found in the multi-component crystal structures formed with acipimox

Hydrogen bonding pattern	Structures	Count
$R_1^2(5)$	ACPAPYR, ACPAPYR, ACPAPYR-W, ACPTRA-W, ACPUREA	5
$R_2^2(8)$	ACPABEN, ACPBEN, ACPISO, ACPUREA	4
$R_2^2(7)$	ACPAPYR, ACPAPYR, ACPISO	3
$R_6^5(28)$	ACPAPYR, ACPAPYR	2
$R_4^4(18)$	ACPAPYR-W, ACPTRA-W	2
$R_4^4(22)$	ACPISO, ACPUREA	2
$R_6^6(31)$	ACPAPYR-W	1
$R_6^6(22)$	ACPAPYR-W	1
$R_8^4(24)$	ACPAPYR-W	1
$R_8^8(34)$	ACPBEN	1
$R_4^2(16)$	ACPISO	1
$R_4^4(26)$	ACPTRA	1
$R_4^4(16)$	ACPTRA	1
$R_4^4(14)$	ACPTRA	1
$R_4^4(32)$	ACPTRA	1
$R_4^3(10)$	ACPTRA-W	1
$R_2^2(18)$	ACPTRA-W	1
$R_4^2(14)$	ACPUREA	1
$R_4^2(8)$	ACPUREA	1

HIRSHFELD SURFACE ANALYSIS

Hirshfeld surface analysis was used to investigate the similarities and differences of the intermolecular interactions in the multi-component crystalline systems presented here. The 3D Hirshfeld surface and corresponding 2D fingerprint is unique for any crystal structure. This method can be used to gain further insight into intermolecular interactions by colour coding long and short contact distances. The fingerprint plot provides a method for quantitatively summarising the nature of the intermolecular interactions.[22–25] In the discussion that follows, since the structure of ACPAPYR contains two crystallographically independent acipimox anions, where appropriate these have been treated individually, while retaining the designations A and B, as in their crystal structure.

The fingerprint plots of the Hirshfeld surfaces of the acipimox moiety in each of the multi-component crystals is shown in Figure 5.110. The overall shapes of the fingerprint plots show the similarities and differences in intermolecular interactions present among the various structures. The most noticeable similarity is the presence of a lower sharp feature in each of the plots. This feature corresponds to the hydrogen bond acceptor (where $d_i > d_e$) of the O···H interactions present in each of the acipimox multi-component crystalline systems. The other sharp feature present in the plots for ACPABEN, ACPBEN and ACPUREA corresponds to the presence of an O···H interaction where acipimox is the donor ($d_i < d_e$). It is expected to be present only in these systems since they contain the carboxylic acid –OH group acting as a hydrogen bond donor.

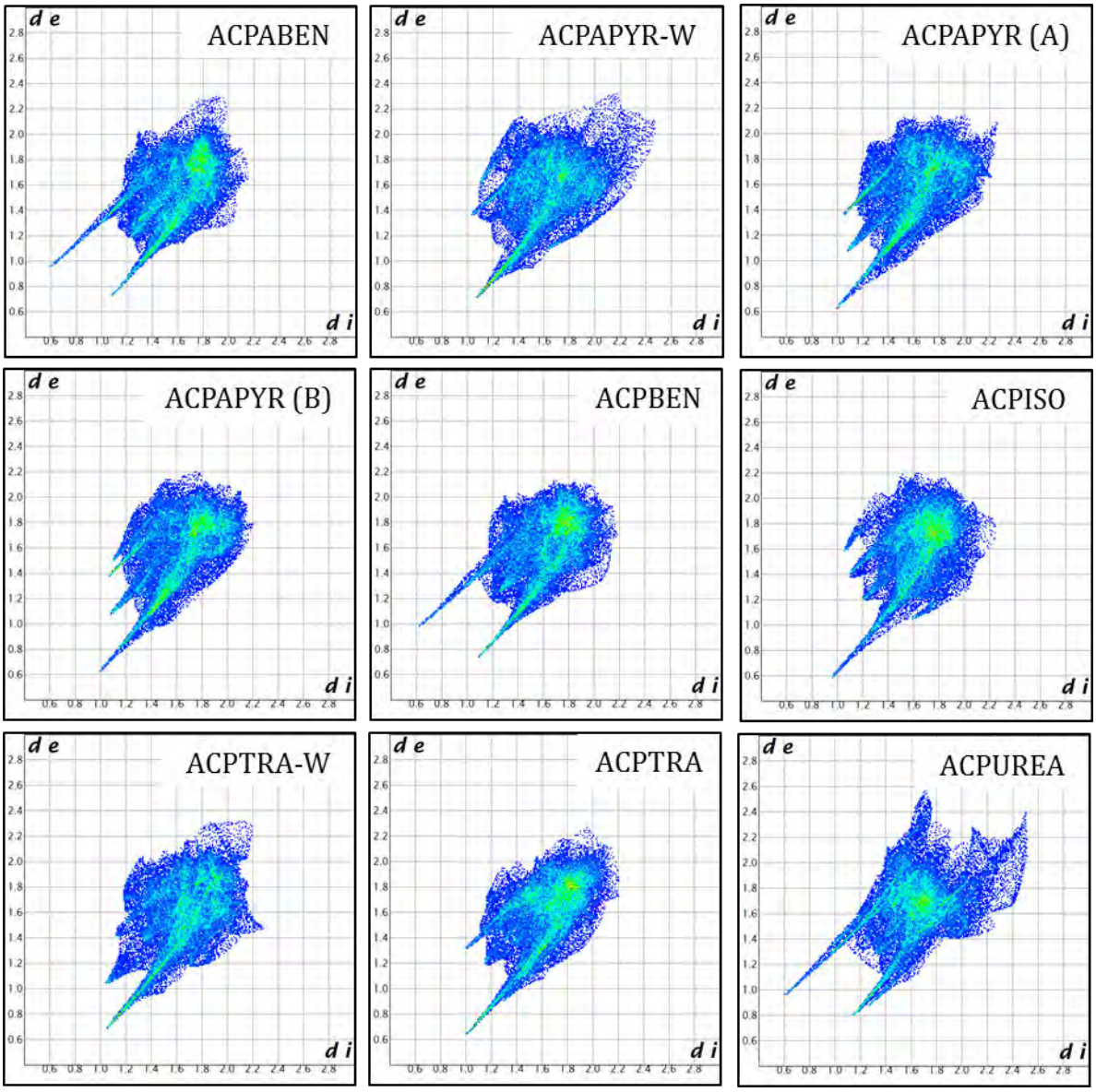

Figure 5.110: Two-dimensional fingerprint plots for the Hirshfeld surfaces of the acipimox moieties

The relative contact contribution for the acipimox moiety in each multi-component crystalline system is shown in Figure 5.111. These values take into account the reciprocal contacts and therefore count the contribution of the acipimox moiety acting as both a donor and an acceptor in each interaction. The relative contributions of the intermolecular close contacts to the Hirshfeld surface of acipimox support the interpretation of the fingerprint plots above. It is clear that the main contributing interaction in each of the crystalline systems is an interaction between oxygen and hydrogen, which contributes over a third to each Hirshfeld surface. Although the structure ACPTRA-W is hydrated, the O···H contribution is less significant than that in the anhydrous structure, ACPTRA. This is due to the anhydrous structure engaging in significantly more interactions involving O···H directly between acipimox and tranexamic acid ions.

While N···H interactions are present in each of the structures, the relative contributions to the Hirshfeld surfaces are significantly less than the O···H contribution. This is because relatively few intermolecular interactions take place between nitrogen and hydrogen atoms. The only such interactions occur when the aromatic nitrogen of acipimox acts as an acceptor atom. All other hydrogen bonding interactions with nitrogen take the form N-H···A, and as such do not contribute to the Hirshfeld surface.

The lack of intensity in the fingerprint plots in the region $d_i = d_e \approx 1.8$ Å indicates that π-π stacking, while present, does not contribute significantly to the overall interactions of these structures. Slightly higher intensity is seen in the Hirshfeld fingerprint plots of ACPABEN, ACPAPYR-W, ACPBEN, ACPTRA and ACPTRA-W in the region $d_i = d_e \approx 1.8$ Å. This is expected since π-π stacking was directly observed in their crystal structures. The statistical analysis of the Hirshfeld surfaces also shows minimal contribution from C···C interactions.

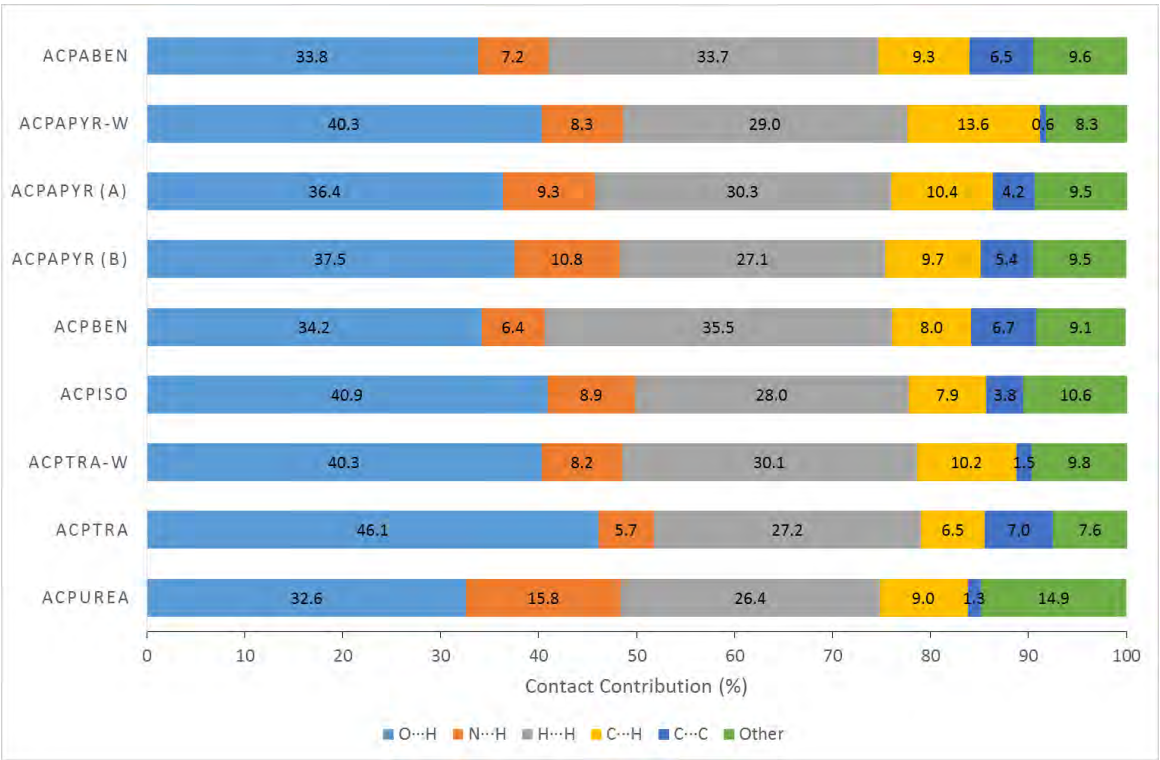

Figure 5.111: Relative contributions to the Hirshfeld surface for the close intermolecular contacts for acipimox moieties in the multi-component crystalline systems

The Hirshfeld surfaces and 2D fingerprint plots were also calculated for the asymmetric unit of each of the structures. The overall shapes of the fingerprint plots (Figure 5.112) are very similar, indicating similar interactions at the Hirshfeld surfaces of the multi-component crystalline systems. The main differences between plots arise due to the H···H interactions, which are shown by the central feature. The sharp features at the lower d_i and d_e values represent the reciprocal

O···H interactions at the surfaces, as in the acipimox plots above. The ACPUREA fingerprint plot shows two additional sharp features in the same region. The outer features correspond to the N···H interactions while the inner represent the O···H interactions at the surface.

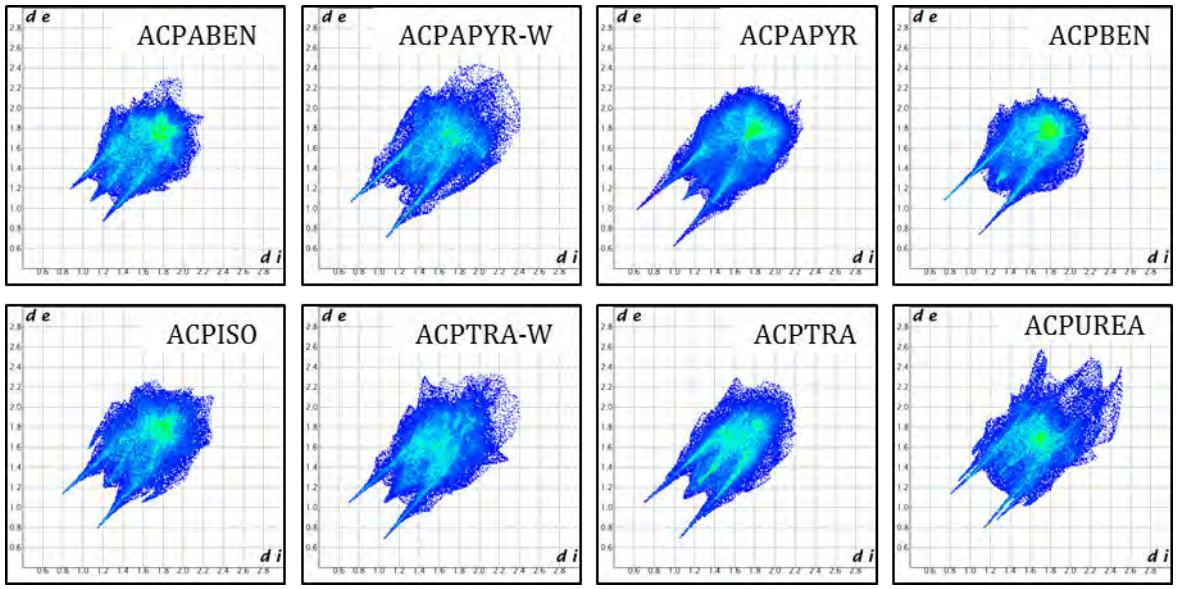

Figure 5.112: Two-dimensional fingerprint plots for the Hirshfeld surfaces of the asymmetric units of the multi-component crystalline systems

The contact contributions to the Hirshfeld surfaces for the asymmetric units, represented in Figure 5.113, show that the main interactions are of the type H···H, as opposed to O···H above. This is due to the fact that many of the O···H interactions occur directly between acipimox and the co-former within the asymmetric unit. This decreases the relative contribution of O···H interactions to the Hirshfeld surface of the asymmetric unit. While the relative contribution has decreased, the O···H interaction is still a significant contributor to the Hirshfeld surface. The N···H contribution to the surfaces, while greater than for acipimox alone, is a minor interaction. As with the decrease of the O···H surface contribution, this is due to the fact that the majority of N···H interactions take place directly between acipimox and the co-former within the repeating unit.

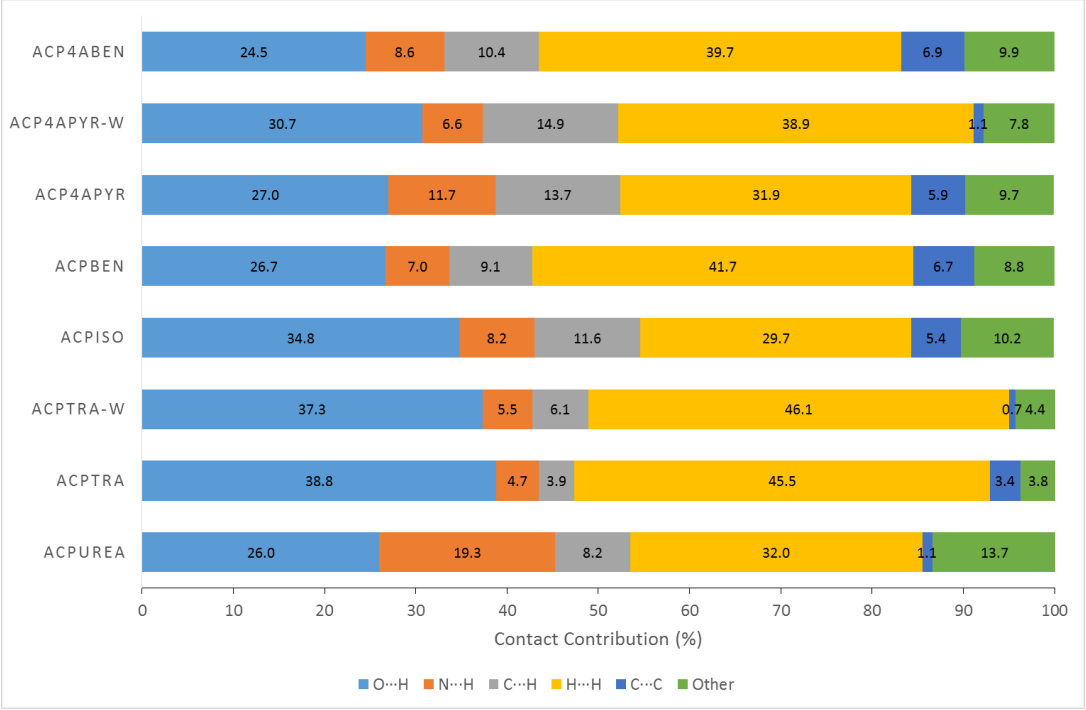

Figure 5.113: Relative contributions to the Hirshfeld surface for the close intermolecular contacts associated with the asymmetric units of the multi-component crystalline systems

CRYSTAL PACKING

The eight crystal structures display some common packing features. All of them form layers that stack during crystal packing. The structure ACPABEN forms infinite ribbons of the network C(15)$R_2^2(8)$. These ribbons then pack along the *b*-axis in layers.

The dihydrate of acipimox with 4-aminopyridine forms stepped layers of a repeated hydrogen bonding network. These networks are then connected through a $R_6^6(22)$ pattern involving the water molecules. The salt ACPAPYR forms layers of interconnected hydrogen bonding patterns. Two of these networks are formed by two independent crystallographic units with identical hydrogen bonding synthons forming concatenated $R_2^2(7)$, $R_1^2(5)$ and $R_6^5(28)$ rings.

The hemihydrate ACPBEN is another structure which forms stepped layers that are interconnected through a water molecule. This water molecule is located on a two-fold rotation axis. These stepped layers are interdigitated.

Acipimox and isonicotinamide react to produce an organic salt that forms layers of ribbons which stack into columns along the *a*-axis. The stacking pattern is such that ribbons in neighbouring columns are inclined to one another at an angle of 50.7°.

The salt ACPTRA packs in layers of an extended hydrogen bonding network. If the acipimox and tranexamic acid ions are viewed independently they stack in columns along the *a*-axis and *b*-axis respectively.

The hydrated form of the acipimox and tranexamic acid salt, ACPTRA-W, has a large repeating hydrogen bonding network which forms sheets. These sheets pack into layers along the *b*-axis.

The final structure, ACPUREA, forms ribbons of repeating hydrogen bonding patterns. Acetonitrile molecules are found in the spaces between these ribbons interacting through C-H···O and C-H···N hydrogen bonds. The ribbons then pack in sheets that stack to form layers.

The crystal packing of these structures is stabilised through various interactions. The aromatic nature of acipimox and many of the co-formers means that π-π stacking is present in ACPABEN, ACPAPYR-W, ACPBEN, ACPTRA-W and ACPTRA. The structures ACPABEN, ACPAPYR, ACPBEN, ACPISO, ACPTRA-W and ACPTRA are further stabilised by C-H···O hydrogen bonding. In the case of ACPUREA, the only interactions stabilising the packing arrangement are van der Waals forces, which are present in all crystal structures.

INFRARED SPECTROSCOPY

Infrared spectroscopy was employed to determine whether the spectra of the multi-component crystalline systems supported their designations as salts or co-crystals. The presence of carbonyl carboxylic acid signals in the regions of 1700 cm^{-1} and 1200 cm^{-1} indicated the presence of a carboxylic acid group (-COOH) in the structure. In the cases of ACPABEN, ACPBEN and ACPUREA, the presence of these absorption peaks in the spectra supported the designation of these systems as co-crystals. The presence of carboxylate anion peaks in the spectra in the region of 1500 cm^{-1} to 1650 cm^{-1} and the area around 1300 cm^{-1} indicated the presence of a carboxylate anion $(-COO)^-$. For ACPAPYR-W, ACPAPYR and ACPISO the presence of these signals in their spectra supported their designation as salts. The multi-component systems containing tranexamic acid contained both carboxylic acid and carboxylate anion signals. From the crystal structures, the tranexamic acid molecules are protonated and the acipimox molecules deprotonated at their respective carboxylic acid moieties. However, pure tranexamic acid is a zwitterion, having a carboxylate group, while acipimox has a carboxylic acid moiety. Therefore, it was not possible to use infrared spectroscopy to confirm the presence of a proton transfer in ACPTRA-W and ACPTRA.

Infrared spectroscopy was further explored as a method of rapid identification of the crystalline systems. By close inspection of the spectra, observing characteristic signals in each case, it was possible to identify the salts and co-crystals. Comparisons were made with the API and co-former

spectra to determine whether FTIR could be used to establish the formation of new phases. The differences in the profiles of the starting material spectra and the crystalline system spectra were clear and unambiguous. Furthermore, the differences in peak positions of functional groups common to both the starting materials and the product were clear. These differences allowed one to unequivocally establish the formation of new phases.

The use of infrared spectroscopy to distinguish salts and co-crystals was successful in most cases and its utility for rapid identification of the multi-component crystalline systems was clearly demonstrated. With the use of an ATR-FTIR spectrometer, spectra can be recorded in a matter of minutes allowing one to rapidly determine the presence of a known salt or co-crystal, or by comparison, the presence of a new phase.

EQUILIBRIUM SOLUBILITY

The formation of multi-component crystalline systems with acipimox was found to successfully modify the equilibrium solubility of the API in water containing 1% DMSO (1:99 DMSO:H_2O, v/v). Acipimox was found to have an equilibrium solubility of 224.9 mM in this medium at 25 °C. As salts and co-crystals have differing solubility behaviour, these systems will be discussed separately.

Three co-crystals were prepared, namely ACPABEN, ACPBEN and ACPUREA, and their equilibrium solubilities were measured. From this experiment it was determined that these co-crystals had apparent acipimox concentrations of 70.7 ± 6.5 mM, 85.9 ± 4.4 mM and 273.6 ± 4.5 respectively. These results showed that the co-formers 4-aminobenzamide and benzamide decreased the apparent solubility of acipimox. A decrease in the apparent API solubility when forming a co-crystal has been reported in the literature.[26–28] The researchers Good and N. Rodríguez-Hornedo[26] reported 25 co-crystal systems containing the APIs caffeine, carbamazepine or theophylline with various co-formers, eight of which displayed reduced solubility relative to their untreated API. Of the 25 co-crystal solubility experiments they presented, only ten were performed in water, and two of the results showed decreases in apparent drug solubility. The two systems, caffeine/salicylic acid and theophylline/salicylic acid displayed solubility ratios [defined as: (solubility of salt or co-crystal/solubility of API)] of 0.3 and 0.4 respectively. This is a similar decrease as those observed with ACPABEN (0.31) and ACPBEN (0.38), at 25 °C, in the present study. Reddy *et al.*[27] prepared five multi-component crystalline systems with gabapentin, all of which displayed lower solubilities than that of the untreated API. The study on multi-component crystals with the API pentoxifylline[28] in one case showed that the apparent concentration of the API was only 0.004 times its intrinsic solubility under the same experimental conditions.

In the present study, the co-crystal prepared with urea showed a slight increase (1.22-fold) in apparent acipimox solubility. It is has been proposed that the changes in apparent co-crystal solubility correlate with the solubilities of the co-former.[26] With the three co-crystals presented in this study we see a similar trend. With increasing co-former solubility (4-aminobenzamide < benzamide < urea)[29] we see increasing apparent solubility of acipimox (ACPABEN < ACPBEN <ACPUREA).

The preparation of salts of poorly soluble APIs is the most common, and generally considered the most effective, procedure for increasing solubility,[30] this is however not always the case. As seen by the work of Reddy *et al.*[27] in some cases the conversion to a molecular salt does not necessarily improve (or may even decrease) the apparent solubility of the API. In the case of ACPISO the apparent solubility of acipimox was determined to be 231.9 ± 10.1 mM. This value is equal to the intrinsic solubility of acipimox within experimental error. A possible explanation for this is that upon dissolving the salt, the components dissociate in solution and acipimox recrystallises as the pure API.[30,31] The remaining two salts increased the apparent solubility of acipimox. The salt of acipimox and tranexamic acid has an apparent API solubility of 330.9 ± 2.1 mM, which is an apparent increase of 1.45-fold. The salt ACPAPYR showed a greater increase in the solubility of acipimox, namely 622.2 ± 31.9 mM, corresponding to a 2.77-fold increase. The increase displayed by ACPAPYR is comparable with that for the carbamazepine/saccharine co-crystal presented by Good and N. Rodríguez-Hornedo.[26] The values of the apparent solubility of acipimox in the salts do not display a trend with respect to the solubilities of the co-formers (4-aminopyridine < isonicotinamide < tranexamic acid).[29]

The relationship between the melting point of a multi-component crystalline system and solubility is complicated and problematic.[30] This assessment was borne out by the data from experiments performed in the present study. When seen as a group there is no clear correlation between melting point and solubility. However, if the salts are treated in isolation there is a trend whereby with increasing melting point we observe increasing apparent solubility (ACPISO < ACPTRA < ACPAPYR). While a trend is observed, the relationship is weak with nearly doubling of the apparent acipimox solubility (330.9 ± 2.1 mM to 622.2 ± 31.9 mM) from ACPTRA to ACPAPYR, but only an increase of 5 °C in melting point (241.5 ± 0.2 °C to 246.2 ± 0.9 °C). While it is generally expected for melting points and solubility to be inversely related, solvent-solute interactions can be the determining factor in the solubility of a product, particularly in water.[26] It is possible that hydrogen bonding interactions between the ACPAPYR and water aid in solubilising the salt, overcoming the lattice energy of the crystalline substance. The existence of the hydrated salt ACPAPYR-W with two water molecules per acipimox/4-aminopyridine unit would indicate that the formation of hydrogen bonding interactions between water and the salt

are favourable. The co-crystals do not exhibit any trend relating their melting point to their equilibrium solubility.

CONCLUSION

The data presented show that acipimox can form multi-component crystalline systems with six GRAS co-formers, producing eight fully characterised products. Of the eight multi-component crystalline systems presented here, six were produced using mechanochemical methods. Liquid-assisted grinding was shown to be more effective than dry grinding, producing five of the six systems. Mechanochemical production of salts and co-crystals is advantageous as these methods do not require large volumes of organic solvents and therefore have less of an environmental impact than the alternatives. Furthermore, mechanochemical production of multi-component crystalline systems is generally easily scalable. Finally, obtaining the product is rapid when compared to co-precipitation, the mechanochemical methods typically produce the product within 20 minutes, while co-precipitation can take several days to yield the desired result. This clearly demonstrates the value of these methods.

The thermal melting and decomposition temperatures of acipimox were exceeded by those of all but two of these systems. The products ACPAPYR, ACPAPYR-W, ACPTRA and ACPTRA-W began to decompose at temperatures over 40 °C greater than the decomposition temperature of acipimox alone. A trend was seen between the melting points of the co-formers and the melting points of the multi-component crystalline systems. It was also observed that the salts formed with acipimox had higher melting points than the co-crystals.

Infrared spectroscopy was shown to be a useful rapid method for identifying the salts and co-crystals presented.

The apparent equilibrium solubility of acipimox was found to have been increased by three of the co-formers, namely 4-aminopyridine, tranexamic acid and urea. These increased the solubility by factors of 2.77, 1.47 and 1.22 respectively. However, the remaining co-formers either did not affect, or decreased, the solubility of acipimox. No apparent trend was observed correlating the melting points of the systems and their aqueous solubility; however, if the salts are regarded in isolation a weak trend is observed between the two properties.

REFERENCES

1 Acipimox only to be used as additional or alternative treatment to reduce high triglyceride levels, *European Medicines Agency*, http://www.ema.europa.eu/ema/index.jsp%3Fcurl%3Dpages/medicines/human/referrals/Nicotinic_acid/human_referral_prac_000020.jsp%26mid%3DWC0b01ac05805c516f (accessed July 2016)

2 L. J. Barbour, *J. Appl. Crystallogr.*, 1999, 32, 351–352.

3 XPREP, Data Preparation and Reciprocal Space Exploration, Version 5.1, © Bruker Analytical X-ray Systems, 1997.

4 Z. Otwinowski and W. Minor, in *Methods in Enzymology*, eds. C. J. Carter and R. Sweet, Academic Press, 1997, pp. 307–326.

5 G. M. Sheldrick, *Acta Cryst.*, 2008, A**64**, 112–122.

6 G. M. Sheldrick, *Acta Cryst.*, 2015, C**71**, 3–8.

7 L. Loots and L. J. Barbour, in *The Importance of Pi-Interactions in Crystal Engineering*, eds. E. R. T. Tiekink and J. Zukerman-Schpector, John Wiley & Sons, Chichester, UK, 2012, Ch. 4 pp. 109–124.

8 Program cell_now, Bruker AXS Inc., Madison, WI, USA, 2008.

9 G. M. Sheldrick, Program TWINABS, University of Göttingen, Germany, 2001.

10 Program SAINT, Version 7.60a, Bruker AXS Inc., Madison, WI, USA, 2006.

11 G. M. Sheldrick, Program SADABS, Version 2.05, University of Göttingen, Germany, 2007.

12 G. R. Desiraju, *Angew. Chem. Int. Ed. (English)*, 1995, **34**, 2311–2327.

13 P. Groth, *Acta Chem. Scand.*, 1968, **22**, 143–158.

14 S. Kadoya, F. Hanazaki, Y. Iitaka, *Acta Cryst.*, 1966, **21**, 38–49.

15 Program TopSpin, Version 3.2, Bruker BioSpin GmbH, 2014.

16 N. Schultheiss and A. Newman, *Cryst. Growth Des.*, 2009, **9**, 2950–2967.

17 W. M. Haynes, Ed., *CRC Handbook of Chemistry and Physics*, CRC Press/Taylor and Francis, Boca Raton, FL, 96th edn., 2016.

18 P. Vishweshwar, A. Nangia and V. M. Lynch, *Cryst. Growth Des.*, 2003, **3**, 783–790.

19 A. D. Bond, *Chem. Commun.*, 2003, 250–251.

20 M. K. Stanton and A. Bak, *Cryst. Growth Des.*, 2008, **8**, 3856–3862.

21 A. R. Katritzky, R. Jain, A. Lomaka, R. Petrukhin, U. Maran and M. Karelson, *Cryst. Growth Des.*, 2001, **1**, 261–265.

22 M. A. Spackman and D. Jayatilaka, *CrystEngComm*, 2009, **11**, 19–32.

23 M. A. Spackman and J. J. McKinnon, *CrystEngComm*, 2002, **4**, 378–392.

24 J. J. McKinnon, M. A. Spackman and A. S. Mitchell, *Acta Cryst.*, 2004, B**60**, 627–668.

25 J. J. McKinnon, D. Jayatilaka and M. A. Spackman, *Chem. Commun.*, 2007, 3814.

26 D. J. Good and N. Rodríguez-Hornedo, *Cryst. Growth Des.*, 2009, **9**, 2252–2264.

27 L. Sreenivas Reddy, S. J. Bethune, J. W. Kampf and N. Rodríguez-Hornedo, *Cryst. Growth Des.*, 2009, **9**, 378–385.

28 D. Stepanovs, M. Jure, L. N. Kuleshova, D. W. M. Hofmann and A. Mishnev, *Cryst. Growth Des.*, 2015, **15**, 3652–3660.

29 D. S. Wishart, C. Knox, A. C. Guo, S. Shrivastava, M. Hassanali, P. Stothard, Z. Chang and J. Woolsey, *Nucleic Acids Res.*, 2006, **34**, D668–72.

30 D. P. Elder, R. Holm and H. L. de Diego, *Int. J. Pharm.*, 2013, **453**, 88–100.

31 M. J. Bowker and P. H. Stahl, in *The Practice of Medicinal Chemistry*, 2008, pp. 747–766.

CHAPTER 6 – CONCLUDING REMARKS

SUPRAMOLECULAR DERIVATISATION

The bioactive molecules selected for study in this thesis were successfully derivatised using cyclodextrins and GRAS co-formers.

CYCLODEXTRIN INCLUSION

Cyclodextrin inclusion complexes with DCB and fenthion showed markedly improved thermal stability and aqueous solubility, fulfilling the aim of improving the physicochemical properties limiting the use of these pesticides.

From the results presented in Chapter 3 and Chapter 4 we can conclude that the thermal stabilities of the pesticides DCB and fenthion are increased significantly by cyclodextrin inclusion. The loss of the pesticides from their respective CD complexes at elevated temperatures further indicates that the volatility of the pesticides is decreased upon complex formation. The increase in thermal stability and decrease in volatility show the potential for producing solid formulations that are safer for handling and transport. Furthermore, the reduction in volatility reduces the risk of exposure through inhalation when handling these toxic substances.

The increases in apparent solubility of DCB with β-CD and HPBCD were not as large as expected; however, the observed changes may provide a sufficient increase in bioavailability to warrant an aqueous CD formulation for plant growth regulation. The large increases in apparent fenthion solubility effected by HPBCD and RAMEB show promise for an aqueous formulation, eliminating the need for organic solvents, such as xylene or gasoline, which are currently in use. The solubilisation of fenthion by CDs may provide a further application in facilitating soil decontamination.

The formation of the solid-state inclusion complexes BCDFEN, TMAFEN and TMBFEN transformed fenthion into a solid material that can be easily transported and handled. This minimises the hazards currently associated with transporting and applying the volatile and toxic liquid.

From the data obtained in this study the cyclodextrins recommended for the formation of stable inclusion complexes with DCB and fenthion having improved stability and solubility over the untreated pesticides are DIMEB and TRIMEA respectively. The inclusion complexes DMBDCB and TMAFEN show the greatest improvement in thermal stability relative to their untreated guest molecules. However, owing to the high cost of the host compounds phase solubility experiments were not performed with these host molecules. In the case of fenthion, RAMEB may serve as an alternative to TRIMEA if a solid inclusion complex can be obtained. The RAMEB/fenthion system showed markedly improved solubility and as this commercially available host is often used as an

alternative to the methylated cyclodextrin hosts it may show similar improvements to the thermal stability of fenthion, as seen with TRIMEA. An alternative to DIMEB would be recommended for inclusion of DCB owing, once again, to the high cost of the selectively methylated cyclodextrins. While phase solubility studies provided erratic results for the RAMEB/DCB system, a dissolution profile may provide the required solubility information to support this choice in future.

MULTI-COMPONENT CRYSTALLINE SYSTEMS

The work described in Chapter 5 has shown that one can tailor the solubility of a product using the formation of salts and co-crystals. The modification of the apparent solubility of acipimox in the multi-component crystalline systems may provide a guide to rapid or slow-release formulation, depending on the desired application. The co-crystals ACPABEN and ACPBEN showed decreased aqueous solubility and could potentially be used in the manufacture of a slow-release dosage of acipimox. If a product with raised aqueous solubility were desired, the salt ACPAPYR showed the greatest increase in solubility. The greatest increase in the melting point relative to untreated acipimox was also observed with this salt. Therefore, if a thermally stable, water soluble formulation of acipimox is desired the recommended co-former is 4-aminopyridine. The salt ACPAPYR has the added advantage of being easily produced by both dry grinding and liquid-assisted grinding.

The co-formers investigated in this study were chosen on the basis of their potential hydrogen bonding interactions. The statistics of the hydrogen bonding motifs presented above show that the most common hydrogen bonding interaction between acipimox and the six co-formers was that between the pyrazine oxide of acipimox and an amine group of a co-former. From the frequency of occurrence of the hydrogen bonding motifs, one can infer that when choosing a suitable co-former for reaction with acipimox, those with an amine or amide moiety are most suitable. The proton transfer from the carboxylic acid of acipimox to a pyridyl nitrogen atom is observed in all structures where the co-former contains a pyridine ring. These interactions provide a guide for investigations with future potential co-formers.

FUTURE WORK

For the cyclodextrin inclusion complexes, studies such as relative humidity stability and long-term thermal stability determination would provide useful information for potential formulations. Investigations into the bioavailability changes imparted by the inclusion complexes could serve as a guide to the justification for pursuing these systems for industrial application. Comparative studies of the kinetics of hydrolysis or photolysis of the untreated and cyclodextrin-encapsulated pesticides could be performed to determine the efficacy of complexation in enhancing their chemical stability. Studies on the environmental impact of the cyclodextrin inclusion complexes with DCB and fenthion compared to the untreated pesticides would provide valuable information for possible implementation and regulation of such formulations.

Dissolution rate studies and bioavailability studies would be of importance moving forward with acipimox multi-component crystalline systems. Detailed study of the thermally-induced transition from the hydrated salts ACPAPYR-W and ACPTRA-W to their anhydrous counterparts (ACPAPYR and ACPTRA) was not pursued here and may provide further insight into the properties of these structures. The procedures for the regulation and intellectual property protection of salts and co-crystals are distinct from those for unsolvated species. Thus, investigation of such systems is of importance to researchers synthesising multi-component crystalline systems with APIs. The occurrence of the solvated salts and co-crystals with acipimox (ACPAPYR-W, ACPBEN, ACPTRA-W and ACPUREA) indicates that more solvated multi-component crystalline systems may exist with this API.

By investigating more co-formers with acipimox, the modification of the physicochemical properties could be tailored to the desired purpose. With the synthons presented in this thesis as a starting point one could limit the vast library of co-formers to likely candidates. As acipimox is prescribed as an additional treatment, co-crystallisation with a second antihyperlipidemic agent, based on the above synthons, may provide a dual dose formulation, assuming dosage differences are not of concern.

FINAL COMMENTS

The work presented here shows the value and applicability of supramolecular derivatisation to the beneficiation of bioactive compounds.

Each of the derivatised systems showed altered physicochemical properties when compared with the untreated bioactive compound. The structural, thermal and solubility data presented in this work will provide important perspective on any potential future developments towards practical applications of the supramolecular systems obtained here. The ability to control the physicochemical properties of medicinal, agrochemical and other functional molecules without altering their inherent biological activities is of fundamental importance for the many and varied bioactive products whose development is hindered by shortcomings of the type addressed in this thesis.

APPENDICES

The appendices have been attached as a zip archive file (Appendices.zip) organised as follows:

Appendix A: Crystallographic data files of the refined single crystal structures are presented. The .cif and .lis files are included and labelled according to the code name designated for each system.

Appendix B: The ^{1}H-NMR spectra, with integration values, used for stoichiometric ratio determinations are presented as PDF files. The files are labelled according to the designated code name of each system.

Appendix C: The geometric parameters and hydrogen bonding parameters for the structure BCDFEN are presented in a PDF file.

Appendix D: A list of the co-formers attempted for the formation of salts and co-crystals with acipimox.

Appendix E: The ^{1}H-NMR spectra and integration values for the solubility experiments of the multi-component crystalline systems formed with acipimox are available in PDF format. The files are labelled according to the code name designated for each system.